EUROPEAN ORGANIZATION FOR NUCLEAR RESEARCH (CERN)

November 12, 2018

Evidence for an $\eta_c(1S)\pi^-$ exotic resonance at LHCb and development of the Experiment Control System for the RICH upgrade

Giovanni Cavallero[1]

[1] *Università di Genova e INFN Genova*

Abstract

The first Dalitz plot analysis of $B^0 \to \eta_c(1S)K^+\pi^-$ decays using the data collected by the LHCb detector is presented. A satisfactory description of the data is obtained when including a contribution representing an exotic $\eta_c(1S)\pi^-$ resonant state. The significance of this exotic resonance, named $Z_c(4100)^-$, is more than three standard deviations, while its mass and width are $4096 \pm 20^{+18}_{-22}$ MeV and $152 \pm 58^{+60}_{-35}$ MeV, respectively. The spin-parity assignments $J^P = 0^+$ and $J^P = 1^-$ are both consistent with the data. In addition, the first measurement of the $B^0 \to \eta_c(1S)K^+\pi^-$ branching fraction is performed and gives $\mathcal{B}(B^0 \to \eta_c(1S)K^+\pi^-) = (5.73 \pm 0.24 \pm 0.13 \pm 0.66) \times 10^{-4}$, where the first uncertainty is statistical, the second systematic, and the third is due to limited knowledge of external branching fractions.

In order to increase the potential of discovery in indirect searches for New Physics in the heavy-flavour sector, the LHCb experiment will undergo a major upgrade in 2019-2020, allowing the detector to operate with a five-fold increase in the instantaneous luminosity. Innovative data acquisition and trigger systems will be implemented, and a brand-new LHCb detector will be installed. The RICH detectors, being of crucial importance in the analyses performed by the LHCb collaboration, will be redesigned, with new photon detectors and front-end electronics. The development, test and characterisation of the the prototypes for the opto-electronics chain of the RICH upgrade, are reported. The development of the prototype of the Experiment Control System and of the Inventory, Bookkeeping and Connectivity database for the RICH upgrade are presented.

CERN-THESIS-2018-243
26/03/2018

Università degli Studi di Genova

Scuola di Scienze Matematiche, Fisiche e Naturali

Tesi di Dottorato di Ricerca in Fisica
XXX Ciclo

Evidence for an $\eta_c(1S)\pi^-$ exotic resonance at LHCb and development of the Experiment Control System for the RICH upgrade

Candidate:
Giovanni Cavallero

Supervisors:
Prof. Alessandro Petrolini
Dr. Roberta Cardinale

External Supervisor:
Dr. Claudia Patrignani

Referees:
Dr. Carmelo D'Ambrosio
Dr. Lucio Anderlini

Contents

1 Introduction

The constituent quark model [1, 2] has successfully described the plethora of strongly interacting particles (hadrons) proliferated around the 1960s as composed by either quark-antiquark $q\bar{q}$ pairs (mesons) or sets of three quarks qqq or $\bar{q}\bar{q}\bar{q}$ (baryons or antibaryons). Such states form multiplets according to the symmetries of their flavour, spin and spatial wave functions. The quark model also hypothesised the existence of multiquark states beyond mesons and baryons, for which no unambiguous evidence have been found for almost 40 years, in spite of considerable experimental efforts in the spectroscopy of hadrons composed by light-quarks. Since the discovery of the $X(3872)$ state in 2003 [3], several exotic hadron candidates have been observed, as reported in recent reviews [4–9] and summarised in Sec. 2. The decay modes of these states indicate that they must contain a heavy quark-antiquark pair in their internal structure; however, they cannot easily be accommodated as an unassigned charmonium ($c\bar{c}$) or bottomonium ($b\bar{b}$) state due to either their mass, decay properties or electric charge, which are inconsistent with those of pure charmonium or bottomonium states. Given the large mass of the c and b quarks, the spectra of these quarkonium states can be well described by potential models based on the main properties of the theory of the strong interaction, the Quantum Chromodynamics (QCD), as confirmed experimentally. The observation of states not fitting with these spectra led to a renaissance of the heavy-hadron spectroscopy. Moreover, provided that the constituents form colour-singlet bound states, there may be additional configurations allowed by QCD beyond the mesons, baryons and multiquark states hypothesised by the quark model, such as glueballs, made of valence gluons, and hybrid mesons, made of both valence quarks and gluons.

Different interpretations have been proposed about the nature of these exotic hadrons [4–6], including their quark composition and binding mechanisms. In order to improve the understanding of these hadrons, it is important to search for new exotic candidates, along with new production mechanisms and decay modes of already observed unconventional states. Thanks to the huge sample of c- and b-hadrons provided by the Large Hadron Collider (LHC) at CERN, the LHCb experiment, having excellent tracking and particle identification systems, has a leading role on the conventional and exotic hadrons spectroscopy. The LHCb experiment, introduced in Sec. 3, has been designed to perform searches for indirect evidence of New Physics (NP) beyond the Standard Model (SM) in *CP* violating processes and rare decays of beauty and charm hadrons. However, the excellent performance of the LHC and of the LHCb experiment allowed to significantly extend the LHCb physics programme. For instance, in the exotic spectroscopy sector, LHCb provided the confirmation of the first unambiguous exotic state, the charged $Z(4430)^-$ charmonium-like state [10, 11], the discovery of two pentaquark candidates [12], and the confirmation of the $X(4140)$ together with the observation of three new neutral charmonium-like candidates [13, 14].

During my PhD I performed a search for exotic hadrons through the first Dalitz plot analysis of $B^0 \to \eta_c(1S)K^+\pi^-$ decays, where the η_c meson is reconstructed into the $p\overline{p}$ final state.[1]. The $B^0 \to \eta_c(\to p\bar{p})K^+\pi^-$ decay channel has a relatively low branching fraction, that can be estimated to be of the order of 10^{-6} from the information available in Ref. [15]. In addition, the trigger efficiency on fully hadronic final-states is limited with the

[1]Natural units with $\hbar = c = 1$ and the simplified notation η_c to refer to the $\eta_c(1S)$ state are used throughout the thesis. In addition, the inclusion of charge-conjugate processes is always implied.

current LHCb detector, and the decay channel presents large backgrounds typical of an hadronic collider. However, using a data sample corresponding to an integrated luminosity of $4.7\,\text{fb}^{-1}$ of pp collision data collected with the LHCb detector at centre-of-mass energies of $\sqrt{s} = 7,\ 8$ and $13\,\text{TeV}$ in 2011, 2012 and 2016, respectively, it has been possible to obtain the first evidence for an $\eta_c\pi^-$ resonance, whose quark content is manifestly exotic. The analysis of the $B^0 \to \eta_c(\to p\bar{p})K^+\pi^-$ decay channel is reported in Sec. 4.

The limitations caused by the current LHCb trigger strategy will be removed after the LHCb upgrade foreseen in 2019, having the main goal to reduce the statistical uncertainties on many key flavour observables to the level of the theoretical errors. This will be achieved with a five-fold increase in the instantaneous luminosity and implementing an innovative and flexible software-based trigger system, requiring the readout of the sub-detectors at the full 40 MHz LHC bunch crossing rate. The new trigger strategy will allow to enhance the detection efficiency of hadronic final states, and analyses of decay channels such as $B^0 \to \eta_c(\to p\bar{p})K^+\pi^-$ will significantly profit from the upgraded readout and trigger architectures. An overview of the LHCb detector upgrade is given in Sec. 5.

In view of the new readout and trigger schemes, the RICH detectors, providing the charged hadrons identification crucial for the LHCb physics programme, and being of fundamental importance in the rejection of the background in decay channels such as $B^0 \to \eta_c(\to p\bar{p})K^+\pi^-$, will be re-designed and new photodetectors and frontend electronics will be installed, as described in Sec. 5. During my PhD I contributed to the test, calibration and validation of the prototypes of the photon detector modules for the RICH upgrade, in the laboratory at CERN and during test-beams. I also actively participated to the integration of the RICH upgrade front-end with the new LHCb data acquisition architecture. In the final part of this thesis, my contributions to the RICH upgrade are reported. They comprise the development of a database accounting for the inventory, bookkeeping and connectivity of the new RICH upgrade components, whose implementation is described in Sec. 6, and the development of the prototype for the RICH upgrade Experiment Control System, reported in Sec. 7.

Generation	Particle	Symbol	Electric charge	Mass [MeV]
I	up quark	u	+2/3	$2.2^{+0.6}_{-0.4}$
	down quark	d	-1/3	$4.7^{+0.5}_{-0.4}$
	electron neutrino	ν_e	0	
	electron	e^-	-1	0.5109989461 (31)
II	charm quark	c	+2/3	1280 ± 30
	strange quark	s	-1/3	96^{+8}_{-4}
	muon neutrino	ν_μ	0	
	muon	μ^-	-1	105.6583745 (24)
III	top quark	t	+2/3	$(173.1 \pm 0.6) \times 10^3$
	bottom quark	b	-1/3	4180^{+4}_{-3}
	tau neutrino	ν_τ	0	
	tau	τ^-	-1	1776.86 ± 0.12

Table 1: The elementary fermions of the SM. Masses taken from PDG [15]. Reported top quark mass is from direct measurements. Neutrino masses are unknown.

2 Theory and experimental observations of exotic hadrons

In this chapter I focus on the latest experimental observations of hadrons not fitting with the conventional mesons and baryons, underlining the properties making them as natural candidates for the so-called exotic hadrons.

The constituent quark model, being the first phenomenological model able to categorise, explain and predict the hadrons composed by light quarks, is introduced in Sec. 2.2. The connection of the quark model with the QCD is reported in Sec. 2.3. Since the unambiguous candidates for exotic hadrons have been discovered studying decays involving $c\bar{c}$ and $b\bar{b}$ mesons in the final state, an introduction to these systems, called quarkonium states, is given in Sec. 2.4. The experimental evidences and observations of exotic hadrons are reported in Sec. 2.6 and the proposed theoretical models for these non-conventional states are summarised in Sec. 2.10.

2.1 The Elementary Particles in the Standard Model

The elementary building blocks of matter in the SM are quarks and leptons, spin-1/2 particles organised in three generations. Quarks and leptons, characterised by different flavours, are listed in Table 1. For any of these particle, a respective antiparticle exists, having the same mass, spin and lifetime but opposite parity and additive quantum numbers.

In the quantum field theory language, all the fundamental interactions between matter fields, the particles, derive from a general principle, the requirement of local gauge invariance. The gauge principle is the requirement that some global symmetries of the lagrangian hold locally, meaning that the associated transformations depend on the space-time coordinate. To keep the invariance of the lagrangian under these local

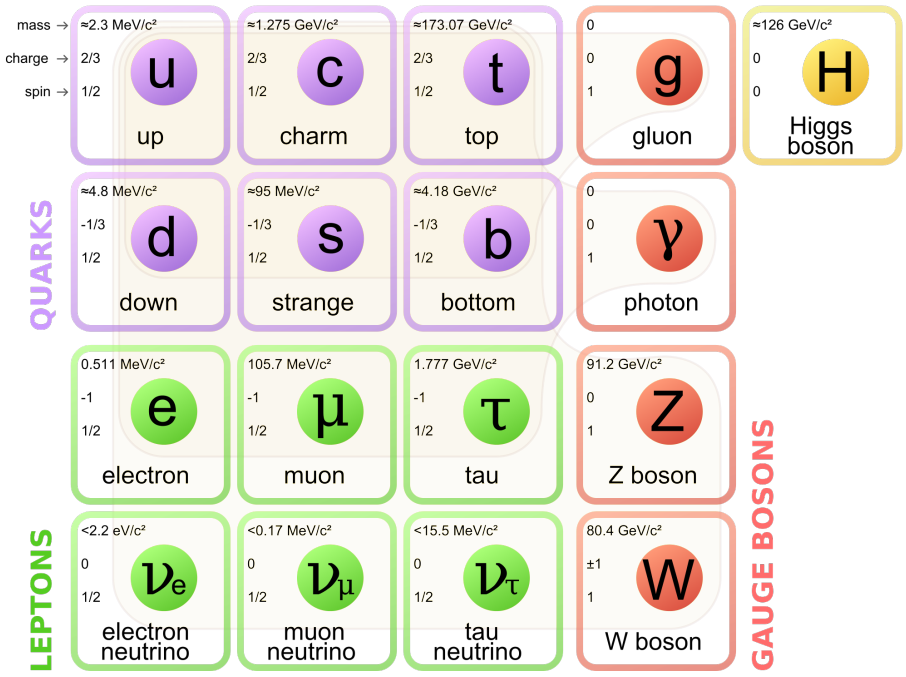

Figure 1: The Standard Model particles.

transformations, an extra-term involving the introduction of a spin-1 field, the gauge boson, is needed. The vertices between matter fields and this gauge boson are generated. These vertices represent the interaction between particles deriving from the required symmetry, parametrised through the fundamental representation of a unitary group, and the gauge boson is the mediator of this interaction. The gauge parameter associated to the transformation is called the coupling constant of the interaction. The SM is a gauge theory based on the symmetry group $SU(3)_C \otimes SU(2)_L \otimes U(1)_Y$, which describes strong, weak and electromagnetic interactions via the exchange of spin-1 gauge fields. The SM particles, including these gauge bosons, are shown schematically in Figure 1.

The Electroweak theory, describing the electromagnetic and weak interactions, is based on the $SU(2)_L \otimes U(1)_Y$ symmetry. The subscript L in $SU(2)_L$ indicates that the weak interaction only acts on fields with left chirality, corresponding to left-handed (right-handed) helicity fermions (antifermions) in the limit of massless particles. All the SM particles can interact through the weak interaction. In particular, neutrinos can only interact through the weak interaction. Doublets composed by the leptons of each generation, *e.g.* $(\nu_e, e^-)_L$, transform as the fundamental representation of $SU(2)_L$, while the fields with right chirality, *e.g.* $\nu_{e,R}$ and e^-_R transform as the trivial representation of this group, *i.e.* they do not enter the weak interaction. The extension of the symmetry group to $SU(2)_L \otimes U(1)_Y$, where the subscript Y identify the hypercharge, allowed the unification of the electromagnetic and weak interactions. Since the right handed neutrinos ν_R has no electric charge, zero hypercharge and does not interact weakly nor strongly, it is not considered in the SM. The experimental data on the decays of strange mesons, lead to the conclusion that the flavour eigenstates in the quarks sector are not the same as the weak eigenstates. As a consequence, for quark fields, the doublet transforming as the fundamental representation of $SU(2)_L$, is of the kind $(u, d')_L$, where d'_L is a linear combination of the down type quarks across each generation.

The local gauge invariance requirement under the $SU(2)_L \otimes U(1)_Y$ symmetry group leads to the introduction of four gauge fields that, after the electroweak unification, are the $W^{\pm}$ boson, charged carriers of the weak interaction, the Z boson, neutral carrier of the weak interaction, and the photon. The structure of the representations of the $SU(2)$ group is non-abelian, generating additional terms in the SM lagrangian describing the self-interactions between these gauge bosons, except between the γ and the Z.

The requirement of gauge invariance under the fundamental representations of the $SU(2)_L \otimes U(1)_Y$ group, forbids the writing of a mass term for these gauge bosons. The masses in the SM are generated through the mechanism of the spontaneous symmetry breaking. The lagrangian remains fully symmetric under the gauge transformations, but the ground state, the vacuum, is not symmetric. With the introduction of the scalar Higgs boson H^0 in the theory, the $W^{\pm}$ and the Z bosons acquire a mass. The spontaneous symmetry breaking also generates fermion masses, with the exception of neutrinos. As shown in Table 1, quarks and leptons come in three generations. Each family corresponds to a copy of the same $SU(2)_L \otimes U(1)_Y$ structure, with masses as the only difference, and inside each generation quarks and leptons are organised in doublets. The global symmetries of the SM do not allow interaction vertices between quarks and leptons, while the interaction mediated by the charged $W^{\pm}$ bosons allows the change of flavour within each doublet.

The quarks mixing, introduced to take into account the experimental observations associated to the weak interaction, allows the transformation of the quarks flavour between one generation and the other. The relation between weak eigenstates and flavour eigenstates, matching the mass eigenstates, is provided by the Cabibbo-Kobayashi-Maskawa (CKM) matrix, introducing a complex term in the SM lagrangian accounting for *CP* violating processes. On the other side, lepton mixing between different generations does not occur, related to the assumption of massless neutrinos in the SM. The absence of leptons mixing, and the association of the same gauge parameters to the $SU(2)_L \otimes U(1)_Y$ transformations required by the group theory, imply the lepton flavour universality within the SM, *i.e.* the leptons of the three generations couples with the same strength to the $W^{\pm}$ or Z bosons independently from their flavour.

The strong interaction is based on the $SU(3)_C$ symmetry. The corresponding gauge fields are the gluons. Only quarks can interact through the strong interaction. The quantum number associated with the $SU(3)_C$ symmetry is the colour and each of the quark types listed in Table 1 come into three colours. Because of QCD properties, summarised in Sec. 2.3, quarks cannot be observed as free but only in bound states called hadrons, that are colour-singlet states. The properties of these bound states are very different from electromagnetic bound states, *e.g.* atoms, due to gluons self-interactions allowed by the non-abelian nature of the $SU(3)_C$ transformations.

The most common hadrons are protons and neutrons, whose constituents are the down (d) and up (u) quarks. Protons and neutrons are uud and udd bound states, respectively. As described later, protons and neutrons contain additional quark-antiquark pairs (sea quarks) besides the constituent quarks (valence quarks). As shown in Table 1 and Fig. 1, six different flavours exist for quarks: down (d), up (u), strange (s), charm (c), bottom (or beauty, b) and top (or truth, t).

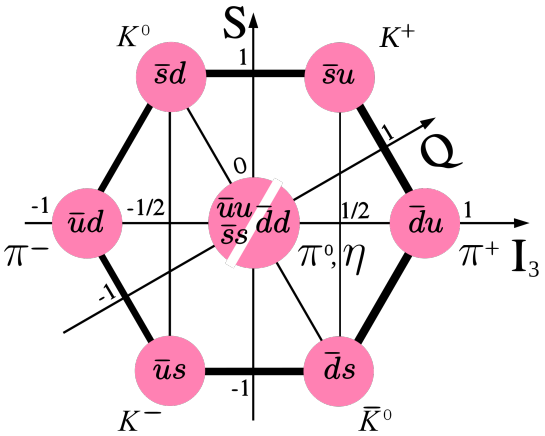

Figure 2: $SU(3)_f$ diagram showing the octet representation for the pseudoscalar mesons made of u, d and s quarks as a function of the isospin component I_3 and the strangeness S.

2.2 The constituent quark model framework

In 1964, Gell-Mann [1] in the USA and Zweig [2] at CERN independently proposed a scheme to classify the plethora of hadrons discovered in the previous years. They proposed that hadrons are made up of constituents, called quarks by Gell-Mann: baryons are made of three quarks, mesons of a quark and an antiquark.

The quark model scheme is based on the $SU(3)_f$ symmetry, where the suffix stands for flavour (to distinguish $SU(3)_f$ from the mathematically equivalent group $SU(3)_C$). Three flavours were sufficient to classify the hadrons at that time, the u, d and s quarks. The two quarks present in normal matter, u and d, are an isospin I doublet, the former with component $I_3 = +\frac{1}{2}$, the latter with $I_3 = -\frac{1}{2}$. The isospin quantum number can be associated to the flavour of each of them. The quantum number identifying the flavour of the quark s is the strangeness S, which takes the value $S = -1$ (the antiquark $\bar{s}$ carries $S = +1$).

The $SU(3)_f$ group has two different fundamental representations, called $\mathbf{3}$ and $\bar{\mathbf{3}}$, that can be associated respectively to quarks and antiquarks with flavour u, d or s. From the fundamental representations of $SU(3)_f$ one can build the mesons as

$$\mathbf{3} \otimes \bar{\mathbf{3}} = \mathbf{1}_\mathrm{A} \oplus \mathbf{8}_\mathrm{S}, \tag{1}$$

where the suffixes A and S stand for antisymmetric and symmetric, respectively, and indicate the properties of the flavour wave function in the interchange of the constituents.

The $SU(3)_f$ multiplets can be drawn in a plane, taking as axes I_3 and the hypercharge Y (that coincides with the strangeness if only u, d and s quarks are considered). For the ground level mesons, where the quark-antiquark system has zero orbital angular momentum, there are two allowed J^P configurations: the pseudoscalar mesons are in a spin-singlet configurations and therefore they have $J^P = 0^-$; the vector mesons are in a spin-triplet configuration and hence they have $J^P = 1^-$. The $SU(3)_f$ octet representation of pseudoscalar mesons is shown in Fig. 2.

If the $SU(3)_f$ symmetry were exact, all particles in a multiplet would have the same mass. Since the u, d and s masses are different, the particles in the multiplets have

different masses. In addition, a second order effect resulting in mass splittings is due to the electromagnetic interaction.

Besides $q\bar{q}$ states, from the $SU(3)_f$ fundamental representations one can build baryons, hadrons composed by three quarks. Baryons (the following is analogue also for antibaryons built using the $\bar{\mathbf{3}}$ representation) can be built as

$$\mathbf{3} \otimes \mathbf{3} \otimes \mathbf{3} = \mathbf{10_S} \oplus \mathbf{8_{MS}} \oplus \mathbf{8_{MS}} \oplus \mathbf{1_A}. \tag{2}$$

As before, each suffix reflects how the states behave for quarks exchange combinations in the flavour wave function. The suffix MS identify states having a mixed symmetric in either quark 1 and 2 or quark 2 and 3. Since the fundamental representations of the $SU(2)$ group, describing the spin states, can be combined as

$$\mathbf{2} \otimes \mathbf{2} \otimes \mathbf{2} = \mathbf{2_{MS}} \oplus \mathbf{2_{MS}} \oplus \mathbf{4_s}, \tag{3}$$

the interplay between spin and flavour symmetries is important when building baryon multiplets, where the Pauli exclusion principle must be taken into account, given that these hadrons can involve identical particles,. The J^P of ground state (*i.e.* symmetric spatial wave-function) baryons can be either $J^P = \frac{1}{2}^+$ or $J^P = \frac{3}{2}^+$. The proton and the neutron belong to the $J^P = \frac{1}{2}^+$ multiplet. The decuplet and the octet are shown in Figure 3.

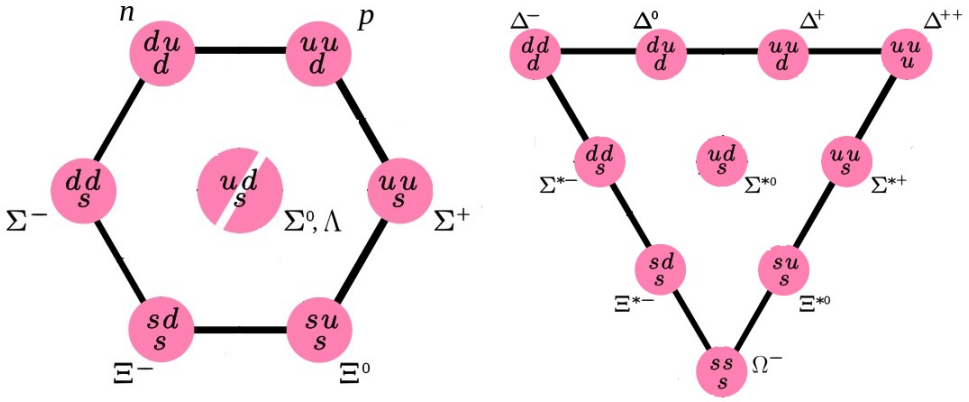

Figure 3: $SU(3)_f$ diagram showing the octet (left) and the decuplet (right) representations for the ground state baryons made of u, d and s quarks.

The discovery of the Ω^- [16], the baryon with three strange quarks, marked a triumph of the quark model. However, since the Δ^{++}, Δ^- and Ω^- are composed of three identical quarks and they are spin-3/2 particles, the wave function could only be made antisymmetric with the introduction of an additional degree of freedom, the colour, assuming there were three quarks for each flavour, each with a different colour charge. The observed restriction to a $J^P = \frac{1}{2}^+$ octet and a $J^P = \frac{3}{2}^+$ decuplet is a consequence of the antisymmetry of the colour wave function, that is a fundamental characteristic of QCD.

When including the charm and beauty quarks, $SU(4)_f$ and $SU(5)_f$ symmetries could be used to build other physical multiplets (the top quark does not hadronise since it decays before the characteristic time scale of the strong interaction, of the order of 10^{-23} s). However, because of the much higher c and b masses, the symmetry breaking is hardly negligible.

2.3 Quantum Chromodynamics

Since the quarks introduced in the formulation of the quark model could not be seen as free particles, they were considered mathematical objects useful to classify hadrons. Historically, the connection between the quark model and the QCD started from experiments studying the nucleon structure, the deep-inelastic scattering experiments. These experiments concluded that the proton and the neutron contain point-like objects, called partons, later identified with quarks and gluons. In particular, the internal structure of these hadrons could be understood in terms of the three quarks that determine the spectroscopy, called valence quarks, the gluons, the quanta of the colour field, and the quark and antiquark of the sea, produced by the interactions between quarks and gluons with decreasing probability for increasing quark masses.

The first experimental evidence of the existence of the colour degree of freedom, introduced ad-hoc in the quark model, came from measurement of the ratio between the cross-section for electron-positron annihilation into hadrons and into the muon-antimuon final state, given by

$$\mathrm{R} = \frac{\sigma(e^+ + e^- \to \text{hadrons})}{\sigma(e^+ + e^- \to \mu^+\mu^-)} = N_C \sum_{\text{flavour}} e_i^2, \tag{4}$$

where N_C is the number of colours, the sum runs over the number of flavours over threshold corresponding to the centre-of-mass energy $\sqrt{s}$ of the collision and e_i is the charge of the quark of flavour i. As shown in Figure 4, all the experimental results are consistent with $N_C = 3$.

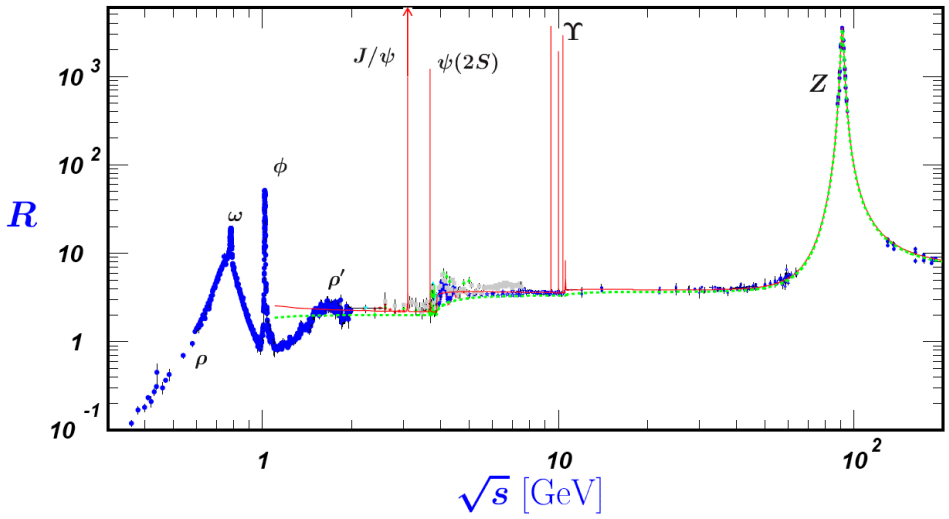

Figure 4: Ratio $R(\sqrt{s})$ from the Particle Data Group (PDG) [15]. The green dashed line is the prediction from the quark model.

These results, together with the explanation of the $\pi^0 \to \gamma\gamma$ decay amplitude provided by the introduction of the colour degree of freedom, led to the interpretation of the colour as the charge of the strong interaction. The resulting gauge theory is similar to QED, but the interaction between quarks is generated by an octet of massless colour gauge bosons, the gluons.

The two fundamental representations of $SU(3)_C$ are **3**, corresponding to the three colour charges (conventionally called red, green and blue), and $\bar{\mathbf{3}}$, corresponding to the anticolour charges. Quarks carry colour charges, antiquarks carry anticolour charges. Due to the non-abelian structure of the $SU(3)_C$ group, also the gluons carry a colour charge, meaning that they can interact with themselves. The gluons belong to the octet that is obtained by combining a colour and an anticolour, preserving the colour charge in the interaction of a quark with a gluon. Hence, while quarks and antiquarks are in the fundamental representation of the $SU(3)_C$ colour gauge group, gluons belong to the adjoint representation.

The direct gluon-gluon interaction leads to the decreasing of the coupling constant at increasing energy. The theory is said to be asymptotically free. Thus, at high energy, the quarks and gluons behave like free particles, the distinctive feature of QCD, according to the deep-inelastic scattering results.

Naively, in QED, the creation of virtual e^+e^- pairs from the vacuum has the effect of screening the interacting fermion: the vacuum acts as a dielectric medium, partially screening the charge at large distance. Probing the fermion at higher energy, *i.e.* approaching closer to it, the less complete is the screening and the greater is the effective charge. In QCD, beside the creation of virtual $q\bar{q}$ pairs leading, as in QED, to a screening of the quark colour, there are mainly virtual gluons interacting with each other and with any probe particle. The action of gluons is a smearing of the colour charge, which results in an effect of the opposite sign from that of quark-antiquark pairs, called antiscreening. The net result is that the colour charge decrease with decreasing distance. Politzer, Gross and Wilczek discovered the asymptotic freedom in 1973 [17,18]. The property is quantified introducing a dependence on the energy scale Q^2 of the process in the QCD coupling constant α_s, that becomes the running coupling constant

$$\alpha_s(Q^2) = \frac{1}{\beta_0 \log \frac{Q^2}{\Lambda^2_{\mathrm{QCD}}}}, \tag{5}$$

where $\beta_0 = \frac{33-2N_f}{3}$, being N_f the number of active quark flavours at the energy scale Q^2. The constant Λ^2_{QCD} depends on the arbitrary scale Q^2, conventionally taken as the mass of the Z boson, as

$$\Lambda^2_{\mathrm{QCD}} = Q_0^2 \exp\left(-\frac{1}{\beta_0}\frac{1}{\alpha_s(Q_0^2)}\right). \tag{6}$$

The energy scale dependence of α_s has been proven by several experiments as shown in Figure 5. The confinement property, related to the increase of α_s at low energy, is the reason why quarks and gluons remain hidden inside hadrons forming colour singlets. The presence of confinement has not been demonstrated analytically thus far.

Non-perturbative effects take over at the energy scale represented by $\Lambda_{\mathrm{QCD}} \sim 200\,\mathrm{MeV}$. For energies much larger than Λ_{QCD}, α_s is much smaller than 1, and perturbation theory provides accurate calculations for strong processes. On the other side, for energies of the order of or below than Λ_{QCD}, the perturbative formalism cannot be used. Consequently, a number of theoretical approaches has been explored, each one having a limited range of validity [19].

Since the low energy regime of QCD is related to the origin of mass, several theoretical and experimental efforts have been put in order to understand this non-perturbative

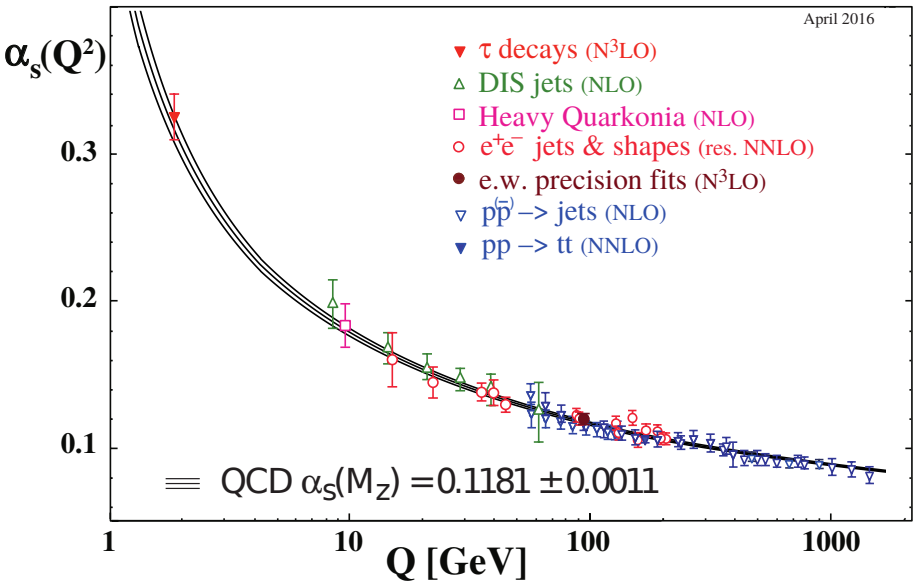

Figure 5: Summary of α_s measurements as a function of the energy scale Q. Picture taken from [15].

regime. Indeed, the coupling of light quarks to the Higgs field is only responsible for $\sim 1\%$ of the visible mass of our present-day universe, the rest is a consequence of the interactions between quarks and gluons. Moreover, the approximate calculations available in the low energy regime of QCD is often the limiting factor in the indirect searches for NP involving the study of hadronic decays.

The average energies and momenta of partons inside hadrons are below the scale where perturbative methods are justified. Hence, the fundamental degrees of freedom of the underlying theory of QCD do not directly manifest themselves in the physical spectrum of hadrons, which are complex, colourless, many-body systems. At present it is still impossible to derive the hadron spectrum analytically from the QCD lagrangian. Many phenomenological models have been developed, which quite successfully described certain aspects of the properties of light hadrons in terms of effective degrees of freedom. The quark model has been the first one, followed by the Bag Model [20, 21], the Flux-Tube Model [22] and the QCD Sum Rules [23]. In the heavy quarks sector, QCD-motivated potential models successfully explain the spectrum of heavy quarkonium states, that are $c\bar{c}$ and $b\bar{b}$ bound states. Moreover, the NRQCD [24, 25] effective field theory is able to explain some of their annihilation and production properties.

Lattice QCD is another approach to QCD, implementing the gauge theory of quarks and gluons on a discretised space-time lattice of finite size. In Lattice QCD, hadronic properties are calculated by evaluating path integrals over the space-time lattice using Monte Carlo methods. In principle, the numerical predictions given by Lattice QCD can be systematically improved by decreasing the lattice spacing and increasing the size of the lattice. However, the required computing power grows dramatically as the masses of the quarks are decreased. In recent years, thanks to algorithmic and computational advances, Lattice QCD calculations allowed to obtain the lowest-lying mesons and baryons spectrum, shown in Figure 6. Despite these progresses, the simulation of excited light mesons and baryons performed using lattice-QCD is not under control thus far.

One of the main goals of the physics of strong interactions is hence the determination and the understanding of the spectrum of all the hadrons observed in nature from the underlying theory of QCD, for which considerable theoretical and experimental efforts are required.

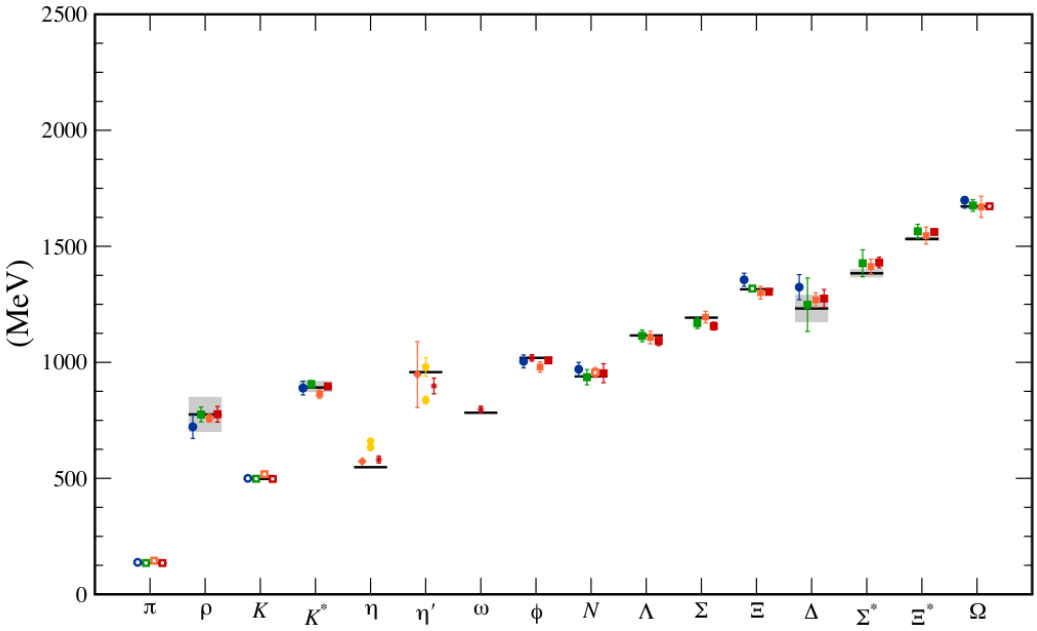

Figure 6: Light hadrons spectrum from Lattice QCD. Symbol shape denotes the formulation used for sea quarks. Asterisks represent anisotropic lattices. Open symbols denote the masses used to fix parameters. Filled symbols (and asterisks) denote results. Red, orange, yellow, green and blue stand for increasing number of ensembles (i.e. lattice spacing and sea quark mass). Horizontal bars (grey boxes) denote experimentally measured masses (widths). Figure taken from [26].

2.4 Quarkonium states

A special category of mesons is the quarkonium, a bound state of a quark and an antiquark of the same flavour. In particular, a quarkonium is called charmonium when composed of a $c\bar{c}$ pair, and bottomonium when made of a $b\bar{b}$ pair. Quarkonium states are categorised according to the total spin of the $q\bar{q}$ system, S, the orbital angular momentum between the quark and the antiquark, L, and the total angular momentum of the system ($J = L \oplus S$). The spectroscopic notation $n^{2S+1}L_J$, where n is the the radial excitation quantum number, is often used to label the quarkonium states. The parity P of a $q\bar{q}$ system is given by $P = (-1)^{L+1}$. The charge-conjugation parity C is given by $C = (-1)^{L+S}$. Therefore, the allowed J^{PC} reads: 0^{-+}, 0^{++}, 1^{--}, 1^{+-}, 1^{++}, etc.

A given quarkonium system has many states characterised by different masses and quantum numbers. The ground state has $S = L = 0$ and no radial excitations of the quark-antiquark system. It is called $\eta_c(1S)$ in the charmonium spectrum and $\eta_b(1S)$ in the bottomonium spectrum. The next higher mass states are $S = 1$ and $L = 0$ vector mesons, called J/ψ and $\Upsilon(1S)$, historically important since their observations have been acknowledged as the first evidences of the charm and beauty quarks, respectively. The

higher mass states differ for spin couplings, orbital angular momenta and radial excitations of the quark-antiquark system. The classification and the study of these states is named spectroscopy.

The quarkonium states with masses below the threshold for decays to open-flavour hadrons to be kinematically allowed ($m_{D\bar{D}} \sim 3.73\,\text{GeV}$ for charmonium and $m_{B\bar{B}} \sim 10.56\,\text{GeV}$ for bottomonium), are typically narrow states which decay via the electromagnetic and strong interactions to lower mass quarkonium states, light hadrons or charged leptons. This property can be understood in terms of the empiric Okubo-Zweig-Iizuka (OZI) rule [2, 27, 28]: decays having diagrams with the quark lines of the initial state connected to those of the final state are favoured, while decays where these lines are disconnected are suppressed. The OZI rule can be qualitatively understood in terms of QCD properties. Since hadrons are colour singlets, the connection between initial and final state quarks must be via a colour-singlet combination. Thus, at least two gluons must be exchanged. The number of exchanged gluons also depends on the J^{PC} quantum numbers of the decaying quarkonium state, *e.g.* at least three for the J/ψ meson. The decay width calculation is proportional to $\alpha_s^{n_g}$, where n_g is the number of intermediate gluons. At the mass scale of the involved quarkonium states, α_s is less than one, and hence the decay width is limited for OZI-suppressed processes. On the other side, quarkonium states above the relevant open-flavour threshold generally have much larger decay widths that are dominated by strong decays to open-flavour hadrons.

Given the large mass of charm and beauty quarks ($m_b > m_c >> \Lambda_{QCD}$), charmonium and bottomonium are very important systems used to improve the understanding of the strong interaction, providing a laboratory where perturbative and non-perturbative aspects of QCD live together. Indeed, α_s at the scale of these quark masses is small enough that some aspects of charmonium and bottomonium can be calculated using perturbation theory. The large masses also allow to treat these states as non-relativistic systems, including non-relativistic potential models standing out due to their simplicity, where quark interaction is modelled using a radial potential in the usual Schrödinger equation. Indeed, it is possible to reproduce the observed quarkonium spectra starting from a simple parameterisation of this potential, named Cornell potential [29], taking into account the confinement property through a linear term and the asymptotic freedom through a Coulomb-like and one-gluon exchange term, given by

$$V(r) = -\frac{k}{r} + \beta r, \tag{7}$$

where the parameters involved are k, depending on the size of the hadrons considered and spanning between 0.25 and 0.53 [30], and $\beta \sim 0.18\,\text{GeV}^2$ [26]. This potential picture can be justified for heavy quarkonia by Effective Field Theories like NRQCD or potential non-relativistic QCD (pNRQCD) [31, 32], with a potential that can be expressed as a quark mass expansion, where the Cornell potential is a good approximation of the first term.

Starting from this simple potential, many different models have been developed and tuned on experimental data. The addition of relativistic corrections allows an excellent agreement between predictions and experimental data, as shown in Figure 7, making the quarkonium system one of the best understood of the non-perturbative QCD domain.

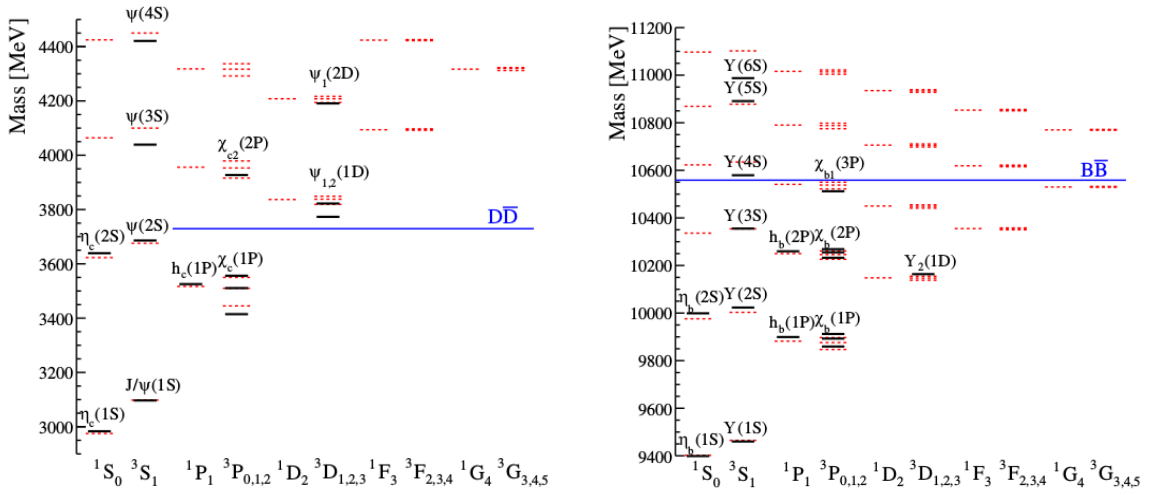

(a) (b)

Figure 7: The spectra of (a) charmonium and (b) bottomonium mesons. The red dashed lines indicate the expected states and their masses based on the Godfrey-Isgur relativised potential model [33]. The black solid lines indicate the experimentally established states. The open flavour threshold is also indicated with the blue line. Pictures taken from [9].

2.4.1 Quarkonium production mechanisms

The main experimental progresses in the quarkonium spectroscopy have been achieved by the BaBar [34] and Belle [35] collaborations, operating respectively at the PEPII and KEKB B-factories, by the CLEO [36] and BESIII [37] collaborations, operating at the c- and τ-factories, and by the CDF [38], D0 [39], ATLAS [40], CMS [41] and LHCb [42] collaborations operating at hadronic colliders, CDF and D0 at the Tevatron, ATLAS, CMS and LHCb at the Large Hadron Collider at CERN.

The BaBar, Belle, BESIII and CLEO experiments exploited e^+e^- collisions, profiting of clean experimental environments. However, the relevant production cross-sections are at the nb level and hence event rates are low. In contrast, the ATLAS, CDF, CMS, D0 and LHCb experiments, exploiting proton-(anti)proton collisions, can profit of larger production cross-sections, of the order of mb for charm pairs and of the order of 100 μb for beauty pairs. Moreover, as described below, while the e^+e^- experiments can only access B^0, $B^\pm$ and to a lesser extent B_s^0 mesons, all the b-hadrons can be produced at hadronic colliders. Charm and beauty particles are produced with a boost, hence the isolation of events of interest is possible thanks to displaced decay vertices. However, the reconstruction of final states containing neutral particles is very challenging since a large number of particles not coming from b-decays, namely the combinatorial background, is produced at hadronic colliders. The quarkonium production mechanisms are different and they also depend on the collider type, as summarised in the following.

2.4.2 B-factories

The $\Upsilon(4S)$, having a mass of $\sim 10.58\,\text{GeV}$, is just above the open-beauty threshold. It decays $\sim 50\%$ of the time into a B^0–$\overline{B}^0$ pair and the other $\sim 50\%$ into a B^+–B^0 pair. The decay properties of the $\Upsilon(4S)$ have been exploited by the B–factories, like PEPII

and KEKB, where the centre-of-mass energy of the e^+e^- collisions has been tuned to match the $\Upsilon(4S)$ mass value, in order to have clean events where only the decay products of the B–$\overline{B}$ pair are present. The high $\sigma_{b\bar{b}}/\sigma_{\text{tot}}$ ratio makes the $e^+e^- \to \Upsilon(4S) \to B\overline{B}$ process one of the main efficient mechanism to produce B^0 and B^+ mesons. Also B_s^0–$\overline{B}_s^0$ pairs can be produced at the B–factories, tuning the e^+e^- energy at the $\Upsilon(5S)$ mass; this process is less efficient, since only the $\sim 20\%$ of the time the $\Upsilon(5S)$ decays into a B_s^0–$\overline{B}_s^0$ pair. Other heavier b-hadrons are not accessible by the B–factories.

The charmonium production mechanisms at the B-factories, shown in Figure 8, includes:

- B–decays: the B^0 (B^+) meson is composed by an antiquark $\bar{b}$ and a quark d (u). B-mesons undergo weak decays, where the dominant contribution is given by the $\bar{b} \to W^+(\to c\bar{s})\bar{c}$ sub-process. The c and $\bar{c}$ can hadronise to form a charmonium state if they are produced close to each other in the phase space. The d (u) spectator quark can combine with the $\bar{s}$ to produce a K^0 (K^+). In the factorisation approximation [43], the possible quantum numbers of the charmonium state are $J^{PC} = 0^{-+},\ 1^{--}$ and 1^{++};

- two-photon fusion: both the e^- and the e^+ radiate photons that subsequently interact producing a C-even final state. The allowed quantum numbers for the charmonium states produced via this process are $J^{PC} = 0^{\pm+}$ and $2^{\pm+}$;

- double charmonium production: Belle observed that the $e^+e^- \to J/\psi c\bar{c}$ process is the dominant mechanism for prompt J/ψ production. Charge conjugation invariance requires that the $c\bar{c}$ system recoiling against the J/ψ is a C-even state. There are some indications that the $e^+e^- \to J/\psi c\bar{c}$ mechanism favours $c\bar{c}$ systems with $J = 0$ [44];

- Initial State Radiation (ISR): if the initial state e^- or e^+ loose energy because of emission of a hard photon, the annihilation occurs at a reduced centre-of-mass energy. Only charmonium states having $J^{PC} = 1^{--}$ can be produced via ISR processes. There is a limitation in the available luminosity of the order of α_{QED} corresponding to the radiation of a hard photon, but the luminosity of the B-factories was such that it allowed to measure J/ψ decays through this QED suppressed process.

The bottomonium states have been studied varying the centre-of-mass energy of the e^-e^+ collisions, in order to match higher mass $b\bar{b}$ states. Their decays to lighter $b\bar{b}$ states through hadronic and radiative transitions have been studied.

2.4.3 c- and τ- factories

The CLEO and BESIII Collaborations have covered measurements of e^+e^- annihilation around the charmonium region using a centre-of-mass energy range of $\sqrt{s} = 2$–$4.6\,\text{GeV}$, studying the inclusive processes $e^+e^- \to (c\bar{c})X$.

2.4.4 Hadronic colliders

Experiments at hadronic colliders can investigate quarkonium produced promptly in high energy hadronic collisions in addition to charmonium produced in b-decays, as

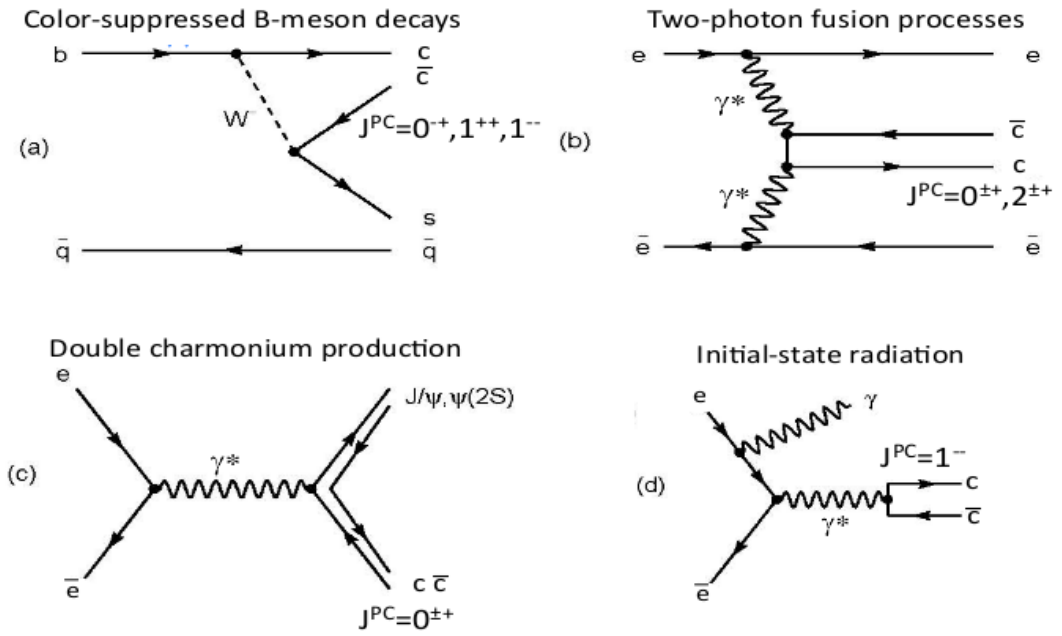

Figure 8: Quarkonium production mechanisms in e^+e^- collisions. (a) $B \to (c\bar{c})K$ decays; (b) two-photon fusion processes; (c) e^+e^- annihilations into $c\bar{c}c\bar{c}$; (d) Initial State Radiation processes.

described above. The CDF and D0 Collaborations, at the Tevatron, studied $p\bar{p}$ collisions at $\sqrt{s} = 1.96\,\text{TeV}$, while the ATLAS, CMS and LHCb experiments study the pp collisions provided by the LHC at centre-of-mass energies of $\sqrt{s} = 7,\ 8$ and $13\,\text{TeV}$ in 2011, 2012 and starting from 2015, respectively.

The heavy quarks production at both the Tevatron and the LHC is due to hard processes, in which the partons inside the colliding particles interact to produce an heavy quark pair, as schematically shown in Figure 9.

In these hard processes, the final state particles carry a large component of the momentum transverse to the collision axis and the perturbative QCD is applicable in describing the partonic process. The Leading-Order (LO) diagrams for heavy quark pairs production are shown in Figure 9(b). Also the next-to-leading processes give important contributions to the total cross-section [45].

These parton-parton scattering processes must be weighted by the probability to find a parton i in the p or in the $\bar{p}$. Such probability is called parton density function, $f(x)$, where the Bjorken variable, x, can be identified as the fraction of the proton momentum carried by the parton i. The introduction of higher order corrections in QCD, taking into account the emission of multiple collinear gluons, leads to a dependency on the energy scale Q of the process within the parton density function of the proton and the antiproton, the so-called scaling violation. The $f(x, Q)$ dependency is determined by the solutions to the DGLAP evolution equations [46, 47], that also take into account the splitting of one gluon into gluons. As Q increases, there will be more splitting processes and the gluon density function will dominate the lower-x region.

At Tevatron and LHC energies, the gluon-fusion processes are dominant. Indeed, the x of the two incoming partons can be written in terms of the pseudorapidites and the

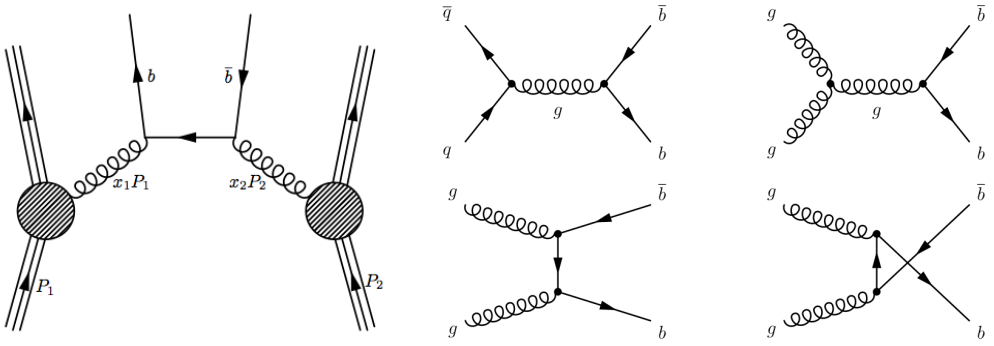

(a) (b)

Figure 9: (a): Feyman diagram showing the production of a $b\bar{b}$ pair through one of the gluon-fusion processes. P_1 and P_2 are the four-momenta of the colliding particles (pp at the LHC and $p\bar{p}$ at the Tevatron) and the four-momenta x_1P_1 and x_2P_2 of the interacting gluons. (b): LO Feynman diagrams showing the hard scattering processes for b-hadrons production. The top-left diagram corresponds to pair creation through quark-antiquark annihilation. The other diagrams represent the gluon-fusion process.

transverse momenta of the outgoing heavy quark Q and antiquark $\bar{Q}$ as

$$x_{1(2)} = \frac{p_T}{\sqrt{s}} \left(e^{(-)y_Q} + e^{(-)y_{\bar{Q}}} \right). \tag{8}$$

Hence, at the pseudorapidity range covered by the experiments at the Tevatron and at the LHC, the high $\sqrt{s}$ leads to low-x values where the probability to find a gluon is much larger than the probability of finding a sea quark, and much larger than the probability to find a valence quark or antiquark.

The main drawback of an hadronic collider is the high background due to hadronic collisions. However the large $c\bar{c}$ and $b\bar{b}$ pairs cross-sections allows to collect a huge sample of $c-$ and b-hadrons. The possibility to produce all the b-hadrons, including B_c^+, Λ_b^0 and other heavy states not accessible by the B-factories, are one of the great advantages of hadronic colliders.

The charmonium states can be produced either promptly, through the $gg \to c\bar{c}X$ sub-process, or through decays of b-hadrons, mainly produced through $gg \to b\bar{b}X$ sub-process. The bottomonium states are produced via the dominant $gg \to b\bar{b}X$ sub-process as well.

2.5 Exotic hadrons

The quark model cannot be derived rigorously from QCD. The quark model spectrum is not necessarily the same as the QCD hadrons spectrum, and QCD may allow a much richer hadron spectrum. As stated before, in QCD, the gluons not only mediate the strong interaction between quarks, but also interact among themselves since they carry colour charges. Two or more gluons may form a colour singlet, which is called glueball. One or more gluons may interact with a pair of quark and antiquark to form an hybrid meson, where the gluon is one of the valence constituents.

At the birth of the quark model, both Gell-Mann and Zweig proposed not only the existence of $q\bar{q}$ mesons and qqq baryons, but also the possible existence of $q\bar{q}q\bar{q}$ and $qqq\bar{q}\bar{q}$

states. Hence, the concept of multiquarks was proposed even before the advent of the QCD. The multiquarks can be further classified into tetraquarks ($q\bar{q}q\bar{q}$), pentaquarks ($qqq\bar{q}\bar{q}$), dibaryon ($qqqqqq$), baryonium ($qqq\bar{q}\bar{q}\bar{q}$), etc.

A conventional $q\bar{q}$ meson in the quark model cannot carry the following quantum numbers: 0^{--}, 0^{+-}, 1^{-+}, 2^{+-}, etc., namely the exotic quantum numbers. Mesons with these J^{PC} quantum numbers would be manifestly exotic. Hybrid mesons, tetraquark states or the glueballs can also carry all the so-called exotic J^{PC} quantum numbers. On the other side, qqq baryons in the Quark Model can assume all the J^P quantum numbers, i.e. $J^P = \frac{1}{2}^{\pm}$, $\frac{3}{2}^{\pm}$, $\frac{5}{2}^{\pm}$, etc.

Although forty years of experimental searches failed to find QCD-motivated exotic hadrons, observations and evidences of mesons that do not fit into the simple $q\bar{q}$ scheme of the original Quark Model has been accumulating during the last 15 years. These include the discovery of two pentaquark candidates, reported by the LHCb collaboration [12], and the X, Y and Z mesons, charmonium-like and bottomonium-like states that do no fit into any of the remaining unfilled states in the $c\bar{c}$ and $b\bar{b}$ spectra [48], respectively.

2.6 Experimental observations of exotic candidates

The X, Y and Z mesons are a class of hadrons that have been observed to decay to final states that contain a heavy quark and a heavy antiquark, but cannot be easily accommodated in an unassigned charmonium or bottomonium level, as shown in Figure 10. For this reason they are called charmonium-like or bottomonium-like states.

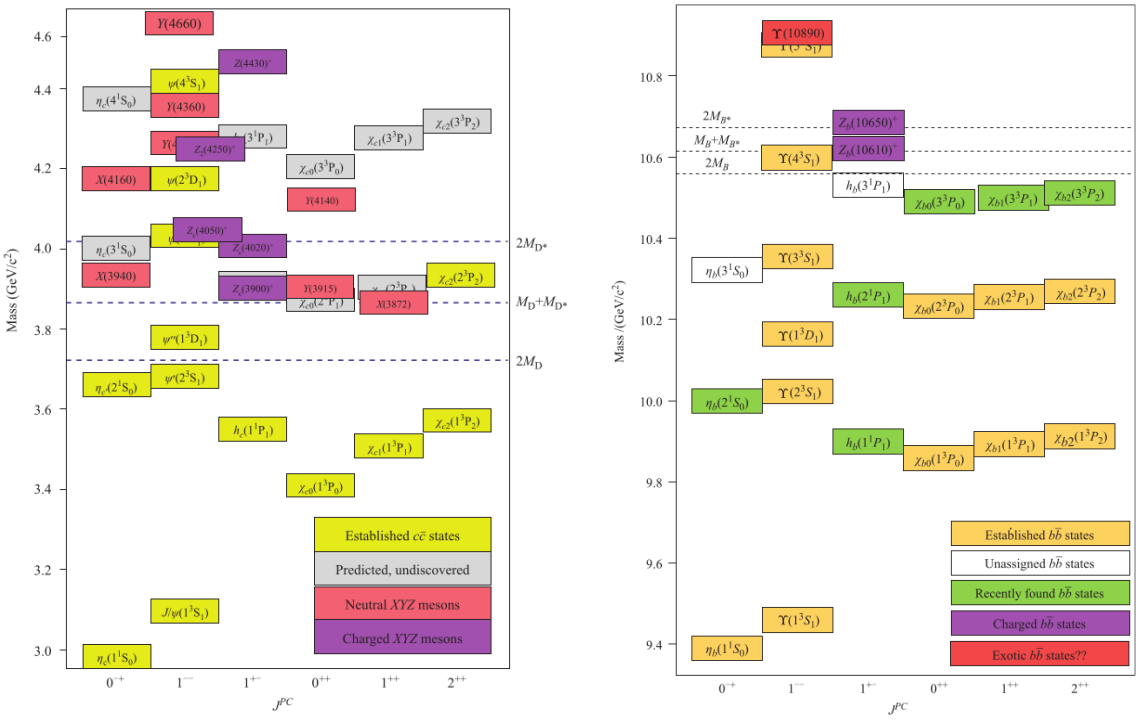

(a) (b)

Figure 10: (a): the spectrum of charmonium and charmonium-like mesons; (b): the spectrum of bottomonium and bottomonium-like mesons.

According to the different production mechanisms, that are the same of the quarkonia mesons, introduced in Section 2.4.1, all the observed charmonium-like states can be categorised into five groups, as shown in Figure 11.

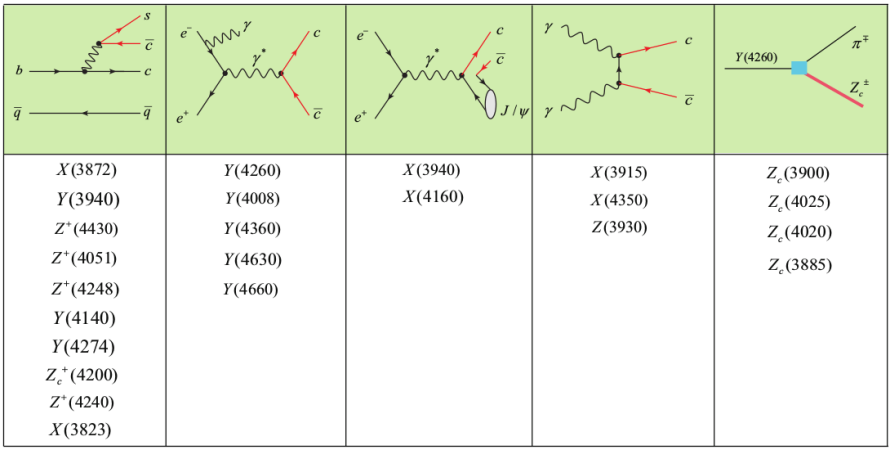

$X(3872)$	$Y(4260)$	$X(3940)$	$X(3915)$	$Z_c(3900)$
$Y(3940)$	$Y(4008)$	$X(4160)$	$X(4350)$	$Z_c(4025)$
$Z^+(4430)$	$Y(4360)$		$Z(3930)$	$Z_c(4020)$
$Z^+(4051)$	$Y(4630)$			$Z_c(3885)$
$Z^+(4248)$	$Y(4660)$			
$Y(4140)$				
$Y(4274)$				
$Z_c^+(4200)$				
$Z^+(4240)$				
$X(3823)$				

Figure 11: The states collected in the first, second, third and fourth columns are produced via B-meson decays, ISR, associate production and two photon fusion processes, respectively. The states in the fifth column have been observed tuning the e^+e^- centre-of-mass energy to the pole mass of the $Y(4260)$ exotic candidate.

The X and Y states are neutral exotic meson candidates. The Y states are characterised by their production mechanism through ISR processes, hence by the $J^{PC} = 1^{--}$ quantum numbers. The mass and decay properties of these states make them fairly conciliable with the conventional charmonium states predicted by the models introduced in Section 2.4.

As described below, distinguishing neutral candidates for non-conventional mesons decaying to quarkonia states, from excitations of quarkonia states is a complex task, at least in some cases, that could lead to ambiguities. In contrast, charged quarkonium-like states, also called Z states, are explicitly non-standard states and the outstanding issue regards their resonant nature, internal structure and dynamics.

In the following I will summarise the experimental observations of quarkonium-like mesons, underlining the properties that make these states as candidates for hadrons beyond the conventional mesons and baryons.

2.7 Neutral exotic meson candidates

The $X(3872)$ state is the first exotic candidate that has been observed. It has been reported by the Belle collaboration in 2003 [3] as a narrow peak in the $J/\psi\pi^+\pi^-$ invariant mass distribution studying the $B^+ \to J/\psi\pi^+\pi^-K^+$ decay channel. The peak corresponding to the $X(3872)$ state is shown in Figure 12. Since its discovery, many experiments, including ATLAS [49], BaBar [50], BESIII [51], CDF [52], CMS [53], D0 [54] and LHCb [55] confirmed its existence, observing it in different production mechanisms, including the prompt production. Hence the $X(3872)$ candidate is experimentally established.

The mass $3871.69 \pm 0.17\,\text{MeV}$ of the $X(3872)$ state is, at the current levels of precision, indistinguishable from the $D^0\bar{D}^{*0}$ mass threshold. Indeed, the mass difference is $\delta = (m_{D^0} + m_{D^{*0}}) - m_{X(3872)} = -0.01 \pm 0.20\,\text{MeV}$ [15]. This close proximity of the $X(3872)$ mass

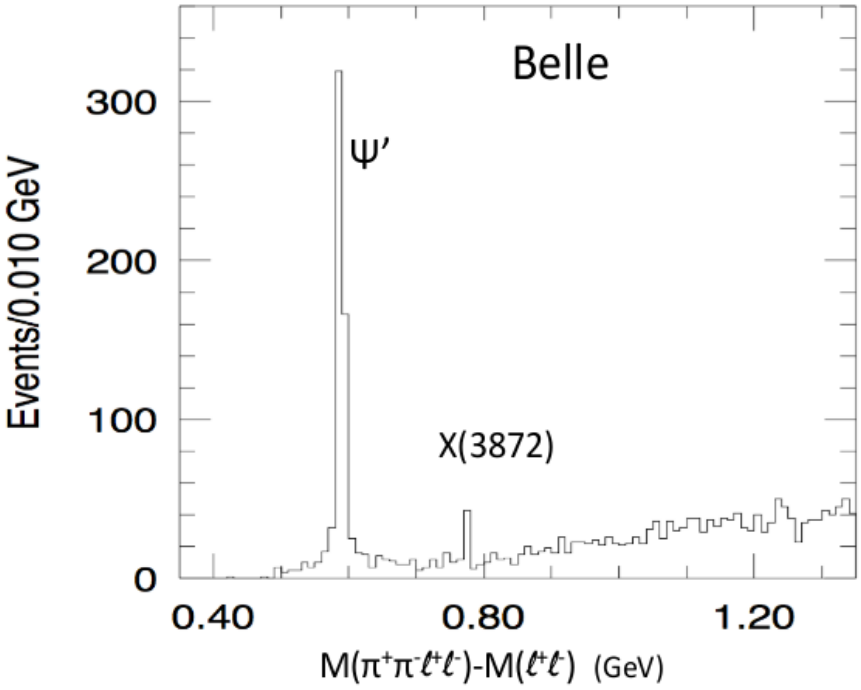

Figure 12: $(M_{\pi^+\pi^-l^+l^-} - M_{l^+l^-})$ invariant mass distribution from Belle, where l is e or μ, in the $\pm 20\,\text{MeV}$ region around the J/ψ peak. The $X(3872)$ peak can be seen.

to the $D^0\bar{D}^{*0}$ has attracted considerable interest and experimental studies. The $X(3872)$ is also narrow; Belle reported a 90% C.L. upper limit on its width of $\Gamma < 1.2\,\text{MeV}$ [56].

LHCb measured its quantum numbers as $J^{PC} = 1^{++}$ [57, 58] with a significance of more than 16σ. The only available $J^{PC} = 1^{++}$ conventional charmonium level that is expected to have a mass near 3872 MeV is the 2^3P_1 state, also known as $\chi_{c1}(2P)$. However, there are several reasons disfavouring the association of the $X(3872)$ with the $\chi_{c1}(2P)$ [59], including its mass and width values. For instance, the BaBar collaboration reported the observation of $B^+ \to X(3872)(\to \omega J/\psi)K^+$ decays [60], supporting the isospin $I = 0$ assignment. Considering the $X(3872) \to \rho^0 J/\psi$ discovery channel, supporting the $I = 1$ assignment, there is an evident isospin violation, not matching the $\chi_{c1}(2P)$ interpretation. These reasons, plus the close correspondence between the $X(3872)$ mass and the $D^0\bar{D}^{*0}$ mass threshold, led to the conclusion that the substructure of the $X(3872)$ is more complex than that of a simple charmonium state.

When searching for the $X(3872)$ in $B^+ \to J/\psi\omega K^+$ decays, the Belle collaboration observed a near-threshold enhancement in the $J/\psi\omega$ invariant mass distribution [61]. The bump has been fitted with a Breit–Wigner shape describing a spin-0 resonance with mass $m = 3943 \pm 17\,\text{MeV}$ and width $\Gamma = 87 \pm 24\,\text{MeV}$. This result has been confirmed by BaBar [60, 62] but with lower mass $3919 \pm 4\,\text{MeV}$ and width $31 \pm 11\,\text{MeV}$ values. An $\omega J/\psi$ mass peak with similar mass and width has also been reported by Belle and Babar in the two-photon fusion process $\gamma\gamma \to \omega J/\psi$ [63, 64], shown in Figure 13, suggesting that this latter process is a different production mechanism for the same state, called $X(3915)$.

The spin-parity analysis performed by BaBar using $\gamma\gamma \to \omega J/\psi$ events favoured the $J^{PC} = 0^{++}$ quantum numbers assignment and it has been argued that the $X(3915)$ could

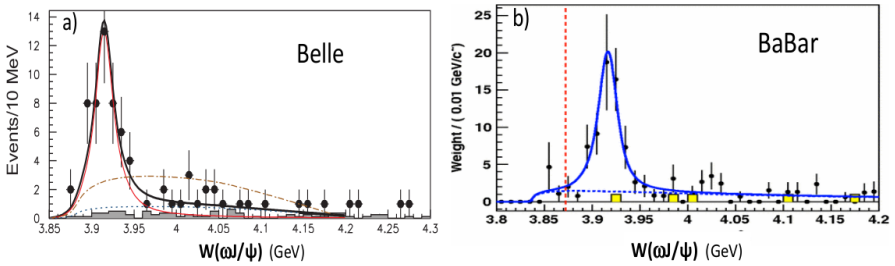

Figure 13: $X(3915) \to \omega J/\psi$ signals in $\gamma\gamma \to \omega J/\psi$ process from (a) Belle and (b) BaBar.

be the 2^3P_0 charmonium state, also known as $\chi_{c0}(2P)$. However, as in the $X(3872)$ case, there are arguments disfavouring this hypothesis. The mass is about 10 MeV above the expectations, the lack of any experimental evidence for $X(3915) \to D\bar{D}$ decays, expected to be the dominant decay mode of the $\chi_{c0}(2P)$, and the strength of the $X(3915) \to \omega J/\psi$ discovery mode, expected to be OZI suppressed if the $X(3915)$ is the $\chi_{c0}(2P)$, make the $X(3915)$ a poor candidate for the $\chi_{c0}(2P)$. More experimental data are required to clarify the nature of the $X(3915)$ and to confirm that the signals seen in b-decays and in the two-photon fusion are due to the same state.

Other neutral exotic candidates have been discovered studying the $J/\psi\phi$ final state. The ease of triggering $J/\psi \to \mu^+\mu^-$ decays and the narrow $\phi \to K^+K^-$ mass peak, provide a clean signature even in hadronic collider experiments, also considering detectors, like CMS, not having specific charged hadron identification systems. The CDF collaboration reported a 3.8σ evidence for a near threshold $J/\psi\phi$ mass peak studying the $B^+ \to J/\psi\phi K^+$ decay channel, called $X(4140)$. CDF measured a mass of $m_{X(4140)} = 4143 \pm 3$ MeV and a narrow width of $\Gamma_{X(4140)} = 11.7^{+9.1}_{-6.2}$ MeV [65].

The $X(4140)$ could not be identified with a conventional charmonium state given its decay properties. Indeed, its mass value above open-charm thresholds would imply a much higher width and dominant decay modes into open-charm pairs. Moreover, the $X(4140) \to J/\psi\phi$ decay mode would be OZI-suppressed for a charmonium state.

Other experiments searched for the $X(4140)$ state. The LHCb collaboration [66], using a little fraction of its data sample, and the BaBar [67] and BESIII [68] collaborations did not find any evidence for this state. On the other side, the CMS [69] and D0 [70] collaborations reported a 5σ observation and a 3σ evidence, respectively, for the $X(4140) \to J/\psi\phi$ signal. While the mass and width values measured by CMS were consistent with the CDF results, the mass reported by D0 is two standard deviations higher than the CDF value. In addition, D0 reported a 4.7σ signal for the prompt $X(4140)$ production in $p\bar{p}$ collisions [71].

Hints of higher mass states have been reported by CMS and D0 in the same papers. The Belle collaboration reported a 3.2σ evidence for a narrow $J/\psi\phi$ peak at 4351 ± 5 MeV in the two-photon fusion process, indicating a $J^{PC} = 0^{++}$ or 2^{++}, and no evidence has been found for the $X(4140)$ in the same analysis [72].

The main limitations of the analyses mentioned above are the limited data sample size and the use of simple Breit–Wigner shapes to represent the signal. The $X(3872)$ and $X(3915)$ charmonium-like states showed up as narrow peaks on a small background, making reasonable the fit with the Breit–Wigner shapes. This approach has the drawbacks to neglect the effects of possible signal interference with other intermediate states, and this is not a reliable method in the study of decay channels where other intermediate

contributions are expected. Moreover, the presence of other intermediate states could induce structures, called reflections, and fake peaks in the invariant mass distribution of interest.

In the $B^+ \to J/\psi\phi K^+$ decay channel, several resonant contributions from $K^{*+} \to \phi K^+$ decays are expected and they have to be taken into account for reliable conclusions on exotic contributions in this decay channel. The LHCb collaboration performed the first amplitude analysis of the $B^+ \to J/\psi\phi K^+$ decay channel, based on a nearly background-free sample that was larger than that for any of the previous analyses [13, 14]. The data across the full, 6-dimensional phase space of invariant masses and decay angles spanned by the five final state particles, could not be described by a model that contains only excited kaons that decay into ϕK^+. An acceptable description of data has been obtained including four coherent $X \to J/\psi\phi$ peaking structures, as shown in Figure 14.

The $X(4140)$ state, with a mass consistent with the $X(4140)$ value from CDF and CMS, has been observed with a 8.4σ significance level as a broad enhancement. The width measured by LHCb is $\Gamma_{X(4140)} = 83 \pm 21^{+21}_{-14}$ MeV, in contrast with the narrow width value reported by CDF. Its quantum numbers have been determined from the LHCb fit to be 1^{++}, ruling out other hypotheses with a significance of 5.7σ or more. The $X(4274)$, with mass $4273.3 \pm 8.3^{+17.2}_{-3.6}$ MeV has been observed with a significance of 6σ, confirming the evidence reported by the CDF Collaboration. The $X(4274)$ quantum numbers have been measured to be 1^{++} at 5.8σ level. Moreover, two 0^{++} resonances, called $X(4500)$ and $X(4700)$, have been observed for the first time with a significance of 6.1σ and 5.6σ, respectively. The assignments for the quantum numbers have a significance of more than 4σ. None of the $J/\psi\phi$ structures are consistent with the state observed by the Belle collaboration in the two-photon fusion process.

Given the $X(4140)$ and $X(4274)$ widths determined by LHCb, these states cannot a priori be considered too narrow to be charmonium states, and their quantum numbers are consistent with the $\chi_{c1}(3P)$ charmonium meson. Hence, either the $X(4140)$ or the $X(4274)$ can be considered as a candidate for the $\chi_{c1}(3P)$. The $X(4500)$ and the $X(4700)$ lie in the predicted mass and width ranges for the $\chi_{c0}(4P)$ and $\chi_{c0}(5P)$. However, the

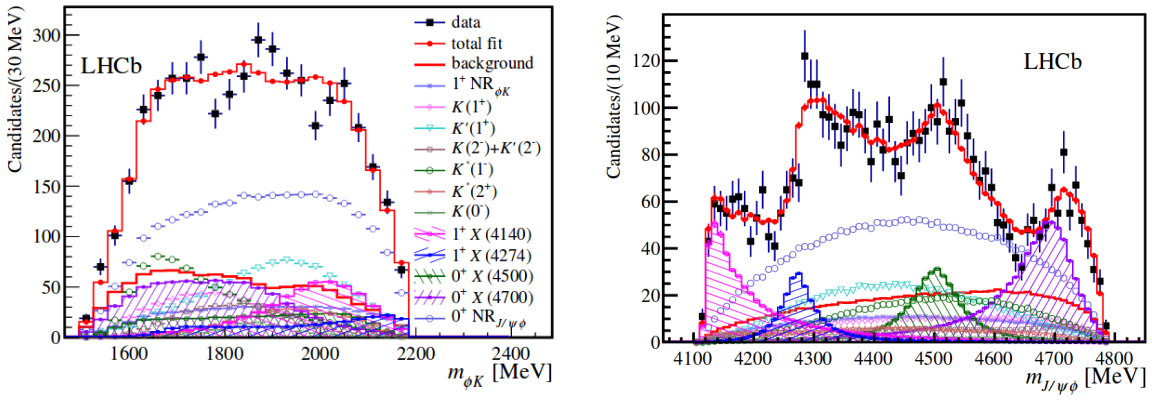

(a) (b)

Figure 14: The ϕK^+ (a) and $J/\psi\phi$ (b) invariant mass distributions compared with the results of the 6D amplitude fit. The contributions due to the K^{*+} excitations and to the exotic contributions are reported in the legend. The four exotic contributions are evident in (b).

couplings for the $\chi_{cJ}(nP)$ states to the $J/\psi\phi$ and $J/\psi\omega$ final states are expected to be very similar, with the latter being enhanced by the larger accessible phase space. Moreover, the coupling to $J/\psi\omega$ would be further enhanced because of the relative ease of producing light $u\bar{u}$ or $d\bar{d}$ pairs with respect to the more massive $s\bar{s}$ pairs, from the vacuum. The analysis of $B^+ \to J/\psi\omega K^+$ decays by BaBar [67], shows no structures in the $J/\psi\omega$ invariant mass distribution, favouring the interpretation of the $X(4140)$, $X(4274)$, $X(4500)$ and $X(4700)$ resonances as neutral exotic mesons.

Other neutral exotic candidates are the $X(3940)$ and the $X(4160)$. The $X(3940)$ has been seen in double charmonium production process by Belle [44]. With subsequent studies of $e^+e^- \to J/\psi D^{(*)}\bar{D}^{(*)}$ decays in the same energy region [73, 74], Belle found a strong signal for $X(3940) \to D\bar{D}^*$, plus two other states: the $X(3860) \to D\bar{D}$ and the $X(4160) \to D^*\bar{D}^*$. The reported significances are above 5σ, but these three states wait confirmation from another experiment.

The $X(3860)$ mass, quantum numbers and strong $D\bar{D}$ decay mode are consistent with the expectations for the $\chi_{c0}(2P)$ charmonium state. The favourite quantum numbers assignment for the $X(3940)$ and the $X(4160)$ states is $J^{PC} = 0^{-+}$, making these states as candidates for the conventional $\eta_c(3S)$ and $\eta_c(4S)$ mesons. However, the expected masses for the latter states are far above the values observed for the $X(3940)$ and $X(4160)$ states. These states require confirmations from other experiments.

2.8 Neutral exotic meson candidates produced with ISR processes

Several neutral exotic hadron candidates have been observed in processes involving ISR in the e^+e^- collisions. The radiation of a hard photon by the e^+ or the e^- results in a decreased centre-of-mass energy of the e^+e^- collision. The exotic candidates are produced with the mechanism shown in the second column of Figure 11, and they carry the quantum numbers of the photon, $J^{PC} = 1^{--}$.

After the discovery of the $X(3872)$ state and before the $J^{PC} = 1^{++}$ assignment, BaBar searched its direct production in the ISR process $e^+e^- \to \gamma_{\rm ISR}\pi^+\pi^- J/\psi$ to check if the $X(3872)$ was consistent with a vector hypothesis [75]. The not observation of the $X(3872)$ meson lead to the conclusion that its quantum numbers were not $J^{PC} = 1^{--}$. An excess of events at $\sim 4.26\,\text{GeV}$ has been found in the $J/\psi\pi^+\pi^-$ invariant mass distribution. This state has been called $Y(4260)$. The bump has been confirmed by the CLEO [76] and Belle [77, 78] collaborations.

The discovery decay mode of the $Y(4260)$ candidate provides strong evidence that it contains a $c\bar{c}$ pair. However, all the $J^{PC} = 1^{--}$ charmonium levels with mass below $4500\,\text{MeV}$ have already been assigned to well established $J^{PC} = 1^{--}$ resonances by the c- and τ- factories. The decay properties of the $Y(4260)$ are opposite to the expectations for the charmonium mesons. As studied by BESIII, there are strong signals of well established $J^{PC} = 1^{--}$ $\psi(3770)$, $\psi(4040)$, $\psi(4160)$ and $\psi(4415)$ charmonium states in $D^{(*)}\bar{D}^{(*)}$ open-charm mesons invariant mass distribution, while they are absent in the $J/\psi\pi^+\pi^-$ decay channel, as expected from the OZI rule. In contrast, there is no evidence for $Y(4260)$ decays into $D^*\bar{D}^{(*)}$ pairs, while there is a strong signal in the $J/\psi\pi^+\pi^-$ decay channel.

Searching for the $Y(4260)$ decaying to $\psi(2S)\pi^+\pi^-$, BaBar found a peak whose mass and width were not compatible with the $Y(4260)$ [79]. A study of the same decay with

more statistics has been later performed by Belle [80], that confirmed a state at an higher mass with respect to the $Y(4260)$. The current mass and width values for this new state, called $Y(4360)$, are $m_{Y(4360)} = 4341 \pm 8\,\text{MeV}$ and $\Gamma_{Y(4360)} = 102 \pm 9\,\text{MeV}$ [15].

In addition, Belle observed a second peak in the $\psi(2S)\pi^+\pi^-$ invariant mass distribution at even higher mass, an observation then confirmed by BaBar [81]. A peak with similar mass and width has also been seen in $e^+e^- \to \gamma_{\text{ISR}}\Lambda_c^+\Lambda_c^-$ events by Belle [82]. The world averages for this second peak, called $Y(4660)$, are $m_{Y(4660)} = 4643 \pm 9\,\text{MeV}$ and $\Gamma_{Y(4660)} = 72 \pm 11\,\text{MeV}$.

The BESIII experiment operated at e^+e^- centre-of-mass energies near to the $Y(4260)$ and $Y(4360)$ peaks and hence it avoided the limitation in luminosity of the order of α_{QED} corresponding to the ISR process suffered by Belle and BaBar. Therefore BESIII had the advantage to accumulate larger samples in the proximity of these states, scanning the e^+e^- centre-of-mass energy. The BESIII collaboration measured the $e^+e^- \to \eta J/\psi$ [83] and $e^+e^- \to \omega\chi_{c0}$ [84] cross sections, finding a much narrower peak for the $Y(4260)$ and a mass value $\sim 40\,\text{MeV}$ lower than the value measured by the BaBar and Belle collaborations in ISR, as shown in Figure 15. Moreover, the $e^+e^- \to \pi^+\pi^- J/\psi$ cross-section measurement [85] showed that the $Y(4260)$ is not well described by a single Breit–Wigner shape, but it requires two interfering resonance amplitudes. The first peak can be identified with the $Y(4260)$, also if the mass $m = 4222 \pm 4\,\text{MeV}$ and width $\Gamma = 44 \pm 5\,\text{MeV}$ values are significantly lower. The second state seen in $\pi^+\pi^- J/\psi$ can be identified with the $Y(4360)$ observed by Belle and Babar.

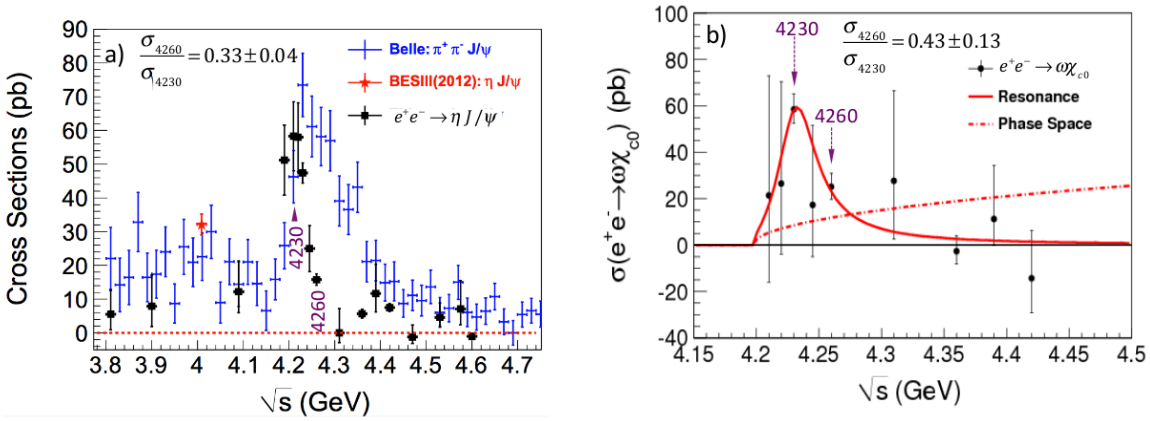

(a) (b)

Figure 15: (a): Cross-section measurements for $e^+e^- \to \eta J/\psi$ from BESIII compared to Belle ISR measurements from $e^+e^- \to \pi^+\pi^- J/\psi$ cross-section; (b): cross-section measurements for $e^+e^- \to \omega\chi_{c0}$ from BESIII

Regarding the bottomonium sector, the large $Y(4260) \to J/\psi\pi^+\pi^-$ signal observed by BaBar, motivated a search for similar behaviour in the $b\bar{b}$ system [86] by Belle [87]. Belle found large $\Upsilon(nS)\pi^+\pi^-$ ($n = 1,\ 2,\ 3$) production rates peaking at $\sim 10.89\,\text{GeV}$, an energy close to the $e^+e^- \to b\bar{b}$ cross-section peak corresponding to the $\Upsilon(5S)$. If these peaks are attributed to $\Upsilon(5S) \to \Upsilon(nS)\pi^+\pi^-$ decays, the $\Upsilon(5S)$ partial widths would be two order of magnitude larger than theoretical predictions [88] and than the measured value of the $\Upsilon(4S)$ width. This suggests that either the peak in the $e^+e^- \to b\bar{b}$ cross-section identified

with the $\Upsilon(5S)$ is not a standard bottomonium but a b-quark sector equivalent of the $Y(4260)$, or there is an overlap of the conventional $\Upsilon(5S)$ with a nearby b-quark sector equivalent of the $Y(4260)$, called $\Upsilon(10890)$, or the $\Upsilon(5S)$ experiences some dynamical effects, such as unexpected intermediate states, not coupling with the $\Upsilon(4S)$.

2.9 Charged exotic meson candidates

The first established candidate for a charged quarkonium-like state has been observed by the Belle collaboration studying $B^- \to \psi(2S)K_s^0\pi^-$ and $B^0 \to \psi(2S)K^+\pi^-$ decays [89]. Belle observed a peak in the $\psi(2S)\pi^-$ invariant mass distribution and called this state $Z(4430)^-$. The BaBar collaboration studied the same decay using a data sample containing a similar number of events and trying to reproduce the $\psi(2S)\pi^-$ structures through reflections due to $K^{*0} \to K^+\pi^-$ decays in a model-independent way [90]. BaBar did not support the Belle observation, but the results were not sensitive enough to rule out the existence of the $Z(4430)^-$. Subsequently, the Belle collaboration reanalysed the data using a 2D and a full 4D amplitude analyses combining coherent $K\pi^-$ and $\psi(2S)\pi^-$ contributions to fit data [91,92]. These analyses confirmed a significant $Z(4430)^-$ signal, but with a larger mass and width with respect to the initial report based on the fit to the $\psi(2S)\pi^-$ invariant mass distribution. Moreover, the Belle collaboration reported the $J^P = 1^+$ assignment, favoured over other possible assignments with a significance of 3.4σ.

The existence of the $Z(4430)^+$ has been confirmed by the LHCb collaboration with a significance of 13.9σ [10] through the full 4D amplitude analysis of $B^0 \to \psi(2S)K^+\pi^-$ decays, using a sample that was an order of magnitude larger than those used by the Belle and BaBar collaborations. The $\psi(2S)\pi^-$ invariant mass projection compared with the fit results is shown in Figure 16(a). The LHCb amplitude analysis results were consistent with the parameters measured by Belle, including the $J^P = 1^+$ spin-parity assignment with a significance of 9.7σ. The average of the Belle and LHCb mass and width values are $m_{Z(4430)^-} = 4478^{15}_{-81}\,\text{MeV}$ and $\Gamma_{Z(4430)^-} = 181 \pm 31\,\text{MeV}$. Moreover, the LHCb collaboration studied $B^0 \to \psi(2S)K^+\pi^-$ decays using a $K^+\pi^-$ model-independent approach [11], similar to the one used by BaBar, demonstrating at 8σ that the $\psi(2S)\pi^-$ invariant mass distribution could not be explained by $K^+\pi^-$ reflections only.

Since the $Z(4430)^+$ is charged, the only argument against its exotic hadron nature is the possibility that it is not a resonance, but a peak due to rescattering mechanisms or coupled-channel cusps. The large event sample collected by the LHCb experiment allowed to measure the $Z(4430)^+$ amplitude dependence on the $\psi(2S)\pi^-$ invariant mass independently of any assumptions about the resonance shape. The resulting Argand diagram, plotting the real part of the 1^+ amplitude against the imaginary part, shows a nearly circular, counter-clockwise motion with a change in the amplitude phase at the peak of its magnitude characterising the Breit–Wigner resonance amplitude, as shown in Figure 16(b). This study ruled out some of the interpretations of the $Z(4430)^+$ as a peak due to the effects of a rescattering process [93]. However, higher statistics studies of the Argand diagram will be needed to distinguish a resonance pole from other types of meson-meson interactions.

The Belle collaboration performed an amplitude analysis of $B^0 \to J/\psi K^+\pi^-$ decays [94], finding that data could not be well described solely with contributions from the K^+pi^- channel. Two additional resonances decaying to $J/\psi\pi^-$ were needed: a very broad $Z(4200)^-$ state having $\Gamma_{Z(4200)^-} = 370 \pm 70^{+70}_{-132}\,\text{MeV}$, $m_{Z(4200)^-} = 4196^{+31}_{-29}\,{}^{+17}_{-13}\,\text{MeV}$ and a

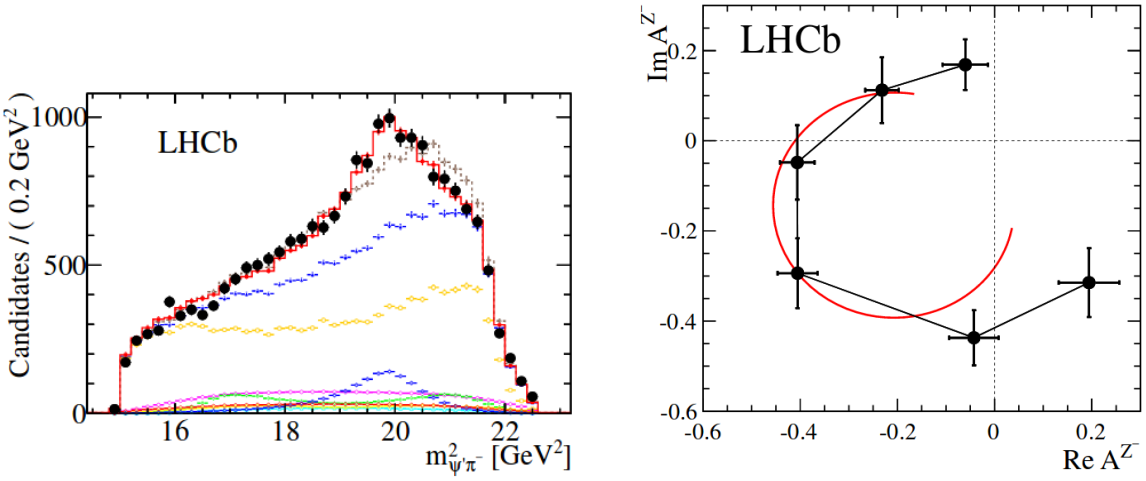

(a) (b)

Figure 16: (a) $m^2_{\psi(2S)\pi^-}$ distribution (black data points) together with the projection of the 4D fit performed by the LHCb collaboration. The red solid (brown dashed) histogram represents the total amplitude with (without) the $Z(4430)^-$. The other points illustrate various subcomponents of the fit that includes the $Z(4430)^-$: the upper (lower) blue points represent the $Z(4430)^-$ component removed (taken alone). The orange, magenta, cyan, yellow, green and red points represent the $K^*(892)$, total S-wave, $K^*(1410)$, $K^*(1680)$, $K^*_2(1430)$ and backgrounds terms, respectively; (b): Values of the $J^P = 1^+$ amplitude in six $m_{\psi(2S)\pi^-}$ bins, shown in an Argand diagram. The red curve is the prediction from the Breit–Wigner formula with a resonance mass (width) of 4475 (172) MeV.

significance of 6.2σ, and a second state corresponding to the $J/\psi\pi^-$ decay mode of the $Z(4430)^-$. The $Z(4200)^-$ requires confirmation from other experiments, but its evidence has been reported by LHCb in its amplitude analysis of $B^0 \to \psi(2S)K^+\pi^-$ decays with either 0^- or 1^+ quantum numbers.

The Belle collaboration also reported evidence for charged $\chi_{c1}\pi^-$ resonances in a 2D amplitude analysis of $B^0 \to \chi_{c1}K^+\pi^-$ decays [95]. A good description of data has been obtained adding the $Z(4050)^-$ and the $Z(4250)^-$ states. The BaBar collaboration neither confirmed nor disproved the Belle results through a model-independent analysis of the same decay channel [96]. These resonant states still await independent confirmation, and a complete 6D amplitude analysis of $B^0 \to \chi_{c1}K^+\pi^-$ is required in order to determine their quantum numbers.

Discoveries of charged exotic candidates have also been reported in the bottomonium sector. In particular, the study of the anomalously large $\Upsilon(nS)\pi^+\pi^-$ ($n = 1,\ 2,\ 3$) production rates led to the discovery of two charged bottomonium-like states decaying to $h_b\pi^-$, the non-conventional $Z_b(10610)^-$ and the $Z_b(10650)^-$ [97]. The production and decays of the two Z_b^- states can explain part of the anomalously large $\Upsilon(5S) \to \Upsilon(nS)\pi^+\pi^-$ decay rates. Moreover, studying the $\Upsilon(nS)\pi^0\pi^0$ system, Belle found a 6.5σ signal for the neutral isospin partner of the $Z_b(10610)^-$, the $Z_b(10610)^0$ [98].

These discoveries in the b-quark sector motivated the BESIII group to search for c-quark sector equivalents of the Z_b states produced in the decays of the $Y(4260)$, assuming the $\Upsilon(5S)$ is the bottomonium counterpart of the $Y(4260)$. BESIII observed a distinct

peak, called $\boldsymbol{Z_c(3900)^-}$, in $Y(4260) \to Z_c(3900)^-(\to J/\psi\pi^-)\pi^+$ decays [99], shown in Figure 17(a). A fit using a Breit–Wigner amplitude to fit the peak led to mass and width values of $m_{Z_c(3900)^-} = 3899.0 \pm 6.1\,\text{MeV}$ and $\Gamma_{Z_c(3900)^-} = 46 \pm 22\,\text{MeV}$. The $Z_c(3900)^-$ has been confirmed by the Belle [78] and CLEO [100] collaborations.

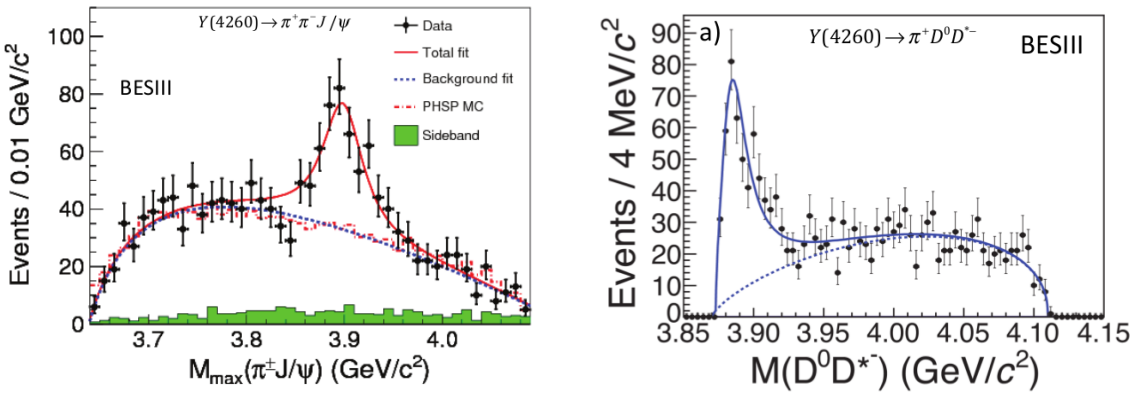

(a) (b)

Figure 17: (a): the $J/\psi\pi^\pm$ invariant mass distribution in $e^+e^- J/\psi\pi^+\pi^-$ events collected by BESIII at $\sqrt{s} = 4.260\,\text{GeV}$. The solid curve shows the fit with a Breit-Wigner parameterising the $Z_c(3900)^-$; (b): the D^0D^{*-} invariant mass distribution in $e^+e^- \to D^0D^{*-}\pi^+$ events collected by BESIII at $\sqrt{s} = 4.260\,\text{GeV}$. The solid curve shows the fit with a Breit-Wigner parameterising the $Z_c(3900)^-$.

Studying $e^+e^- \to D^0D^{*-}\pi^+$ decays with the e^+e^- centre-of-mass energy near to the $Y(4260)$, BESIII found a very strong near threshold peak [101]. The mass of this state is $\sim 2\sigma$ lower than the $Z_c(3900)^-$, but the simple 1D fit could lead to a bias in the mass measurements by amounts similar to the resonance widths. Hence this state can be likely identified with the $Z_c(3900)^-$ decaying to a different final state. The large $Z_c(3900)^- \to D^0\bar{D}^{*-}$ signal, shown in Figure 17(b), allowed BESIII to determine its J^P spin-parity as 1^+. BESIII also reported neutral counterparts of the $Z_c(3900)^-$ in the $J/\psi\pi^0$ [102], $J/\psi D^+D^{*-}$ and $J/\psi D^0\bar{D}^{*0}$ [103] decay channels, the $Z_c(3900)^0$. The relative signal yields in the charged and neutral channels are consistent with the expectations based on isospin conservation.

With the data accumulated at the peaks of the $Y(4260)$, $Y(4360)$ and nearby energies, BESIII made a study of $h_c\pi^+\pi^-$ final states [104], finding a peak near 4020 MeV in the $h_c\pi^-$ distribution, called $\boldsymbol{Z_c(4020)^-}$. The fit to this peak with a BW amplitude, assuming $J^P = 1^+$ plus a smooth background, returns a $\sim 9\sigma$ significance signal. Also in this case BESIII observed the corresponding isospin partner in the $h_c\pi^0\pi^0$ system [105]. Similarly to the $Z_c(3900)^-$ case, a study of $e^+e^- \to D^{*+}\bar{D}^{*0}\pi^-$ decays led BESIII to find another decay mode of the $Z_c(4020)^- \to D^{*+}\bar{D}^{*0}$ [106].

2.10 Models for the exotic candidates

Several theoretical models, described in Ref. [4–9], have been proposed attempting to explain the non-conventional hadron candidates discussed above, but a coherent and complete picture for these states is not yet available. Different approaches led to good

results for some states but fail or are not applicable to others. This is due to the lack of understanding about the nature of these states, that could be related to an underlying mechanism that has not yet been discovered or to different and unrelated mechanisms leading to the existence of different types of these non-conventional hadrons.

The striking feature of these exotic candidates is their decay pattern, shown in Figures 18 and 19 for charmonium-like and bottomonium-like states, respectively, together with the corresponding conventional quarkonium states.

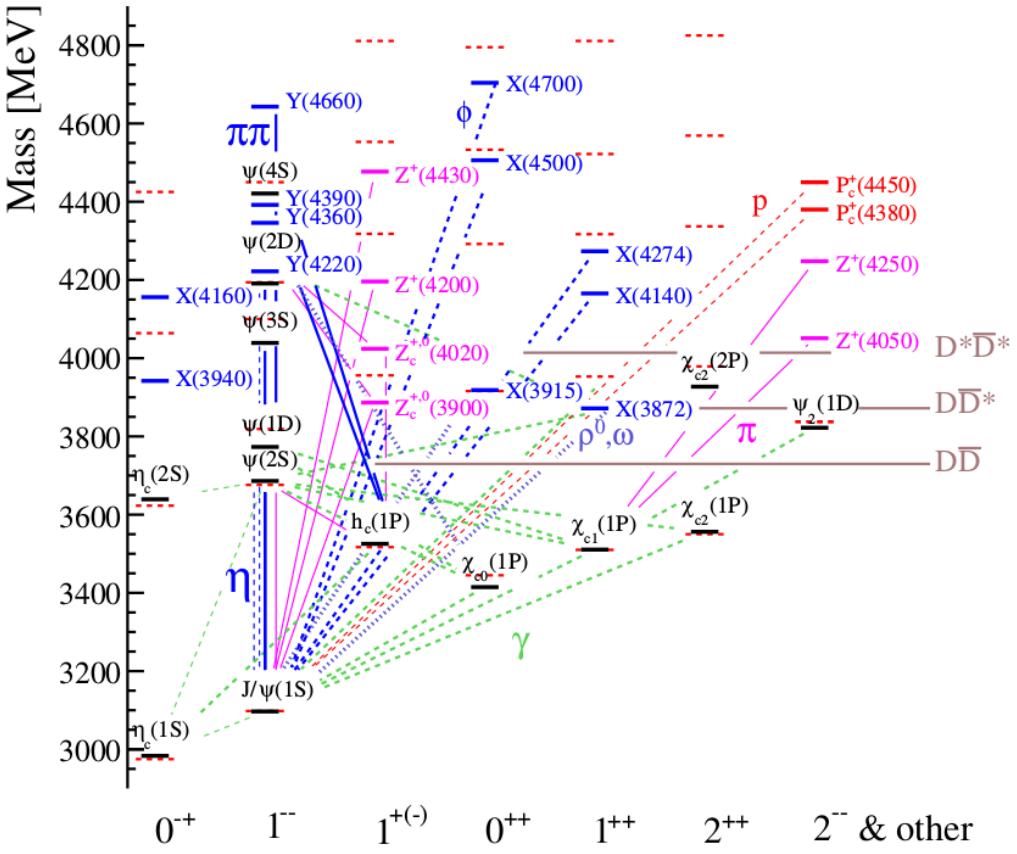

Figure 18: The spectra and decay patterns of charmonium and charmonium-like mesons. The red dashed lines indicate the expected states and their masses based on the Godfrey-Isgur relativised potential model [33]. The black solid lines indicate the experimentally established states. The open flavour threshold is also indicated with longer, solid, brown lines. The candidates for exotic quarkonium-like states are shown with shorter solid blue or magenta lines. The last column includes states with unknown quantum numbers. The decay patterns are shown with lines connecting known states: dashed-green are γ transitions (thick E1, thin M1), solid-magenta are π, dashed-blue are η (thin) or ϕ (thick), dashed-red are p, dotted-blue are ρ^0 or ω, solid-blue other $\pi\pi$ transitions. Pictures taken from [9].

While there is a number of known charmonium states above the open-charm threshold with their dominant decay mode into open-charm pairs, and hence respecting the expected behaviour, about double the number of charmonium-like states exist above this threshold favouring their decay into hidden-charm states. Therefore, while charmonium models work very well below the open-charm threshold, they fail at higher masses, where some new degrees of freedom have become relevant. The biggest challenge to current theoretical

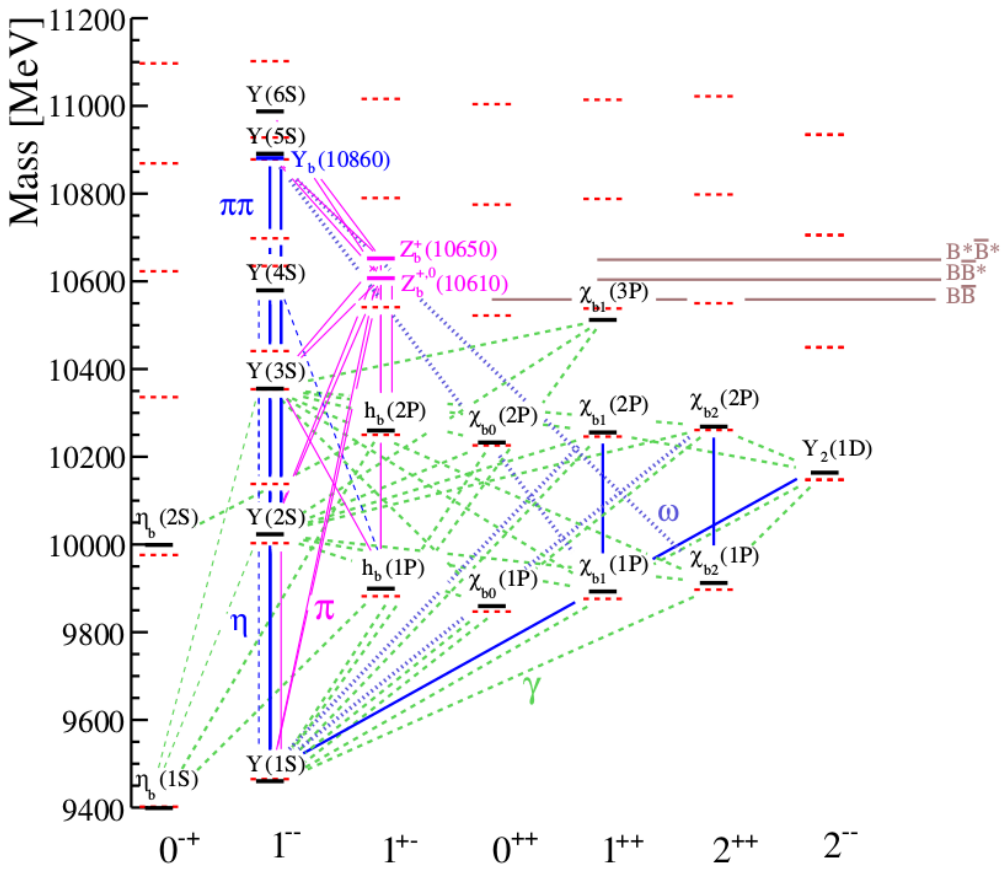

Figure 19: The spectra and decay patterns of bottomonium and bottomonium-like mesons. The red dashed lines indicate the expected states and their masses based on the Godfrey-Isgur relativised potential model [33]. The black solid lines indicate the experimentally established states. The open flavour threshold is also indicated with longer, solid, brown lines. The candidates for exotic quarkonium-like states are shown with shorter solid blue or magenta lines. The decay patterns are shown with lines connecting known states: dashed-green are γ transitions (thick E1, thin M1), solid-magenta are π, dashed-blue are η (thin) or ϕ (thick), dashed-red are p, dotted-blue are ρ^0 or ω, solid-blue other $\pi\pi$ transitions. Pictures taken from [9].

models of hadronic structures is the finding and the understanding of these new degrees of freedom.

Also if the bottomonium system is more challenging from the experimental point of view, and it requires more studies and more statistics, some states not fitting with the conventional $b\bar{b}$ mesons have been found with characteristics similar to those observed in the $c\bar{c}$ system, as expected from heavy-quark symmetry.

Currently, the models proposed to describe the configuration of quarks within XYZ states include:

- hadronic molecules: nuclei can be pictured as baryon-baryon molecules, and it has been proposed that some of the XYZ states can behave as an analogue meson-antimeson molecule, where a heavy open-flavour meson binds to a heavy open-flavour antimeson, and the meson-antimeson pair is separated by a distance larger than $\sim 1\,\text{fm}$, the typical size of a meson. The meson-antimeson interaction is nuclear

force-like through exchange of pions and other light mesons;

- diquarks: QCD predicts a binding between two quarks (diquark) in a spin-0 configuration with an attractive strength that is one-half of the strength between a quark and an antiquark in a standard meson. Therefore, diquarks and diantiquarks could bind to form some of the multi-quark hadrons [107]. States made out of diquarks must be compact due to the confinement of colour and the diquark and the diantiquark interact by exchange of gluons;

- QCD hybrids: states composed by quark-antiquark and a valence gluon. Hence the gluonic degrees of freedom plays a role in the J^{PC} quantum numbers, making accessible other quantum number combinations like $J^{PC} = 0^{--},\ 0^{+-},\ 1^{-+}$ etc., forbidden in conventional quarkonia. Hence the striking experimental feature for QCD hybrids would be their exotic quantum numbers;

- hadroquarkonium: this model [108] has been proposed in order to explain why most of the non-conventional hadrons above open-flavour thresholds have been discovered in decays involving quarkonia instead of open-charm mesons. In this model, the two heavy quarks form a compact colour-singlet tightly bound system whose wave function is close to that of one of the heavy quarkonium states. The heavy quark pair is embedded in a cloud of excited state of light mesonic matter and interacts with it by a QCD version of van der Waals force. In this model, decays to the hidden charmonium core state are enhanced to a level where they are competitive with those for open-charm modes [109];

If the resonant behaviour of an exotic candidate is established, most likely its wave function is a quantum admixture of all types of configuration listed above and consistent with the overall quantum numbers, including a conventional quarkonium. The difference between the listed clustering models is in the assumed prevalent configuration, with the other ones being considered as a relatively small admixture. It is interesting to understand which one is the dominant component, since it may provides new insights into the underlying strong dynamics of multiquark systems.

For instance, the favoured hypothesis for the internal structure of the $X(3872)$ state is a mixture of a tightly bound $c\bar{c}$ core in the 2^3P_1 configuration, the $\chi_{c1}(2P)$, and a $D\bar{D}^*$ S-wave molecule combination [110]. The molecule component is responsible for the isospin violation, while the charmonium component takes into account the $X(3872)$ prompt and from b-decays production modes.

However, not all the peaks in a mass spectrum are genuine hadron states. Indeed, some resonance-like structures could be due near-threshold kinematic effects. Some models are trying to explain at least some of these exotic candidates as kinematically induced resonance-like peak. These includes:

- threshold cusps: in a three-body decay, the production of a virtual pair in an S-wave configuration may produce a peaking structure called cusp near the virtual pair threshold mass value in the corresponding final state. However, genuine cusp effects are expected to be small;

- anomalous triangle singularity: in a three-body decay, diagrams that contain internal triangles may contribute. This diagram becomes singular when the three virtual

particles are all simultaneously on the mass shell. In kinematic regions where the conditions for this singularity are satisfied, resonance-like structures could appear.

The discrimination between the different models and the establishment of exotic hadron candidates require further experimental investigations. In this thesis, a search for charged charmonium-like mesons using the data sample collected by the LHCb detector is presented and described in the next chapters.

3 The Large Hadron Collider and the LHCb experiment

The Large Hadron Collider (LHC), currently the world's highest energy accelerator, is a proton-proton and heavy ion (lead) colliding synchrotron located at CERN. The machine is installed in the same 27 km long tunnel used formerly by the Large Electron-Positron collider (LEP) at the Franco-Swiss border. The LHC delivered the first pp collision in 2009, recorded by the four large experiments: ALICE, ATLAS, CMS and LHCb. An introduction to the LHC and the large experiments is given in Sec. 3.1.

The first important result obtained at the LHC is the discovery of the Higgs boson, the last missing brick of the SM, announced by the ATLAS and CMS collaborations [111, 112]. The main goal of the LHC experiments is to find NP beyond the SM. Direct searches, carried out by the ATLAS and CMS collaborations, confirmed the SM predictions at an unprecedented level of precision. The LHCb experiment is designed to search for indirect evidences of NP through precision measurements of processes involving the b or the c-quark. Deviations from theoretical predictions, *e.g.* enhanced decay and production rates due to new particles in loops, would indicate NP contributions. Therefore, the LHCb experiment is sensitive to particles beyond the SM not accessible through direct searches at the LHC energies. Some deviations from SM predictions have been already observed. The LHCb experiment is described in Sec. 3.2.

3.1 The Large Hadron Collider

The LHC [113] is a pp, p-Pb and Pb-Pb collider containing two beam pipes for the particle beams accelerated in opposite directions. The choice of using hadronic collisions instead of e^-e^+ collisions as done by LEP and by B-factories, is motivated by the higher events rate due to the largest cross-sections of strongly interacting particles with respect to leptons. Another motivation is given by the largest energy that can be achieved given the lower synchrotron radiation ($\propto 1/m^4$) emitted by heavier particles during their circulation. Moreover, the usage of pp collisions avoids the need for the production of antiprotons, the principal limitation to the achievable luminosity at Tevatron.

The peculiarity of the LHC is the usage of superconducting bending magnets to have the two beams of protons bent and circulating in opposite directions in the same structure of repeated sequences of dipole and higher-order multipole magnets. LHC comprises 1232 dipoles, providing magnetic fields up to 8.3 T, and 392 quadrupoles to focalise the beams. The power required to accelerate the beams is delivered by radiofrequency (RF) cavities working in a superconducting state. The LHC uses eight cavities per beam, each delivering 2 MV at 400 MHz. The ideally timed proton, with exactly the right energy, will see zero accelerating voltage when the LHC is at full energy. Protons with slightly different energies arriving earlier or later will be accelerated or decelerated in order to correct for the longitudinal spread of the protons distribution. In this way the particle beam is sorted and kept into discrete packets called bunches. The bending power of the magnets allows LHC to circulate protons at the current energy of 6.5 TeV per beam, corresponding to a centre of mass energy of $\sqrt{s} = 13\,\text{TeV}$.

3.1.1 The LHC accelerator chain

The CERN accelerator chain comprises a sequence of machines boosting the energy of a beam of particles, before injecting the beam into the next machine in the sequence. Most of the accelerators in the chain have their own experimental halls where beams are used for experiments at lower energies. A schematic representation of the CERN accelerator complex is shown in Figure 20.

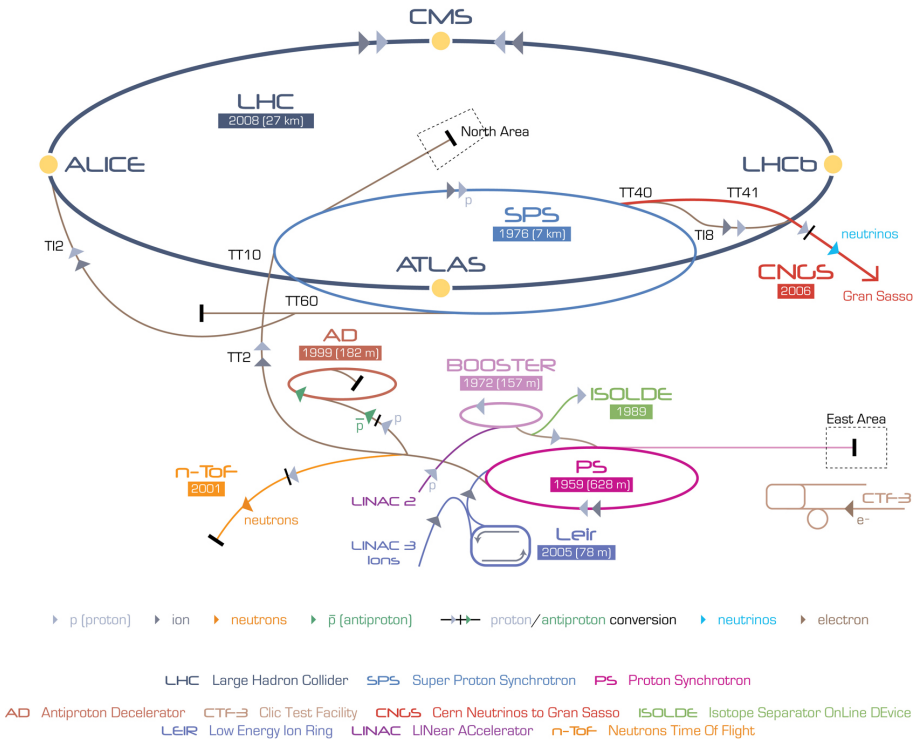

Figure 20: The CERN accelerator complex. The accelerator complex includes the Antiproton Decelerator (AD) used for antimatter experiments like AEGIS, the Online Isotope Mass Separator (ISOLDE) facility and the CERN Neutrinos to Gran Sasso (CNGS) facility for neutrino oscillations studies.

The protons source is a bottle of hydrogen gas. An electric field is used to strip hydrogen atoms of their electrons to yield protons. The first linear acceleration stage is provided by the LINAC 2, accelerating protons to the energy of 50 MeV and injecting them into the Proton Synchrotron Booster, which accelerates the protons up to 1.4 GeV. The booster is followed by the Proton Synchrotron (PS), accelerating the protons up to 25 GeV. The Super Proton Synchrotron (SPS) is the next acceleration stage, pushing the beam to 450 GeV. SPS operated from 1981 to 1991 as a $p\bar{p}$ collider providing beams for the UA1 and UA2 experiments that discovered the $W^{\pm}$ and the Z bosons. Protons can then be extracted for fixed target experiments located in the CERN North Area or to fill the LHC storage rings. It takes about 4 minutes to fill each LHC ring, and 20 minutes for the protons to reach their maximum energy of 6.5 TeV.

The LHC also accelerates lead ions provided by a different source using vaporised lead fully ionised. The ions are accelerated by the LINAC 3 and injected into the Low Energy Ion Ring (LEIR). The next acceleration stages are the same as for the protons, PS, SPS and LHC, resulting in an energy of 2.76 GeV per nucleon.

3.1.2 The LHC large experiments

There are four large experiments designed to exploit pp, p-Pb and Pb-Pb collisions delivered by the LHC: ALICE, ATLAS, CMS and LHCb.

ATLAS (A Toroidal LHC ApparatuS) and CMS (Compact Muon Solenoid) are general purpose detectors devoted to direct searches of particles beyond the SM and to precision measurements of the SM physics at the TeV scale. Both ATLAS and CMS are barrel-shaped detectors composed by various concentric subdetectors around the interaction point. They have been designed to cover almost the full solid angle and they adopted a trigger strategy centred on high transverse momentum (p_T) physics. CMS is characterised by a very compact structure allowed by a superconducting solenoidal magnet generating a magnetic field of 3.8 T. On the other side ATLAS is the largest collider experiment ever built, being 46 m long with a diameter of 25 m. Both ATLAS and CMS are currently setting tight constraints on NP scenarios beyond the SM.

ALICE (A Large Ion Collider Experiment) has been designed to study nuclear matter at extreme temperature and pressure conditions obtained in Pb-Pb collisions. In such conditions the matter undergoes a phase transition to form the quark-gluon plasma, where quarks and gluons are expected not to be confined inside hadrons and QCD can be described as a perturbative theory. In order to study QCD and quark confinement under these extreme conditions, ALICE comprises the implementation of most of the particle detection techniques, using a set of 18 subdetectors.

LHCb is the LHC experiment dedicated to flavour physics, allowing for indirect searches for physics beyond the SM through precision studies of b and c-hadron decays. The LHCb detector is a forward spectrometer whose design is motivated by the properties of $b\bar{b}$ pairs production in pp collisions at high energy. The LHCb experiment is described in Section 3.2.

3.1.3 The LHC beam structure and luminosity

The LHC beams structure derives from the properties of the RF cavities used to accelerate the protons. Given the revolution frequency of ~ 11 kHz of a proton travelling approximately at the speed of light within the LHC length of ~ 27 km, and the RF frequency of 400 MHz, there are ~ 35640 segments, named RF buckets, of the LHC circumference wherein the injected protons can see an accelerating voltage. A particle exactly synchronised with the RF frequency is called a synchronous particle. All the other protons will oscillate longitudinally around the synchronous particles under the influence of the RF system. The result is that the protons are grouped around the synchronous proton in a bunch, contained in an RF bucket. Each bunch contains up to $\sim 10^{11}$ protons. In principle LHC might accelerate a beam made up of 3564 bunches but a number of buckets in a row must be left empty for safety reasons related to the beam dump system, in order to allow the beam dump kicker magnets the time to switch on. The bucket configuration determines where the protons in the two beams will cross-over and collide, i.e. in which detector the specific bunches will collide. By design LHC can be filled with up to 2808 bunches, with PS responsible for providing the bunch packets with 25 ns spacing that finally will be injected from SPS in the LHC. In conclusion the bunches are generally separated by about 7.5 m, corresponding to 25 ns and to 10 RF buckets. The biggest hole in the bunch structure is the beam abort gap of 3 μs, corresponding to 900 m. The purpose of this gap is that in the dump process it takes a short, but significant time,

to switch on the magnets which divert the beam from the LHC to the dump. There are also other smaller gaps in the beam which arise from similar needs from the SPS and LHC injection kicker magnets.

The instantaneous luminosity $\mathcal{L}$ is the accelerator parameter allowing to estimate the event rate R for a process when its cross-section σ is known. Indeed, the event rate is given by

$$R = \frac{dN}{dt} = \mathcal{L}\,\sigma. \tag{9}$$

$\mathcal{L}$ depends on various machine parameters and it is given by

$$\mathcal{L} = f\frac{n_1 n_2}{4\pi\sigma_x\sigma_y}F, \tag{10}$$

where $f \sim 11\,\text{kHz}$ is the frequency of colliding proton bunches, n_1 and n_2 are the number of protons per beam, σ_x and σ_y represent the overlap area between the two beams in the transverse plane with respect to the direction of motion and F is a geometrical reduction factor that takes into account the beams crossing angle. The peak luminosity of the LHC is $\mathcal{L} = 10^{34}\,\text{cm}^{-2}\text{s}^{-1}$. $\mathcal{L}$ changes in time during a data-taking fill because of the variation of n_1 and n_2 due to beam-beam collisions which eject protons from the beams, and because of the increase in σ_x and σ_y due to beam warming. In order to estimate the number of events in a given data sample, the integrated luminosity, $\text{L} = \int \mathcal{L}\,\text{dt}$, is used and it is expressed in fb^{-1} or its multiples.

Another important parameter is the average number, μ, of pp collisions per bunch crossing visible in the detector, depending on the instantaneous luminosity of the accelerator, as shown in Figure 21. The number of pp collisions per bunch crossing follows a Poisson distribution with a mean given by

$$\mu = \frac{\sigma_{\text{inel}} \cdot \mathcal{L}}{f \cdot \epsilon_{filled}}, \tag{11}$$

where σ_{inel} is the pp inelastic cross section and ϵ_{filled} is the fraction of non-empty bunch crossings. As described later, the physics programme of LHCb requires a precise event reconstruction, motivating the choice by the LHCb collaboration to run at a luminosity not larger than $\mathcal{L} = 4 \times 10^{32}\,\text{cm}^{-2}\text{s}^{-1}$, corresponding to $\mu \sim 1.7$. This is achieved displacing the beams in the transversal direction in order to reduce the effective overlap area.

3.1.4 The $b\bar{b}$ production cross section

The cross-sections of various processes as functions of the centre-of-mass energy, $\sqrt{s}$, are shown in Figure 22. As it can be seen, the $b\bar{b}$ production cross-section increases significantly with $\sqrt{s}$, with a steeper slope than the total pp cross-section. At the nominal value of $\sqrt{s} = 14\,\text{TeV}$, the $b\bar{b}$ cross-section at the LHC is $\sim 600\,\mu\text{b}$, with respect to the $10\,\mu\text{b}$ at $\sqrt{s} = 1.96\,\text{TeV}$ in the CDF acceptance at Tevatron. For comparison, the e^+e^- cross section at the centre-of-mass energy corresponding to the mass of the $\Upsilon(4S)$ resonance is of the order of the nb.

As introduced in Section 2.4 and as shown in Figure 23, the angular distribution of the $b\bar{b}$ production is peaked in a small region at low polar angles, in the (same) forward or backward direction. This phenomenon can be naively explained considering that the partons interacting to produce the $b\bar{b}$ pair have a variable fraction of the colliding protons

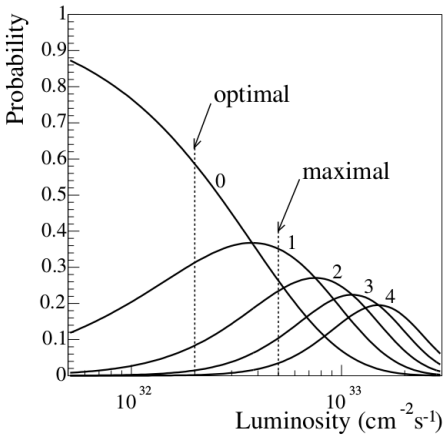

Figure 21: The probability for 0,1,2,3 and 4 inelastic collisions occurring per bunch crossing as a function of the luminosity.

momentum, hence there is a boost given by the direction of the parton with higher momenta.

Therefore, LHCb has been designed as a forward spectrometer. Despite it covers the 4% of the solid angle, it collects the $\sim 25\%$ of the $b\bar{b}$ pairs produced at the LHC.

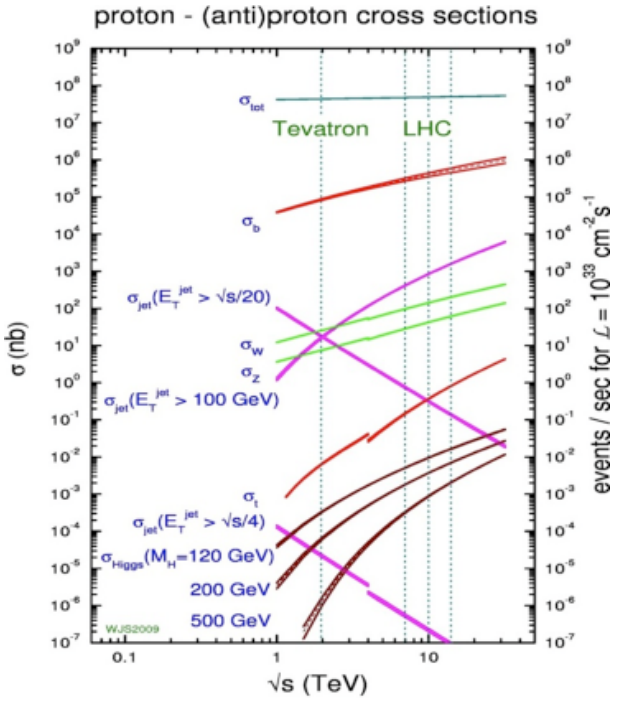

Figure 22: Cross-sections for different final states from $p\bar{p}$ or pp collisions as a function of the centre of mass energy $\sqrt{s}$. The vertical dotted lines indicate the $\sqrt{s}$ of Tevatron and of the LHC. Measurements up to 57 TeV are available from the Auger experiment [114].

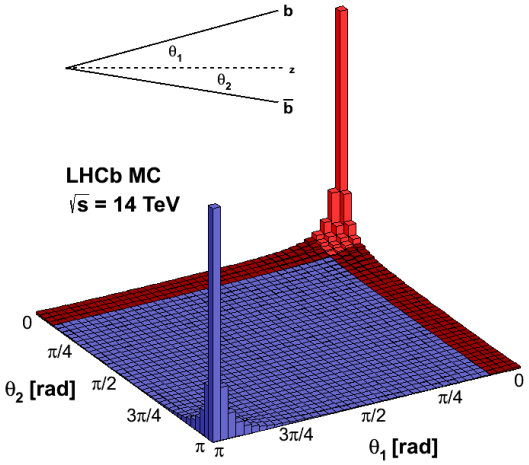

Figure 23: Correlation of the polar angles, i.e. the angle with respect to the beam axis, of the hadrons containing the b or the $\bar{b}$ quark as generated by a PYTHIA [115] simulation of $pp \to B\bar{B}X$ events at LHC.

3.2 The LHCb detector

The primary goal of the LHCb experiment is to search for new physics in *CP* violating processes and rare decays of beauty and charm hadrons, by looking for the effects of new particles in loop processes that are precisely predicted in the SM. These new physics effects could manifest themselves through enhanced decay or production rates. In order to fulfil its physics goals, the LHCb detector must be able to separate the large number of b-hadrons produced by the LHC from the overwhelming background, since the charm and beauty cross-sections are approximately a factor 10 and 200 smaller than the total pp cross-section, respectively.

The LHCb detector [42] is a single-arm spectrometer in the forward region covering an angular range from 15 mrad to 300 mrad (250 mrad) in the bending (non-bending) plane of the dipole magnet. This geometrical acceptance corresponds to a pseudorapidity range of $2 < \eta < 5$, where the pseudorapidity is defined in terms of the polar angle θ, i.e. the angle with respect to the beam line, as

$$\eta = -\log(\tan(\theta/2)), \tag{12}$$

that in terms of a particle kinematical variables can be written as

$$\eta = \frac{1}{2}\log\left(\frac{p + p_{\mathrm{L}}}{p - p_{\mathrm{L}}}\right), \tag{13}$$

where p is the particle momentum and p_{L} is the longitudinal momentum. This range was chosen to optimise the acceptance for the produced b- and c-hadrons produced as described in Section 3.1.4.

The layout of the LHCb detector is shown in Figure 24. The origin of the coordinate system adopted by LHCb is located at the pp interaction point, namely the primary vertex

(PV). The z axis is aligned with the beam axis and points in the downstream direction, towards the end of the detector. The y axis points vertically upwards. The x axis points horizontally towards the centre of the LHC ring. The bending plane of the magnet is the x-z plane.

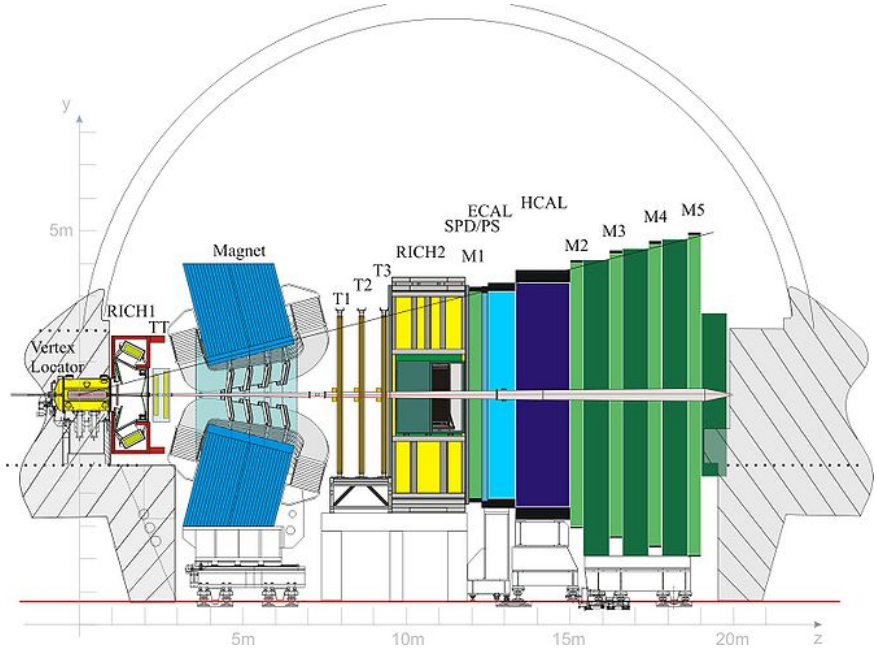

Figure 24: Schematic view of the LHCb detector in the non-bending vertical plane with the subdetectors labelled.

Due to their relatively long lifetime, b and c-hadron decays are characterised by a displaced decay vertex, namely the secondary vertex (SV). The identification of these decays in the LHCb detector requires an excellent vertex and proper time resolution. In order to reject the background due to random combinations of tracks (combinatorial background), typical of hadronic colliders, a precise invariant-mass reconstruction is required, that implies a very good momentum resolution. Given the possibility to have topologically identical decay modes, a precise particle identification (PID) system is required, especially for charged hadrons separation. Finally, in order to collect high statistics samples and to efficiently reconstruct decays having very small branching fractions, a versatile trigger scheme has been implemented. These requirements are accomplished by the LHCb subdetectors. They can be logically grouped in two categories based on their function:

- the tracking system, comprising a vertex locator (VELO) around the interaction point, a tracking detector (TT) immediately upstream the magnet and three tracking stations (T1,T2,T3) immediately downstream the magnet;
- the PID system, composed of two Ring Imaging Cherenkov (RICH) detectors, the calorimeter system (PS, SPD, ECAL and HCAL) and five muon stations.

3.2.1 The tracking system

The purpose of the tracking system is to reconstruct the trajectories of charged objects (tracks) using the positions where the charged particles interacted with the tracking detectors (hits). The momentum p of a particle is determined from its angle of deflection after traversing the magnetic field provided by a dipole warm magnet. In order to achieve a momentum resolution of $\delta p/p = 4 \times 10^{-3}$ for 10 GeV particles, an integrated field of 4 Tm is required between the VELO and the tracking stations, with the constraint for the magnetic field to be small in the region of RICH1, since the photodetectors are sensitive to magnetic fields. The B_y component along the z coordinate is shown in Figure 25(b). The magnetic field is inverted periodically (i.e. the same amount of recorded luminosity is taken by LHCb for the two magnet polarity configurations) during the data-taking to check for detection asymmetries, in order to reduce systematics effects in particular in *CP* violation measurements.

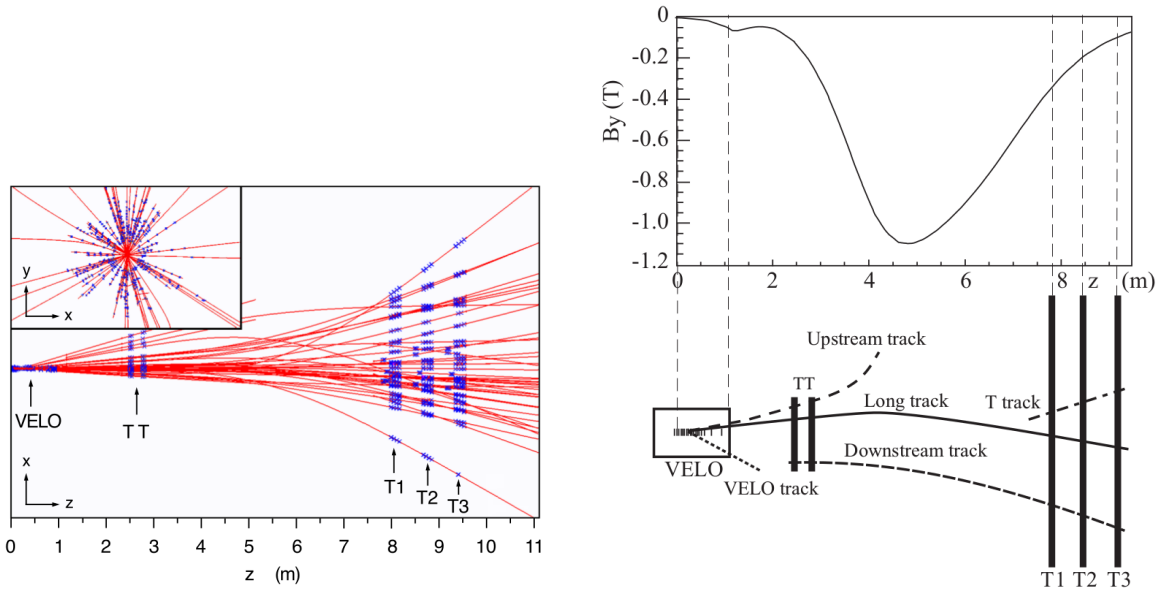

(a) (b)

Figure 25: (a): Display of the reconstructed tracks and assigned hits in an event in the x-z plane, i.e. the bending plane. The insert shows a zoom into the VELO region in the x-y plane, i.e. the transverse plane; (b): A schematic illustration of the various track types. For reference, the main B-field component (B_y) is plotted above as a function of the z coordinate.

The sensitive parts of the tracking system are shown in Figure 25(a). The following track types, illustrated in Figure 25(b) and depending on their paths through the spectrometer, can be defined:

- long tracks, having hits in both the VELO and in the tracking stations T1, T2 and T3 after the magnet, and optionally in TT. They have the most precise momentum estimate and therefore they are the most important set of tracks for physics analyses;
- upstream tracks, having hits in the VELO and the TT, but not in the downstream tracking stations T1, T2 and T3. Upstream tracks corresponds to low momentum

objects that are deflected outside the acceptance by the magnetic field before reaching the downstream trackers. The information of the momentum of these tracks is given by the bending provided by the residual magnetic field between the VELO and the TT;

- downstream tracks, having hits in the TT and in T1, T2 and T3, but not in the VELO. They are important to reconstruct neutral long lived hadrons, such as the K_s^0 and the Λ, that decay between the VELO and the TT;
- VELO tracks, having hits only in the VELO. They are typically large angle or backward tracks, useful for the PV reconstruction;
- T-tracks, passing only through the downstream tracking stations. They are very rarely used for physics analyses, but are useful for calibration and detector studies.

3.2.2 The Vertex Locator

The Vertex Locator (VELO) [116] is a silicon detector providing precise measurements of particle trajectories close to the interaction point. The goal of the VELO is to accurately determine the locations of the PV and of the SV in oder to precisely reconstruct the flight distance of heavy quark hadrons. The VELO consists of 42 silicon strip modules positioned in the plane perpendicular to the beam axis. Each module provides a measure of the radial distance from the origin r and of the azimuthal angle ϕ. The choice of the cylindrical coordinate system is done in order to speed up the tracks reconstruction used in the trigger.

In order to achieve its goals, the VELO must be located as close as possible to the interaction point. It is designed to be located at $\sim 7\,\text{mm}$ from the LHC interaction point, also considering the needs in term of radiation tolerance imposed by the severe radiation environment. Since during injection the beam is not focused enough, the VELO must be retractable to avoid damage to the sensors. For this reason the VELO is split vertically into two retractable halves, each with an equal number of modules on either side of the beam line. Before the LHC ring is filled, the two halves move away from the interaction region by 30 mm. Once the beams reach stable conditions, the two halves move back to the nominal position transversally centred around the interaction region. Each half of the VELO is enclosed in a box of thin aluminium maintaining the vacuum around the sensors. The inner faces of the vessels, called RF-foils, separate the VELO vacuum from the machine vacuum, also protecting the sensors from RF background of the machine. The RF-foils are designed to minimise the material traversed by a charged particle before it crosses the sensors, in order to have a negligible impact on the VELO performance. Furthermore, the geometry of the RF-foils is such that it makes the two halves of the VELO to overlap when it is moved to the closed position when stable beam conditions are declared. A sketch of the VELO is shown in Figure 26.

The r-sensor strips are concentric rings with a variable pitch that increases linearly from $38\,\mu\text{m}$ at the inner edge to $102\,\mu\text{m}$ at the outer edge. The ϕ-sensor strips are wedge-shaped and divided into two regions at $r = 17.25\,\text{mm}$ in order to reduce the occupancy and to avoid large strip pitches at the outer edge of the sensors, that would reduce the hit resolution. The strips have a pitch of $38\,\mu\text{m}$ in the inner region (increasing to $78\,\mu\text{m}$ at the outer edge), while the strips in the outer region have a pitch of $39\,\mu\text{m}$ (increasing to

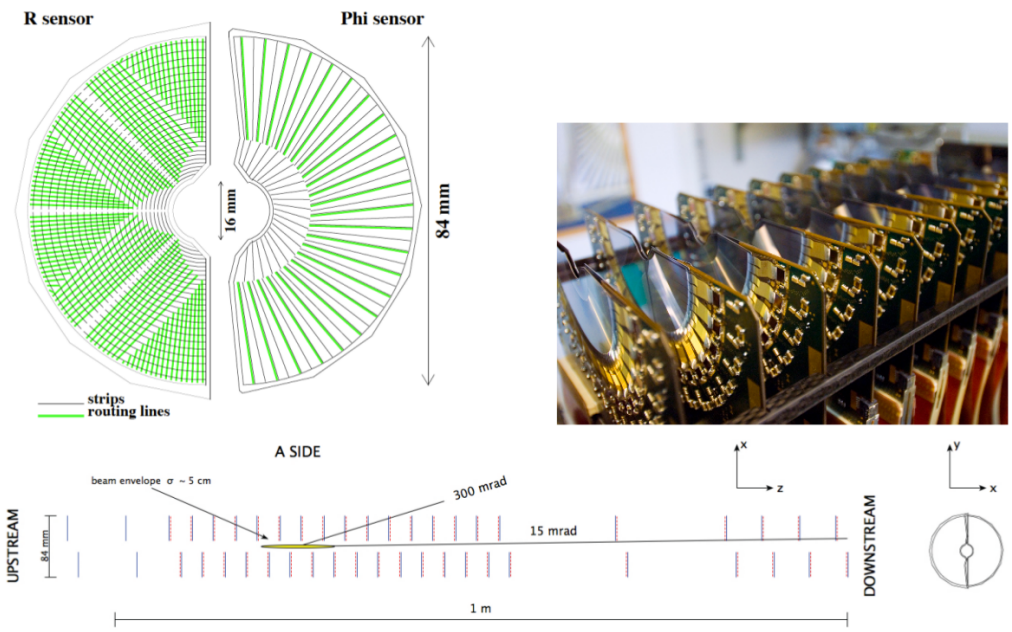

Figure 26: Top left: sketch illustrating the $r\phi$ geometry of the VELO sensors. Top right: photograph of an half of the VELO detector. Bottom: cross-section in the x-y plane with the VELO in the closed position. The solid blue lines represent the r-strip layers, while ϕ-strip layers are shown as dashed red lines.

97 μm at the outer edge). To reduce ambiguities in the pattern recognition, the ϕ-sensor strips are 20° skewed from the radial direction in the inner region and 10° in the outer region.

The VELO covers the angular acceptance of the downstream detectors, detecting charged particles emerging from PV in the range $z < 10.6\,\text{cm}$ within the pseudorapidity range $1.6 < \eta < 5$. Such tracks are required to cross at least three VELO modules.

The resolution on the position of the PV obtained with the VELO varies between 9 μm and 35 μm for the x and y coordinates, and between 50 μm and 280 μm for the z coordinate, depending on the number of tracks used to reconstruct the vertex. Typical events with 25 tracks originating from the PV have a transversal resolution of $\sim 15\,\mu$m and a longitudinal resolution of $\sim 71\,\mu$m.

Another important parameter measured by the VELO is the impact parameter (IP). The IP is defined as the distance of closest approach of the extrapolated particle trajectory to the PV and it is illustrated in Figure 27(a). It is extensively used in the physics analyses to discriminate between signal and combinatorial background tracks. Indeed, signal particles, typically produced in the decay of a b-hadron having a displaced SV, will have an higher IP with respect to the background particles coming from the PV.

The VELO has the highest resolution on the IP of charged tracks among the large experiments at the LHC, varying between 10 μm and 80 μm, depending on the transverse momentum of the considered track. Indeed, the dominant uncertainty on the IP is due to the multiple scattering of the tracks crossing the VELO modules. Hence, an inverse relation with the p_T of the track is expected and observed, as shown in Figure 27(b).

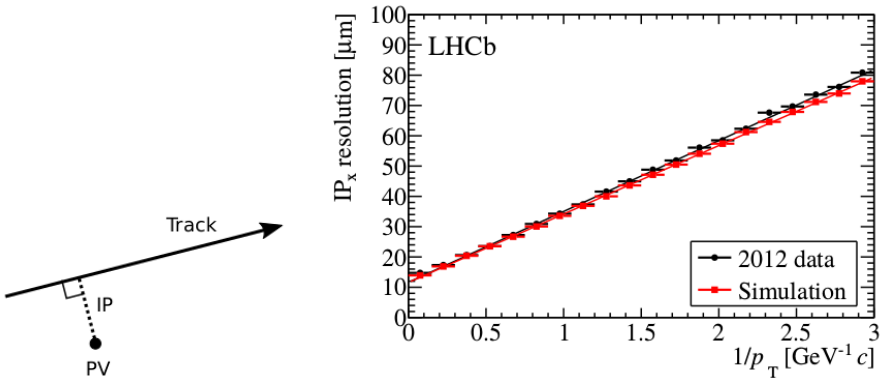

(a) (b)

Figure 27: (a): Illustration of the IP (length of the dotted line) of a track (solid line) in relation to the PV. The figure is drawn in the plane containing the track and the PV; (b): IP resolution as a function of p_T from simulation (red) and data (black).

3.2.3 The Tracker Turicensis

The Tracker Turicensis (TT) [116] is located immediately before the dipole magnet and its primary goal is to reconstruct the decay vertex of neutral hadrons decaying outside the VELO acceptance, such as the K_s^0 or the Λ. The TT consists of four layers of silicon microstrip sensors with a pitch of 183 μm between the strips. The first and last layers are oriented vertically, and the second and third are rotated respectively by -5° and +5° from the vertical. This structure allows a spatial resolution of $\sim 50\,\mu$m in the x coordinate. The first two TT layers are sketched in Figure 28.

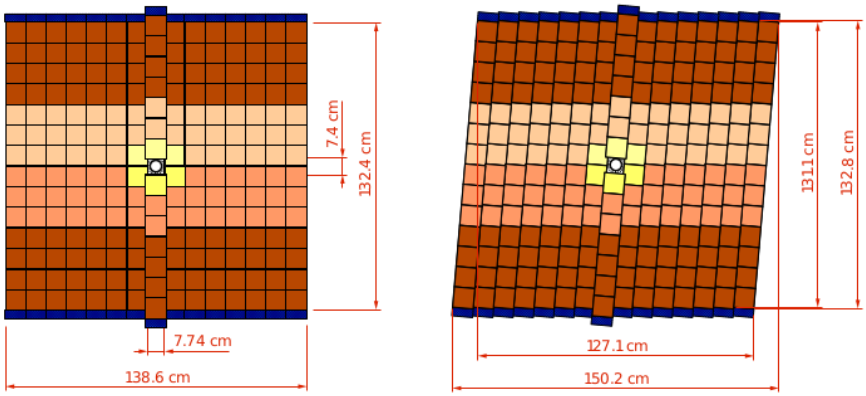

Figure 28: The first two layers of the TT, showing the vertical and 5° orientations of the modules.

Each detection layer is composed of a set of half-modules covering half of the height of the LHCb acceptance. A half-module is a row of seven silicon devices. The main advantage of this detector design is that all the frontend electronics and the cooling infrastructure are located outside of the acceptance of the experiment, above or below the active area of the detector.

3.2.4 Inner and Outer Tracker

The tracking stations located downstream of the magnet (T1, T2 and T3) are required to measure the momentum of charged particles deflected by the dipole magnetic field. The three tracking stations make use of two different technologies, motivated by the unbalance in the particle flux within the LHCb acceptance. The inner tracker (IT) [117], closer to the beams, is made of silicon detectors, while the outer tracker (OT) [118] is made of drift tubes, gas detectors used to minimise the material budget before the calorimeters. Inner trackers cover a region of $\sim 2\%$ of the total area ($5\,\mathrm{m} \times 6\,\mathrm{m}$) of a tracking station, but due to the low-angle peak in particle distributions, they measure the $\sim 20\%$ of the total particle flux.

Each IT station has four boxes arranged around the beam pipe as shown in Figure 29. Each IT box consists of four detection layers arranged, like the TT layers, at 0°, −5°, +5° and 0° from the vertical. Each IT layer consists of seven detector modules made of silicon strips having a pitch of $196\,\mu\mathrm{m}$. Unlike the TT, the frontend electronics and the cooling system are inside the LHCb acceptance.

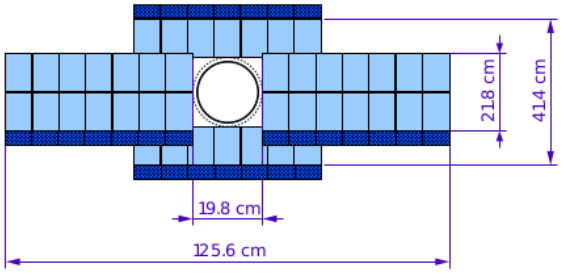

Figure 29: Position of the four boxes composing an IT station.

Each OT station consists of 12 double layers of drift tubes. The modules have the same orientation as the strips in each layer of the TT and the IT. The layout of the OT stations is shown in Figure 30. The drift chambers are 2.4 m long with 4.9 mm inner diameter, and are filled with a gas mixture of $\mathrm{Ar/CO_2/O_2}$ (70/28.5/1.5) which guarantees a fast drift-time below 50 ns and good ageing properties. The tubes are fixed to carbon-fibre panels resulting in gas-tight boxes enclosing stand-alone detector modules. Each module is composed of two layers of 64 drift tubes each. The complete OT detector consists of 168 long and 96 short modules and comprises 53760 single drift tube channels.

The hit resolution along the x-axis is $50\,\mu\mathrm{m}$ and $200\,\mu\mathrm{m}$ for the inner and outer trackers, respectively [119].

3.2.5 Mass and momentum resolution

The momentum resolution for long tracks in data is extracted using $J/\psi \to \mu^+\mu^-$ decays. Figure 31 shows the relative momentum resolution, $\delta p/p$, as a function of the momentum p. The momentum resolution is about 5 per mille for particles below 20 GeV, rising to about 8 per mille for particles around 100 GeV.

The mass resolution is compared for six different dimuon resonances: the J/ψ, $\psi(2S)$, $\Upsilon(1S)$, $\Upsilon(2S)$ and $\Upsilon(3S)$ mesons and the Z boson. These resonances are chosen as they share the same decay topology and exhibit a clean mass peak. The mass resolution

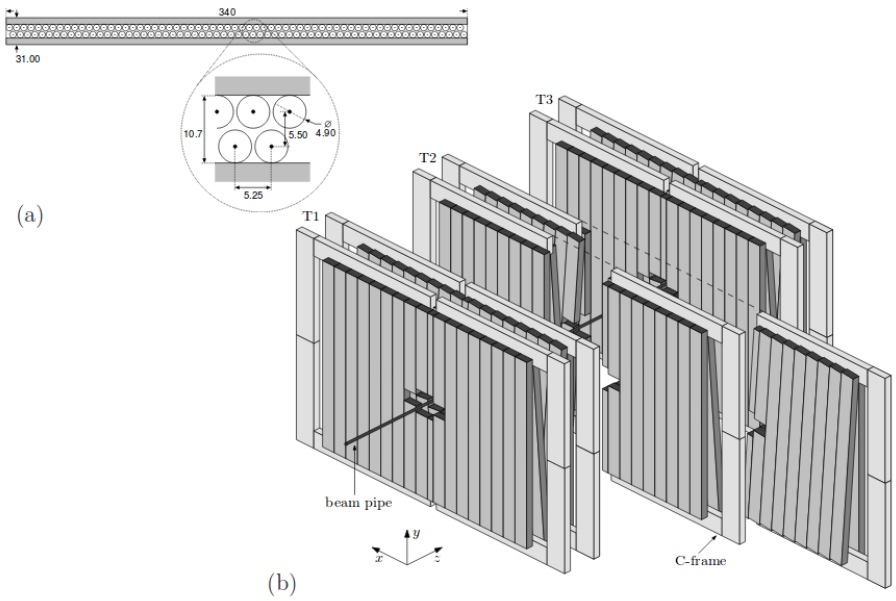

Figure 30: (a): Module cross section; (b): arrangement of OT drift tube modules in layers and stations.

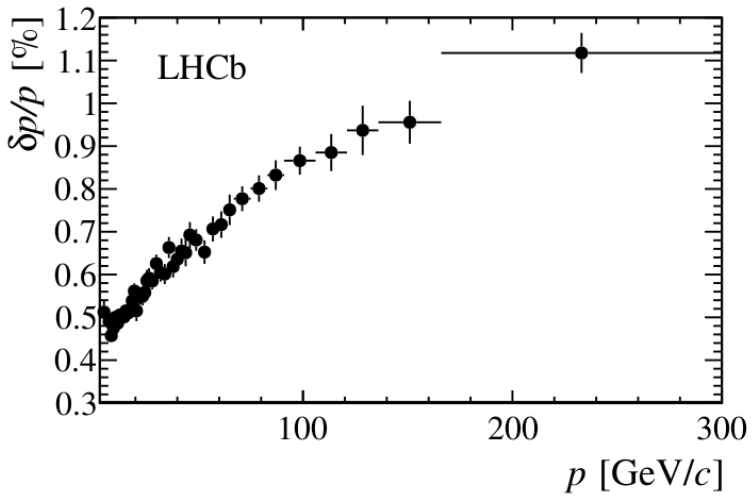

Figure 31: Relative momentum resolution versus momentum for long tracks in data obtained using J/ψ decays.

obtained from the fits to the invariant-masses of the dimuon resonances are listed in Table 2. The mass resolution and the relative mass resolution versus the mass of the resonances are shown in Figure 32. The relative mass resolution, σ_m/m, is about 5 per mille up to the $\Upsilon(nS)$ masses.

The calibration of the momentum measurement, the so-called momentum scale calibration, is achieved comparing the measured masses of known resonances with the world average values [15]. This is done using, for instance, large samples of $J/\psi \to \mu^+\mu^-$ and $B^+ \to J/\psi K^+$ decays. A systematic uncertainty of 0.03% on the momentum scale is obtained. The momentum scale calibration, applying corrections to the particle momenta at the sub-per-mille levels, is used in the analysis described in Chapter 4.

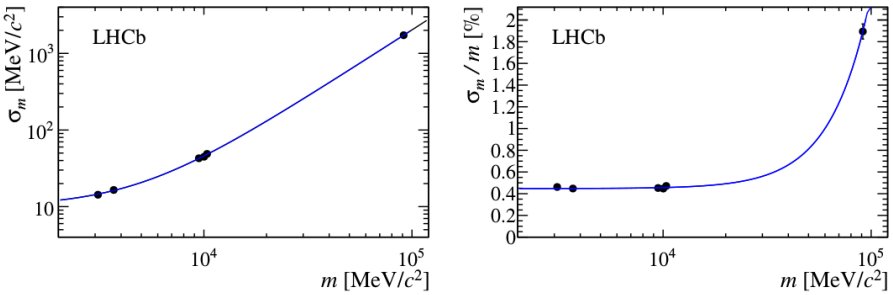

Figure 32: Mass resolution σ_m (left) and relative mass resolution (right) as a function of the mass m of the dimuon resonance. The mass of the muons can be neglected in the invariant-mass calculation of these resonances. The mass resolution is obtained from a fit to the mass distributions. The superimposed curve is an extrapolation obtained from an empirical power-law fit.

Resonance	Mass resolution [MeV]
J/ψ	14.3 ± 0.1
$\psi(2S)$	16.5 ± 0.4
$\Upsilon(1S)$	42.8 ± 0.1
$\Upsilon(2S)$	44.8 ± 0.1
$\Upsilon(3S)$	48.8 ± 0.2
Z	1727 ± 64

Table 2: Mass resolution for the six different dimuon resonances used in the momentum scale calibration.

3.2.6 Charged hadrons PID: the RICH system

The LHCb detector contains two RICH detectors [120] providing an efficient system of charged particle identification to mainly discriminate between charged pions, charged kaons and protons produced in b and c-hadrons decays.

Cherenkov radiation is emitted when a charged particle passes through a dielectric medium, namely the radiator, with a speed β greater than the phase velocity of light $1/n$ in the medium, where n is the refractive index of the material [121]. The Cherenkov effect can be naively explained as an asymmetric polarisation of the medium in front and at the rear of the charged particle, giving rise to a net and varying with time electric dipole momentum. For sufficiently fast particles, a polarised region is generated following an axial symmetry. In this region, individual atoms or molecules act as electric dipoles and create a net overall dipole field, responsible for the emission of the electromagnetic pulses of the Cherenkov radiation when atoms or molecules relax back. If $\beta > 1/n$, there is a constructive interference between wavelets propagated from successive areas along the particle path, producing a coherent wavefront. This wavefront is generated in the form of a cone and moves with a velocity $1/n$ at a constant polar angle (Cherenkov angle) from the trajectory of the particle, whose cosine is given by

$$\cos\theta_c = \frac{1}{n\beta}. \tag{14}$$

A RICH detector employs spherical mirrors to focus the light cones into rings. The radius of a Cherenkov ring is the product of θ_c and the focal length of the mirror. The measurement of the radius of these rings gives information on the velocity of the corresponding particle. When the rings are associated to tracks which momentum has been measured by the tracking system, the mass of the particle can be inferred.

The minimum particle speed required for Cherenkov radiation to be emitted by the traversed medium at $\theta_c = 0°$ is then given by

$$\beta_{\text{th}} = \frac{1}{n}. \tag{15}$$

Conversely, the maximum angle of emission occurs when the particle speed approach the speed of light ($\beta \to 1$), and it is given by

$$(\theta_c)_{\max} = \arccos \frac{1}{n}, \tag{16}$$

In this conditions different charged particles cannot be distinguished anymore. These saturated tracks can be used to determine the Cherenkov angle resolution of a RICH detector, given the known refractive index of the medium and the refractive index inferred by the measurement of θ_c from saturated tracks.

Cherenkov radiation is prompt in time, being the timing of photons hitting the photodetector planes distributed around few hundreds picoseconds, and it has a frequency spectrum that is continuous. The number of Cherenkov photons emitted per unit length of particle path in the radiator and per unit of wavelength is given by

$$\frac{\mathrm{d}^2 N_\gamma}{\mathrm{d}x \mathrm{d}\lambda} = \frac{2\pi z^2 \alpha}{\lambda^2} \left(1 - \frac{1}{\beta^2 n^2}\right), \tag{17}$$

where ze is the charge of the particle and α is the electromagnetic coupling constant [122]. This equation shows that short wavelengths of the spectrum dominate the Cherenkov radiation. Photomultipliers are used to detect Cherenkov light from the UV to the near infrared wavelengths.

The refractive index $n = n(\nu)$ varies with frequency in such a way that the number of emitted Cherenkov photons cannot continue to increase at ever shorter wavelengths. Indeed, at X-ray frequencies or above, the refractive index become less than unity and hence no Cherenkov emission is observed. Another consequence of the dispersion of the refractive index is that the emission angle $\theta_c = \theta_c(\nu)$ depends on the frequency of the emitted Cherenkov photons. Hence different photons from the same charged track can have different Cherenkov angles. This spread in angles gives rise to the chromatic uncertainty when measuring θ_c, that must be taken into account in the choice of the radiator used in a RICH detector.

The LHCb RICH detectors, shown in Figure 33, have gas-tight volumes filled with fluorocarbon gas radiators. They have a very low material budget to affect as little as possible the momentum measurement performed by the tracking system. RICH 1, placed before the magnet, aims to measure low momentum particles which can be deflected out of the detector acceptance by the magnetic field. RICH 1 has a material budget of only about 8% X_0. RICH 2 is placed after the magnet and aims to measure higher momentum particles that are supposed to remain within the geometrical acceptance after the magnetic

deflection. RICH 2 material budget is about 15% X_0. Both RICH detectors have similar optical systems, with a tilted spherical focusing primary mirror, and a secondary flat mirror to limit the length of the detectors along the beam direction and to redirect the photons onto the photodetector planes installed outside the acceptance. Each optical system is divided into two halves on either side of the beam pipe, with RICH 1 being divided vertically and RICH 2 horizontally. A reflectivity of about 90% has been achieved for the mirrors, averaged over the wavelength region of interest (200-600 nm).

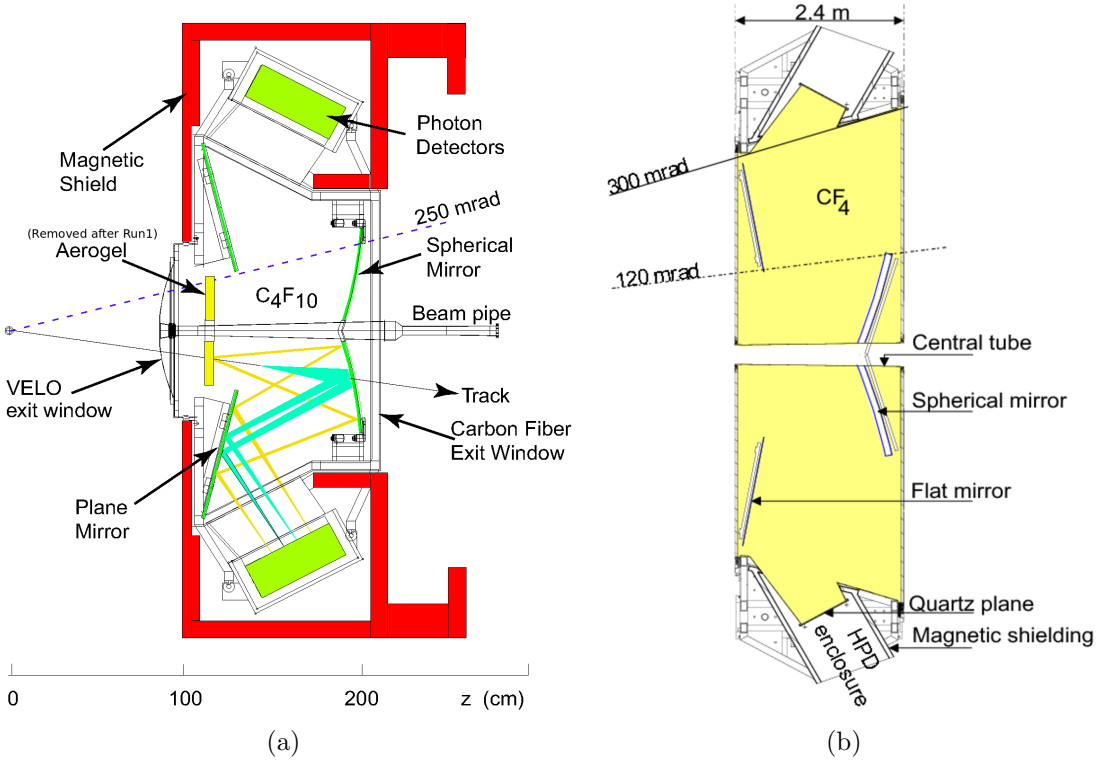

Figure 33: (a): Side view of RICH1 during Run1. The Cherenkov photons path is drawn. The Aerogel radiator has been removed just before the beginning of Run2. (b): Top view of RICH2.

RICH 1 is positioned between the VELO and the TT. A magnetic shield is used in order to prevent the residual magnetic field to affect the performance of the photodetectors. During Run 1, it used both silica aerogel and C_4F_{10} as Cherenkov radiators. Silica aerogel has a refractive index tuned to $n = 1.03$ and it provides PID at low momentum, *i.e.* between $\sim 2\,\text{GeV}$ and $\sim 10\,\text{GeV}$. C_4F_{10} has a refractive index slightly dependent on the wavelength ($n = 1.0014$ at $\lambda = 400\,\text{nm}$, $T = 0\,^\circ\text{C}$ and $p = 1\,\text{atm}$). Aerogel has been removed before the beginning of Run 2 since its performance would have been compromised by the larger track multiplicity environment due to the increased centre-of-mass energy of pp collisions. As a result, RICH 1 was able to identify charged hadrons in the low and intermediate momentum region ~ 2 - $60\,\text{GeV}$, while currently it is performing optimal PID in the $\sim$ 10-60 GeV range. Actually, because of the not optimal Aerogel performance, in many Run 1 physics analysis the effective lower limit for charged hadrons PID is $\sim 8\,\text{GeV}$.

RICH 2 is located after the third tracking station and before the first muon station. It uses CF_4 as Cherenkov radiator, having a refractive index of $n = 1.0005$ at $\lambda = 400\,\text{nm}$, $T = 0\,^\circ\text{C}$ and $p = 1\,\text{atm}$. About 5% of CO_2 has been added to CF_4 in order to quench

the scintillation in the gas. RICH2 covers the high momentum region 15-100 GeV.

The Cherenkov photons are focused into ring images on the photodetector planes, located outside of the LHCb acceptance. Hybrid Photon Detectors (HPDs) are used to detect the Cherenkov light. The HPDs employ vacuum tubes with a 75 mm active diameter, with a quartz window and multialkali photocathode. The photoelectrons are focused onto a silicon pixel array, using an accelerating voltage of -16 kV. The pixel size is $2.5 \times 2.5\,\mathrm{mm}^2$. The photodetector planes are separated from the radiator gas volumes by quartz windows, and photodetector volumes are maintained in an atmosphere of CO_2. The frontend electronics chip is encapsulated within the HPD vacuum tube, and bump-bonded to the silicon pixel sensor, which results in extremely low noise (typically 150 e^- RMS per pixel for a signal of 5 ke$^-$). The tubes also feature an high active area of about 82%. The quantum efficiency is about 30% at 270 nm.

The overall Cherenkov angle resolution determines the quality of the RICH detectors, since it is the fundamental parameter on which is based the separation of two particle types, especially at high particle momentum where Cherenkov angles tend to saturate. Apart from chromatic dispersion, other factors limit the Cherenkov angle resolution: the imperfect focusing of the optics, giving rise to the uncertainty related to the emission point of the Cherenkov radiation, and the pixel size of the photodetectors. The Cherenkov angle resolution is in average 1.65 mrad for RICH 1 and 0.67 mrad for RICH 2.

Figure 34 shows the relation between the Cherenkov angle and momentum for various particle species in each of the radiators used in the LHCb RICH detectors. The Cherenkov thresholds for pions and kaons for the different radiators are reported in Table 3.

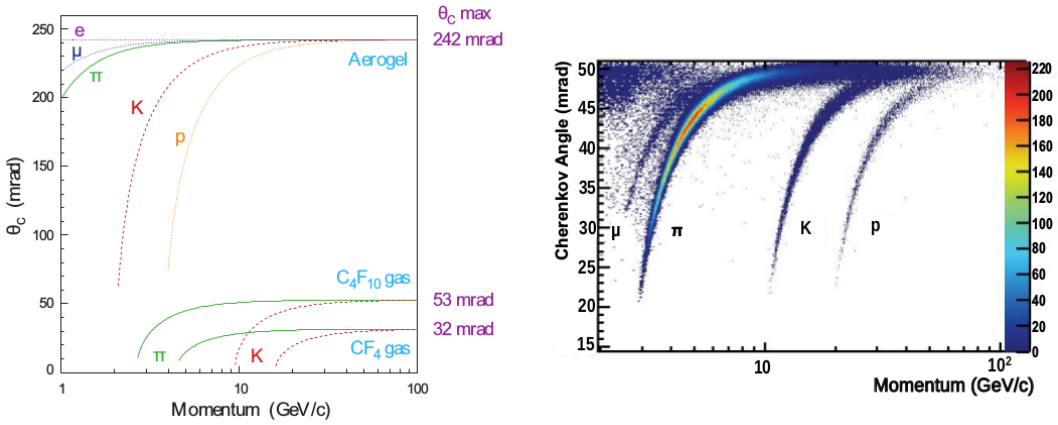

Figure 34: Left: Cherenkov angle as a function of the momentum for various charged particle species in each of the RICH radiators. Right: reconstructed Cherenkov angle from isolated tracks in C_4F_{10} as a function of track momentum using data from RICH1.

To identify a charged particle, the information on its direction and the momentum is taken from the tracking system. One ring for each possible mass hypothesis is constructed and the likelihood of each test ring against the positions of the HPD hits is evaluated and a likelihood is constructed. The combination of the likelihood with the information from the calorimeters and the muon system is associated to each track, allowing to define PID criteria that can be used in physics analyses. Another approach, used in the analysis described in Chapter 4, has been developed to improve upon the likelihood variables both by taking into account correlations between the detector systems and also by including

	Aerogel	C_4F_{10}	CF_4
Length [cm]	5	86	196
$(\theta_c)_{\max}$ [mrad]	242	53	32
$\pi^{\pm}_{\text{th}}$ [GeV]	0.6	2.6	4.4
$K^{\pm}_{\text{th}}$ [GeV]	2.0	9.3	15.6

Table 3: Properties of the radiators used in the LHCb RICH detectors. The radiator length, the angle for saturated tracks and the Cherenkov thresholds for charged pions and kaons are reported.

tracking information. This is carried out using multivariate techniques, combining PID information from each subsystem into a single probability value (ProbNN) for each particle hypothesis.

The performance of the RICH detectors is measured using control samples of $K^0_s \to \pi^+\pi^-$, $\Lambda \to p\pi^-$ and $D^{*+} \to D^0(\to K^-\pi^+)\pi^+$ decays, which can be selected by using kinematic requirements alone. With these, the pion, kaon and proton identification efficiencies and misidentification rates are calculated for a range of track momenta. An example is given in Figure 35, where the K identification efficiency and the $\pi \to K$ misidentification probability for two different PID requirements are shown as a function of the particle momenta.

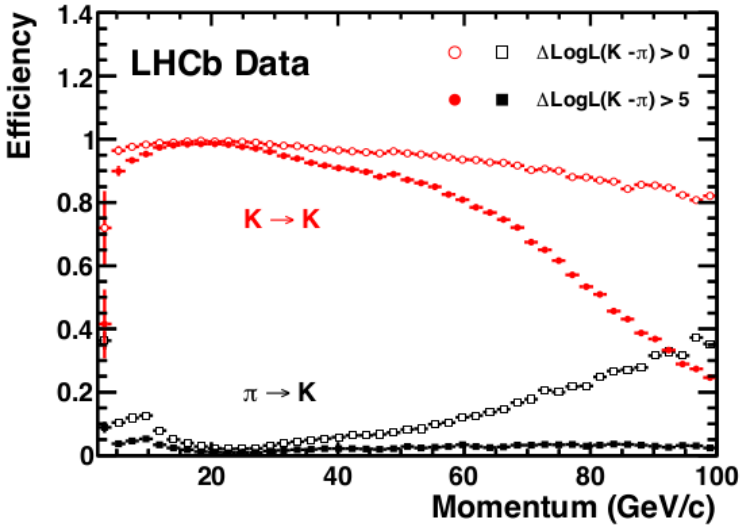

Figure 35: Kaon identification efficiency (red) and pion misidentification rate (black) as a function of track momentum for two different cuts on the log likelihood difference for the kaon and pion hypotheses.

3.2.7 The calorimeters

The LHCb calorimeter system [123] is placed between the first and the second muon detector stations and it is composed by four subdetectors: the Scintillator Pad Detector (SPD), the Pre-Shower (PS) detector, the Electromagnetic CALorimeter (ECAL) and the

Hadronic CALorimeter (HCAL). They are sampling calorimeters based on scintillating plastics and wavelength shifting (WLS) fibres that are coupled to Photo-Multiplier Tubes (PMT). The calorimeter system provide:

- transverse energy [2] measurement for charged hadrons, $e^{\pm}$, π^0 and γ, to be used in the lower level trigger decision;
- energy measurement of $e^{\pm}$ and γ;
- PID to distinguish hadrons, $e^{\pm}$ and γ, contributing to the Muon ID through the HCAL.

Since the hit density close to the beam pipe is about two orders of magnitude larger than at the edge of the acceptance, each of the subdetectors in the calorimetry system has a variable segmentation, shown in Figure 36.

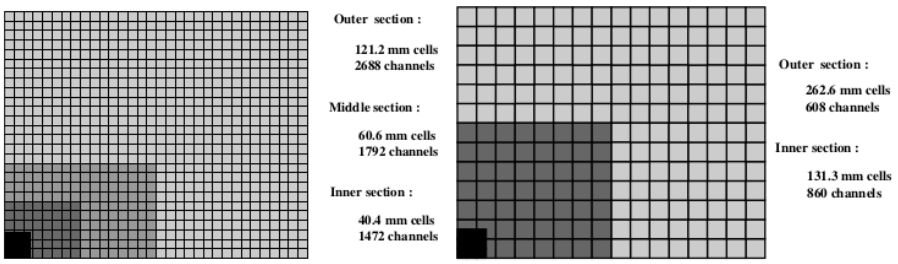

Figure 36: Left: segmentation of the SPD, PS and ECAL. Right: segmentation of the HCAL.

The SPD/PS systems are two planes of scintillator tiles with 1.5 cm thick lead plane between them. The scintillator tiles are 15 mm thick. The light is captured and re-emitted by WLS fibres to Multi-Anode PMTs (MaPMTs). The function of the SPD/PS is to distinguish electrons from charged hadrons and neutral pions. The SPD identifies charged particles, and allows electrons to be separated from photons. Charged particle, *e.g.* electrons, deposit energy in the SPD and can thus be distinguished from neutral particles, such as photons, which do not. Both electrons and photons interact in the lead plate and the deposited energy is collected by the PS. Hadrons have a longer interaction length and therefore pass through the lead plate depositing a tiny amount of energy.

The ECAL is composed by multiple and alternated layers of 2 mm thick lead plates and 4 mm thick scintillator tiles, readout by plastic optical fibres. The thickness of the ECAL is 25 X_0. The ECAL measures the energy deposit of electromagnetic showers with an energy resolution given by

$$\frac{\sigma_E}{E} = \frac{(8 \div 10)\%}{\sqrt{E}(\text{GeV})} \oplus 0.9\%, \tag{18}$$

where the symbol $\oplus$ indicates a squared sum root.

The HCAL is made from layers of of iron absorber and scintillator tiles. Unlike most calorimeters, the tiles run parallel to the beam axis. The HCAL thickness corresponds to 5.6 interaction lengths, which are not sufficient to ensure the whole containment of the

[2] Transverse energy is defined as $E_{\text{T}} = \sqrt{m^2 + p_{\text{T}}^2}$, where m and p_{T} are the particle mass and the component of the particle momentum in the transversal direction with respect to the beam line.

hadronic shower, but are enough to achieve a reasonable measurement of the energy, with a resolution given by

$$\frac{\sigma_E}{E} = \frac{(69 \pm 5)\%}{\sqrt{E}(\text{GeV})} \oplus (9 \pm 2)\%. \tag{19}$$

3.2.8 The muon system

The muon system [124] consists of five stations (M1-M5) and it is of fundamental importance for the triggering of interesting events providing high-p_{T} muon trigger at the lower level trigger. The muon system also has to provide muon identification.

The M1 station is located between RICH 2 and the calorimeters and it is used to improve the measurement of transverse momentum for the trigger. The M2-M5 stations are placed after the HCAL. Iron absorbers with a thickness of 80 cm are placed between each detector station after M2. The total absorber thickness is about 20 nuclear interaction lengths.

The muon stations provide spatial point measurements for charged tracks not absorbed by the ECAL nor by the HCAL. Since the hit density is much higher in the inner region, the stations are divided into four concentric regions from the beam axis to the outer region, with the inner regions being more finely segmented. In order to improved the measurement of the transverse momentum, the segmentation is finer in the bending direction than in the vertical one. The pads composing the muon stations use Multi-Wire Proportional Chambers (MWPCs) using a gas mixture of $Ar/CO_2/CF_4$ (40:55:5), with the exception of the innermost region of M1, where the pads are triple Gas Electron Multipliers (GEMs), since in that region the detector is required to stand at a rate up to 500 kHz/cm^2 of charged particles and hence it has to be radiation hard.

3.3 The LHCb trigger system

The LHCb trigger system [125] is structured in two levels, the Level-0 trigger (L0) and the High Level Trigger (HLT). L0 is implemented in hardware and it reduces the rate at which the whole detector is readout to 1 MHz, the maximum rate being imposed by the frontend electronics of the various subdetectors. The HLT is a software trigger performing a full reconstruction of the event in a computer farm consisting of up to roughly 25000 CPU cores in roughly 1600 physical nodes each equipped with at least 1 TB of local storage space. The role of the trigger is to reduce the pp collision rate to 2-5 kHz at which events can be written to tape. A set of conditions which, if satisfied, causes any level of the trigger to pass the event to the next stage, or write it to storage, is called trigger line.

3.3.1 The L0 trigger

L0 is implemented using custom hardware which synchronises with the 40 MHz collision rate and which processes data with a fixed latency of 4 μs. L0 trigger is divided into two independent systems: the calorimeter trigger and the muon trigger. The calorimeter and muon triggers take advantage of the typical large E_T and transverse momentum p_T of the decay products of b hadron decays. The calorimeter and muon systems feed into the L0 decision unit, making the final decision whether to pass the full event to the HLT or not.

The L0-calorimeter system uses information from the SPD, PS, ECAL and HCAL detectors and it makes a decision looking for high E_{T} electrons, photons and hadrons.

The transverse energy E_{T} is determined separately for each subdetector in clusters of 2 × 2 cells, following the projective geometry of the experiment, and it is defined as

$$E_{\mathrm{T}} = \sum_{\mathrm{cell}=1}^{4} E_{\mathrm{cell}} \sin\theta_{\mathrm{cell}}, \tag{20}$$

where E_{cell} is the energy deposited in the cell and θ_{cell} is the angle between the beam axis and a particle assumed to come from the LHCb interaction point and hitting the centre of the cell. The sum runs over the cluster cells. The clusters with the highest E_{T} are selected. Using the information from the SPD/PS system it is possible to identify the clusters as electrons, photons or hadrons. Three independent candidates, used in the analysis described in Chapter 4, may be created:

- L0Hadron is the highest E_{T} HCAL cluster. If this cluster also coincides with the highest E_{T} cluster in the ECAL, the E_{T} of the hadron candidates is taken as the sum of the HCAL and ECAL clusters;
- L0Electron is the highest E_{T} ECAL cluster with one or two hits in the SPD and in the corresponding PS cells;
- L0Photon is the highest E_{T} ECAL cluster with no hits in the SPD and one or two hits in the corresponding PS cells.

The L0 trigger retains the event if the E_{T} of any candidate is above a certain threshold. Typical values from Run 1 are reported in Table 4. The total number of hits in the SPD is used to veto high-multiplicity events that would take too long to process in the HLT.

Decision	p_{T} or E_{T}	SPD hits
muon	1.76 GeV	600
dimuon $p_{\mathrm{T}_1} \times p_{\mathrm{T}_2}$	$1.6\,\mathrm{GeV}^2$	900
hadron	3.7 GeV	600
electron	3.0 GeV	600
photon	3.0 GeV	600

Table 4: Typical L0 trigger thresholds used in 2012 data taking. The trigger is ignored if the event contains too many tracks and it is therefore too difficult to reconstruct. This is achieved imposing an upper limit on the SPD hits in the corresponding event for each candidate.

The L0-muon trigger looks for the two highest p_{T} muons in each quadrant. The muon system is able to perform standalone track reconstruction. M1 and M2 are used to measure the p_{T} of the tracks. Tracks are built from hits that form a straight line through all five muon stations and must be consistent with originating from the interaction point. An event is retained if either the highest p_{T} of any muon candidate in the event is above a certain threshold (L0Muon) or the product of the highest and second-highest p_{T} is above another threshold (L0DiMuon). Typical threshold are reported in Table 4. The L0Muon and L0DiMuon candidates have been used in the analysis subject of this thesis.

3.3.2 The High Level Trigger

The HLT is the software trigger, running asynchronously with respect to the collision rate, on a processor farm. It reduces the event rate from 1 MHz to 2-5 kHz and all such events are written to storage as raw data. An event accepted by L0, *i.e.* it contains at least an L0Electron, L0Photon, L0Hadron, L0Muon or L0DiMuon candidate, is processed by the HLT merging data from the different subdetectors. The HLT is divided into two layers: HLT1 and HLT2.

HLT1 uses a partial event reconstruction to perform an inclusive selection of interesting signatures and reducing the rate to $\sim 50\,\text{kHz}$. The HLT1 stage refines candidates retained by L0 using reconstructed candidate tracks and vertices from the VELO and the tracking stations and it retains events with at least one track which satisfies minimum requirements in IP, p, p_{T} and track quality. The L0 decision unit provides HLT1 with information about which trigger conditions are met, in order to inform HLT1 about which sequence of algorithms to run. The algorithms in each sequence work to verify the decision made by the previous step using progressively more of the event information. If multiple L0 candidates are found, the corresponding sequences will run independently, with HLT ensuring that the same track or vertex is not reconstructed twice, to save CPU time. The HLT1 selection that was the most efficient for hadronic charm and beauty decays in Run 1 is called Hlt1TrackAllL0. It selects events with good quality track candidates with high p_{T} ($p_{\text{T}} > 1.6\,\text{GeV}$) and displaced with respect to the primary vertex. It has been improved in Run 2, when two different selections have been developed, called Hlt1TrackMVA and Hlt1TwoTrackMVA. These HLT1 lines are used in the analysis described in Chapter 4.

The HLT2 stage searches for displaced secondary vertices, and applies loose decay length and mass cuts to reduce the rate to the level at which the events can be written to storage and processed offline. The input rate to HLT2 is low enough that a simplified version of the full offline event reconstruction can be run. It first performs a complete pattern recognition to find all particle tracks in the event. Then, a set of different selections are applied. Some of them are inclusive, aiming for generic b-hadron decays or for resonances like J/ψ or D^0, and some of them are exclusive, aiming to provide the highest possible efficiency on specific b-hadron decay channels. The so-called HLT2 inclusive topological trigger lines are used in the analysis presented in this thesis. These are designed to trigger on partially reconstructed b-hadron decays with at least two charged particles in the final state and a displaced secondary vertex. Tracks are selected using fit quality, IP and PID information. Vertices are constructed using combinations of two, three or four of the selected tracks. Signal candidates are selected based on several kinematic and isolation variables using a multivariate algorithm.

Since the LHC delivered collisions $\sim 30\%$ of the time during 2011, the computing power was idle 70% of the time causing an inefficient exploitation of resources. This motivated the introduction in 2012 of the deferral, allowing for the data to be buffered in local storage after L0, and processed later between LHC fills, also allowing for more CPU consuming algorithms to be used in the trigger. Starting from 2015, a full deferral has been introduced, allowing more time for the HLT2 algorithms. The buffer stage has been moved from after L0 to after HLT1, allowing for a buffer at the level of kHz rather than MHz and making possible the online alignment and calibration of the detector, the running of an offline-like reconstruction, called Turbo stream, and the calculation of offline-like PID likelihoods, giving the ability to be more efficient at the HLT2 level.

3.3.3 TIS and TOS

Trigger decisions at LHCb are classified into two categories: Triggered On Signal (TOS) and Triggered Independently of Signal (TIS). An event is classified as TOS if the only presence of the signal under study would be sufficient to retain the event. An event classified as TIS is one event for which the event would also have been retained without the signal under study. The analysis described in Chapter 4 uses a combination of both these two trigger categories.

3.4 The Online System

The Online System provides the infrastructure for the control, configuration, monitoring, operation and running of the entire experiment. The areas of the Online System are:

- the Detector Control System (DCS), including the control and monitoring of high voltages, low voltages, temperatures, gases, etc;
- the Data Acquisition System (DAQ) comprising the frontend (FE) electronics, the readout network, storage, etc;
- the Timing and Fast Control System (TFC) distributing the LHC clock and the trigger to the subdetectors FE electronics;
- the L0 trigger components;
- the HLT Farm, where alignment tasks and thousands of trigger algorithms are running on a large CPU farm;
- the Monitoring Farm, running monitoring tasks to produce histograms in order to check the data quality of the data being acquired;
- the Experiment Infrastructure, comprising the control and monitoring of magnet, cooling, electricity distribution, detector safety, etc;
- the interaction with the LHC accelerator, CERN safety system, CERN technical services, etc;

The Online System is handled by the Experiment Control System (ECS). A schematic view of the organisation of the Online components within the ECS is shown in Figure 37. The ECS provides the unique interface between the users and all the experimental equipment.

The ECS has been developed within the Joint Control Project (JCOP) [126], a common project between the four LHC experiments and a central Controls group at CERN. It defines a common architecture and a framework providing common guidelines and tools used by the experiments in order to build their detector control systems. JCOP uses a SCADA (Supervisory Control and Data Acquisition) system called WinCC-OA [127]. The size and complexity of the LHC experiments control systems have driven the adoption of a hierarchical, highly distributed, tree-like structure to represent the structure of sub-detectors, sub-systems and hardware components. This architecture allows a high degree of independence between components while allowing integrated control, both automated and user-driven, during physics data taking. LHCb adopted this architecture and extended it to cover all areas of the experiment.

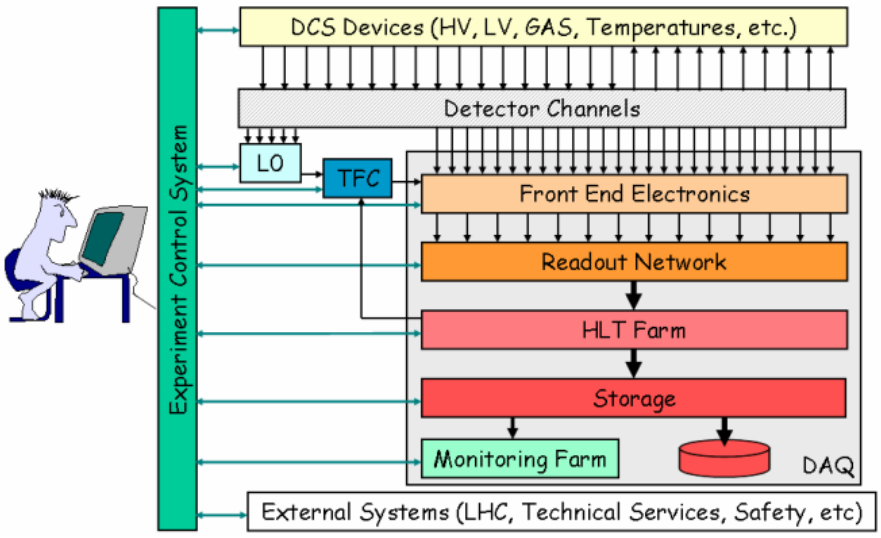

Figure 37: Scope of the Experiment Control System.

In order to prevent human mistakes and to speed up standard procedures, the system is, as much as possible, fully automated in order to achieve the best overall efficiency. Some examples are the Auto-Pilot, responsible to keep the system running, and the Big-Brother, shown in Figure 38, handling the dependencies between LHCb and the LHC accelerator. Through graphical user interfaces the operation of the detector is fully automated and the operator can send commands to the hardware and read back the status and eventual alarms.

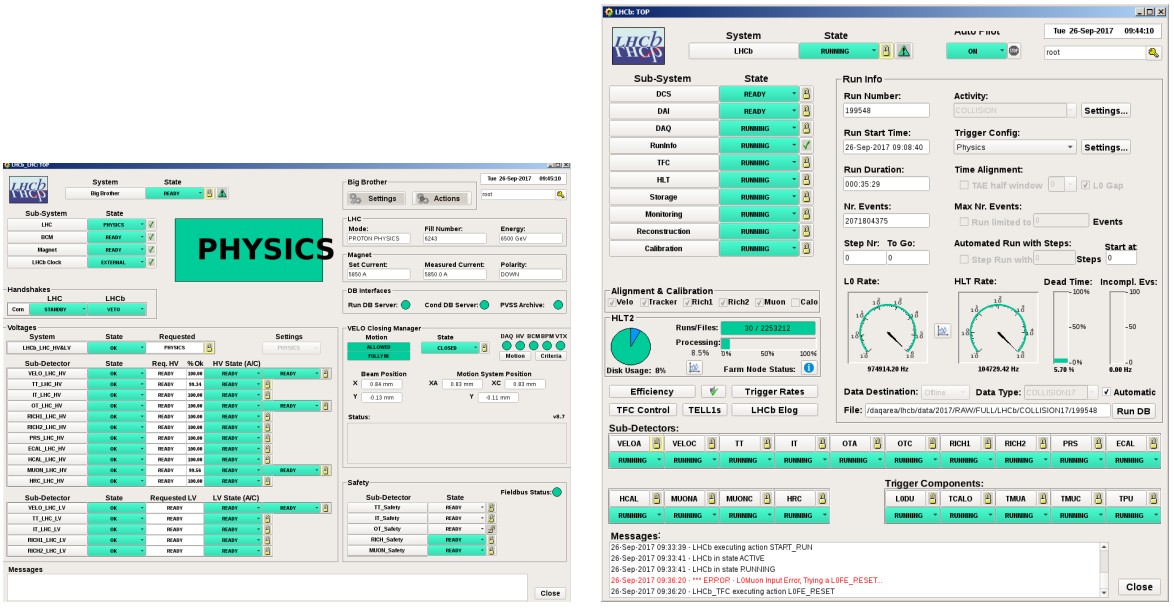

(a) (b)

Figure 38: Detector operation main User Interfaces. (a): Big Brother; (b): Run Control.

3.5 The LHCb data-taking

As introduced in Section 3.1.3, the LHCb experiment runs at a lower luminosity with respect to the ATLAS and CMS experiments, using an approximately constant instantaneous luminosity in order to reduce the pile-up, i.e. the number of primary vertices in every bunch-crossing. Indeed, flavour precision physics relies on resolving properly the vertex structure and event pile-up significantly complicates this task. In order to run at two order of magnitude lower luminosity than the LHC design, a luminosity-levelling technique has been implemented introducing an offset between the two colliding beams. An automated procedure is used to realign the beams in order to keep constant the luminosity along the duration of an LHC fill. The realignment is driven by the luminosity online monitoring. The instantaneous luminosity collected by LHCb is compared to the luminosity collected by ATLAS and CMS in Figure 39.

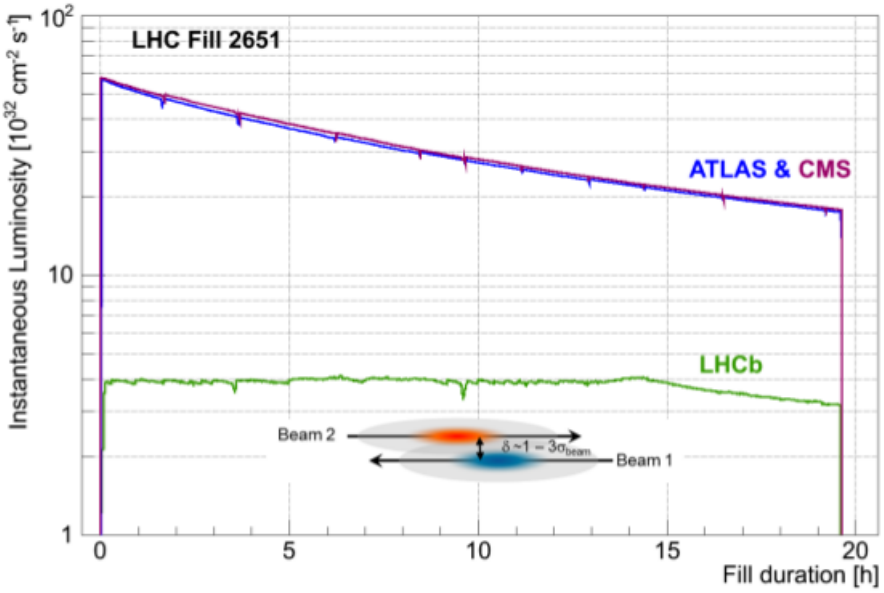

Figure 39: Evolution of the instantaneous luminosity at LHCb (green), ATLAS (blue) and CMS (purple) during a long fill in Run1. The LHCb luminosity is constant for about 14 hours. After this amount of time, the beams have zero separation, and the LHCb instantaneous luminosity starts to decrease.

The LHCb detector recorded about $7\,\text{fb}^{-1}$ of integrated luminosity in pp collisions between 2010 and 2017 as shown in Figure 40. The pp centre of mass energy in 2010 and 2011 was $\sqrt{s} = 7\,\text{TeV}$, rising to $\sqrt{s} = 8\,\text{TeV}$ in 2012. The period between 2010 and 2012 is referred to as Run 1, when a total integrated luminosity of $3.2\,\text{fb}^{-1}$ of pp collisions has been recorded, $1.15\,\text{fb}^{-1}$ at $\sqrt{s} = 7\,\text{TeV}$ and $2.1\,\text{fb}^{-1}$ at $\sqrt{s} = 8\,\text{TeV}$. After the two years Long Shutdown 1 (LS1), where detector maintenance and upgrades have been done, data-taking restarted in 2015 with $\sqrt{s} = 13\,\text{TeV}$. In this data-taking phase, called Run 2, $3.71\,\text{fb}^{-1}$ of pp collisions have been recorded so far. By the end of Run2, in December 2018, a total integrated luminosity of $\sim 9\,\text{fb}^{-1}$ is foreseen before the LS2, when the LHCb detector will undergo a major upgrade described in Chapter 5.

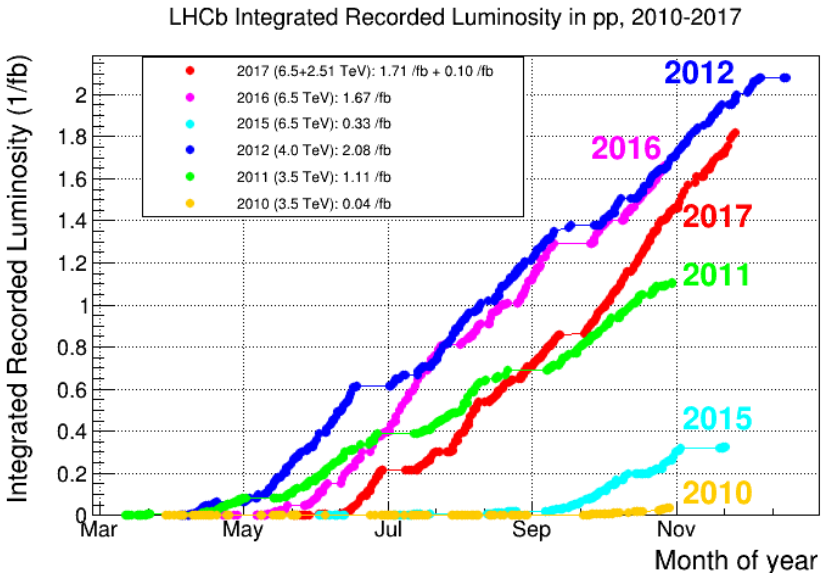

Figure 40: Integrated luminosity recorded by LHCb between 2010 and 2017. The different curves correspond to different data-taking years.

3.6 The LHCb data-flow and software

The LHC provides *pp* collisions to LHCb at 40 MHz that would correspond to ~ 1 TB/s of recorded data by LHCb, impossible to handle from the point of view of storage with the current techniques and from the computing point of view for the analyses to be feasible. Collisions recorded by the LHCb detector go through a specific data-flow designed to maximise the data-taking efficiency and the data quality. This consists of several steps, each one being controlled by a software application that processes the data event-by-event, using the data from the previous step and creating the results ready for the next one. These steps are the following:

- data from the detector are filtered through the trigger, as described in 3.3. The application responsible for the HLT is Moore [128]. Data retained by the trigger processing are saved on tape as raw data, containing raw information from the trigger and the subdetectors, named raw banks;

- triggered raw data, replicated and stored world wide in large computing centres connected through the LHC Computing Grid (LCG), are reconstructed in parallel on the LCG different machines running on different events, to transform the detector hits into objects such as tracks and clusters. PID information is associated to each candidate in the form of likelihood. The raw data processing is done by the Brunel application [129]. The objects are stored into an output file in a Full Data Summary Tape (FullDST) format. The pattern recognition algorithms in Brunel makes use of calibration and alignment constants stored in the CondDB and in the Detector Description DataBase (DDDB), storing the data-taking conditions and the detector geometrical properties respectively;

- the reconstructed FullDST files would be suitable for analysis, but they are not accessible to users due to computing restrictions. Data are further filtered through a set

of selections, the so-called the stripping, controlled by the DaVinci application [130]. During the stripping physics candidates are created combining tracks and/or neutral objects, e.g. four charged tracks candidates for p, $\bar{p}$, K^+ and π^- are combined to create a $B^0 \to p\bar{p}K^+\pi^-$ decay candidate, as described in Chapter 4. Data are written either in the DST format, storing the candidates created during the stripping along the full reconstructed event, or in the microDST (μDST) format, only storing the candidates identified by the stripping algorithms. Each event typically takes about 150 kB of disk space in the DST format. In the μDST format the raw event, which takes about 50 kB per event, is discarded. To save disk space and make easier the handling of data for analysts, the output files are grouped into streams which contain similar selections. By grouping all the hadronic beauty selections together, for example, analysts interested in the reconstruction of hadronic b-hadron decays do not waste time running over the output of other selections, e.g. the dimuon stream.

- users can run their own analysis tools to extract variables for their analysis with the DaVinci application, including vertex fitting, flavour tagging, calculation of decay angles and track momentum smearing and scaling.

Data simulation, the process of simulating pp collisions and the detector response in the reconstruction of a decay, is essential in every physics analysis, e.g. for the selection procedures used to unfold the signal candidates from the background and for the determination of the efficiency. In the simulation, the pp collision events are processed through the same work-flow as real data in order to compare the reconstructed information (mass, momentum, etc.) with the information used in the generation of the event, named truth information. There are two simulation steps which replace the pp collisions and the detector response:

- the simulation of pp collisions, the hadronisation and the decay of the resulting particles are controlled by the Gauss application [131], responsible for calling the various Monte Carlo (MC) generators such as Pythia (the default in LHCb), and for controlling EvtGen and Geant4. EvtGen is used to describe the decays of simulated particles, while Geant4 is used to simulate the propagation and interaction of particles within the detector;

- the interaction of particles with the geometry of the detector and hence the simulated energy depositions into hits, are converted to signals (digitisation) that mimic the real detector electronics channels response by the Boole application [132]. The output of Boole is designed to closely match the output of the real detector, in order for the simulated data to pass through the usual data processing chain described above, beginning with the trigger.

The different LHCb applications are constructed within the Gaudi framework [133], implementing the data-flow through the concept of Transient Event Store (TES), a set of containers for all the temporary objects in event processing, including track parameters, vertex quality, PID likelihoods, etc. In other words Gaudi implements the Data-Oriented Programming, where data objects, e.g. representing a track object, are containers which are filled by independent algorithm objects. The LHCb data-flow and the associated applications are shown in Figure 41.

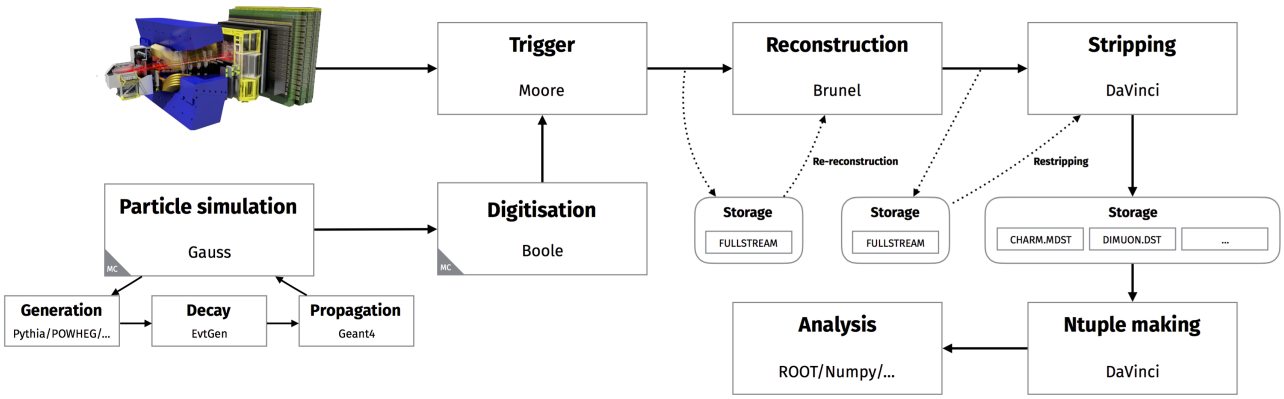

Figure 41: The LHCb data-flow and the applications associated to each step.

4 Evidence for an $\eta_c\pi^-$ resonance in $B^0 \to \eta_c K^+\pi^-$ decays

In this section I present the analysis that I carried out using the data collected by the LHCb detector during 2011, 2012 and 2016 data-taking years. In Sec. 4.1 I summarise the motivations of the analysis, whose strategy is described in Sec. 4.2. Data and simulated samples that are used in the analysis are reported in Sec. 4.3. The $B^0 \to p\bar{p}K^+\pi^-$ candidates selection and the $B^0 \to p\bar{p}K^+\pi^-$ signal extraction are described in Sec.s 4.4 and 4.5, respectively. The efficiency evaluation and the amplitude analysis are described in Sec. 4.6.3 and 4.6. The results are summarised in Sec. 4.8.

As reported in Chapter 2, several evidences or observations for charged quarkonium-like states have been reported by different experiments. All the established charged exotic mesons reported so far have been observed in the $Q\bar{Q}\pi^-$ final state, where the heavy quark pair, denoted by $Q\bar{Q}$, is in a $J^P = 1^-$ state. Therefore, these exotic candidates have $J^P = 1^+$. From the experimental point of view, it is easier to trigger on the dimuon final state, hence explaining why the charged states observed so far have quantum numbers $J^P = 1^+$, allowing the $Q\bar{Q} \to \mu^+\mu^-$ decay mode, corresponding to large statistics and optimal signal to background ratios. From the point of view of the theoretical interpretations for these exotic hadrons, it is interesting to search for charged exotic mesons having different quantum numbers. It would allow to eventually populate the multiplets predicted by different phenomenological models based on the interpretations of these exotic candidates.

4.1 Physics motivations for the $B^0 \to \eta_c(\to p\bar{p})K^+\pi^-$ decay channel analysis

Theoretical studies on the $Z_c(3900)^-$ structure, whose discovery has been introduced in Chapter 2, are one of the main motivations for this analysis. The $Z_c(3900)^-$ state, discovered by the BESIII collaboration in the $J/\psi\pi^-$ final state [99], and confirmed by the Belle [134] and CLEO [135] collaborations, can be interpreted as a hadrocharmonium state, where the compact heavy quark-antiquark pair interacts with the surrounding light quark mesonic excitation by a QCD analogue of the van der Waals force [136]. This interpretation of the $Z_c(3900)^-$ state predicts an as-yet-unobserved charged charmonium-like state with a mass of approximately 3800 MeV whose dominant decay mode is to the $\eta_c\pi^-$ system.[3] Alternatively, states like the $Z_c(3900)^-$ meson could be interpreted as analogues of quarkonium hybrids, where the excitation of the gluon field (the valence gluon) is replaced by an isospin-1 excitation of the gluon and light-quark fields [137]. This interpretation, which is based on lattice QCD, predicts different multiplets of charmonium tetraquarks, comprising states with quantum numbers allowing the decay into the $\eta_c\pi^-$ system. The $\eta_c\pi^-$ system carries isospin $I = 1$, G-parity $G = -1$, spin $J = L$ and parity $P = (-1)^L$, where L is the orbital angular momentum between the η_c and the π^- mesons. Lattice QCD calculations [138,139] predict the mass and quantum numbers of these states, comprising a $I^G(J^P) = 1^-(0^+)$ state of mass 4025 ± 49 MeV, a $I^G(J^P) = 1^-(1^-)$ state of mass 3770 ± 42 MeV, and a $I^G(J^P) = 1^-(2^+)$ state of mass 4045 ± 44 MeV. The $Z_c(4430)^-$

[3] Natural units with $\hbar = c = 1$ and the simplified notation η_c to refer to the η_c state are used throughout. In addition, the inclusion of charge-conjugate processes is always implied.

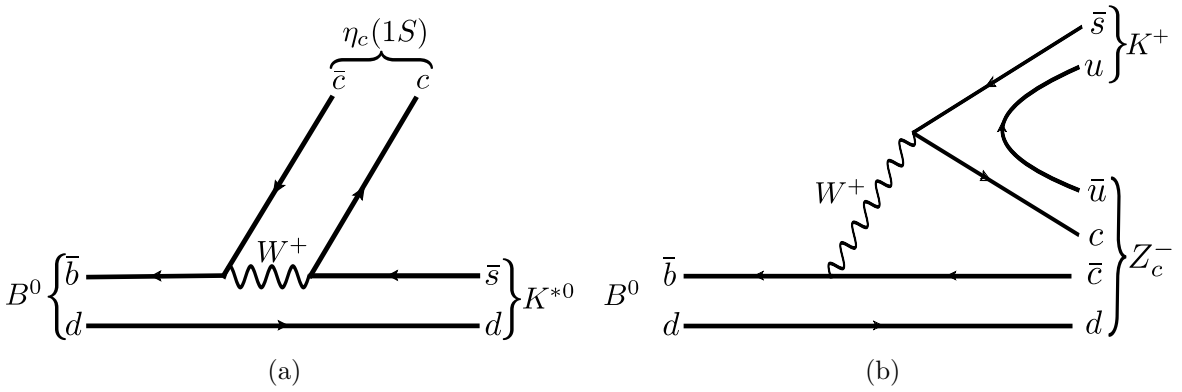

Figure 42: Feynman diagrams for (a) $B^0 \to \eta_c K^{*0}$ and (b) $B^0 \to Z_c^- K^+$ decay sequences.

resonance, discovered by the Belle collaboration [91] and confirmed by LHCb [10, 11], could also fit into this scenario. Another prediction of a possible exotic candidate decaying to the $\eta_c\pi^-$ system is provided by the diquark model [140], where quarks and diquarks are the fundamental units to build a rich spectrum of hadrons, including the exotic states observed thus far. The diquark model predicts a $J^P = 0^+$ candidate below the open-charm threshold that could decay into the $\eta_c\pi^-$ final state. Therefore, the discovery of a charged charmonium-like meson in the $\eta_c\pi^-$ system would provide important input towards understanding the nature of exotic hadrons.

The non-observation of $Z_c(3900)^- \to J/\psi\pi^-$ in b-hadron decays [94, 141] and in the photo-production $\gamma p \to J/\psi\pi^+ n$ [142] mode, could indicate that the $Z_c(3900)^-$ is a kinematic effect, e.g. a threshold cusp [143]. Furthermore, some lattice QCD calculations show no candidate for the $Z_c(3900)^-$ [144]. However, the discrimination power between different scenarios is not significant given the present data and it has been suggested to perform studies with high-statistics measurements together with combined analysis of other reactions [145].

The $B^0 \to \eta_c K^+\pi^-$ [4] decay is expected to proceed through $K^{*0} \to K^+\pi^-$ intermediate states, where K^{*0} refers to any neutral kaon resonance, following the Feynman diagram shown in Figure 42(a). If the decay also proceeds through exotic resonances in the $\eta_c\pi^-$ system, denoted by Z_c^- states in the following, a diagram like that shown in Figure 42(b) would contribute.

If no significant exotic states will be observed in the $m_{\eta_c\pi}$ invariant mass distribution, the $B^0 \to \eta_c K^+\pi^-$ is interesting to study the $K^+\pi^-$ system and, in particular, its S-wave structure. The $K^+\pi^-$ S-wave is a long-standing puzzle in light-meson spectroscopy. In recent years many experiments have performed searches for CP violation and searches for exotic resonances and charmed mesons through studies of heavy-flavour hadron decays with the $K^+\pi^-$ system in the final state. The $K^+\pi^-$ S-wave also enters some LFU tests, e.g. the $B^0 \to K^*\mu^+\mu^-$ analysis. The poor knowledge of the $K^+\pi^-$ S-wave structure is an important source of systematic uncertainties. Given the current level of statistics, the analysis of the $B^0 \to \eta_c K^+\pi^-$ channel can be considered as a starting point for the study of the $K^+\pi^-$ S-wave up to 2.3 GeV.

The $B^0 \to \eta_c K^+\pi^-$ decay involves only pseudoscalar mesons, hence it is fully described

[4] The inclusion of charged conjugated modes is implied throughout the thesis.

by two independent kinematic quantities. Therefore, the Dalitz plot (DP) analysis technique can be used to completely characterise the decay. The DP formalism is described Sec. 4.2.1. The main advantage of this decay channel is that there is no need for an angular analysis that would complicate the formalism required to build the decay amplitude, since it would not add any discriminant power to the results.

The $B^0 \to \eta_c K^+\pi^-$ channel is reconstructed with the η_c decaying to a $p\overline{p}$ pair. Indeed, the dimuon final state is helicity suppressed in η_c decays. A first estimate of the branching ratio, using the available information from the PDG [15], gives a branching ratio of $\mathcal{B}(B^0 \to \eta_c(\to p\bar{p})K^+\pi^-) \sim 10^{-6}$. The $\eta_c \to p\bar{p}$ decay has a lower branching fraction with respect to other η_c decay modes, like $\eta_c \to K^0_S K^+\pi^-$, whose branching fraction is about ten times larger. However, this loss in statistics is more than compensated by the larger acceptance and trigger and reconstruction efficiency, since the $\eta_c \to p\bar{p}$ decay mode has only two tracks instead of four in the final state. Moreover, having four different particles in the final state, there is no swapping between pions and kaons coming from the η_c decay vertex and the pions and kaons coming from the B^0 decay vertex.

4.2 Analysis Strategy

The usage of a fully hadronic final state implies a not optimal trigger efficiency, if compared to decays involving muons in the final state. The lower trigger efficiency and branching ratio require the usage of a data sample corresponding to an integrated luminosity of $4.7\,\text{fb}^{-1}$ of pp collision data collected with the LHCb detector at centre-of-mass energies of $\sqrt{s} = 7,\ 8$ and $13\,\text{TeV}$ in 2011, 2012 and 2016, respectively. Data collected in 2011 and 2012 are referred to as Run 1 data, while data collected in 2016 are referred to as Run 2 data.

The candidates selection of $B^0 \to p\bar{p}K^+\pi^-$ events is a crucial point of the analysis. The online and offline selections are driven by the need to have an high efficiency on the $B^0 \to \eta_c K^+\pi^-$ signal, while suppressing the large background present in a fully hadronic final state like $p\bar{p}K^+\pi^-$. In particular the PID requirements are very important to suppress the combinatorial background and the misidentification (misID) backgrounds, where one hadron is misidentified with another.

The unfolding of the $B^0 \to \eta_c K^+\pi^-$ component in $B^0 \to p\bar{p}K^+\pi^-$ decays is another very important point. This is achieved through a 2D mass fit to joint $p\bar{p}K^+\pi^-$ and $p\bar{p}$ invariant mass distributions. The ranges used in the 2D mass fit are optimised to remove the residual misID contributions after the selection procedure. The 2D mass fit is used to determine the signal and background yields and to determine the background models to be used in the amplitude analysis. A particular care must be taken in order to check that neither the p nor the $\overline{p}$ do not form any resonance with the K^+ and the π^- under the η_c region, that would prevent the 2D treatment of the $B^0 \to \eta_c K^+\pi^-$ decay channel.

The data sample resulting from the selection procedure, the signal and background yields, the background models and the efficiency parametrisation across the phase space of the decay, are used as inputs to the amplitude fit performed using the Laura^{++} package [146]. A 2D amplitude fit profits from the DP formalism, described in Sec. 4.2.1. In order to take into account eventual differences between the Run 1 and 2 data-taking periods, a joint amplitude fit keeping separated the Run 1 and 2 inputs, is carried out. The correct parametrisation of the $K^+\pi^-$ system is essential within the DP analysis. Beside the established $K^{*0} \to K^+\pi^-$ contributions, other $K^+\pi^-$ resonances, fitting with

the quark model but not confirmed yet, could contribute to the $B^0 \to \eta_c K^+\pi^-$ decays. Their presence must be probed to get the full uncertainty in the search for $Z_c^- \to \eta_c\pi^-$ intermediate states.

In addition, the $B^0 \to \eta_c K^+\pi^-$ branching fraction is measured. The intermediate contributions to the decay channel are quantified by multiplying the branching fraction with the fit fractions resulting from the DP fit, in order to determine the quasi-two-body branching fractions.

4.2.1 Three-body decays and Dalitz Plot formalism

The kinematics of three-body decays involving spin-0 particles are uniquely defined by two variables. These variables form the coordinate axes of the DP and are commonly chosen to be two of the three two-body square invariant masses. The third two-body square invariant mass is fixed by the relationship

$$m_{12}^2 + m_{13}^2 + m_{23}^2 = M^2 + m_1^2 + m_2^2 + m_3^2, \tag{21}$$

where the three children are labelled 1, 2 and 3 and M is the mass of the decaying parent particle. In terms of these two-body square invariant masses, the differential partial decay width of the parent to the final state particles can be written as

$$d\Gamma = \frac{1}{(2\pi)^3}\frac{1}{32M^3}\overline{|\mathcal{A}|}^2 dm_{12}^2 dm_{23}^2, \tag{22}$$

where $\overline{|\mathcal{A}|^2}$ is the square matrix element averaged (summed) over the initial (final) states, i.e. the square decay amplitude, describing the dynamics of the decay. If $\overline{|\mathcal{A}|^2}$ is constant, the density of events per unit area (*i.e.* per unit of $dm_{12}^2 dm_{23}^2$) of the DP is constant and the DP is uniformly populated. If $\overline{|\mathcal{A}|^2}$ depends on the momenta and angles of the children, the density at any point is a measure of the square matrix element, giving information on the interactions of the final state particles. Hence the DP of the decay, named after it's inventor Richard Dalitz who developed this representation technique in order to analyse the $K^+ \to \pi^+\pi^+\pi^-$ decay [147], provides a complete description of the decay, including its decay sequence involving the production of intermediate resonant or non-resonant states, the spin of these intermediate states and the interference patterns between the different decay sequences. These underlying decay channels may be resonant, where the parent first decays via a weak process into two particles and one of these particles (the resonance) quickly decays via a strong process into two children. As shown in Figure 43, resonances in two of the two-body pairs form horizontal and vertical bands in the DP (resonances in the third pair produce diagonal bands running from top-left to bottom-right with low mass resonances appearing closer to the upper-right kinematic limit). The decay may also proceed via intermediate states that do not correspond to a resonance but that are characterised by final state interactions of one of the children pairs corresponding to a given spin of this pair. All of the resonant and non-resonant contributions with the same spin J in the same pair of children can be grouped together in the so-called partial wave of spin J.

Since the parent is a spin-0 particle, the conservation of the angular momentum in the initial two-body decay implies that the resonance is polarised along its direction of flight in the rest frame of the parent. As described in some more details later, the angular

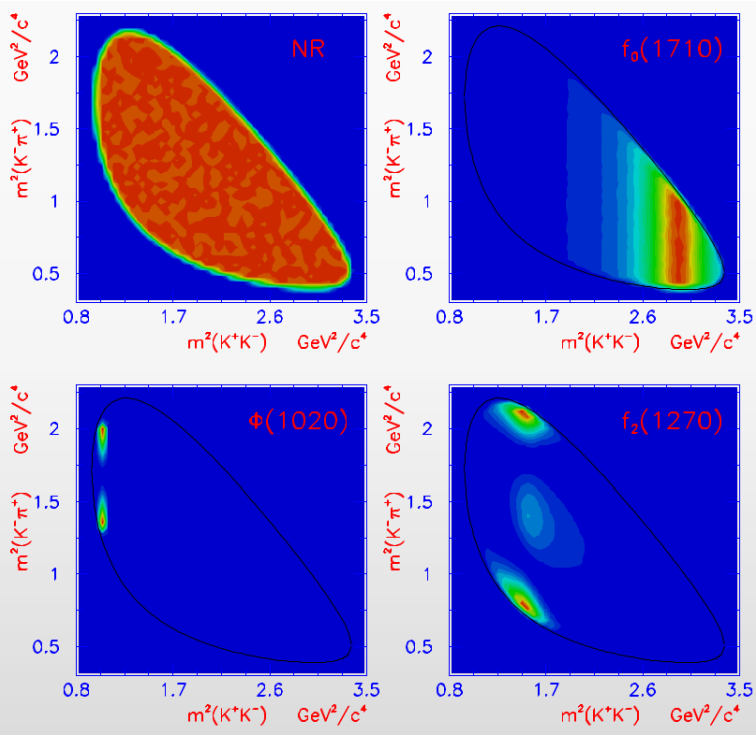

Figure 43: DP of simulated $D_s^+ \to R(\to K^+K^-)\pi^+$ events, where R represents a resonance formed by the K^+K^- pair. Each quadrant corresponds to a different decay sequence. Top left: $D_s^+ \to K^+K^-\pi^+$ proceeds without intermediate states, $\overline{|\mathcal{M}|^2}$ is constant and hence the DP is uniformly populated. Top right: the final state interaction of the K^+K^- pair produces the $f_0(1710)$ resonance, hence the $D_s^+ \to K^+K^-\pi^+$ decay proceeds through the $D_s^+ \to f_0(1710)(\to K^+K^-)\pi^+$ sequence, being the $f_0(1710)$ a spin-0 resonance. Therefore the $\overline{|\mathcal{M}|^2}$ is a function of final state angles and momentum and a uniform band appears in the DP at the $m^2_{K^+K^-}$ value corresponding to the square mass of the $f_0(1710)$. Bottom left: the same as the previous one, but now the intermediate state is the spin-1 $\phi(\to K^+K^-)$ resonance. The characteristic of spin-1 resonances is the presence of one dip in the corresponding band. Bottom right: the same of before, but now the intermediate state is the spin-2 $f_2(1270)(\to K^+K^-)$ state. Hence there are two dips in the corresponding band.

probability distribution of the resonance children, with respect to the resonance spin axis, depends on the spin of the resonance. This angular distribution leads to the features described in Figure 43, where the bands corresponding to resonances with different spin have a number of dips corresponding to the spin of that resonance.

The DP is then a scatter plot in the m^2_{12} and m^2_{23} variables, where each dot corresponds to an event of the decay of interest. Such dots are confined to a certain boundary depending on the kinematics of the decay, whose limits correspond to different kinematic configurations of the final state particles, as shown in Figure 44.

The Dalitz boundaries can also be rewritten in the Gottfried-Jackson frame, introducing the helicity angle θ_R, defined as the angle between the momentum $\vec{q}$ of one of the resonance children and the momentum $\vec{p}$ of the other particle in the decay, both evaluated in the rest frame of the resonance R. The helicity angle definition for the $B^0 \to \eta_c K^+\pi^-$ decay is shown in Figure 45. The cosine of the helicity angle can be written, in terms of kinematic

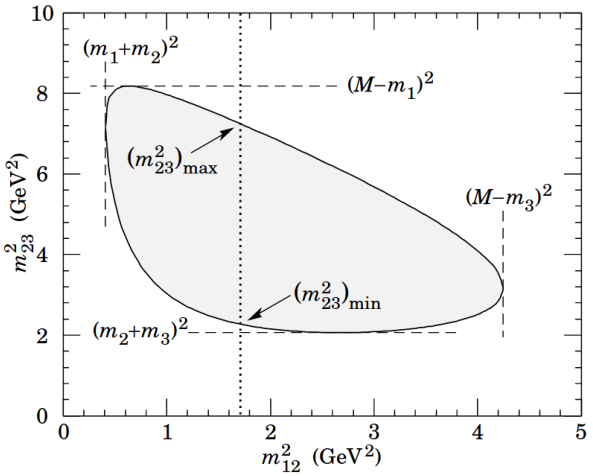

Figure 44: The DP boundary is completely described by the energy and momentum conservation. Some special spots are shown in the plot above, taken by [15]. From the three-body kinematics: $(m^2_{ij})_{\text{min}} = (m_i + m_j)^2$ and $(m^2_{ij})_{\text{max}} = (M - m_k)^2$.

quantities of the final state particles, as

$$\cos\theta_{K^*} = \frac{m^2_K + m^2_{\eta_c} + 2E_{K_{(K^+\pi^-)}} E_{\eta_{c(K^+\pi^-)}} - m^2(\eta_c K^+)}{2qp}, \tag{23}$$

where $E_{K_{(K^+\pi^-)}}$ and $E_{\eta_{c(K^+\pi^-)}}$ are respectively the energy of the K and the η_c in the $K^+\pi^-$ rest frame. $m^2(\eta_c K^+)$ has its maximum value when $\theta_{K^*} = 0$, while $m^2(\eta_c K^+)$ assumes its minimum value when $\theta_{K^*} = \pi$. The helicity angle and the $\vec{p}$ and $\vec{q}$ momenta enter the definition of the complex amplitudes used to parametrise the final state interactions.

Given the sizeable natural width of the η_c meson, the invariant mass $m(p\overline{p})$ is used instead of the known value of the η_c mass [15] to compute all the kinematic quantities such as $m^2(\eta_c K^+)$, $m^2(\eta_c\pi^-)$ and the helicity angles.

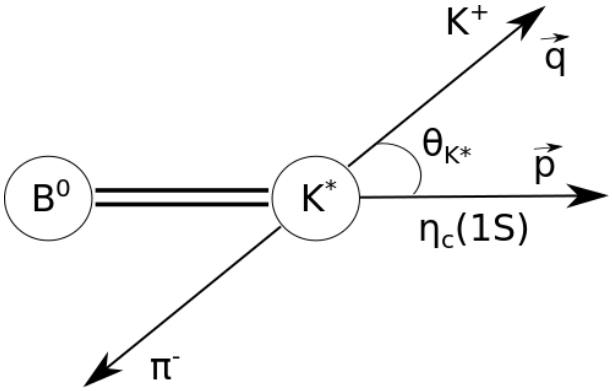

Figure 45: Helicity angle θ_{K^*} for the $B^0 \to \eta_c K^+\pi^-$ decay. It is defined as the angle between the K^+ momentum $\vec{q}$ and the η_c momentum $\vec{p}$ both evaluated in the rest frame of the K^* resonance. Note that the η_c is produced directly from the parent decay vertex.

4.2.2 The isobar model

The total decay amplitude can be parametrised using the isobar model, which models the overall amplitude across the DP phase space as a coherent sum of resonant and non-resonant processes where one child is a spectator. The isobar model does not include coupled channels and three-body effects, but the simplifications of this approach are not a problem for low statistics samples of charm and beauty decays, as in the $B^0 \to \eta_c K^+\pi^-$ case. In the isobar model the total amplitude is given by

$$\mathcal{A}(m^2_{12}, m^2_{23}) = \sum_{j=1}^{N} c_j \mathcal{F}_j(m^2_{12}, m^2_{23}), \tag{24}$$

where $\mathcal{F}_j(m^2_{12}, m^2_{23})$ is the dynamical amplitude whose contribution is associated with the complex coefficient c_j (isobar coefficient). In this analysis $m^2_{12} = m^2(K^+\pi^-)$ and $m^2_{23} = m^2(\eta_c\pi^-)$. The $\mathcal{F}_j[m^2(K^+\pi^-), m^2(\eta_c\pi^-)]$ complex functions describe the resonance dynamics and are normalised such that the integral of their squared magnitude over the DP is unity

$$\int_{\mathrm{DP}} |\mathcal{F}_j[m^2(K^+\pi^-), m^2(\eta_c\pi^-)]|^2 \mathrm{d}m^2(K^+\pi^-)\ \mathrm{d}m^2(\eta_c\pi^-) = 1. \tag{25}$$

Each $\mathcal{F}_j[m^2(K^+\pi^-), m^2(\eta_c\pi^-)]$ contribution is composed of the product of several factors. For a $K^+\pi^-$ resonance, for instance,

$$\mathcal{F}[m^2(K^+\pi^-), m^2(\eta_c\pi^-)] = \mathcal{N} \times X(|\vec{p}|r_{\mathrm{BW}}) \times X(|\vec{q}|r_{\mathrm{BW}}) \times Z(\vec{p}, \vec{q}) \times T[m(K^+\pi^-)], \tag{26}$$

where $\mathcal{N}$ is a normalisation constant and $\vec{p}$ and $\vec{q}$ are the momentum of the accompanying particle (the η_c meson in this case) and the momentum of one of the resonance decay products, respectively, both evaluated in the $K^+\pi^-$ rest frame. The $Z(\vec{p}, \vec{q})$ term describes the angular probability distribution, and the $X(z)$ terms are the Blatt–Weisskopf barrier factors.

Different approaches can be used to parameterise the angular probability distribution term. In b-hadron decays, the large available phase space requires the description of the resonance amplitude to be well-behaved at masses significantly different from the pole mass. This requires to enforce transversality in the amplitudes, achieved using the Zemach tensor formalism. The angular distribution terms are shown in Table 5. They are proportional to the Legendre polynomials $P_J(x)$, where x is the cosine of the helicity angle.

The Blatt–Weisskopf barrier factors of Eq. (26) are associated to the decays of the parent particle $X_J(|\vec{p}|r_{\mathrm{BW}})$ and of the resonance $X_J(|\vec{q}|r_{\mathrm{BW}})$. They depend on the spin J of the decaying particle and are shown in Table 6, where $z = |\vec{p}|r_{\mathrm{BW}}$. The parameter r_{BW} is the radius of the barrier, i.e. the size of the decaying particle, which in the analysis it is assumed to be 4.0 GeV for both the K^{*0} and the eventual charmonium-like contributions. The parameter z_0 represents the value of z when the invariant mass is set equal to the pole mass m_0 of the resonance. The Blatt–Weisskopf factors, also called orbital angular momentum barrier factors, take into account the difficulty in creating the orbital angular momentum J in the B^0 decay.

J	$Z_J(\vec{p},\vec{q})$
0	1
1	$-2\vec{p}\cdot\vec{q}$
2	$\frac{4}{3}\left[3(\vec{p}\cdot\vec{q})^2 - (\lvert\vec{p}\rvert\lvert\vec{q}\rvert)^2\right]$
3	$-\frac{8}{5}\left[5(\vec{p}\cdot\vec{q})^3 - 3(\vec{p}\cdot\vec{q})(\lvert\vec{p}\rvert\lvert\vec{q}\rvert)^2\right]$
4	$\frac{16}{35}\left[35(\vec{p}\cdot\vec{q})^4 - 30(\vec{p}\cdot\vec{q})^2(\lvert\vec{p}\rvert\lvert\vec{q}\rvert)^2 + 3(\lvert\vec{p}\rvert\lvert\vec{q}\rvert)^4\right]$
5	$-\frac{32}{63}\left[63(\vec{p}\cdot\vec{q})^5 - 70(\vec{p}\cdot\vec{q})^3(\lvert\vec{p}\rvert\lvert\vec{q}\rvert)^2 + 15(\vec{p}\cdot\vec{q})(\lvert\vec{p}\rvert\lvert\vec{q}\rvert)^4\right]$

Table 5: Angular distributions in the Zemach tensor formalism up to $J = 5$, where J is the spin of the resonance.

J	$X_J(z)$
0	1
1	$\sqrt{\frac{1+z_0^2}{1+z^2}}$
2	$\sqrt{\frac{z_0^4+3z_0^2+9}{z^4+3z^2+9}}$
3	$\sqrt{\frac{z_0^6+6z_0^4+45z_0^2+225}{z^6+6z^4+45z^2+225}}$
4	$\sqrt{\frac{z_0^8+10z_0^6+135z_0^4+1575z_0^2+11025}{z^8+10z^6+135z^4+1575z^2+11025}}$
5	$\sqrt{\frac{z_0^{10}+15z_0^8+315z_0^6+6300z_0^4+99225z_0^2+893025}{z^{10}+15z^8+315z^6+6300z^4+99225z^2+893025}}$

Table 6: Blatt-Weisskopf functions up to $J = 5$, where J is the decaying particle spin. The parameter z is defined as $z = |\vec{p}|r_{\mathrm{BW}}$ and the parameter z_0 indicates z evaluated at the resonance peak mass.

The function $T[m(K^+\pi^-)]$ of Eq. (26) is the mass lineshape. Most of the resonant contributions are described by the relativistic Breit–Wigner (RBW) function

$$T(m) = \frac{1}{m_0^2 - m^2 - im_0\Gamma(m)}, \tag{27}$$

where the mass-dependent width is given by

$$\Gamma(m) = \Gamma_0 \left(\frac{|\vec{q}|}{q_0}\right)^{(2L+1)} \left(\frac{m_0}{m}\right) X^2(|\vec{q}|r_{\mathrm{BW}}) \tag{28}$$

and q_0 is the value of $|\vec{q}|$ for $m = m_0$, m_0 being the pole mass of the resonance.

The amplitude parameterisations using RBW functions lead to unitarity violation within the isobar model if there are overlapping resonances or if there is a significant interference with a NR component, both in the same partial wave [148]. This is the case for the $K^+\pi^-$ S-wave at low $K^+\pi^-$ mass, where the $K_0^*(1430)^0$ resonance interferes strongly with a slowly varying NR S-wave component. Therefore, the $K^+\pi^-$ S-wave at low mass is modelled using a modified LASS lineshape [149], given by

$$T(m) = \frac{m}{|\vec{q}|\cot\delta_B - i|\vec{q}|} + e^{2i\delta_B}\frac{m_0\Gamma_0\frac{m_0}{q_0}}{m_0^2 - m^2 - im_0\Gamma_0\frac{|\vec{q}|}{m}\frac{m_0}{q_0}}, \tag{29}$$

with

$$\cot\delta_B = \frac{1}{a|\vec{q}|} + \frac{1}{2}r|\vec{q}|, \tag{30}$$

and where m_0 and Γ_0 are the pole mass and width of the $K_0^*(1430)^0$ state, and a and r are the scattering length and the effective range, respectively. The parameters a and r depend on the production mechanism and hence on the decay under study. The slowly varying part (the first term in Eq. (29)) is not well modelled at high masses and it is set to zero for $m(K^+\pi^-)$ values above 1.7 GeV.

The probability density function for signal events across the DP, neglecting reconstruction effects, can be written as

$$\mathcal{P}_{\text{sig}}[m^2(K^+\pi^-), m^2(\eta_c\pi^-)] = \frac{|\mathcal{A}|^2}{\int_{\text{DP}}|\mathcal{A}|^2\text{d}m^2(K^+\pi^-)\,\text{d}m^2(\eta_c\pi^-)}, \tag{31}$$

where the dependence of $\mathcal{A}$ on the DP position has been suppressed for brevity. The natural width of the η_c meson is set to zero when computing the DP normalisation shown in the denominator of Eq. (31). The effect of this simplification is determined when assessing the systematic uncertainties.

The complex coefficients, given by c_j in Eq. (24), depend on the choice of normalisation, phase convention and amplitude formalism. Fit fractions and interference fit fractions are convention-independent quantities that can be directly compared between different analyses. The fit fraction is defined as the integral of the amplitude for a single component squared divided by that of the coherent matrix element squared for the complete DP,

$$\text{FF}_i = \frac{\int_{\text{DP}}|c_i\mathcal{F}_i[m^2(K^+\pi^-), m^2(\eta_c\pi^-)]|^2\text{d}m^2(K^+\pi^-)\,\text{d}m^2(\eta_c\pi^-)}{\int_{\text{DP}}|\mathcal{A}[m^2(K^+\pi^-), m^2(\eta_c\pi^-)]|^2\text{d}m^2(K^+\pi^-)\,\text{d}m^2(\eta_c\pi^-)}. \tag{32}$$

In general, the fit fractions do not sum to unity due to the possible presence of net constructive or destructive interference over the whole DP area. This effect can be described by interference fit fractions defined for $i < j$ by

$$\text{FF}_{ij} = \frac{\int_{\text{DP}}2\mathcal{R}e\left[c_ic_j^*\mathcal{F}_i\mathcal{F}_j^*\right]\text{d}m^2(K^+\pi^-)\,\text{d}m^2(\eta_c\pi^-)}{\int_{\text{DP}}|\mathcal{A}|^2\text{d}m^2(K^+\pi^-)\,\text{d}m^2(\eta_c\pi^-)}, \tag{33}$$

where the dependence of $\mathcal{F}_i^{(*)}$ and $\mathcal{A}$ on the DP position is omitted.

4.2.3 Dalitz Plot fitting

The LAURA^{++} package [146] is used to perform the unbinned DP fit, with the Run 1 and 2 subsamples fitted simultaneously using the JFIT framework [150]. The free parameters in the amplitude fit are in common between the two subsamples, while the signal and background yields and the maps describing the efficiency variations across the phase space, are different. Within the DP fit, the signal corresponds to $B^0 \to \eta_c K^+\pi^-$ decays, while the background comprises both combinatorial background and NR $B^0 \to p\bar{p}K^+\pi^-$ contributions. The likelihood function is given by

$$\mathcal{L} = \prod_i^{N_c} \left[\sum_k N_k \mathcal{P}_k[m_i^2(K^+\pi^-), m_i^2(\eta_c\pi^-)] \right], \tag{34}$$

where the index i runs over the N_c candidates, k runs over the signal and background components, and N_k is the yield of each component. The probability density function for the signal, $\mathcal{P}_{\rm sig}$, is given by Eq. (31) where the $|\mathcal{A}[m^2(K^+\pi^-), m^2(\eta_c\pi^-)]|^2$ term is multiplied by the efficiency function described in Sec. 4.6.3. The amplitude fits are repeated many times with randomised initial values to ensure the absolute minimum is found.

Both the efficiency and the backgrounds have been parametrised in the form of 2D histograms using the Square Dalitz Plot (SDP) coordinates, described in Sec. 4.2.4.

4.2.4 The Square Dalitz Plot

In order to avoid the problems related to the curved boundaries of the DP, it is useful to define the Square Dalitz Plot (SDP) coordinates, defined as

$$m' \equiv \frac{1}{\pi} \arccos\left(2\frac{m(K^+\pi^-) - m^{\rm min}_{K^+\pi^-}}{m^{\rm max}_{K^+\pi^-} - m^{\rm min}_{K^+\pi^-}} - 1 \right), \tag{35}$$

$$\theta' \equiv \frac{1}{\pi}\theta(K^+\pi^-), \tag{36}$$

where $m^{\rm max}_{K^+\pi^-} = m_{B^0} - m_{\eta_c}$, $m^{\rm min}_{K^+\pi^-} = m_{K^+} + m_{\pi^-}$ are the kinematic boundaries of $m(K^+\pi^-)$ allowed in the $B^0 \to \eta_c K^+\pi^-$ decay, and $\theta(K^+\pi^-)$ is the helicity angle of the $K^+\pi^-$ system (the angle between the K^+ and the η_c mesons in the $K^+\pi^-$ rest frame). $m^{\rm min}_{K^+\pi^-}$ and $m^{\rm max}_{K^+\pi^-}$ are the phase space boundaries of the $K^+\pi^-$ invariant mass and their values are respectively 0.63 GeV and 2.3 GeV. Using the SDP coordinates, the kinematically allowed phase space is mapped to a unit square and the phase space limits become $0 < \theta' < 1$ and $0 < m' < 1$.

4.3 Data and simulated samples

I use the data sample collected by LHCb at $\sqrt{s} = 7$ TeV in 2011, at $\sqrt{s} = 8$ TeV in 2012 and at $\sqrt{s} = 13$ TeV in 2016, corresponding to an integrated luminosity of about 4.7 fb^{-1}. The momentum scale calibration, introduced in Sec. 3.2.5, is applied to the data samples. The data samples are summarised in Table 7. Several simulated samples are used to optimise the event selection, evaluate the efficiency and to validate the parameterisation of the components in the data spectra. The decay modes are generated using the Gauss

Luminosity (pb^{-1})	**Year**	**Magnetic Field Polarity**
560	2011	Down
428	2011	Up
991	2012	Down
999	2012	Up
850	2016	Down
797	2016	Up

Table 7: $B^0 \to \eta_c K^+\pi^-$ data samples used in the analysis. Luminosity, year and magnetic field orientation are shown.

Particle	**cuts**
B^0	$\tau > 10^{-4}\,\mathrm{ns}$
$p, \bar{p}$	$p_T > 250\,\mathrm{MeV}$ && inAcc
$K^\pm, \pi^\pm$	$p_T > 150\,\mathrm{MeV}$ && inAcc

Table 8: Tight generator level cuts applied to the initial and final state particles. The inAcc cut corresponds to the requirement that the particle is produced inside the LHCb acceptance, i.e. within the polar angle range $5 < \theta < 400\,\mathrm{mrad}$.

application. Run 1 simulated samples used in the analysis are summarised in Table 9 for B^0 decay modes and in Table 11 for B_s^0 and Λ_b^0 decay modes, used to study cross-feed effects. The Run 2 simulated samples are summarised in Tables 10 and 12. Tight generator level cuts are applied to some samples in order to increase the available number of events in the final simulated sample. The summary of these cuts is reported in Table 8. All the samples are generated uniformly in the phase space, with the exception of the 11134002 event type, where the events are generated uniformly in the SDP space.

4.4 $B^0 \to p\bar{p}K^+\pi^-$ candidates selection

This section outlines the strategy used to select $B^0 \to p\bar{p}K^+\pi^-$ events while suppressing as much as possible the backgrounds. After having introduced the variables used in the selection steps, the selection procedure will be described.

4.4.1 Variables

The variables used to discriminate between the $B^0 \to p\bar{p}K^+\pi^-$ signal events and the background can be classified in track quality, vertex quality, geometric and PID variables.

Tracks are reconstructed from hits in the VELO, TT and the tracking stations T1, T2 and T3, as described in Sec. 3.2.1. The final step of the track reconstruction, after the execution of a sequence of algorithms attempting to combine the hits in the different subdetectors, is to fit the tracks based on a Kalman-filter [151]. This takes into account multiple scattering and corrects for energy loss due to ionisation. The χ^2 per degrees of

Decay Mode	**Event Type**	**# events**
$B^0 \to p\bar{p}K^+\pi^-$	11104071	788083
$B^0 \to p\bar{p}K^+\pi^-$	11104072	3166108
$B^0 \to p\bar{p}\pi^+\pi^-$	11104076	1574656
$B^0 \to p\bar{p}K^+\pi^-\pi^0$	11104421	1570664
$B^0 \to \eta_c K^+\pi^-$	11134000	1562233
$B^0 \to \eta_c K^+\pi^-$	11134001	3157085
$B^0 \to \eta_c K^+\pi^-$	11134002	6101483
$B^0 \to J/\psi K^+\pi^-$	11134010	777481

Table 9: Run 1 simulated samples with the B^0 meson as initial state used in this analysis. The η_c and the J/ψ decay to the $p\bar{p}$ final state.

Decay Mode	**Event Type**	**# events**
$B^0 \to p\bar{p}K^+\pi^-$	11104072	5521526
$B^0 \to \eta_c K^+\pi^-$	11134001	5084863
$B^0 \to \eta_c K^+\pi^-$	11134002	5493062
$B^0 \to J/\psi K^+\pi^-$	11134010	2047050

Table 10: Run 2 simulated samples with the B^0 meson as initial state used in this analysis. The η_c and the J/ψ decay to the $p\bar{p}$ final state.

Decay Mode	**Event Type**	**# events**
$B_s^0 \to p\bar{p}K^+\pi^-$	13104065	1552480
$B_s^0 \to J/\psi K^+\pi^-$	13134081	1572031
$B_s^0 \to p\bar{p}K^+K^-$	13104061	777748
$B_s^0 \to J/\psi\phi$	13134010	776498
$B_s^0 \to J/\psi\pi^+\pi^-$	13134030	1555292
$\Lambda_b^0 \to J/\psi pK^-$	15134020	6375882

Table 11: Run 1 simulated samples with the B_s^0 meson and Λ_b^0 baryon as initial states used in this analysis. The J/ψ decays to the $p\bar{p}$ final state, the ϕ decays to the K^+K^- final state

Decay Mode	Event Type	# events
$B_s^0 \to J/\psi K^+\pi^-$	13134081	2011660
$B_s^0 \to J/\psi\phi$	13134010	2007148

Table 12: Run 2 simulated samples with the B_s^0 meson as initial state used in this analysis. The J/ψ decays to the $p\bar{p}$ final state, the ϕ decays to the K^+K^- final state

freedom of the fit, referred as **Track χ^2/ndof**, is used to determine the quality of the reconstructed tracks.

Ghost tracks are those which are reconstructed from combinations of hits that do not correspond to the trajectory of a charged particle. Most of the ghost tracks result from an incorrect matching of VELO and tracking stations hits. A neural network is used to identify and remove ghost tracks, based on the result of the track fit, track kinematics and the number of measured and expected hits in the tracking stations. The output of this neural network gives a probability for the track to be a ghost, the **Track Ghost Prob**. It can be used to reduce the number of background events.

A secondary vertex is reconstructed from a fit to several long tracks. The χ^2 of this fit can be used as a measure of the vertex quality. $B^0 \to p\bar{p}K^+\pi^-$ decay candidates, where the p, $\bar{p}$, K^+ and π^- tracks originate from the B^0 decay vertex, tend to have a better secondary **Vertex χ^2** than combinatorial background events.

The geometric variables used in the selection procedure take advantage from the displaced secondary vertices typical of b-hadron decays to identify $B^0 \to p\bar{p}K^+\pi^-$ events.

The IP of a particle is the distance of closest approach of its extrapolated trajectory to the primary vertex. The IP has been defined in Sec. 3.2.2 and it has been illustrated in Figure 27(a). The **IP χ^2** is defined as the difference in the χ^2 of the primary vertex reconstructed with and without the particle in question, and it gives a measure of how significant is the displacement of the track from the primary vertex. Particles originating from the primary vertex, i.e. combinatorial background tracks, should have a small IP χ^2.

The distance between the particle production and decay vertices, namely the flight distance (FD), is commonly used to identify displaced secondary vertices. The **FD χ^2** is defined as the difference in the χ^2 of the production vertex reconstructed with and without the particle in question, and it gives a measure of how significant is the displacement between the production and decay vertices. In particular B^0 candidates should have a large FD χ^2.

The distance of closest approach (DOCA) between two tracks can be used to determine how likely they are originating from the same decay vertex. The **χ^2 DOCA** is the χ^2 obtained from a vertex fit of the two tracks. Particles originating from the same decay vertex should have a small χ^2 DOCA.

The direction angle, DIRA, is the angle between the momentum vector of the B^0 candidate and the 3D displacement vector between the associated primary and secondary vertices. It is shown in Figure 46.

Hence the DIRA is a measure of the consistency of the B^0 candidate with the reconstructed vertices. The cosine of the DIRA is used to separate $B^0 \to p\bar{p}K^+\pi^-$ from combinatorial background events and it should close to one for $B^0 \to p\bar{p}K^+\pi^-$ events. In the following **DIRA** will refer to the cosine of the direction angle.

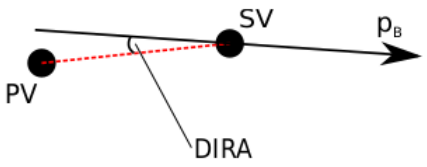

Figure 46: The DIRA is defined as the angle between the B momentum vector p_B and the displacement vector (red dashed line) from the PV to the SV.

The **pointing** variable is defined as

$$\frac{|\vec{p}_B| \sin\theta}{|\vec{p}_B| \sin\theta + \sum_i |\vec{p}_i| \sin\theta_i}, \tag{37}$$

where $\vec{p}_B$ is the momentum of the B^0 candidate, θ is the angle between the direction of $\vec{p}_B$ and the displacement vector from PV to SV, as shown in Figure 46, $\vec{p}_i$ is the momentum of child i, θ_i is the angle between the direction of $\vec{p}_i$ and the displacement vector from PV to SV and the sum runs over the candidate B^0 children. Also this variable is used to discriminate between particles coming from the PV and B^0 children coming from the SV. Indeed, for the B^0 signal children the value of the pointing variable should peak at zero, because of the large contribution given by the $\sum_i |\vec{p}_i| \sin\theta_i$, for combinatorial background events θ_i is smaller and hence the distribution peak move towards higher values.

Artificial neural networks are used to assign a probability, the **ProbNN**, that a given charged track is a kaon, a pion or a proton with respect to some other mass hypotheses. The input variables used to train the neural network contain information from the RICH detectors combined with the information from the tracking system, muon detectors and the calorimeters. The output of the network is a value between 0 and 1. In the case of a true proton, for example, the pProbNNp variable gives the probability for the track to be consistent with the proton mass hypothesis, and it should be close to 1. On the other side, a variable like pProbNNk gives the probability that the track is misidentified as a kaon, and it should close to 0. In addition, a boolean variable called **hasRich** is used to select tracks having hits in at least one of the RICH detectors.

4.4.2 Trigger selection

Different trigger lines, whose variables have been defined in Sec. 3.3 are studied in order to get the best signal to background ratio. From the hardware level trigger responses the logical OR between the L0HadronDecision_TOS (Trigger On Signal) and the L0Physics_TIS (Trigger Independent of Signal) lines are used, where L0Physics is the OR between L0Electron, L0Photon, L0Muon, L0DiMuon and L0Hadron lines. Events that passed the L0 lines are retained if they also satisfy the HLT1TrackAllL0Decision_TOS line. At the HLT2 trigger level the events are required to satisfy at least one of the topological b-decays trigger lines (HLT2Topo(2,3,4)BodyDecision_TOS).

Starting from Run 2 data, the HLT1TrackAllL0Decision_TOS line is replaced by the OR between the Hlt1TrackMVADecision_TOS and the Hlt1TwoTrackMVADecision_TOS lines.

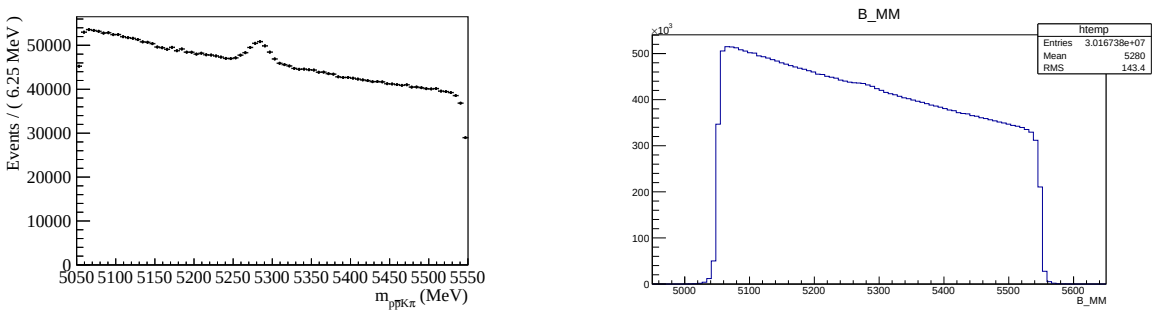

Figure 47: The Run 1 (left) and Run 2 (right) $m(p\bar{p}K^+\pi^-)$ spectrum after the corresponding stripping and trigger requirements.

4.4.3 Stripping selection

A stripping line dedicated to study $B^0_{(s)} \to p\bar{p}h_1^+h_2^-$ decays, where $h_{1,2} = K^\pm, \pi^\pm$ is used, whose requirements are listed in Table 13. There are common cuts on the momentum p and the transverse momentum $p_\perp$ of the children. A good track quality is also ensured cutting on the track χ^2/ndof and on the ghost probability associated to the track. Minimal particle identification (PID) requirements are applied to each child. In order to exclude particles coming from the primary vertex (PV) there are requirements on the impact parameter (IP) χ^2 for the children with respect to the PV.

Cuts are also applied to the $p\bar{p}$ pair and to the $p\bar{p}K^+$ combination, in order to speed up the algorithm that selects and combines the final state particles. The particles in the combinations are required to come from the same vertex through a requirement on the χ^2 distance of closest approach (DOCA). There are requirements on the invariant masses of the combinations. Specific kinematical cuts are applied to the $p\bar{p}$ pair. A further PID cut is applied to the proton-antiproton pair.

The reconstructed B^0 are selected with topological requirements as the maximum DOCA of the children, the cosine of the angle between the momentum of the B^0 and the direction flight from the PV to the SV (DIRA), and the minimum IP to the PV. A good fit quality of the vertex is required too. There are also kinematical requirements on the reconstructed B^0 and a global cut on the maximum number of long tracks reconstructed in the event.

4.4.4 Offline selection: introduction

The $m(p\bar{p}K^+\pi^-)$ spectra corresponding to the Run 1 and Run 2 data samples after the trigger and stripping line selections are shown in Figure 47.

As it can be seen, the data contain a large contribution from combinatorial and misidentified events. Therefore the offline selection is crucial to obtain an acceptable signal to background ratio in order to further proceed with the analysis. Particle identification (PID) plays a very important role in this analysis, since the decay has a purely hadronic final state. Data provided by the the RICH detectors, the muon stations, the electromagnetic and hadronic calorimeters are reconstructed to build variables that discriminate between pions, kaons, protons, muons and electrons. The RICH detectors simulation is challenging because of the variations in the detectors occupancy, which can be different from event to event and sensitive to beam conditions. As a second order effect, the actual running

Variable	Run 1	Run 2
Kaons		
p	$> 1500\,\text{MeV}$	
$p_\perp$	$> 300\,\text{MeV}$	
Track χ^2/ndof	< 3.0	$< 4.0^{(*)}$
Track Ghost Prob	< 0.35	$< 0.4^{(*)}$
ProbNNk	> 0.05	
IP χ^2	> 4.0	> 5.0
Pions		
p	$> 1500\,\text{MeV}$	
$p_\perp$	$> 300\,\text{MeV}$	
Track χ^2/ndof	< 3.0	$< 4.0^{(*)}$
Track Ghost Prob	< 0.35	$< 0.4^{(*)}$
ProbNNπ	> 0.05	> 0.1
IP χ^2	> 6.0	> 8.0
Protons		
p	$> 1500\,\text{MeV}$	
$p_\perp$	$> 300\,\text{MeV}$	
Track χ^2/ndof	< 3.0	$< 4.0^{(*)}$
Track Ghost Prob	< 0.35	$< 0.4^{(*)}$
ProbNNp	> 0.05	
IP χ^2	> 2.0	> 3.0
$p\bar{p}$ combination		
$M_{p\bar{p}}$	$< 5000\,\text{MeV}$	
$\sum p_\perp$	$> 750\,\text{MeV}$	
$\sum p$	$> 700\,\text{MeV}$	
Minimum $p_\perp$	$> 400\,\text{MeV}$	
Minimum p	$> 4000\,\text{MeV}$	
ProbNNp·ProbNN$\bar{p}$	> 0.05	> 0.01
χ^2 DOCA	< 20	
$p\bar{p}K^+$ combination		
$M_{p\bar{p}K^+}$	$< 5600\,\text{MeV}$	
χ^2 DOCA	< 20	
B^0		
Max DOCA	$< 0.3\,\text{mm}$	$< 0.25\,\text{mm}$
χ^2 DOCA	< 20	
DIRA	> 0.9999	
Vertex χ^2	< 30	< 25
Min IP	$< 0.2\,\text{mm}$	
$p_\perp$	$> 1000\,\text{MeV}$	
$\sum p_\perp$ of the children	$> 3000\,\text{MeV}$	
Mass range	[5.05,5.55] GeV	
Number of Long Tracks	< 200	

Table 13: Stripping line requirements. In the column Run 2 are reported the cuts that are different with respect to Run 1 cuts. The Track Ghost Probability and Track χ^2/ndof in Run 2 (marked with $(*)$) are set a priori of the stripping line, at the track reconstruction level. All the other cuts remained the same of Run 1 ones.

conditions, like temperature and gas pressure, make difficult the RICH detectors simulation. For this reason there are discrepancies between data and simulated and this motivates the decision to avoid merging in the same MVA the topological and kinematical selection from the PID selection. This choice also makes easier the systematics treatment.

A multivariate analysis (MVA) based selection is performed for the topological and kinematical selection, described in section 4.4.6 for Run 1 and in section 4.4.10 for Run 2. The response of the MVA is optimised using a set of PID criteria, in the way described in section 4.4.9 for Run 1 and in section 4.4.11 for Run 2.

4.4.5 Preselection

A preselection to the final state particles is applied, comprising a fiducial cut on the pseudorapidity requiring the p, $\bar{p}$, K^+ and π^- candidates to be in the RICH acceptance with $2.0 < \eta < 4.9$. Moreover, for the reasons introduced in Sec. 3.2.6, a requirement on the proton and antiproton momenta to be greater than 8 GeV in Run 1 data sample and than 11 GeV in Run 2, is applied.

4.4.6 MVA selection for Run 1

The multivariate based selection is carried out using the algorithms provided by the TMVA package [152, 153]. The training samples consist of simulated b-decays for the signal and data in a region of invariant mass which is expected to contain purely combinatorial background. The samples are split in two, with one half used for training and the other for testing.

Simulated samples of $B^0 \to p\bar{p}K^+\pi^-$ events, generated according to the phase space of the decay, are used as signal training sample. The choice of $B^0 \to p\bar{p}K^+\pi^-$ instead of $B^0 \to \eta_c(\to p\bar{p})K^+\pi^-$ simulated samples is motivated by the will to avoid biasing the selection for a specific $p\bar{p}$ invariant mass. The preselection and the trigger and stripping line selections are applied to the simulated samples.

The $(5450, 5550)\,\mathrm{MeV/c^2}$ $m(p\bar{p}K^+\pi^-)$ range from data is used as the background training sample. This region only contains combinatorial background events, hence it does not include partially reconstructed or B_s^0 events.

The input variables to the MVA algorithms are chosen based on their ability to discriminate between signal and combinatorial background events. Several kinematical and topological distributions are investigated in order to find the set of variables that better discriminate between signal and background. The chosen variables are:

- minimum IP χ^2 of the B^0 to the PV (MINIPCHI2);
- maximum DOCA of the tracks to the B^0 vertex (B_AMAXDOCA);
- log of the χ^2 distance of the B^0 vertex from the PV (log(B_BPVVDCHI2);
- pointing variable;
- χ^2 of the B^0 vertex (VCHI2);
- log of the minimum p_T between the two protons (log(B_pPTmin));
- log of the maximum p_T between the two protons (log(B_pPTmax));

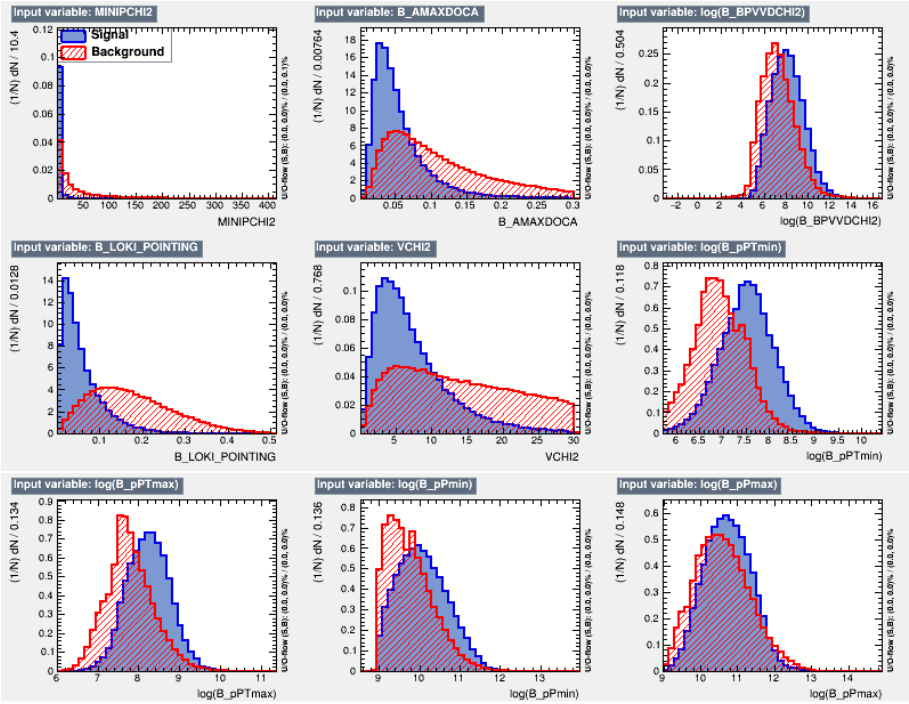

Figure 48: Comparison of Run 1 signal (blue filled) and background (red dashed) distributions used as MVA discriminating variables.

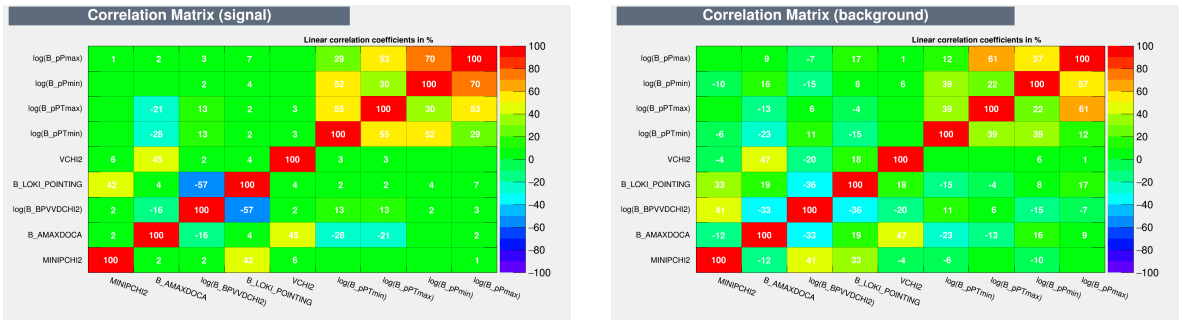

Figure 49: Correlation matrices for Run 1 signal (left) and background (right) MVA input variables

- log of the minimum p between the two protons (log(B_pPmin));
- log of the maximum p between the two protons (log(B_pPmax)).

The comparison between the signal and background discriminating variables is shown in Figure 48. The correlation matrices for the signal and background variables are shown in Figure 49. The signal and background different correlation coefficients between MVA input variables are exploited by the MVA algorithms, introduced in Sec. 4.4.7.

4.4.7 MVA algorithms

The types of MVA algorithms, also called classifiers, used in this analysis are Boosted Decision Trees (BDT) and Multi-Layer Perceptrons (MLP), a type of artificial neural network (ANN).

A decision tree is a binary classifier applying a sequence of selection criteria, based on the values of the input variables, to separate the N-dimensional space of the N input variables in regions mainly composed by signal or background candidates. A BDT is the combination of many decision trees. A BDT algorithm builds decision trees in an iterative process based on a weighted dataset. In the so-called boosting procedure, misclassified events are weighted more strongly for the next tree.

Three types of Boosted Decision Trees are used in this analysis. The BDT algorithm uses the most popular boosting algorithm, the so-called Adaptive Boost. The BDTD method, using the Adaptive Boost, applies a priori a decorrelation of the input variables, applying a transformation to the input variables to remove the linear correlations between the Gaussian distributed variables. The BDTG algorithm uses a different boosting technique, the so-called Gradient Boost.

An ANN consists of a collection of connected neurons, which are functions that have a number of inputs and a single output. Each neuron has an associated set of weights that are used to perform a weighted sum of the inputs. The output of the neuron is the activation function evaluated on the weighted sum. Training consists of finding the optimal set of weights for each neuron. A feed-forward neural network consists of ordered layers of neurons, with the outputs of the neurons from one layer feeding into the inputs of those in the next.

A MLP is a feed-forward ANN with at least three layers, including the input and output layers. The activation function is typically a sigmoid, e.g. $\mathrm{erf}(x)$, since this is useful for generally approximating non-linear functions. Training is performed using back-propagation, which is an iterative procedure that adjust the weights based on how much the output of the network differs from the desired output.
In the training phase of all the algorithms, care must be taken to avoid the so-called overtraining, which is a form of bias where the algorithm interprets statistical fluctuations in the training sample as being significant. Overtraining can be identified by a difference in performance between the training and test samples.

The performance of an algorithm can be determined from its curve in the space formed by background rejection and signal efficiency, called a receiver operating characteristic (ROC) curve. Better performance is indicate by the curve proximity to the ideal performance of 100% background rejection and signal efficiency.

4.4.8 MVA results for Run 1

The ROC curves for the four classifiers used in this analysis are shown in Figure 50. The BDT has been chosen for the application since it has a slightly better performance with respect to the other classifiers. The result of the Kolmogorov-Smirnov test for each classifier is reported in Figure 51. There is no evidence for overtraining.

4.4.9 PID cuts and optimisation of the selection for Run 1

Several sets of PID cuts, reported in Table 14, are considered in order to optimise the MVA selection.

Optimal cuts are determined by maximising a figure of merit (FOM), the choice of which depends on the goal of the analysis. A common FOM, used in this analysis, is the "signal significance" FOM: the ratio of the number of signal candidates to the Poisson

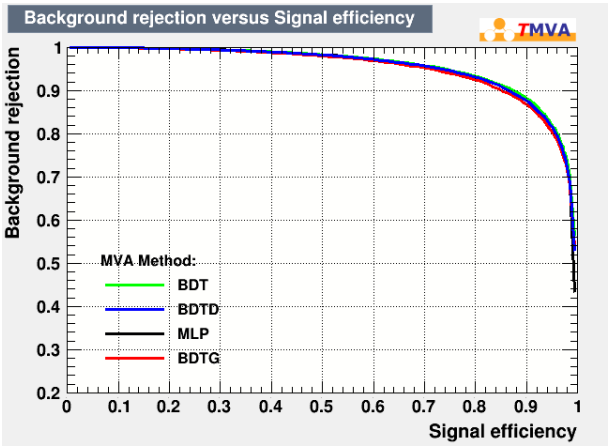

Figure 50: ROC curves for the algorithms used in the Run 1 MVA analysis.

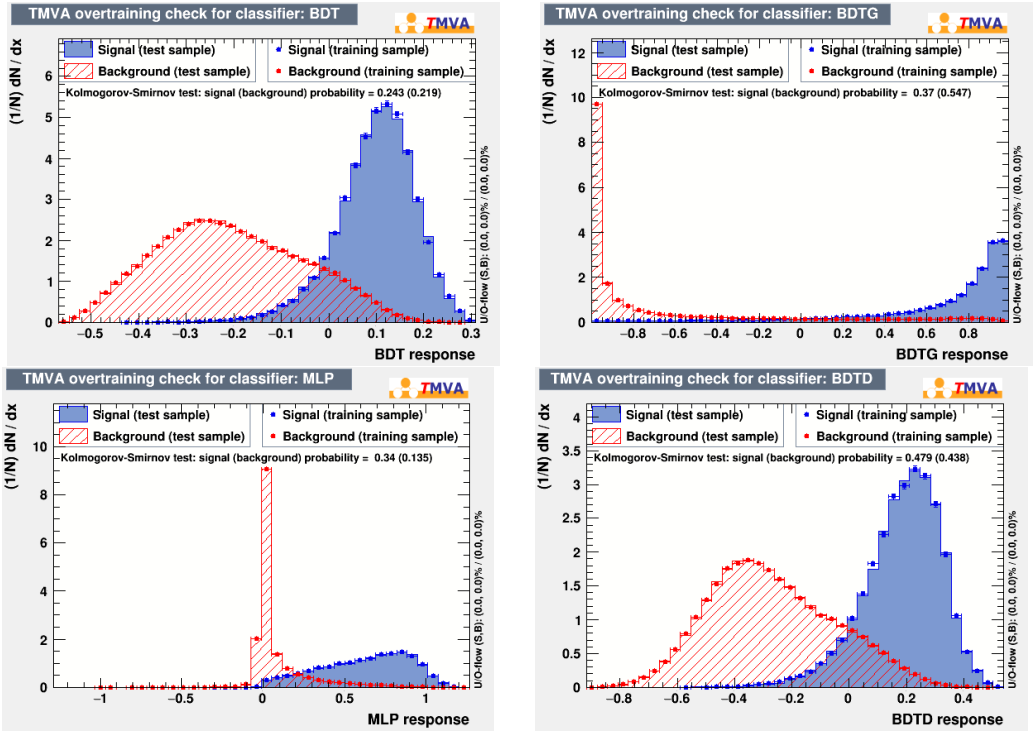

Figure 51: Results of the Kolmogorov-Smirnov test for each method to check for possible overtraining in Run 1 MVA analysis.

error on the sample size. Therefore, the BDT and PID cuts combination providing the best performance has been chosen in terms of the FOM defined as

$$\text{FOM} = \frac{S}{\sqrt{S+B}} \tag{38}$$

where S and B are respectively the number of signal and background events.

After the choice of the PID cuts, the $m(p\bar{p}K^+\pi^-)$ distribution from data is fitted in the $5200 < m(p\bar{p}K^+\pi^-) < 5360$ range. The background is parameterised with a linear

variable	cuts
pProbNNp	$> 0.15, > 0.175, > 0.225, > 0.25, > 0.3$
kProbNNk	$> 0, > 0.1, > 0.2, > 0.25$
kProbNNp	$< 1, < 0.8, < 0.4, < 0.15$
kProbNNπ	$< 1, < 0.8, < 0.4, < 0.15$
πProbNNπ	$> 0.125, > 0.15, > 0.2$
πProbNNk	$< 1, < 0.8, < 0.4, < 0.15$
πProbNNp	$< 1, < 0.8, < 0.4, < 0.15$

Table 14: Cuts used for the ProbNN variables during the PID selection.

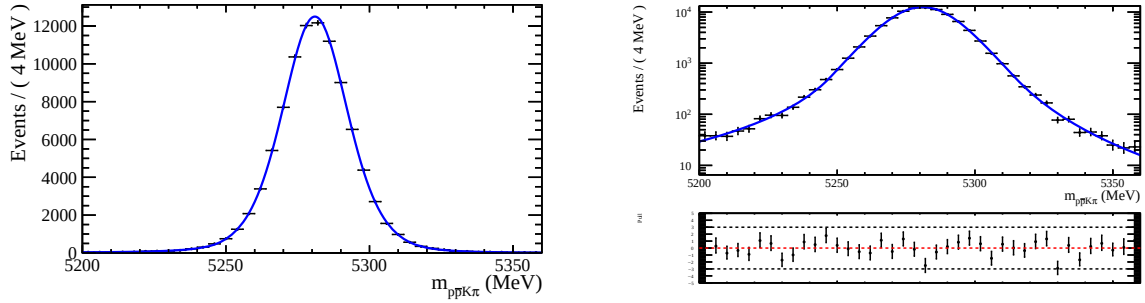

Figure 52: Fit to Run 1 the $B^0 \to p\bar{p}K^+\pi^-$ invariant mass spectrum for Run 1 simulated events in linear (left) and logarithmic scale (right). The pull distribution is shown under the log scale plot.

PDF, while the signal has been parameterised with a two tails Hypatia PDF, defined as

$$f(m|\mu,\sigma,l,\zeta,\beta,\alpha_1,\alpha_2,n_1,n_2) = \begin{cases} \frac{A}{(B+m-\mu)^{n_1}}, & \text{if } \frac{m-\mu}{\sigma} < -\alpha_1 \\ \frac{C}{(D+m-\mu)^{n_2}}, & \text{if } \frac{m-\mu}{\sigma} > \alpha_2 \\ ((m-\mu)^2+\delta^2)^{\frac{1}{2}l-\frac{1}{4}} \exp\left(\beta(x-\mu)\right) K_{l-\frac{1}{2}}(\alpha\sqrt{(x-\mu)^2+\delta^2}) & \text{otherwise} \end{cases} \tag{39}$$

where $K_l(z)$ is the modified Bessel function of the second kind of order l, A, B, C and D are obtained requiring the PDF to be continuous and differentiable.

The signal PDF is validated using the $B^0 \to p\bar{p}K^+\pi^-$ simulated sample as shown in Figure 52. In the fit to the $m(p\bar{p}K^+\pi^-)$ distribution the shape parameters of the Hypatia PDF are fixed to the parameters reported in Table 15. The signal N_{sig} and background yields are extracted in the $\pm$ 3σ region around the B^0 peak. The BDT cut is varied from -0.15 to 0.13 in steps of 0.02. Using the phase space $B^0 \to p\bar{p}K^+\pi^-$ simulated sample, the efficiency ϵ as a function of the BDT cut is determined at the given PID cut. This procedure provides the number of signal events defined as

$$S(BDT) = N_{sig} \cdot \epsilon(BDT) \tag{40}$$

Data are refitted to calculate the yield of background events B(BDT) as a function of the BDT value, again in the $\pm$ 3σ region around the peak. In this way the FOM(BDT) curve is extracted and the maximum value for the chosen PID cuts is obtained. The procedure is repeated for every combination of the ProbNN cuts shown in Table 14.

μ	5280.98 ± 0.04
σ	13.61 ± 0.11
ζ	$(9.0 \pm 2.6) \times 10^{-4}$
l	-3.68 ± 0.22
a_1	2.45 ± 0.10
n_1	2.10 ± 0.27
a_2	2.49 ± 0.12
n_2	3.4 ± 0.5

Table 15: The Hypatia parameters, defined in Eq. (39), extracted from the fit to the $B^0 \to p\bar{p}K^+\pi^-$ invariant mass spectrum for Run 1 simulated events. The parameters μ and σ are left floating in the optimisation procedure.

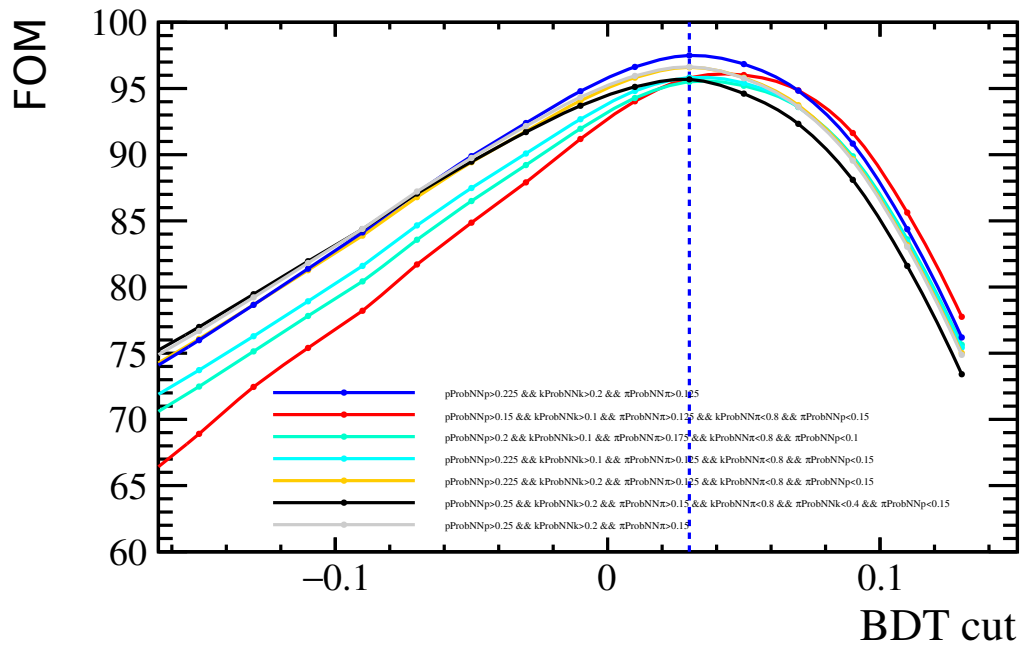

Figure 53: Run 1 FOM curves obtained for the subset of PID cuts shown in the legend. The blue curve corresponds to the nominal PID cut. The blue dashed vertical line corresponds to the nominal BDT cut.

A comparison of some FOM curves at different PID cuts is shown in Figure 53. The combination of MVA and PID cuts providing the best performance is

BDT>0.03 & pProbNNp>0.225 & kProbNNk>0.2 & πProbNNπ>0.125

4.4.10 MVA selection for Run 2

The same strategy described in 4.4.6 is used. The comparison between signal and background discriminating variables is shown in Figure 54. The correlation matrices for the signal and background variables are shown in Figure 55.

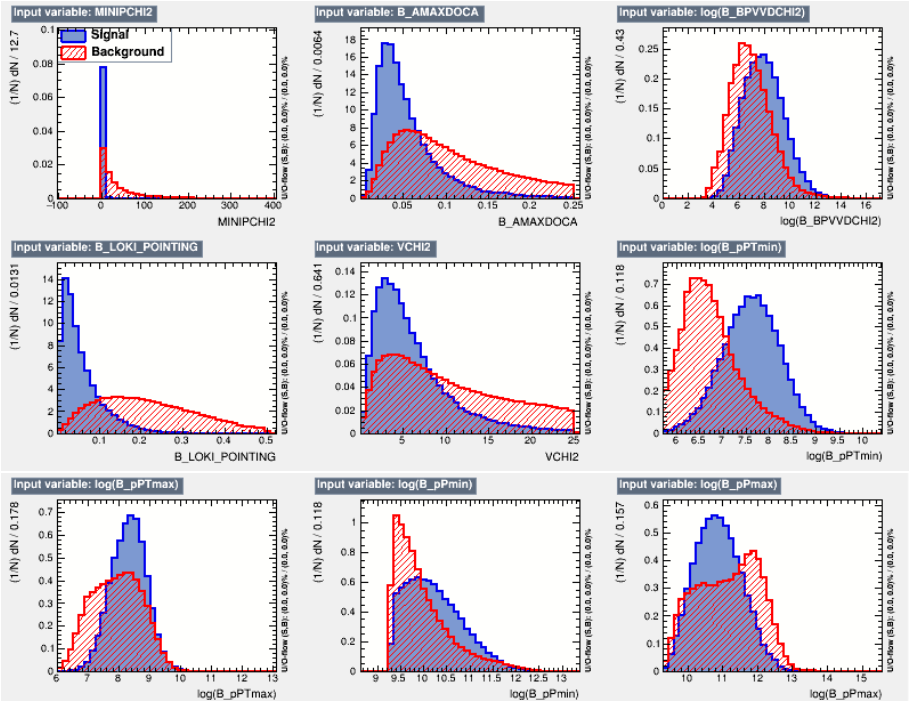

Figure 54: Comparison of Run 2 signal (blue filled) and background (red dashed) distributions used as MVA discriminating variables.

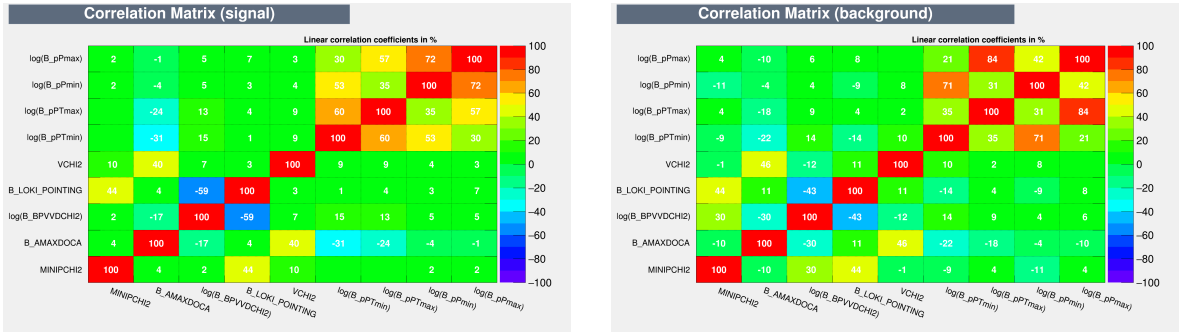

Figure 55: Correlation matrices for Run 2 signal (left) and background (right) MVA input variables

The ROC curves for the classifiers are shown in Figure 56. Also in the Run 2 case the BDT classifier is used and applied to data since it has a slightly better performance with respect to the other algorithms. The result of the Kolmogorov-Smirnov test for each classifier is reported in Figure 57. There is no evidence for overtraining.

4.4.11 PID cuts and optimisation of the selection for Run 2

The strategy is similar to the one used for Run 1. Given the different BDT response, a loose BDT cut equal to -0.15 has been set a priori of the procedure. The BDT cut is varied between -0.11 and 0.33. The same set of PID cuts used for Run 1, reported in Table 14, is also used for Run 2. The signal PDF is validated using the $B^0 \to p\bar{p}K^+\pi^-$ simulated sample as shown in Figure 58, applying the loose BDT cut and the preselection.

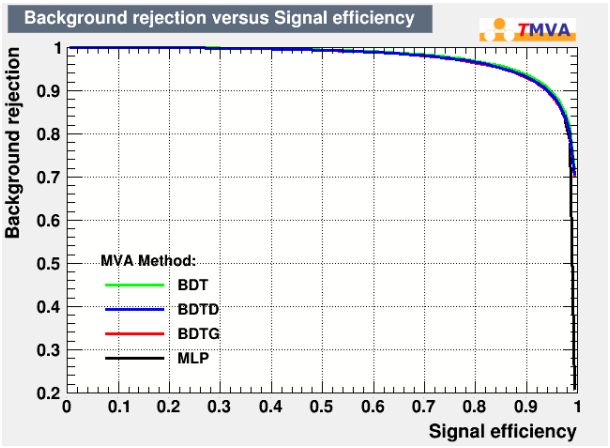

Figure 56: ROC curves for the algorithms used in the Run 2 MVA analysis.

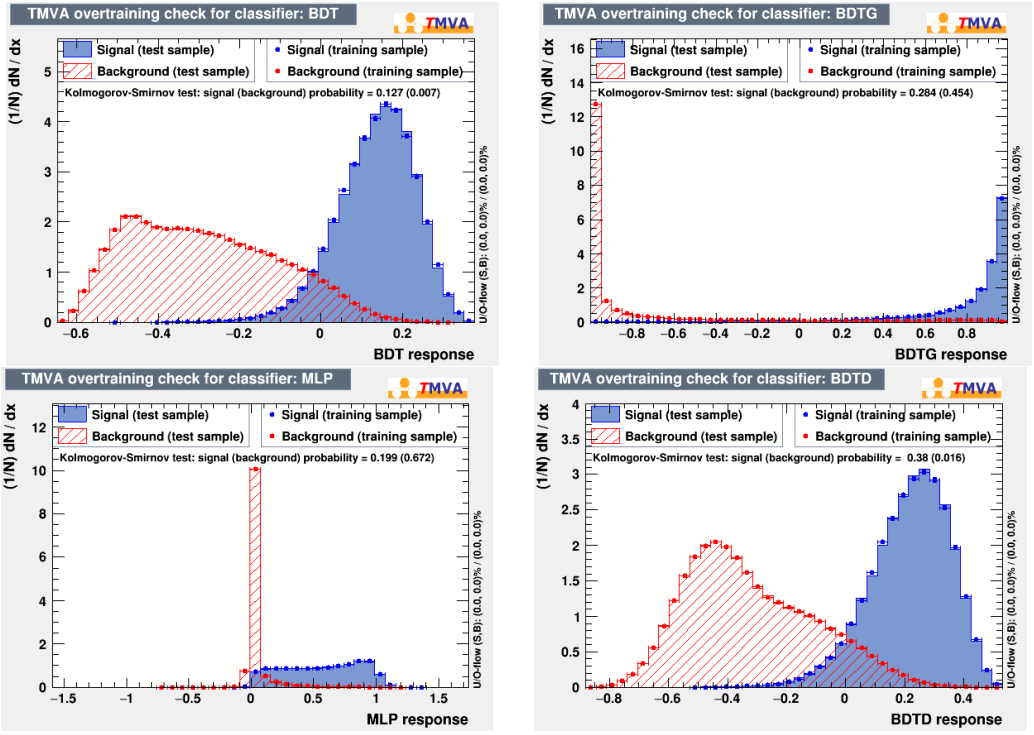

Figure 57: Results of the Kolmogorov-Smirnov test for each method to check for possible overtraining in Run 2 MVA analysis.

In the fit to the $m(p\bar{p}K^+\pi^-)$ distribution from data, the shape parameters of the Hypatia PDF are fixed to the parameters reported in Table 16. This procedure provides the signal N_{sig} and background yields in the $\pm\, 3\sigma$ region around the B^0 peak.

A comparison of some FOM curves at different PID cuts is shown in Figure 59. The combination of MVA and PID cuts providing the best performance is

BDT>0.09 & pProbNNp>0.25 & kProbNNk>0.25 & πProbNNπ>0.2

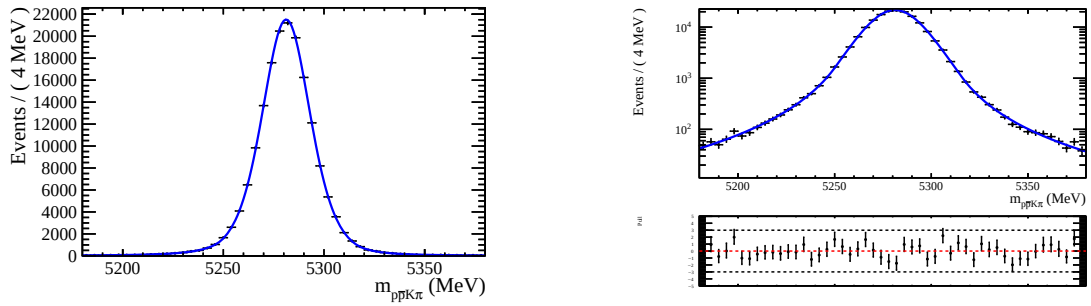

Figure 58: Fit to $B^0 \to p\bar{p}K^+\pi^-$ invariant mass for Run 2 simulated events in linear (left) and logarithmic scale (right). The pull distribution is shown under the log scale plot.

μ	5281.21 ± 0.04
σ	15.05 ± 0.10
z	$(8.1 \pm 3.1) \times 10^{-4}$
l	-3.30 ± 0.13
a_l	2.15 ± 0.04
n_l	2.36 ± 0.13
a_r	2.39 ± 0.06
n_r	2.36 ± 0.13

Table 16: The Hypatia parameters, defined in Eq. (39), extracted from the fit to the $B^0 \to p\bar{p}K^+\pi^-$ invariant mass spectrum for Run 2 simulated events. The parameters μ and σ are left floating in the optimisation procedure.

4.4.12 Multiple candidates

Multiple candidates are mainly due to an ambiguous K/π or K/p mass hypothesis assigned to a track. The p/π ambiguity is also existing, though to a lesser extent. Around the 3% of multiple candidates has been found in both Run 1 and Run 2 samples after all the selection cuts. In case of multiple candidates for the same event, one of them has been retained randomly.

4.5 Fit models, extraction of the $B^0 \to \eta_c K^+\pi^-$ candidates and branching fraction measurement

The $m(p\bar{p}K^+\pi^-)$ spectra for the Run 1 and Run 2 data samples after the corresponding selection procedure are shown in Figure 60. The B^0 signal peak is clearly visible. There are partially reconstructed events in the left sideband, for example due to $B^0 \to p\bar{p}K^+\pi^-\pi^0$ events where the π^0 has not been reconstructed. Contributions from the $B_s^0 \to p\bar{p}K^+\pi^-$ decays are expected as well. Misidentified (MisID) events from the $B_s^0 \to p\bar{p}K^+K^-$ decays, where the negative kaon has been misreconstructed as a pion, and from $B^0 \to p\bar{p}\pi^+\pi^-$ decays, where the positive pion has been misreconstructed as a kaon, are expected. Possible $\Lambda_b^0 \to p\bar{p}pK^-$ contamination, where one of the protons would be misreconstructed as a pion, are found to be negligible. The PDFs used to build the fit model are validated on

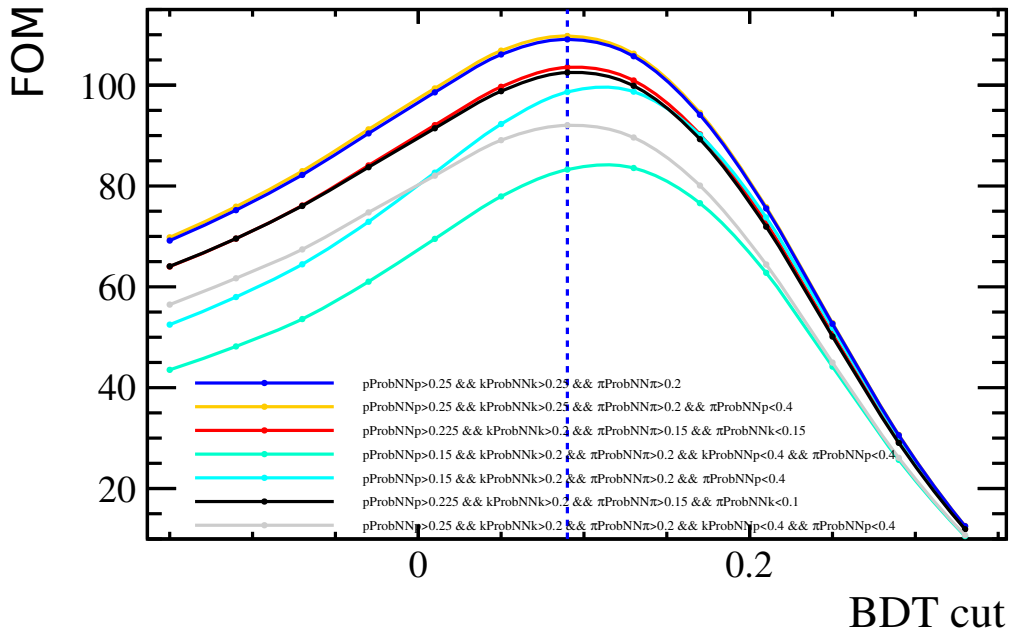

Figure 59: FOM curves for Run 2 data obtained for the subset of PID cuts shown in the legend. The blue dashed vertical line corresponds to the nominal BDT cut. There is a negligible difference between the yellow and blue curves due to the addition, in the yellow curve, of the πProbNN$p < 0.4$ cut. In order to cut on the same set of variables in Run 1 and Run 2 data, the cuts corresponding to the blue curve has been chosen.

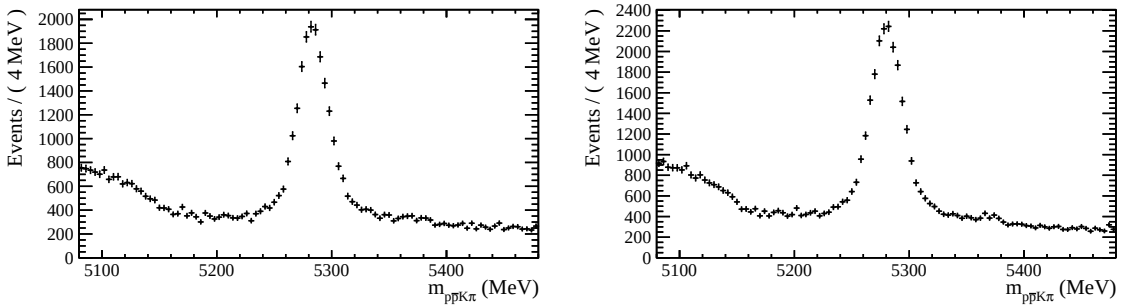

Figure 60: The $m(p\bar{p}K^+\pi^-)$ Run 1 (left) and Run 2 (right) spectra after selection requirements.

the corresponding simulated sample.

The mass fit to Run 1 and Run 2 data is carried out using the extended unbinned maximum likelihood formalism provided by the RooFit package [154]. The fit to the $m(p\bar{p}K^+\pi^-)$ invariant mass distribution is performed, as described in Sec. 4.5.1, to extract the B^0 yield, to validate the model and to find eventual background contributions to be vetoed in the $B^0 \to \eta_c K^+\pi^-$ amplitude fit.

A 2D mass fit to the $m(p\bar{p}K^+\pi^-)$ and $m(p\bar{p})$ invariant mass distributions is carried out, as described in Sec. 68, to extract the signal and background yields and to determine the background shapes to be used in the amplitude fit.

4.5.1 Mass fit to the $m_{p\bar{p}K\pi}$ invariant mass distribution

The fit model consists of:

- the $B^0 \to p\bar{p}K^+\pi^-$ signal;
- the $B^0_s \to p\bar{p}K^+K^-$ misID component;
- the $B^0 \to p\bar{p}\pi^+\pi^-$ misID component;
- the $B^0_s \to p\bar{p}K^+\pi^-$ component;
- the combinatorial background component.

The signal and $B^0_s \to p\bar{p}K^+\pi^-$ components are parametrised using the Hypatia PDF, defined in Eq. (39). The B^0 and the B^0_s resolutions are constrained to be the same, according to the compatibility found between the resolutions extracted from the fit to the corresponding simulated samples. The combinatorial background component is parametrised with an exponential PDF. The MisID components are parametrised using the two tails Crystal Ball PDF, defined as

$$f(m|n_1,n_2,\alpha_1,\alpha_2,\mu,\sigma) = \begin{cases} \left(\frac{n_1}{|\alpha_1|}\right)^{n_1} \exp\left(-\frac{|\alpha_1|^2}{2}\right)\left(\frac{n_1}{|\alpha_1|} - |\alpha_1| - \frac{m-\mu}{\sigma}\right)^{-n_1}, & \text{if } \frac{m-\mu}{\sigma} < -\alpha_1 \\ \left(\frac{n_2}{|\alpha_2|}\right)^{n_2} \exp\left(-\frac{|\alpha_2|^2}{2}\right)\left(\frac{n_2}{|\alpha_2|} - |\alpha_2| - \frac{m-\mu}{\sigma}\right)^{-n_2}, & \text{if } \frac{m-\mu}{\sigma} > \alpha_2 \\ \exp\left(-\frac{(m-\mu)^2}{2\sigma^2}\right), & \text{otherwise} \end{cases} \tag{41}$$

The shape parameters are fixed from the fit to the corresponding simulated samples.

The Run 1 fit and extracted parameters are shown respectively in Figure 61 and in Table 17. The Run 2 fit and extracted parameters are shown respectively in Figure 62 and in Table 18.

The *sPlot* procedure [155], using the $m(p\bar{p}K^+\pi^-)$ invariant mass distribution as the discriminant variable to compute the signal weights of the $B^0 \to p\bar{p}K^+\pi^-$ component, is used to perform background studies in the η_c region, described in Sec. 4.5.2.

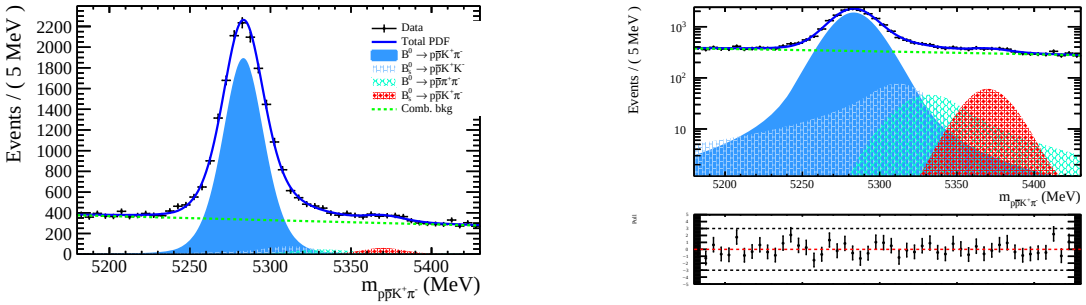

Figure 61: Fit to the Run 1 $B^0 \to p\bar{p}K^+\pi^-$ invariant mass distribution shown in linear (left) and logarithmic scale (right). The pull distribution is shown under the log scale plot.

m_{B^0}	$5283.19 \pm 0.21\,\text{MeV}$
m_{B_s}	$5371.2 \pm 3.2\,\text{MeV}$
σ	$15.33 \pm 0.28\,\text{MeV}$
Comb.bkg. slope	$(-1.11 \pm 0.14) \times 10^{-3}$
N_{B^0}	13723 ± 270
$N_{B_s^0}$	426 ± 91
$N_{B_s^0 \to p\bar{p}K^+K^-}$	838 ± 573
$N_{B^0 \to p\bar{p}\pi^+\pi^-}$	593 ± 232
$N_{\text{Comb.bkg}}$	17611 ± 240

Table 17: Parameters extracted from the fit to the Run 1 $B^0 \to p\bar{p}K^+\pi^-$ invariant mass distribution.

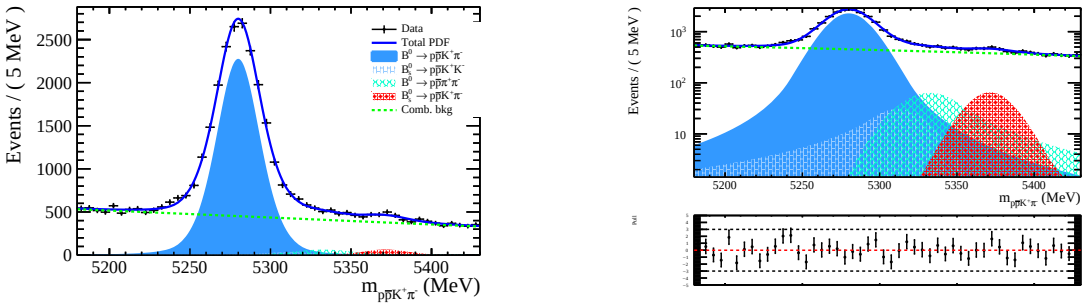

Figure 62: Fit to the Run 2 $B^0 \to p\bar{p}K^+\pi^-$ invariant mass distribution shown in linear (left) and logarithmic scale (right). The pull distribution is shown under the log scale plot.

m_{B^0}	$5280.00 \pm 0.19\,\text{MeV}$
m_{B_s}	$5370.5 \pm 3.1\,\text{MeV}$
σ	$16.01 \pm 0.25\,\text{MeV}$
Comb.bkg. slope	$(-1.65 \pm 0.11) \times 10^{-3}$
N_{B^0}	17454 ± 277
$N_{B_s^0}$	500 ± 105
$N_{B_s^0 \to p\bar{p}K^+K^-}$	453 ± 344
$N_{B^0 \to p\bar{p}\pi^+\pi^-}$	642 ± 236
$N_{\text{Comb.bkg}}$	23238 ± 277

Table 18: Parameters extracted from the fit to the Run 2 $B^0 \to p\bar{p}K^+\pi^-$ invariant mass distribution.

4.5.2 Background studies using the $B^0 \to p\bar{p}K^+\pi^-$ signal weights

It is important to check there are no intermediate states, in any invariant mass combination of the final state particles (with the exception of the $K^+\pi^-$ system), falling into the η_c region, defined in the $2900 < m_{p\bar{p}} < 3080\,\text{MeV}$ range. In particular it is possible that

the proton or the antiproton that should come from the η_c decay vertex, is actually a product of another resonance, i.e. some Λ resonances. For this reason the invariant mass distributions of the $\bar{p}K^+$, $\bar{p}K^+\pi^-$, $\bar{p}\pi^-$, pK^+, $pK^+\pi^-$ and $p\pi^-$ systems are investigated, weighted using the signal weights corresponding to the $B^0 \to p\bar{p}K^+\pi^-$ component. The 2D histogram of the invariant masses versus the $m_{p\bar{p}}$ distribution are built as a further cross-check. Only the $\bar{p}K^+\pi^-$ distribution has a clear peak corresponding to $\Lambda_c^- \to \bar{p}K^+\pi^-$ events, as shown in Figures 63 and 64. A veto to the $2236 < m(\bar{p}K\pi) < 2336\,\text{MeV}$ region is applied, also removing partially reconstructed b-hadron decays. There is also a structure between 2800 and 2900 MeV removed after applying the $D^0 \to K^-\pi^+$ veto, defined as the $1845 < m(K^+\pi^-) < 1885\,\text{MeV}$ region, as shown in Figure 65. This makes the structure as a candidate for $\Lambda_c^+ \to D^0 p$ events. The D^0 veto is applied in the following, also motivated by the need to reduce non-resonant $p\bar{p}$ events. The $pK^+\pi^-$ distributions are shown for comparison.

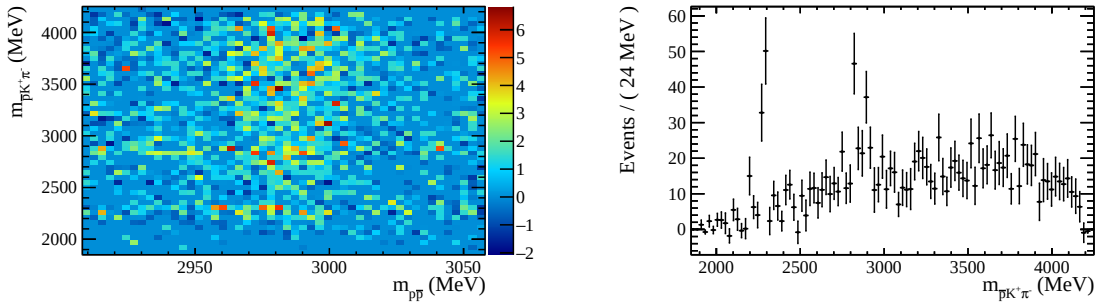

Figure 63: Left: Run 1 $m_{\bar{p}K^+\pi^-}$ invariant mass distribution versus the $m_{p\bar{p}}$ invariant mass distribution in the η_c region. An horizontal band corresponding to events resulting from Λ_c^- decays is visible. Right: projection over the $m_{\bar{p}K^+\pi^-}$ axis.

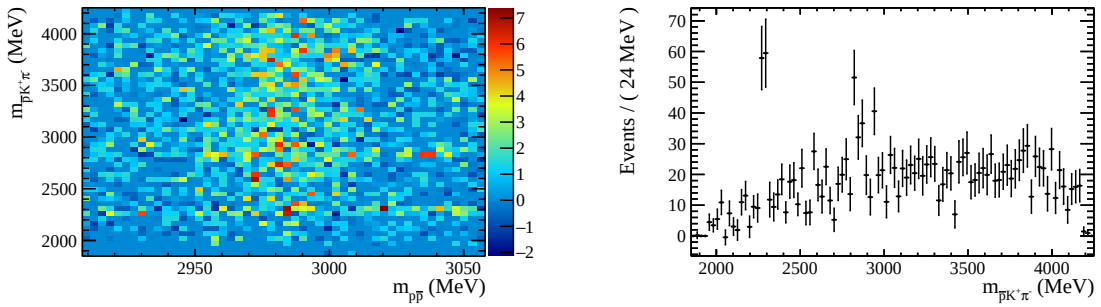

Figure 64: Left: Run 2 $m_{\bar{p}K^+\pi^-}$ invariant mass distribution versus the $m_{p\bar{p}}$ invariant mass distribution in the η_c region. An horizontal band corresponding to events coming from Λ_c^- decays is visible. Right: projection over the $m_{\bar{p}K^+\pi^-}$ axis.

4.5.3 2D mass fit to the $m(p\bar{p}K^+\pi^-)$ and $m_{p\bar{p}}$ invariant mass distributions

The $B^0 \to \eta_c K^+\pi^-$ events are unfolded performing a two dimensional mass fit to joint $m(p\bar{p}K^+\pi^-)$ and $m(p\bar{p})$ invariant mass distributions. The signal and background yields, to be used in the amplitude fit, can be determined. Using this pair of masses as discriminant variables, it is also possible to use the *sPlot* technique to compute the signal weights

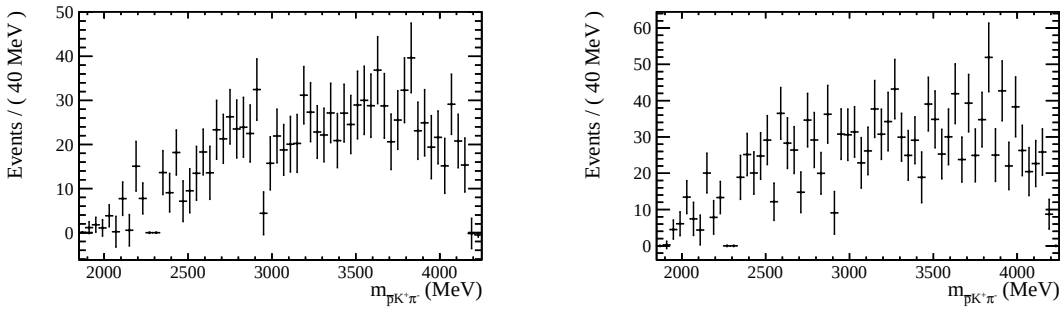

Figure 65: Run 1 (left) and Run 2 (right) $m_{\bar{p}K^+\pi^-}$ invariant mass distributions weighted with the weights coming from the 1D mass fit *sPlot* where the D0 veto is applied. The Λ_c^- veto is applied a priori.

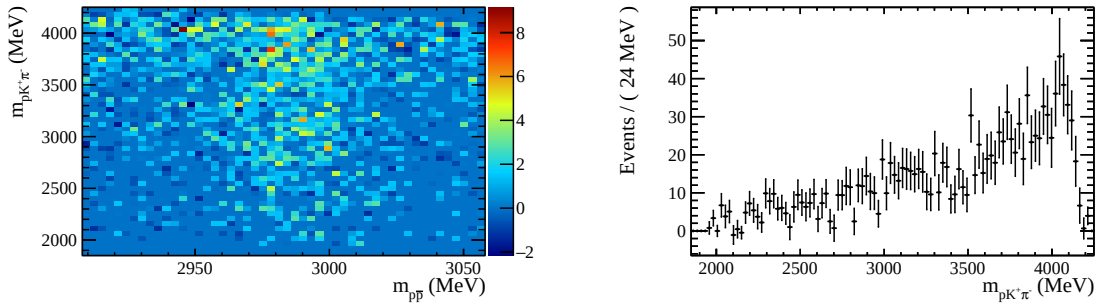

Figure 66: Run 1 $m_{pK^+\pi^-}$ invariant mass distribution versus the $m_{p\bar{p}}$ distribution in the η_c region.

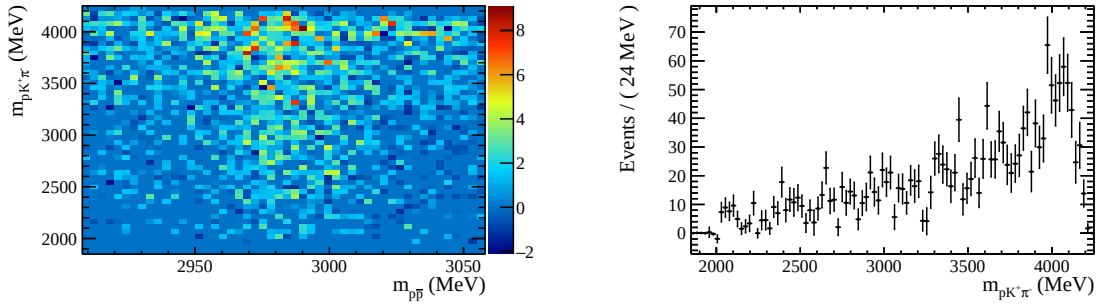

Figure 67: Run 2 $m_{pK^+\pi^-}$ invariant mass distribution versus the $m_{p\bar{p}}$ distribution in the η_c region.

for the $B^0 \to \eta_c K^+\pi^-$ component. The signal weights can then be used to build the combinatorial background and non-resonant background histograms to be used later on in the amplitude fit. Moreover, it is possible to build the corresponding DP projections in order to make consistency checks between the Run 1 and Run 2 data samples.

The $(5220, 5340)\,\text{MeV}$ $m(p\overline{p}K^+\pi^-)$ range and the $(2908, 3058)\,\text{MeV}$ $m(p\overline{p})$ range are chosen. As anticipated in section 4.5.2, the Λ_c^- and D^0 vetoes are applied before the fit. Moreover, because of concerns in the parametrisation of the efficiency at the phase space boundaries, a cut of $\pm 70\,\text{MeV}$ is applied in the $m(K^+\pi^-)$, $m(\eta_c\pi^-)$ and $m(\eta_c K^+)$ distributions. The $m(p\overline{p})$ range corresponds to the $\pm 75\,\text{MeV}$ region around the η_c peak. In

this range more than the 90% of the total η_c events are present and the misID contributions fall outside the chosen $m(p\bar{p}K^+\pi^-)$ or $m(p\bar{p})$ ranges. In these mass ranges, the expected contributions are given by:

- the $B^0 \to \eta_c K^+\pi^-$ signal;
- the $B^0 \to p\bar{p}K^+\pi^-$ non-resonant component;
- the combinatorial background component.

Another possible contribution is given by the η_c combined with spurious K^+ and π^-. This contribution is investigated and added to the fit. Since its yield is compatible with zero, it is not included in the nominal fit model.

The RooFit package allows to perform the 2D fit treating the $m(p\bar{p}K^+\pi^-)$ and $m(p\bar{p})$ invariant mass distributions as independent. The validity of the factorisation approach is verified checking for no linear correlation between the variables. Moreover, the 2D mass fit is repeated in slices of $m(p\bar{p})$ of 30 MeV each and checking that the parameter values are consistent within the statistical uncertainties. The procedure is also repeated using the $m(p\bar{p})$ range in the J/ψ region to increase the available statistics.

Since the factorisation approach is valid, the PDFs describing the three expected contributions can be written as $f(m(p\bar{p}K^+\pi^-), m(p\bar{p})) = g\,[m(p\bar{p}K^+\pi^-)] \times h\,[m(p\bar{p})]$. The B^0 meson is parameterised with an Hypatia PDF and the η_c meson with a Voigtian PDF, *i.e.* the convolution of a Breit–Wigner shape with a Gaussian PDF taking into account the resolution effects. The Hypatia shape parameters are the same used in the 1D fit. The η_c width has been gaussian constrained to the world average [15]. The combinatorial background and the non-resonant component are parametrised using exponential functions. The slope parameters for the combinatorial background components are α in the $m(p\bar{p}K^+\pi^-)$ invariant mass projection and β in the $m(p\bar{p})$ invariant mass projection. The slope parameter corresponding to the $B^0 \to p\bar{p}K^+\pi^-$ non-resonant component in the $m(p\bar{p})$ projection, is γ.

The fit projections of the 2D mass fit are shown in Figure 68. The extracted parameters are reported in Table 19.

To investigate the goodness of the 2D fits, the 2D pull distribution is computed as $(N_{\rm toy} - N_{\rm data})/\sqrt{N_{\rm data}}$. An adaptive binning algorithm is used to build the ($m(p\bar{p}K^+\pi^-)$,$m(p\bar{p})$) data histogram in order to have at least 20 events per bin. The 2D pull histogram is computed from the data ($m(p\bar{p}K^+\pi^-)$,$m(p\bar{p})$) histogram and the histogram filled with the values obtained generating $N_{\rm gen} = 10000 \times N_{\rm fit}$ events (where $N_{\rm fit}$ is the total yield from the fit) from the PDF resulting from the fit. The pull distributions are shown in Figure 69.

The 2D mass fit is repeated to the combined Run 1 and 2 data sample, and the *sPlot* technique is applied to determine the background-subtracted DP and SDP distributions shown in Fig. 70.

In order to check the consistency between the Run 1 and Run 2 distributions, the Kolmogorov test is carried out on the DP projections. Results are shown in Figs. 71 and 72. The procedure shows that the distributions are consistent between Run 1 and Run 2. The Kolmogorov results are consistent using other choices of binning.

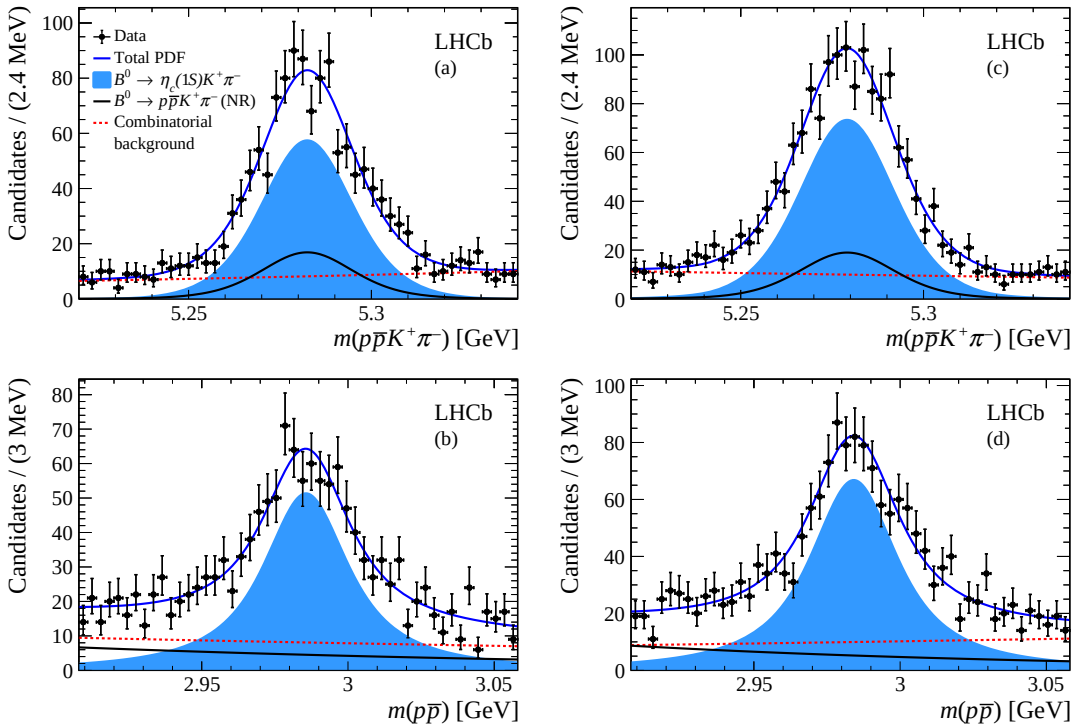

Figure 68: Results of the 2D mass fit to the joint $[m(p\bar{p}K^+\pi^-),\ m(p\bar{p})]$ distribution for the (a) Run 1 $m(p\bar{p}K^+\pi^-)$ projection, (b) Run 1 $m(p\bar{p})$ projection, (c) Run 2 $m(p\bar{p}K^+\pi^-)$ projection, and (d) Run 2 $m(p\bar{p})$ projection. The legend is shown in the top left plot.

Parameter	Run 1	Run 2
m_B	5282.4 ± 0.6 MeV	5279.1 ± 0.5 MeV
σ_B	15.1 ± 0.7 MeV	15.4 ± 0.6 MeV
α	$(3.6 \pm 1.7) \times 10^{-3}$	$(-2.2 \pm 1.5) \times 10^{-3}$
m_{η_c}	2985.6 ± 1.0 MeV	2984.2 ± 0.9 MeV
Γ_{η_c}	31.9 ± 0.8 MeV	32.0 ± 0.8 MeV
$\sigma_{p\bar{p}}$	4.77 ± 0.10 MeV	5.29 ± 0.10 MeV
β	$(-2.0 \pm 1.7) \times 10^{-3}$	$(1.5 \pm 1.5) \times 10^{-3}$
γ	$(-5.0 \pm 3.5) \times 10^{-3}$	$(-6.7 \pm 3.4) \times 10^{-3}$
$N_{B^0\to\eta_c K\pi}$	805 ± 48	1065 ± 56
$N_{B^0\to p\bar{p}K\pi}$ (non-resonant)	234 ± 48	273 ± 56
$N_{\text{Comb. bkg}}$	409 ± 36	498 ± 41

Table 19: Parameters extracted from the 2D mass fit.

4.5.4 Branching fraction measurement

The measurement of the $B^0 \to \eta_c K^+\pi^-$branching fraction is performed relative to that of the $B^0 \to J/\psi\, K^+\pi^-$ normalisation channel, where the J/ψ meson is also reconstructed in the $p\bar{p}$ decay mode. A two-stage fit procedure to the combined Run 1 and 2 data sample is

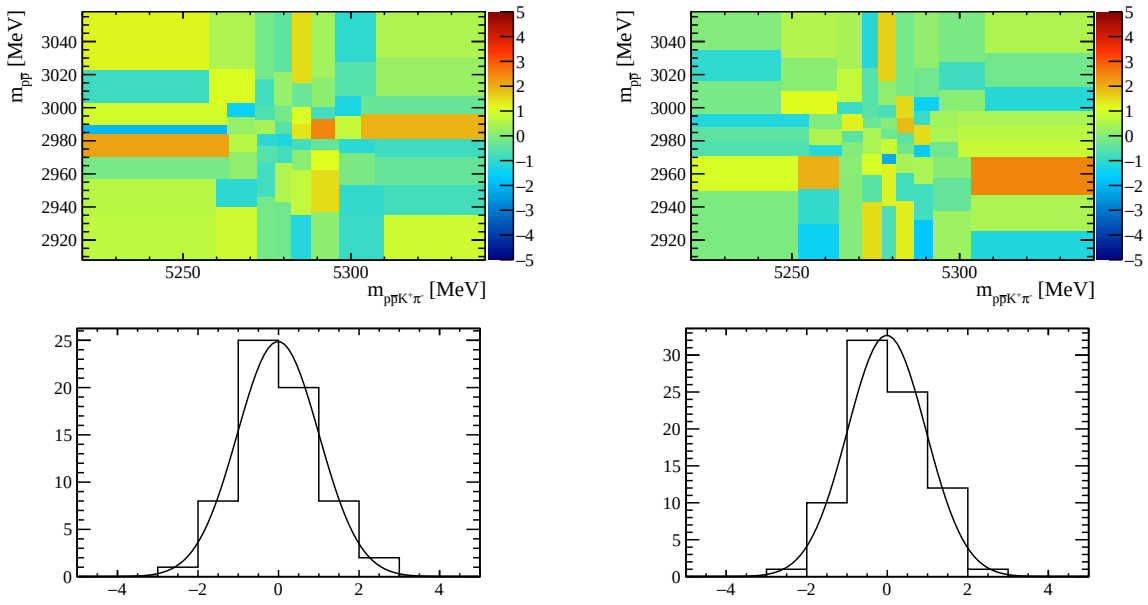

Figure 69: Top left: Run 1 2D pull distribution, Bottom left: 1D pull distribution computed from the bin contents of the Run 1 2D pull histogram ($\mu = -0.01 \pm 0.14$, $\sigma = 1.01 \pm 0.11$, $\chi^2/\text{ndof} = 0.94/3$), Top right: Run 2 2D pull distribution, Bottom right: 1D pull distribution computed from the bin contents of the Run 2 2D pull histogram ($\mu = -0.01 \pm 0.11$, $\sigma = 0.97 \pm 0.08$, $\chi^2/\text{ndof} = 1.3/3$).

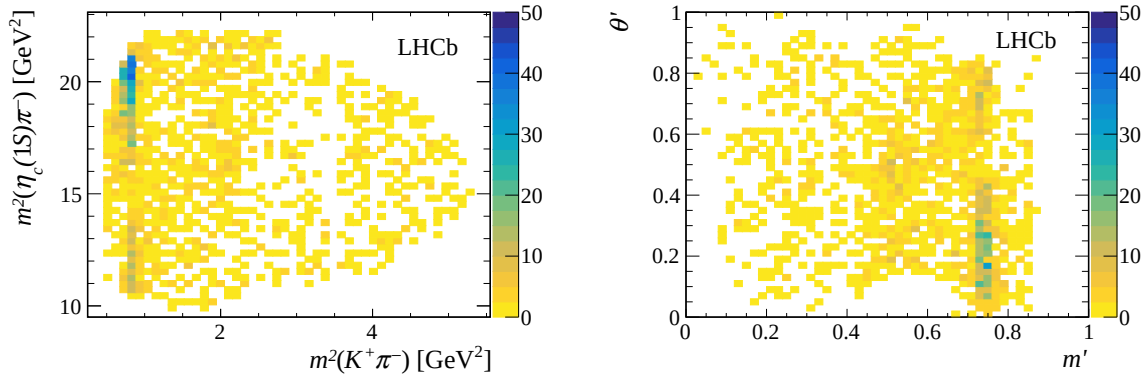

Figure 70: Background-subtracted (top) DP and (bottom) SDP distributions corresponding to the total data sample used in the analysis. The structure corresponding to the $K^*(892)^0$ resonance is evident. The veto of $B^0 \to \eta_c K^+\pi^-$ decays in the $\overline{D}^0$ region is visible in the DP.

used. In the first stage, an extended unbinned maximum-likelihood (UML) fit is performed to the $m(p\bar{p}K^+\pi^-)$ distribution in order to separate the $B^0 \to p\bar{p}K^+\pi^-$and background contributions. The RooFit package is used to perform the fit, and the *sPlot* technique is applied to assign weights for each candidate to subtract the background contributions. In the second stage, a weighted UML fit to the $p\bar{p}$ invariant-mass spectrum is performed to disentangle the η_c, J/ψ, and nonresonant (NR) contributions. The efficiency-corrected yield ratio is

$$R = \frac{N_{\eta_c}}{N_{J/\psi}} \times \frac{\epsilon_{J/\psi}}{\epsilon_{\eta_c}}, \tag{42}$$

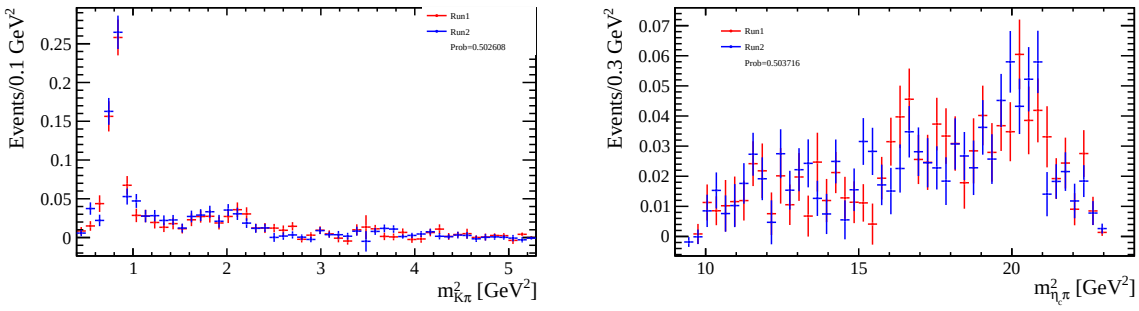

Figure 71: Kolmogorov test result checking the consistency between the Run 1 and Run 2 normalised $m^2(K^+\pi^-)$ (left) and $m^2(\eta_c\pi^-)$ (right) DP projections.

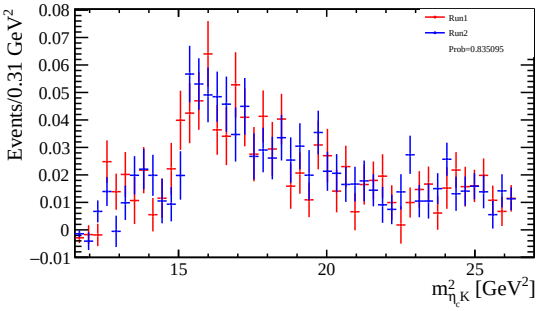

Figure 72: Kolmogorov test result checking the consistency between the Run 1 and Run 2 normalised $m^2(\eta_c K^+)$ DP projections.

where N_{η_c} and $N_{J/\psi}$ are the observed η_c and J/ψ yields, while ϵ_{η_c} and $\epsilon_{J/\psi}$ are the total efficiencies, which are obtained from a combination of simulated and calibration samples. The $B^0 \to \eta_c K^+\pi^-$branching fraction is determined as

$$\mathcal{B}(B^0 \to \eta_c K^+\pi^-) = R \times \mathcal{B}(B^0 \to J/\psi\, K^+\pi^-) \times \frac{\mathcal{B}(J/\psi \to p\overline{p})}{\mathcal{B}(\eta_c \to p\overline{p})}, \tag{43}$$

where $\mathcal{B}(B^0 \to J/\psi\, K^+\pi^-) = (1.15 \pm 0.05) \times 10^{-3}$, $\mathcal{B}(J/\psi \to p\overline{p}) = (2.121 \pm 0.029) \times 10^{-3}$ and $\mathcal{B}(\eta_c \to p\overline{p}) = (1.52 \pm 0.16) \times 10^{-3}$ are the external branching fractions taken from Ref. [15].

The first-stage UML fit to the $m(p\overline{p}K^+\pi^-)$ distribution is performed in the 5180–5430 MeV range and the fit components are the same that are used in the separate fit to Run 1 and 2 data. The $\overline{D}^0 \to K^+\pi^-$ and $\overline{\Lambda}_c^- \to \overline{p}K^+\pi^-$ decays are removed by excluding the mass range 1845–1885 MeV in the $m(K^+\pi^-)$ distribution and the range 2236–2336 MeV in the $m(\overline{p}K^+\pi^-)$ distribution, respectively. The veto to the phase space borders is applied as well.

The second-stage UML fit is then performed to the weighted $p\overline{p}$ invariant-mass distribution in the mass range 2700–3300 MeV, which includes η_c, J/ψ, and NR $B^0 \to p\bar{p}K^+\pi^-$ contributions. In addition to the components used in the $m(p\overline{p})$ projection of the 2D mass fit, the J/ψ resonance, having a small natural width, is parametrised using an Hypatia function, with tail parameters fixed to the values obtained from the corresponding simulated sample. The same resolution parameter is used for the η_c and J/ψ contributions, which is free to vary in the fit to the data. The η_c and J/ψ masses are also floating,

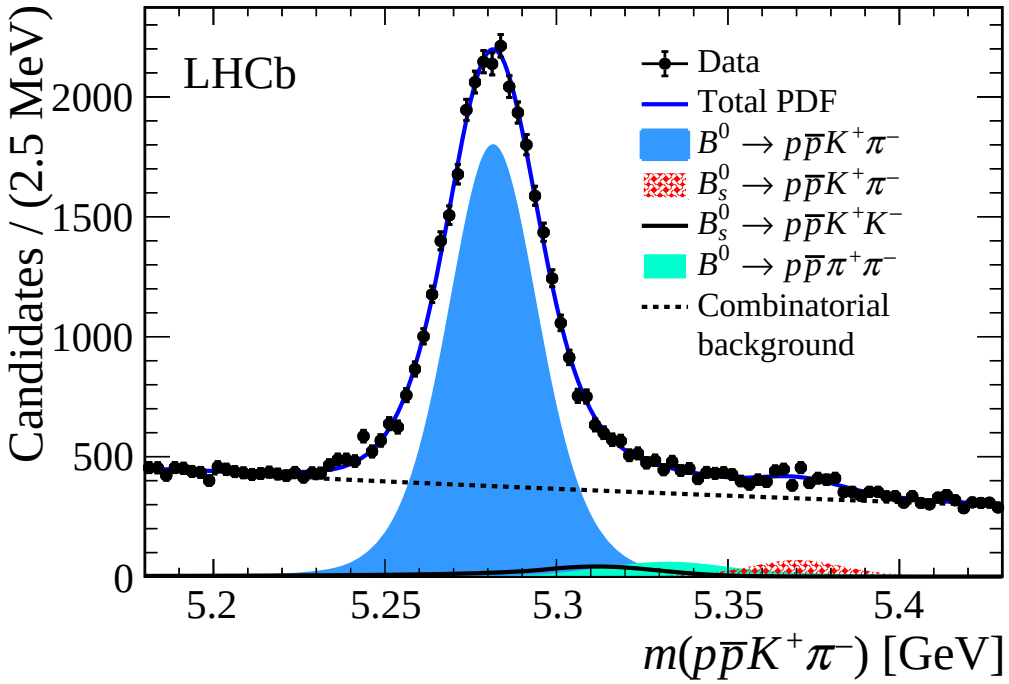

Figure 73: Distribution of the $p\bar{p}K^+\pi^-$ invariant mass. The solid blue curve is the projection of the total fit result. The components are shown in the legend.

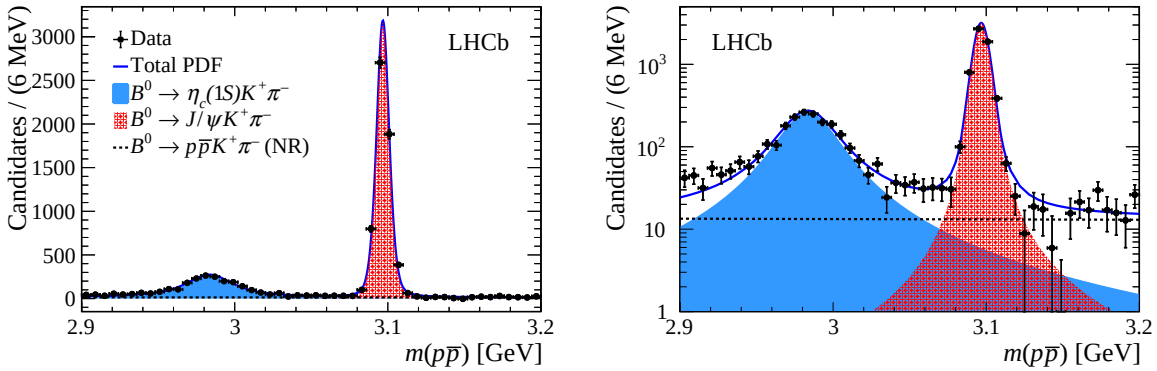

Figure 74: Distribution of the $p\bar{p}$ invariant mass in (left) linear and (right) logarithmic vertical-axis scale for weighted $B^0 \to p\bar{p}K^+\pi^-$candidates obtained by using the *sPlot* technique. The solid blue curve is the projection of the total fit result. The full azure, tight-cross-hatched red and dashed-black line areas show the η_c, J/ψ and NR $p\bar{p}$ contributions, respectively.

while the η_c natural width is Gaussian constrained to the known value [15]. All yields are left unconstrained in the fit. A possible term describing the interference between the η_c resonance and the NR $p\bar{p}$ S-wave is investigated and found to be negligible. The result of the fit to the weighted $p\bar{p}$ invariant-mass distribution is shown in Fig. 74. The yields of the $B^0 \to \eta_c K^+\pi^-$and $B^0 \to J/\psi\, K^+\pi^-$ fit components, entering Eq.(42), are 2105 ± 75 and 5899 ± 86, respectively.

The ratio of efficiencies of Eq. (42) is obtained from $B^0 \to \eta_c K^+\pi^-$and $B^0 \to J/\psi\, K^+\pi^-$ simulated samples, both selected using the same criteria used in data. Since these decays

have the same final-state particles and similar kinematic distributions, the ratio of efficiencies is expected to be close to unity. The efficiencies are computed as the product of the geometrical acceptance of the LHCb detector, the reconstruction efficiency and the efficiency of the offline selection criteria, including the trigger and PID requirements. The efficiency of the PID requirements is obtained using calibration samples of pions, kaons and protons, as a function of the particle momentum, pseudorapidity and the multiplicity of the event, *e.g.* the number of charged particles in the event [156]. The final ratio of efficiencies is given by

$$\frac{\epsilon_{J/\psi}}{\epsilon_{\eta_c}} = 1.000 \pm 0.013, \tag{44}$$

which is compatible with unity as expected.

Table 20 summarises the systematic uncertainties on the measurement of the ratio R of Eq. (42). Since the kinematic distributions of the signal and normalisation channel are similar, the uncertainties corresponding to the reconstruction and selection efficiencies largely cancel in the ratio of branching fractions. A new value of the ratio R is computed for each source of systematic uncertainty, and its difference with the nominal value is taken as the associated systematic uncertainty. The overall systematic uncertainty is assigned by combining all contributions in quadrature.

The systematic uncertainty arising from fixing the shape parameters of the Hypatia functions used to parametrise the B^0 and J/ψ components is evaluated by repeating the fits and varying all shape parameters simultaneously. These shape parameters are varied according to normal distributions, taking into account the correlations between the parameters and with variances related to the size of the simulated samples.

To assign a systematic uncertainty arising from the model used to describe the detector resolution, the fits are repeated for each step replacing the Hypatia functions by Crystal Ball functions, whose parameters are obtained from simulation.

The systematic uncertainty associated to the parametrisation of the NR $B^0 \to p\bar{p}K^+\pi^-$ contribution is determined by replacing the exponential function with a linear function.

The systematic uncertainty associated to the determination of the efficiency involves contributions arising from the weighting procedure of the calibration samples used to determine the PID efficiencies. The granularity of the binning in the weighting procedure is halved and doubled.

The free shape parameters in the first stage UML fit lead to uncertainties that are not taken into account by the *sPlot* technique. In order to estimate this effect, these parameters are varied within their uncertainties and the signal weights are re-evaluated. The variations on the ratio R resulting from the second stage UML fit are found to be negligible.

The ratio R is determined to be

$$R = 0.357 \pm 0.015 \pm 0.008,$$

where the first uncertainty is statistical and the second systematic. The statistical uncertainty includes contributions from the per-candidate weights obtained using the *sPlot* technique. The value of R is used to compute the $B^0 \to \eta_c K^+\pi^-$branching fraction using Eq. (43) which gives

$$\mathcal{B}(B^0 \to \eta_c K^+\pi^-) = (5.73 \pm 0.24 \pm 0.13 \pm 0.66) \times 10^{-4},$$

Table 20: Relative systematic uncertainties on the ratio R of Eq. (42). The total systematic uncertainty is obtained from the quadratic sum of the individual sources.

Source	Systematic uncertainty (%)
Fixed shape parameters	0.8
Resolution model	0.3
NR $p\bar{p}$ model	1.7
Efficiency ratio	1.1
Total	2.2

where the first uncertainty is statistical, the second systematic, and the third is due to the limited knowledge of the external branching fractions.

4.6 Dalitz Plot analysis

As usually done in searches performed using the amplitude analysis technique, all the possible known states must be included in the model in order to check if the eventual structures appearing in the invariant mass distributions of interest are actually due to reflections of known states in other projections. The expected contributions in the $B^0 \to \eta_c K^+\pi^-$ decay channel are due to the $K^* \to K^+\pi^-$ intermediate states and they are introduced in Sec. 4.6.1.

I use the JFIT framework [150] to perform a joint amplitude fit keeping separated the Run 1 and Run 2 inputs, including the dataset, described in Sec. 4.6.2, the total efficiency map shown in Sec. 4.6.3 and the backgrounds parameterization, determined as described in Sec. 4.6.4.

The amplitude fit using a Default Model, only comprising the significant K^* states, is carried out as described in Sec. 4.6.5. The amplitude fit adding exotic resonances decaying to the $\eta_c\pi^-$ final state is described in Sec. 4.6.6. The significance of these exotic contributions is determined as described in Sec. 4.6.7.

4.6.1 K^* contributions

In the $B^0 \to \eta_c K^+\pi^-$ decay, the invariant mass range of the $K^+\pi^-$ system is up to $\sim 2.3\,\text{GeV}$. This means that all the neutral K^* resonances known to decay to $K^+\pi^-$ should in principle be included in the model. They are listed in Table 21. Their mass, width and quantum numbers, taken by [15], are reported as well. In addition, the $K_2^*(1980)$, listed by [15] and having the same quantum numbers of the $K_2^*(1430)$, hence to be potentially included into the model, has not been observed yet in the $K\pi$ final state.

4.6.2 Input data

The input data to the amplitude fit are the events contained in the $m(p\bar{p}K^+\pi^-)$ and $m(p\bar{p})$ ranges used for the 2D mass fit, that are the 5220-5340 MeV $m(p\bar{p}K^+\pi^-)$ and 2908-3058 MeV $m(p\bar{p})$ invariant mass ranges. The D^0 veto is applied within the amplitude

State	Mass [MeV]	Width [MeV]	J^P	$\mathcal{B}(K^{*0} \to K^+\pi^-)$
$K^*(800)$	682 ± 29	547 ± 24	0^+	$\sim 100\%$
$K^*(892)$	895.81 ± 0.19	47.4 ± 0.6	1^-	$\sim 100\%$
$K^*(1410)$	1414 ± 15	232 ± 21	1^-	$(6.6 \pm 1.3)\%$
$K_0^*(1430)$	1425 ± 50	270 ± 80	0^+	$(93 \pm 10)\%$
$K_2^*(1430)$	1432.4 ± 1.3	109 ± 5	2^+	$(49.9 \pm 1.2)\%$
$K^*(1680)$	1717 ± 27	322 ± 110	1^-	$(38.7 \pm 2.5)\%$
$K_3^*(1780)$	1776 ± 7	159 ± 21	3^-	$(18.8 \pm 1.0)\%$
$K_0^*(1950)$	1945 ± 22	201 ± 90	0^+	$(52 \pm 14)\%$
$K_2^*(1980)$	1974 ± 26	376 ± 70	2^+	not seen
$K_4^*(2045)$	2045 ± 9	198 ± 30	4^+	$(9.9 \pm 1.2)\%$
$B^0 \to \eta_c K^+\pi^-$ phase space limit				
$K_5^*(2380)$	2382 ± 24	178 ± 50	5^-	$(6.1 \pm 1.2)\%$

Table 21: Known neutral K^* resonances seen in the $K^+\pi^-$ final state plus the established $K_2^*(1980)$ resonance not seen yet in the $K^+\pi^-$ final state. The $K_5^*(2380)$ width is such that it could give contributions to the $B^0 \to \eta_c K^+\pi^-$ decay channel.

analysis. This is handled by LAURA^{++} setting the signal efficiency to zero inside a vetoed region. Since the effect of explicit vetoes in the phase space is separately accounted for, the D^0 veto has not been applied when constructing the efficiency histograms shown in Sec. 4.6.3. The signal and background yields, fixed in the amplitude fit, are determined from the 2D mass fit described in Sec. 68.

4.6.3 Resolution and efficiency evaluation

In order to perform the amplitude fit of the $B^0 \to \eta_c K^+\pi^-$ decay channel, the efficiency and resolution variations across the phase space of the decay must be taken into account. The efficiency variations are caused by detector effects, affecting the reconstruction of the candidates, and by the selection procedure. In the context of the amplitude analysis, the interest is not in the absolute value of the efficiency, but in the relative variations within the DP area.

The efficiency distribution is achieved in the form of a 2D histogram in the θ' vs m' distributions. The m' and θ' distributions, which expression is reported in Sec. 4.2.4, have been built starting from the simulated proton, antiproton, kaon and pion momenta resulting by the fit to their B^0 parent vertex with its mass constrained to the world average [15] value and its direction pointing to the primary vertex [151]. The efficiency due to detector effects and to the stripping, trigger and offline selections is referred as the geometric and kinematic efficiency. The efficiency due to the PID selection is determined using the data driven tools available at LHCb within the PIDCalib package [156] and is referred to as the PID efficiency.

The efficiency variations are parameterised, for each (m',θ') bin, as

$$\epsilon_{\rm bin} = \mathrm{N}_{\rm gen}\epsilon_{\rm genCuts}\epsilon_{\rm reco|genCuts}\epsilon_{\rm strip|reco}\epsilon_{\rm trig|strip}\epsilon_{\rm offline|trig}\epsilon_{\rm PID|offline} = \mathrm{N}_{\rm true}\frac{\mathrm{N}_{\rm reco}}{\mathrm{N}_{\rm true}}\frac{\mathrm{N}_{\rm strip}}{\mathrm{N}_{\rm reco}}\frac{\mathrm{N}_{\rm trig}}{\mathrm{N}_{\rm strip}}\frac{\mathrm{N}_{\rm offline}}{\mathrm{N}_{\rm trig}}\epsilon_{\rm PID}, \quad (45)$$

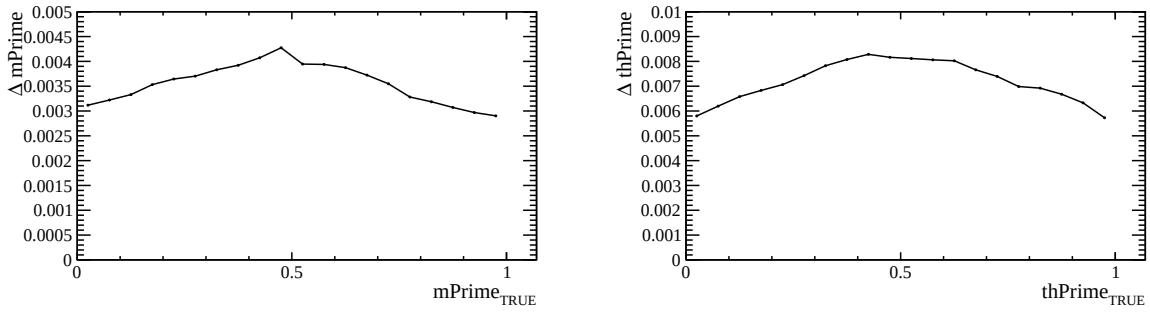

Figure 75: Resolution curves for Run 1 m' (left) and θ' (right) as a function of the corresponding true variable.

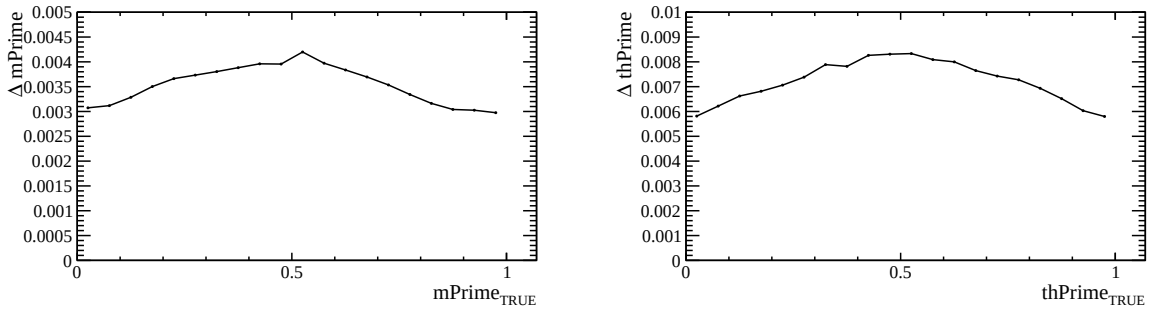

Figure 76: Resolution curves for Run 2 m' (left) and θ' (right) as a function of the corresponding true variable.

where N is the number of events in the (m',θ') bin after the corresponding selection requirements and ϵ_{PID} is the efficiency of the PID requirements coming from the PIDCalib procedure, in the same (m',θ') bin. Due to different selections and data taking conditions the efficiency maps for Run 1 and Run 2 data are possibly different. The breakdown of efficiency for both Run 1 and Run 2 data is shown in the following.

The experimental resolution for the variables θ' and m' is evaluated as the difference between the reconstructed and the generated values of the truth matched reconstructed candidates of the 11134002 simulated sample (the truth information concept has been introduced in Sec. 3.6). The behaviour of the resolution as a function of the generated value of each variable is shown in Figure 75 for Run 1 and in Figure 76 for Run 2. The resolution does not vary dramatically across the SDP. The resolution values in the θ' and m' ranges are smaller than the bin widths used for the efficiency maps. In addition, the $K^+\pi^-$ mass resolution is $\approx 5\,\text{MeV}$, which is much smaller than the $K^*(892)^0$ meson width $\Gamma_{K^*(892)^0} \approx 50\,\text{MeV}$, the narrowest contribution to the DP; therefore, the resolution has negligible effects and is not considered further.

The ratio between the reconstructed truth matched candidates and the generator level candidates is used to determine the reconstruction efficiency. The obtained 30x30 2D histograms, $\epsilon_{\text{reco|genCuts}}$, of θ' vs m' distributions are shown in Figure 77.

The stripping line cuts shown in 4.4.3 are applied, without the PID requirements, to the truth matched simulated sample, in order to obtain the stripping line selection efficiency. The resulting 2D histograms, $\epsilon_{\text{strip|reco}}$, are shown in Figure 78.

The trigger lines described in 4.4.2 are applied to the sample described in the previous

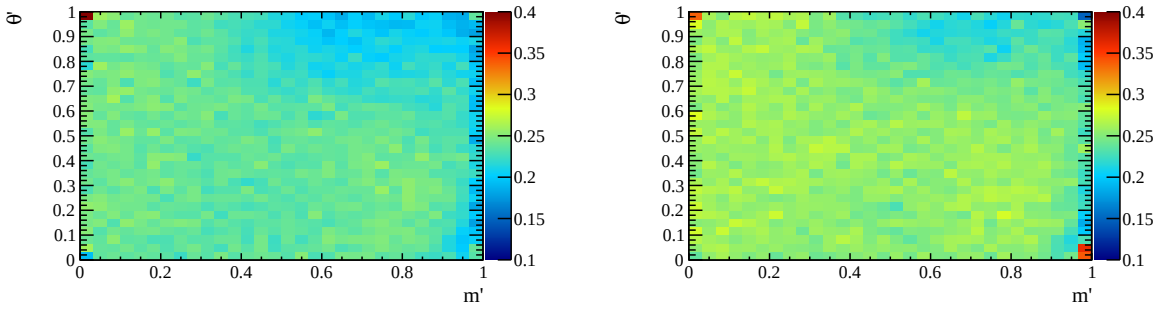

Figure 77: The reconstruction efficiency across the $B^0 \to \eta_c K^+\pi^-$ Run 1 (left) and Run 2 (right) SDP space.

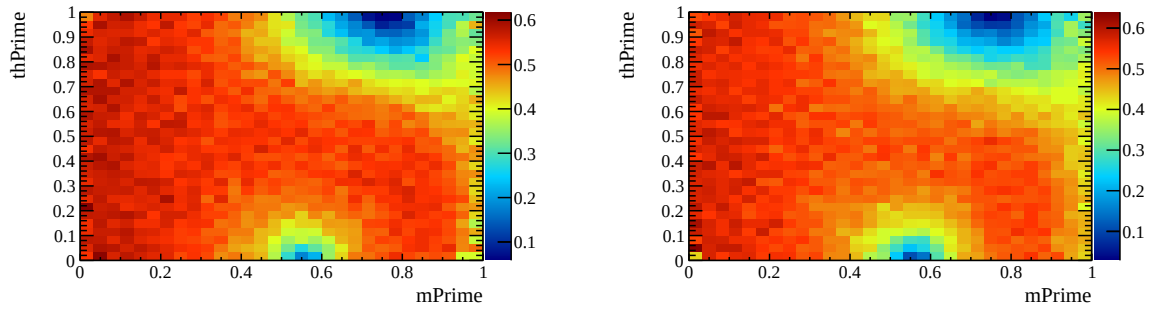

Figure 78: The stripping efficiency across the $B^0 \to \eta_c K^+\pi^-$ Run 1 (left) and Run 2 (right) SDP space.

section, in order to obtain the trigger selection efficiency. The resulting 2D histograms, $\epsilon_{\text{trig|strip}}$, are shown in Figure 79.

The preselection (proton and antiproton momenta and fiducial cut), the BDT cut and the Λ_c^- veto are applied to obtain the offline selection efficiency. The D^0 veto is not applied since it is handled by the amplitude fitter. The resulting 2D histograms, $\epsilon_{\text{offline|trig}}$, are shown in Figure 80.

The PIDCalib package allows to compute per-event weights applying PID requirements to unbiased calibration samples taken from data, divided in data taking years (2011, 2012, 2016) and magnet polarities (Up, Down). The RICH detectors response depends on the track momentum and pseudorapidity and on the event multiplicity. Therefore it is

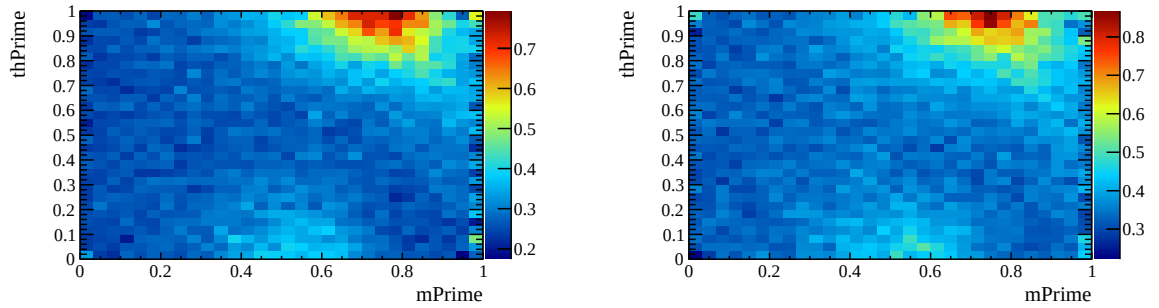

Figure 79: The trigger efficiency across the $B^0 \to \eta_c K^+\pi^-$ Run 1 (left) and Run 2 (right) SDP space.

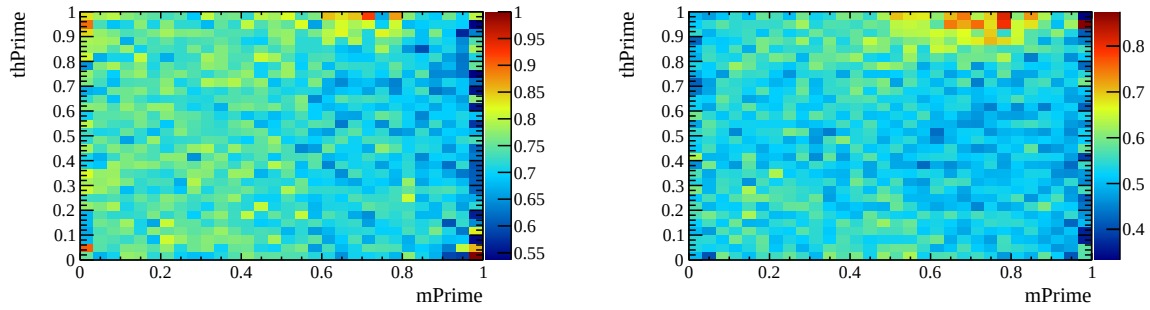

Figure 80: The offline selection efficiency across the $B^0 \to \eta_c K^+\pi^-$ Run 1 (left) and Run 2 (right) SDP space.

Particles	Momentum [GeV]	η
$p, \bar{p}$ from Λ^0	(0, 12.5, 24, 38, 50, 200)	(3.4, 3.8, 4.0, 4.3, 5.5)
$p, \bar{p}$ from Λ_c	(0, 14, 22, 45, 200)	(1.5, 2.6, 2.9, 3.1, 3.25, 3.4)
K, π	(0, 10, 18, 35, 50, 200)	(1.5, 3, 3.8, 5.5)

Table 22: Momentum and pseudorapidity η Run 1 binning schemas used in the PIDCalib package.

important to consider the kinematics distributions in the $B^0 \to \eta_c K^+\pi^-$ SDP simulated sample (reference sample) in order to find a suitable binning scheme to be used in the procedure. The chosen binning is a trade-off between the statistics of the calibration sample in a given bin and the kinematics of the reference sample. Due to the low size of the protons calibration samples collected in Run 1, I integrate over the event multiplicity in Run 1.

The following calibration samples are used for Run 1:

- $D^0 \to K^-\pi^+$ from $D^{*+} \to D^0\pi^+$ decays for kaons and pions ProbNN cuts efficiency;
- $\Lambda^0 \to p\pi^-$ and $\Lambda_c^- \to \bar{p}K^+\pi^-$ from $\Lambda_b^0 \to \Lambda_c^-\pi^+$ decays for protons and antiprotons ProbNN cuts efficiency. The Λ^0 sample has an high statistics but has a low sample size for low pseudorapidity protons. On the other side the Λ_c^- sample has a limited size but has a better coverage of the Run 1 signal.

The chosen binning schemas for Run 1 are reported in Table 22.

Starting from the Run 2 data taking, the Turbo stream is used to build the calibration samples. Some calibration sample types are added to the ones available during Run 1. For example, high p_T and very high p_T samples have been added to the Λ^0 sample, allowing a better coverage of the (p, η) space. Thanks to the larger statistics available in the Run 2 calibration samples I also bin in the nSPDHits variable, defined as the number of hits in the SPD detector introduced in Sec. 3.2.7, giving a measure of the event multiplicity. The nSPDHits distribution is not well reproduced by the simulation. For this reason a reweighting of the simulated events is required in order to reproduce the nSPDHits distribution obtained applying the signal weights corresponding to the

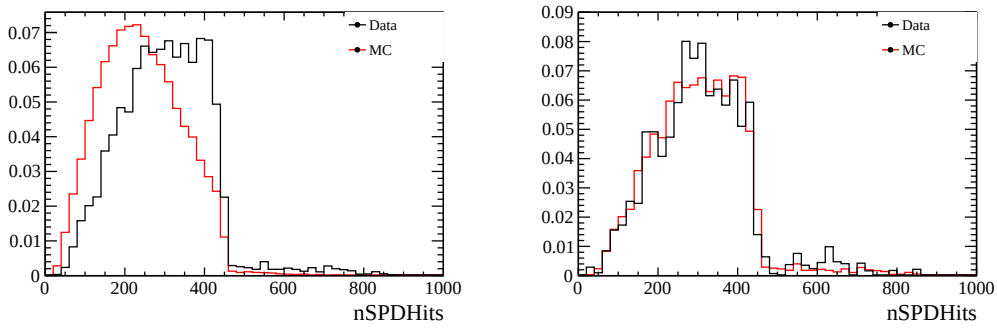

Figure 81: Left: comparison between the simulated and the $B^0 \to J/\psi K^+\pi^-$ data component sWeighted nSPDHits distribution. Right: comparison between the simulated and the $B^0 \to \eta_c K^+\pi^-$ data component sWeighted nSPDHits distribution after the reweighting.

Particles	Momentum [GeV]	η	nSPDHits
$p, \bar{p}$	(11, 15, 20, 30, 50, 200)	(2.0, 2.5, 2.5, 3.0, 3.5, 4.0, 4.9)	(0, 200, 300, 400, 1200)
K, π	(0, 20, 40, 60, 200)	(2.0, 2.5, 3.0, 3.5, 4.0, 4.9)	(0, 200, 300, 400, 1200)

Table 23: Momentum, pseudorapidity (η) and event multiplicity (nSPDHits) Run 2 binning schema used in the PIDCalib package.

$B^0 \to J/\psi K^+\pi^-$ component from the 2D mass fit (in order to have more statistics to perform the reweighting). The nSPDHits distribution before and after the simulated reweighting is shown in Figure 81.

For the Run 2 efficiency map, the default calibration samples and the binning schemas reported in Table 23 are used.

For each calibration sample, the tools provided by the PIDCalib package are used to compute the efficiency of a PID cut in a bin of momentum and pseudorapidity (and nSPDHits in Run 2). In this way the PID cut efficiency for a value of momentum and pseudorapidity of the considered track type is univocally (assuming that the PID variable responses do not change inside each bin) determined, as the ratio between the number of events in that bin before the cut over the number of events in the same bin after the PID cut.

A reference simulated sample for each year, magnet polarity (and pseudorapidity region for Run 1) is built. All the geometric and kinematic cuts are applied to them. The efficiency is assigned to each bin of to the reference subsample. The PID efficiency (relative to the kinematic one) of the ProbNN cuts is $\sim 70\%$ for each subsample in Run 1 and $\sim 85\%$ for each subsample in Run 2. The interesting quantity is in the per-event efficiency w_{PID}. It is used to build the 2D PID efficiency maps over the $B^0 \to \eta_c K^+\pi^-$ SDP space, shown in Figure 82. The binning is changed from 30x30 to 10x10 in order to reduce the statistical fluctuations from bin to bin, allowing to obtain a better description of the efficiency since a smoothing procedure is used for the total efficiency map.

The 2D histogram parameterising the total efficiency variations in the (m',θ') space is shown in Figure 83. Each histogram is normalised to its total number of entries. These histograms, after a smoothing procedure through a cubic spline interpolation, are the

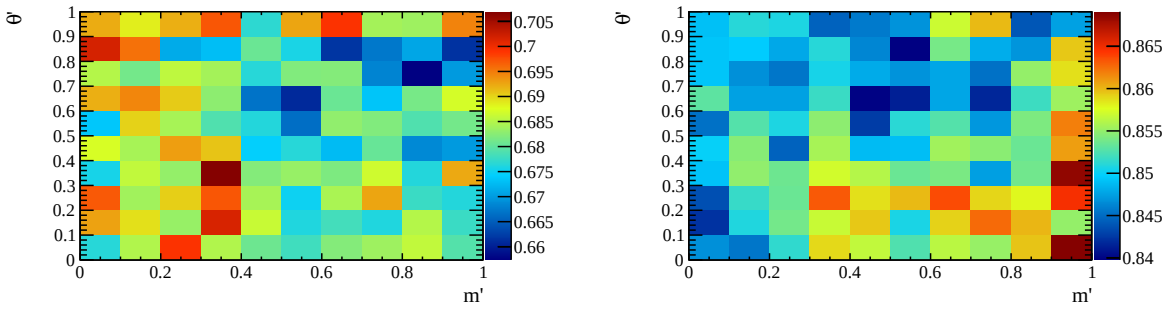

Figure 82: The PID efficiency over the $B^0 \to \eta_c K^+\pi^-$ Run 1 (left) and Run 2 (right) SDP space.

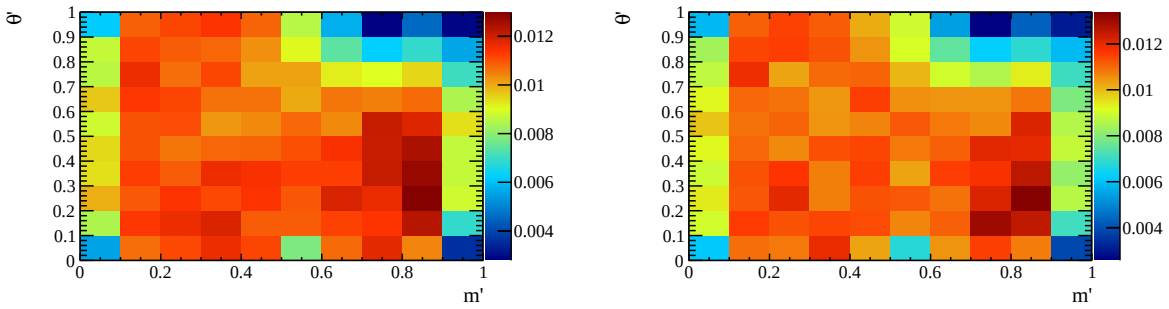

Figure 83: The total efficiency variations over the $B^0 \to \eta_c K^+\pi^-$ Run 1 (left) and Run 2 (right) SDP space.

efficiency models given as input to LAURA^{++} to take into account the efficiency variations across the phase space during the amplitude fits to the Run 1 and Run 2 data.

4.6.4 Background parameterisation

The 2D mass fit to the Run 1 and Run 2 data samples added together is performed in order to obtain the combinatorial and non-resonant background PDFs. The *sPlot* procedure is applied to determine the weights corresponding to the combinatorial background and non-resonant background components to build the corresponding background histograms, parameterised using the SDP variables. For each type of background histogram, the corresponding Run 1 and Run 2 map is built, scaling the number of events using the yields resulting from the 2D mass fit. The background histograms are shown in Fig. 84. Both the Λ_c^- and the D^0 vetoes are applied when the background histograms are made as suggested in [146]. These histograms are interpolated with a cubic spline before the amplitude fit.

4.6.5 Amplitude fit using the Baseline Model

The Baseline Model, *i.e.* the model including K^{*0} contributions without any exotic component, is built including one by one the well established K^{*0} states until no significant improvements in the likelihood are found. The K^{*0} states used in the Baseline Model are the $K^*(892)^0$, the $K^*(1410)^0$, the $K_0^*(1430)^0$, the $K_2^*(1430)^0$, the $K^*(1680)^0$ and the $K_0^*(1950)^0$. The non-resonant $K^+\pi^-$ S-wave is considered as well. The well established

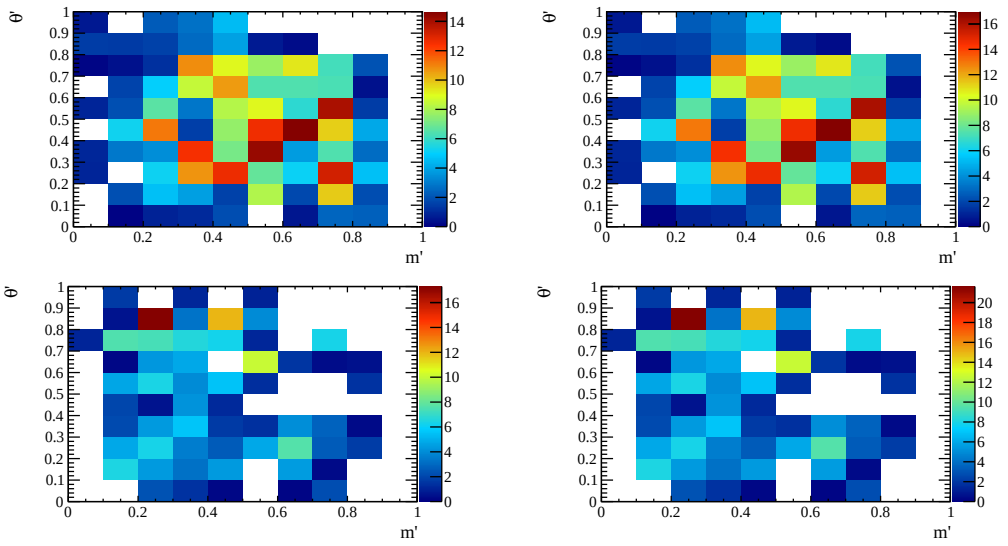

Figure 84: Background histograms for top left: Run 1 combinatorial background; bottom left: Run 1 nonresonant background; top right: Run 2 combinatorial background; bottom right: Run 2 nonresonant background.

$K_3^*(1780)^0$ and the $K_4^*(2045)^0$ are not significant and they are not included in the Baseline Model. The variation in the negative log-likelihood (NLL) Δ(NLL) is -0.5 when adding the $K_3^*(1780)^0$ and -0.2 when adding the $K_4^*(2045)^0$.

The $K^+\pi^-$ S-wave is parameterised using the LASS PDF. The $K_0^*(1430)^0$ mass and width are Gaussian constrained to the world average value [15], while the scattering length and the effective range of the non-resonant part are left floating in the fit. All the other resonances are parameterised using a RBW. Mass and width of each contribution are fixed to the world average value [15]. The $K^*(892)^0$ is the reference amplitude and the real and imaginary part of its isobar coefficients are fixed to 1.00 and 0.00, respectively. Therefore the values of the isobar coefficients of other amplitudes are relative to the $K^*(892)^0$ ones.

The amplitude fit is repeated 100 times randomising the values of the isobar coefficients in order to check for local minima, common in DP fits. The absolute minimum is found at the negative log-likelihood (NLL) value of NLL $= -12521.5$. Local minima are found at ΔNLL $= +37.5$ and ΔNLL $= +34.2$, far enough from the absolute minimum.

The resulting isobar coefficients using the Baseline Model are shown in Table 24. The half-matrix of the resulting fit fractions using the Baseline Model is shown in Table 25. The resulting LASS parameters are shown in Tab. 26.

The comparison between the DP projections from data and from toy events, generated with Laura^{++} according to the amplitude fit model, the efficiency map and taking into account the background pdfs, are used to test the quality of the amplitude fits. 100 toy experiments are generated for both Run 1 and Run 2 data, each pseudo-experiment having the same number of signal and background events in the corresponding data sample. In the data-fit model comparison of the DP projections, Run 1 and Run 2 data are added together. The DP projections for the amplitude fit using the Baseline Model are shown in Fig. 85.

The background subtracted data distributions, using the background DP projections generated by Laura^{++}, are compared with the fit signal components. The comparison of

Amplitude	Real part	Imaginary part
$K^*(892)$	1.00	0.00
$K^*(1410)$	0.22 ± 0.06	0.04 ± 0.08
LASS	-0.80 ± 0.04	0.05 ± 0.09
$K_2^*(1430)$	0.20 ± 0.06	-0.21 ± 0.05
$K^*(1680)$	-0.21 ± 0.06	-0.13 ± 0.07
$K_0^*(1950)$	0.14 ± 0.12	-0.23 ± 0.08

Table 24: Isobar coefficients resulting from the amplitude fit using the Baseline Model.

	$K^*(892)$	$K^*(1410)$	LASS	$K_2^*(1430)$	$K^*(1680)$	$K_0^*(1950)$
$K^*(892)$	51.3 ± 1.9	-0.1 ± 1.1	0.0	0.0	-3.3 ± 1.7	0.0
$K^*(1410)$		2.5 ± 1.2	0.0	0.0	-3.3 ± 2.1	0.0
LASS			32.8 ± 3.0	0.0	0.0	6.2 ± 1.5
$K_2^*(1430)$				4.1 ± 1.3	0.0	0.0
$K^*(1680)$					3.3 ± 1.5	0.0
$K_0^*(1950)$						3.8 ± 0.9

Table 25: Half-matrix of the fit fractions [%] resulting from the fit using the Baseline Model.

the background subtracted DP projections are shown in Figures 86 for the amplitude fit results using the Baseline Model.

Using an adaptive binning algorithm, I compare data and toys distributions in bins of the SDP phase space to determine the value of the χ^2/ndf, where ndf $= \mathrm{n_{bins}} - \mathrm{n_{par}} - 1$ ($\mathrm{n_{par}}$ is the number of free parameters in the fit). The binning is computed requiring at least ~ 20 events in each bin. The pulls squared is used as the χ^2 statistic. A pull in a given bin is calculated as

$$\frac{N^{\mathrm{data}} - N^{\mathrm{toys}}}{\sigma}, \tag{46}$$

where σ takes into account the statistical error in each bin of the data distribution.

The pull distribution for the amplitude fit results using the Baseline Model is shown

Parameter	value	default values
$m_{K_0^*(1430)}$	$(1434 \pm 21)\,\mathrm{MeV}$	$(1425 \pm 50)\,\mathrm{MeV}$
$\Gamma_{K_0^*(1430)}$	$(268 \pm 40)\,\mathrm{MeV}$	$(270 \pm 80)\,\mathrm{MeV}$
a	$(4.1 \pm 1.1)\,\mathrm{GeV}^{-1}$	$2.07\,\mathrm{GeV}^{-1}$
r	$(5.0 \pm 1.6)\,\mathrm{GeV}^{-1}$	$3.32\,\mathrm{GeV}^{-1}$

Table 26: Parameters of the LASS pdf resulting from the fit using the Baseline Model shown in the second column. In the third column are shown the values for the $m_{K_0^*(1430)}$ and $\Gamma_{K_0^*(1430)}$ from [15] and the values quoted by the LASS experiment for the a and r parameters

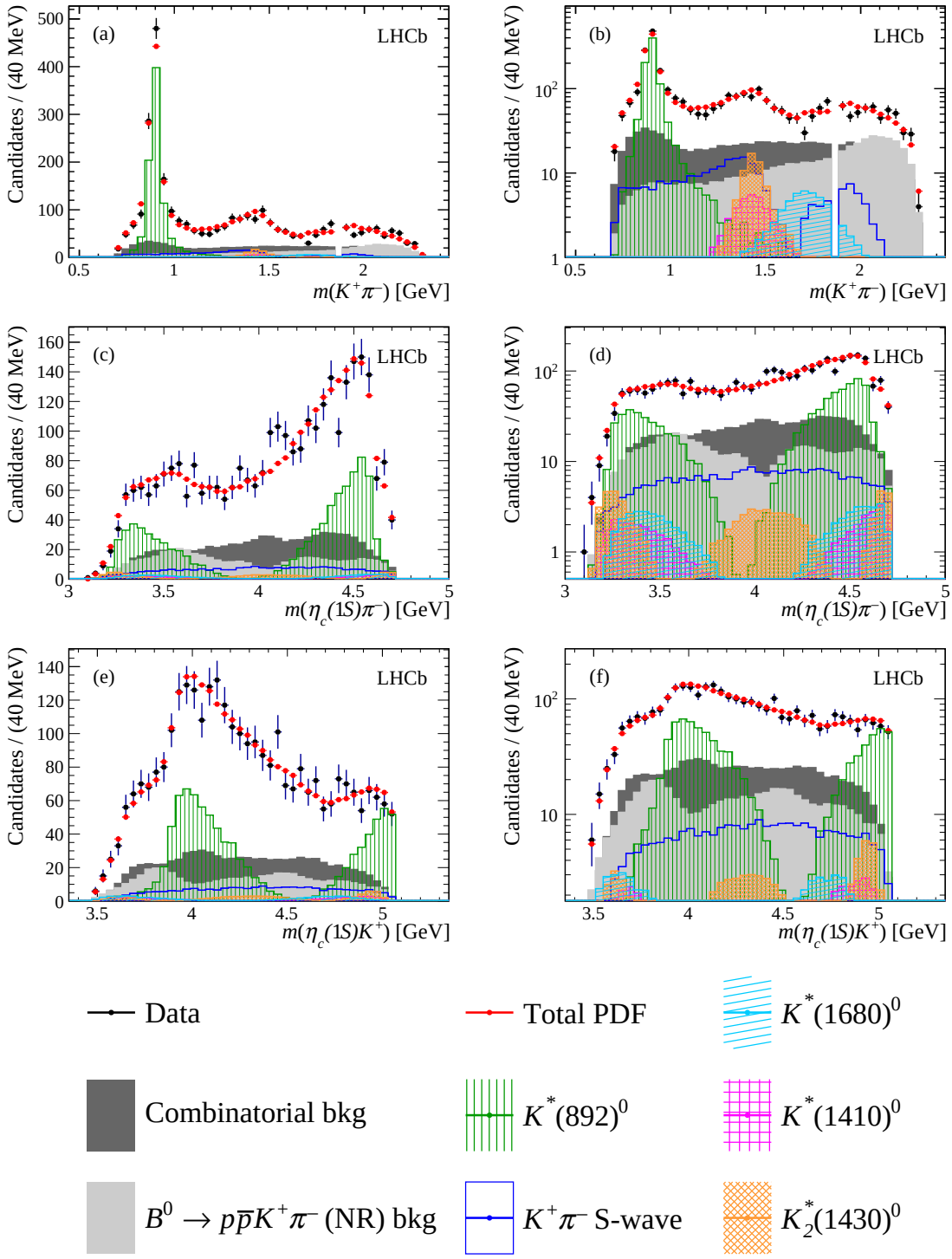

Figure 85: Projections of the data and amplitude fit using the baseline model onto (a) $m(K^+\pi^-)$, (c) $m(\eta_c\pi^-)$ and (e) $m(\eta_c K^+)$, with the same projections shown in (b), (d) and (f) with a logarithmic vertical-axis scale. The veto of $B^0 \to p\bar{p}\overline{D}^0$ decays is visible in plot (b). The $K^+\pi^-$ S-wave component comprises the LASS and $K_0^*(1950)^0$ meson contributions. The components are described in the legend at the bottom.

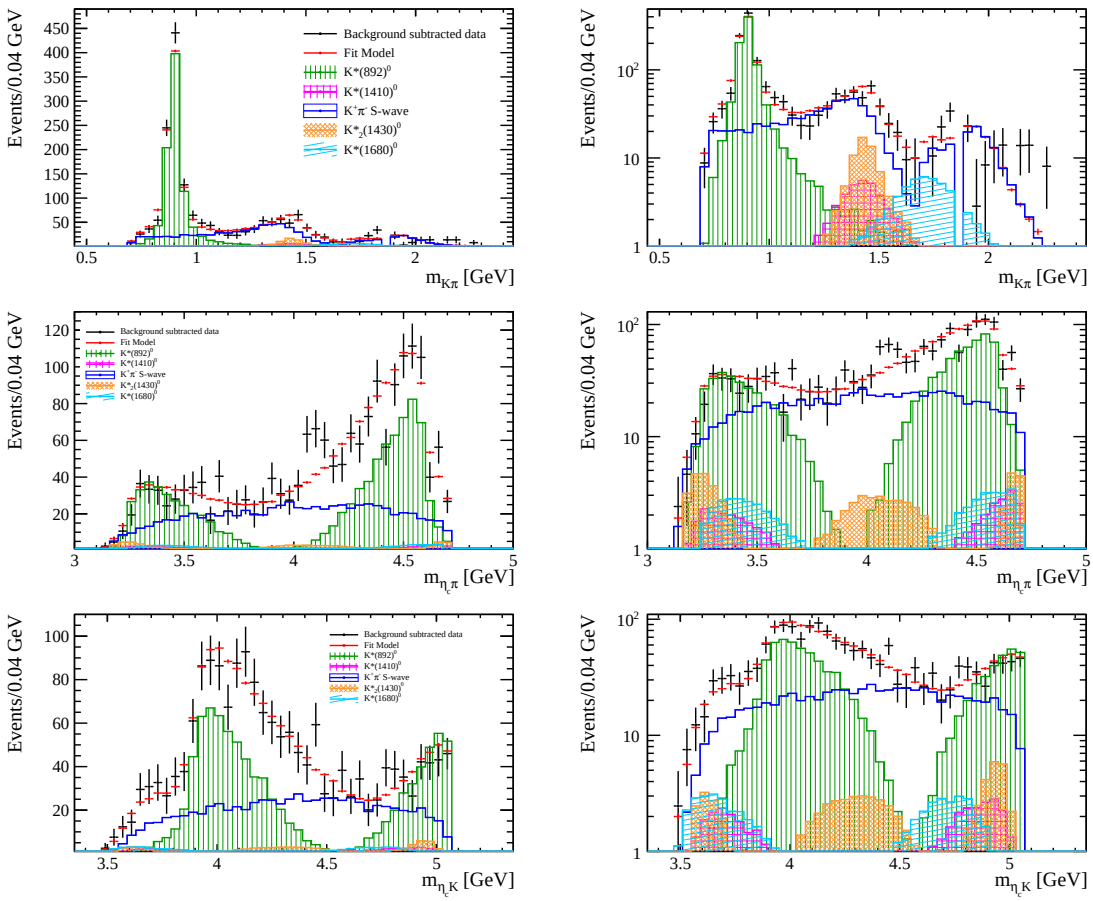

Figure 86: Projections of the background-subtracted data and amplitude fit using the baseline model onto (a) $m(K^+\pi^-)$, (c) $m(\eta_c\pi^-)$ and (e) $m(\eta_c K^+)$, with the same projections shown in (b), (d) and (f) with a logarithmic vertical-axis scale. The veto of $B^0 \to p\overline{p}\overline{D}^0$ decays is visible in plot (b). The $K^+\pi^-$ S-wave component comprises the LASS and $K_0^*(1950)^0$ meson contributions. The components are described in the legend at the bottom.

in Figure 87 and the χ^2/ndof computed as the square of the pulls is 194.6/129 = 1.51.

4.6.6 Addition of exotic amplitudes

A $Z_c^- \to \eta_c\pi^-$ exotic resonance is added to the Baseline Model leaving floating its mass and width. The $J^P = 0^+$ and $J^P = 1^-$ quantum numbers hypotheses for the eventual Z_c^- resonance are tested as described in the following. The same amplitude fit and fit quality test procedures described in Sec. 4.6.5 are used.

For the $J^P = 0^+$ hypothesis the absolute minimum is found at NLL = −12532.9, hence at ΔNLL = −11.4 with respect to the Baseline Model without the Z_c^- component. Local minima are found at ΔNLL = +25.1 and ΔNLL = +31.4 with respect to the new absolute minimum.

The resulting isobar coefficients are shown in Table 27. The half-matrix of the interference fit fractions is shown in Table 28. The resulting LASS parameters are shown in Table 30.

The DP projections for the amplitude fit adding a $J^P = 0^+$ exotic component to

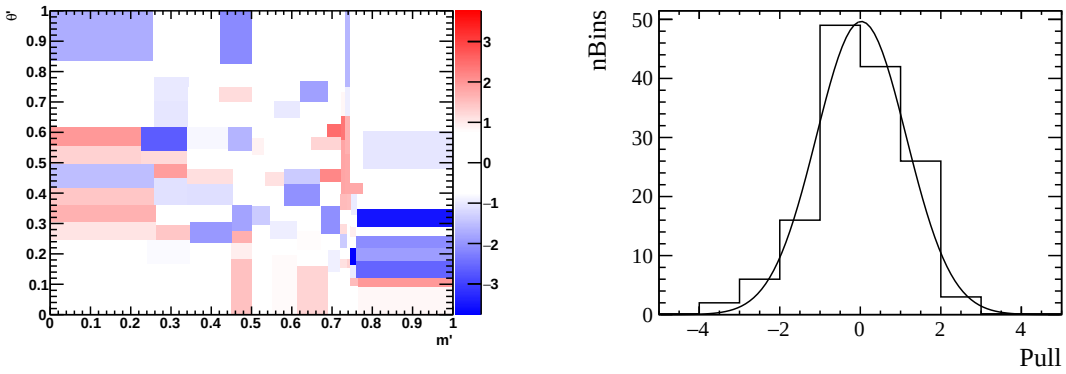

Figure 87: Left: 2D pull distribution for the Baseline Model. Right: 1D pull distribution computed from the bin contents of the 2D pull distribution. This distribution is fitted with a Gaussian obtaining $\mu = 0.02 \pm 0.10$ and $\sigma = 1.11 \pm 0.08$.

Amplitude	Real part	Imaginary part
$K^*(892)$	1.00	0.00
$K^*(1410)$	0.26 ± 0.09	0.05 ± 0.09
LASS	-0.68 ± 0.06	-0.03 ± 0.11
$K_2^*(1430)$	0.09 ± 0.06	-0.20 ± 0.05
$K^*(1680)$	-0.21 ± 0.09	-0.25 ± 0.13
$K_0^*(1950)$	-0.03 ± 0.17	-0.25 ± 0.06
Z_c^-	-0.25 ± 0.06	0.05 ± 0.13

Table 27: Isobar coefficients resulting from the fit adding the $J^P = 0^+$ $Z_c^- \to \eta_c\pi^-$ exotic component to the Baseline Model.

the Baseline Model are shown in Fig. 88. The corresponding background-subtracted distributions are shown in Fig. 89.

The pull distribution for the amplitude fit results adding a $J^P = 0^+$ exotic component to the the Baseline Model is shown in Figure 90 and the χ^2/ndof computed as the square of the pulls is $176.2/125 = 1.41$.

	$K^*(892)$	$K^*(1410)$	LASS	$K_2^*(1430)$	$K^*(1680)$	$K_0^*(1950)$	Z_c^-
$K^*(892)$	52.3 ± 2.0	-0.10 ± 0.15	0.0	0.0	-2.6 ± 2.1	0.0	3.4 ± 2.0
$K^*(1410)$		3.5 ± 1.9	0.0	0.0	-5.7 ± 2.9	0.0	0.8 ± 0.9
LASS			24.6 ± 4.0	0.0	0.0	5.8 ± 1.4	3.7 ± 1.3
$K_2^*(1430)$				2.6 ± 1.3	0.0	0.0	0.6 ± 0.5
$K^*(1680)$					5.4 ± 2.2	0.0	-1.7 ± 1.2
$K_0^*(1950)$						3.3 ± 1.0	0.6 ± 0.5
Z_c^-							3.5 ± 1.6

Table 28: Half-matrix of the fit fractions [%] resulting from the fit adding the $J^P = 0^+$ $Z_c^- \to \eta_c\pi^-$ exotic component to the Baseline Model.

Parameter	value
m_Z	$(4059 \pm 30)\,\text{MeV}$
Γ_Z	$(163 \pm 67)\,\text{MeV}$

Table 29: Mass and width of the Z_c^- resonance candidate resulting from the fit adding the $J^P = 0^+$ $Z_c^- \to \eta_c\pi^-$ exotic component to the Baseline Model.

Parameter	value	default values
$m_{K_0^*(1430)}$	$(1426 \pm 21)\,\text{MeV}$	$(1425 \pm 50)\,\text{MeV}$
$\Gamma_{K_0^*(1430)}$	$(249 \pm 38)\,\text{MeV}$	$(270 \pm 80)\,\text{MeV}$
a	$(4.1 \pm 1.4)\,\text{GeV}^{-1}$	$2.07\,\text{GeV}^{-1}$
r	$(7.2 \pm 3.4)\,\text{GeV}^{-1}$	$3.32\,\text{GeV}^{-1}$

Table 30: Parameters of the LASS pdf resulting from the fit adding the $J^P = 0^+$ $Z_c^- \to \eta_c\pi^-$ exotic component to the Baseline Model. In the third column are shown the world average values [15] for the $m_{K_0^*(1430)}$ and $\Gamma_{K_0^*(1430)}$ and the values quoted by the LASS experiment for the a and r parameters

For the $J^P = 1^-$ hypothesis the absolute minimum is found at NLL $= -12542.2$, hence at $\Delta\text{NLL} = -20.7$ with respect to the Baseline Model without the Z_c^- component. Local minima are found at $\Delta\text{NLL} = +11$ and $\Delta\text{NLL} = +52.1$ with respect to the new absolute minimum.

The resulting isobar coefficients are shown in Table 31. The half-matrix of the interference fit fractions is shown in Table 32. The resulting LASS parameters are shown in Table 34.

The DP projections for the amplitude fit adding a $J^P = 1^-$ exotic component to the Baseline Model are shown in Fig. 91 and the corresponding background-subtracted distributions are shown in Fig. 92.

The pull distribution for the amplitude fit results adding a $J^P = 1^-$ exotic component

Amplitude	Real part	Imaginary part
$K^*(892)$	1.00	0.00
$K^*(1410)$	0.17 ± 0.07	0.11 ± 0.08
LASS	-0.77 ± 0.05	-0.00 ± 0.09
$K_2^*(1430)$	0.16 ± 0.06	-0.23 ± 0.05
$K^*(1680)$	-0.11 ± 0.08	-0.18 ± 0.06
$K_0^*(1950)$	0.27 ± 0.04	0.04 ± 0.14
Z_c^-	-0.25 ± 0.04	-0.01 ± 0.08

Table 31: Isobar coefficients resulting from the fit adding the $J^P = 1^-$ $Z_c^- \to \eta_c\pi^-$ exotic component to the Baseline Model.

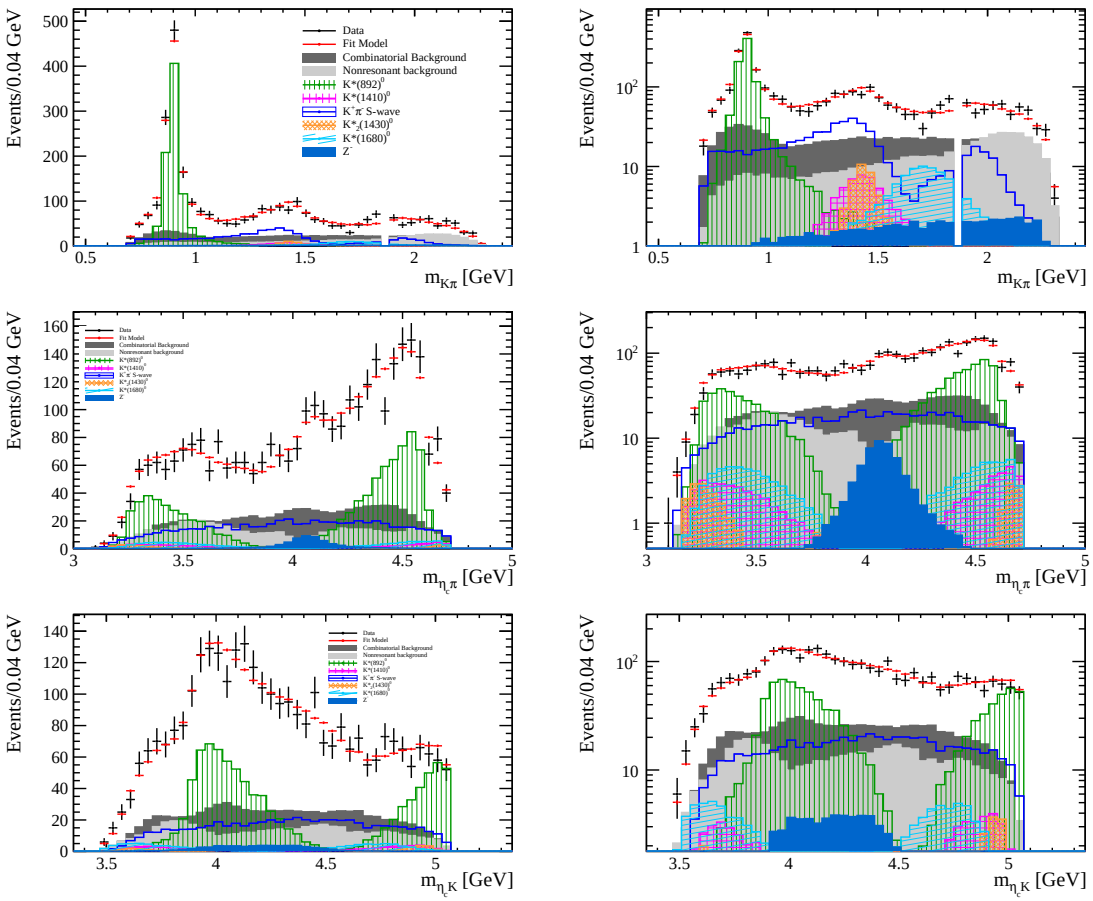

Figure 88: Projections of the data and amplitude fit using the baseline model plus a $J^P = 0^+$ component onto (a) $m(K^+\pi^-)$, (c) $m(\eta_c\pi^-)$ and (e) $m(\eta_c K^+)$, with the same projections shown in (b), (d) and (f) with a logarithmic vertical-axis scale. The veto of $B^0 \to p\overline{p}\overline{D}^0$ decays is visible in plot (b). The $K^+\pi^-$ S-wave component comprises the LASS and $K_0^*(1950)^0$ meson contributions. The components are described in the legend at the bottom.

to the the Baseline Model is shown in Figure 93 and the χ^2/ndof computed as the square of the pulls is $164.1/125 = 1.31$.

	$K^*(892)$	$K^*(1410)$	LASS	$K_2^*(1430)$	$K^*(1680)$	$K_0^*(1950)$	Z_c^-
$K^*(892)$	51.4 ± 2.0	1.7 ± 1.1	0.0	0.0	-2.1 ± 1.9	0.0	1.4 ± 0.83
$K^*(1410)$		2.1 ± 1.2	0.0	0.0	-2.5 ± 1.6	0.0	-0.4 ± 0.5
LASS			30.2 ± 4.2	0.0	0.0	-0.6 ± 1.6	4.2 ± 1.5
$K_2^*(1430)$				4.1 ± 1.9	0.0	0.0	0.7 ± 0.4
$K^*(1680)$					2.2 ± 0.9	0.0	0.7 ± 0.9
$K_0^*(1950)$						3.8 ± 1.1	0.6 ± 0.5
Z_c^-							3.3 ± 1.3

Table 32: Half-matrix of the fit fractions [%] resulting from the fit adding the $J^P = 1^-$ $Z_c^- \to \eta_c\pi^-$ exotic component to the Baseline Model.

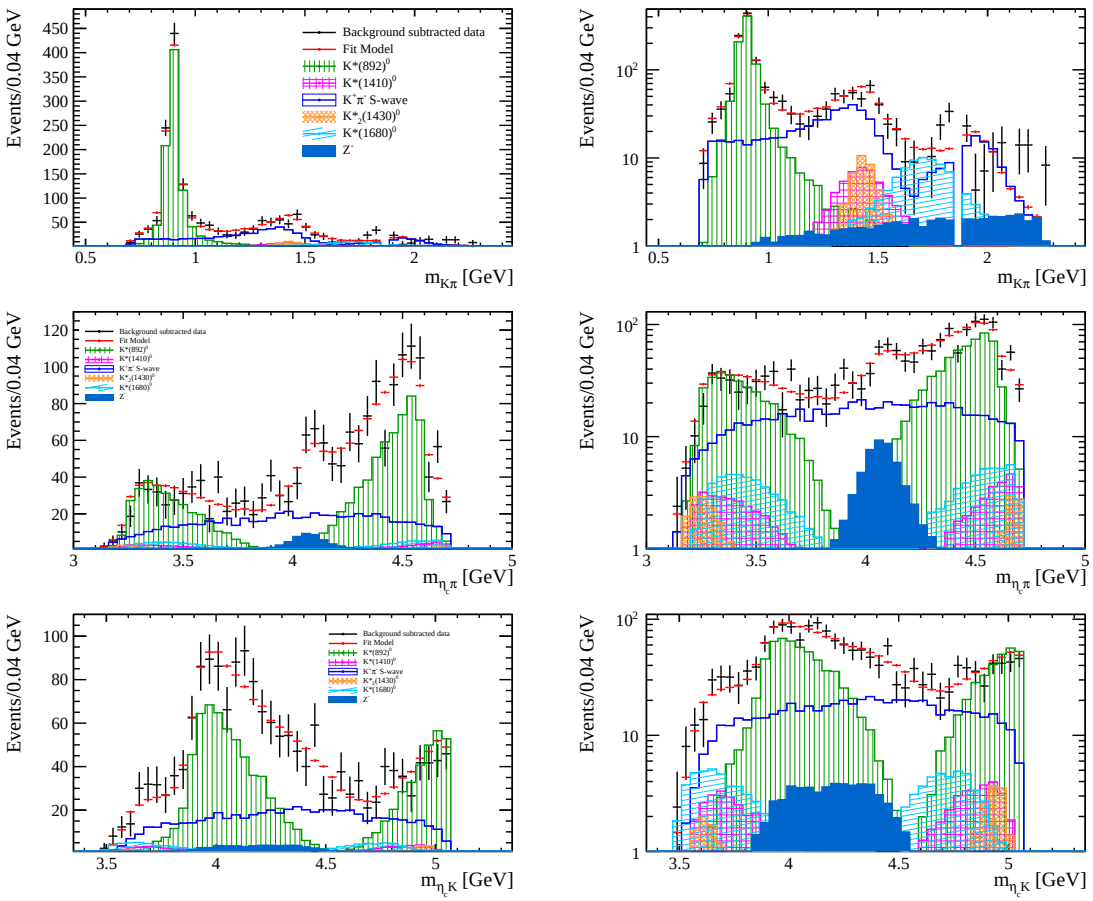

Figure 89: Projections of the background-subtracted data and amplitude fit using the baseline model plus a $J^P = 0^+$ component onto (a) $m(K^+\pi^-)$, (c) $m(\eta_c\pi^-)$ and (e) $m(\eta_c K^+)$, with the same projections shown in (b), (d) and (f) with a logarithmic vertical-axis scale. The veto of $B^0 \to p\bar{p}\bar{D}^0$ decays is visible in plot (b). The $K^+\pi^-$ S-wave component comprises the LASS and $K_0^*(1950)^0$ meson contributions. The components are described in the legend at the bottom.

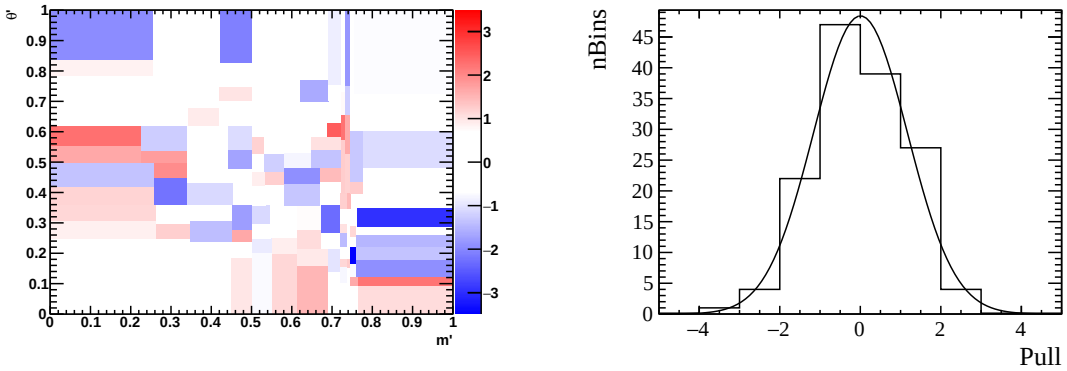

Figure 90: Left: 2D pull distribution for the Baseline Model plus a $J^P = 0^+$ component. Right: 1D pull distribution computed from the bin contents of the 2D pull distribution. This distribution is fitted with a Gaussian obtaining $\mu = 0.00 \pm 0.10$ and $\sigma = 1.12 \pm 0.07$.

Parameter	value
m_Z	$(4096 \pm 20)\,\text{MeV}$
Γ_Z	$(152 \pm 58)\,\text{MeV}$

Table 33: Mass and width of the Z_c^- resonance candidate resulting from the fit adding the $J^P = 1^-$ $Z_c^- \to \eta_c\pi^-$ exotic component to the Baseline Model.

Parameter	value	default values
$m_{K_0^*(1430)}$	$(1427 \pm 21)\,\text{MeV}$	$(1425 \pm 50)\,\text{MeV}$
$\Gamma_{K_0^*(1430)}$	$(256 \pm 33)\,\text{MeV}$	$(270 \pm 80)\,\text{MeV}$
a	$(3.1 \pm 1.0)\,\text{GeV}^{-1}$	$2.07\,\text{GeV}^{-1}$
r	$(7.0 \pm 2.4)\,\text{GeV}^{-1}$	$3.32\,\text{GeV}^{-1}$

Table 34: Parameters of the LASS pdf resulting from the fit adding the $J^P = 1^-$ $Z_c^- \to \eta_c\pi^-$ exotic component to the Baseline Model. In the third column are shown the world average values [15] for the $m_{K_0^*(1430)}$ and $\Gamma_{K_0^*(1430)}$ and the values quoted by the LASS experiment for the a and r parameters

The unnormalised Legendre moments of the $K^+\pi^-$, $\eta_c\pi^-$ and $\eta_c K^+$ systems are extracted from background subtracted data (using the corresponding background DP projection generated by LAURA^{++}) and compared to the moments computed using the total signal component resulting from the amplitude fit. Moments are computed in 20 MeV wide bins for the $K^+\pi^-$ system and in 40 MeV wide bins for the $\eta_c\pi^-$ and $\eta_c K^+$ systems. For each invariant mass bin, the expression for the unnormalised Legendre moment of order J is given by

$$(< P_J^U >)_k = \sum_{i=1}^{(N_e)_k} P_J(\cos(\theta)_i), \tag{47}$$

where θ is θ_{K^*} (the angle between the K^+ and the η_c in the $K^+\pi^-$ rest frame), θ_Z (the angle between the K^+ and the π^- in the $\eta_c\pi^-$ rest frame) or $\theta_{\eta_c K}$ (the angle between the π^- and the K^+ in the $\eta_c K^+$ rest frame). For instance the expression for $\cos\theta_{K^*}$ has been reported in eq. 23. The sum runs over the corresponding number of events in the invariant mass bin k.

The comparison of the first four unnormalised Legendre moments between data and toys generated according to the Baseline Model plus a $J^P = 1^-$ exotic component is reported in Figs. 94, 95 and 96 for the $K^+\pi^-$, $\eta_c\pi^-$ and $\eta_c K^+$ systems, respectively.

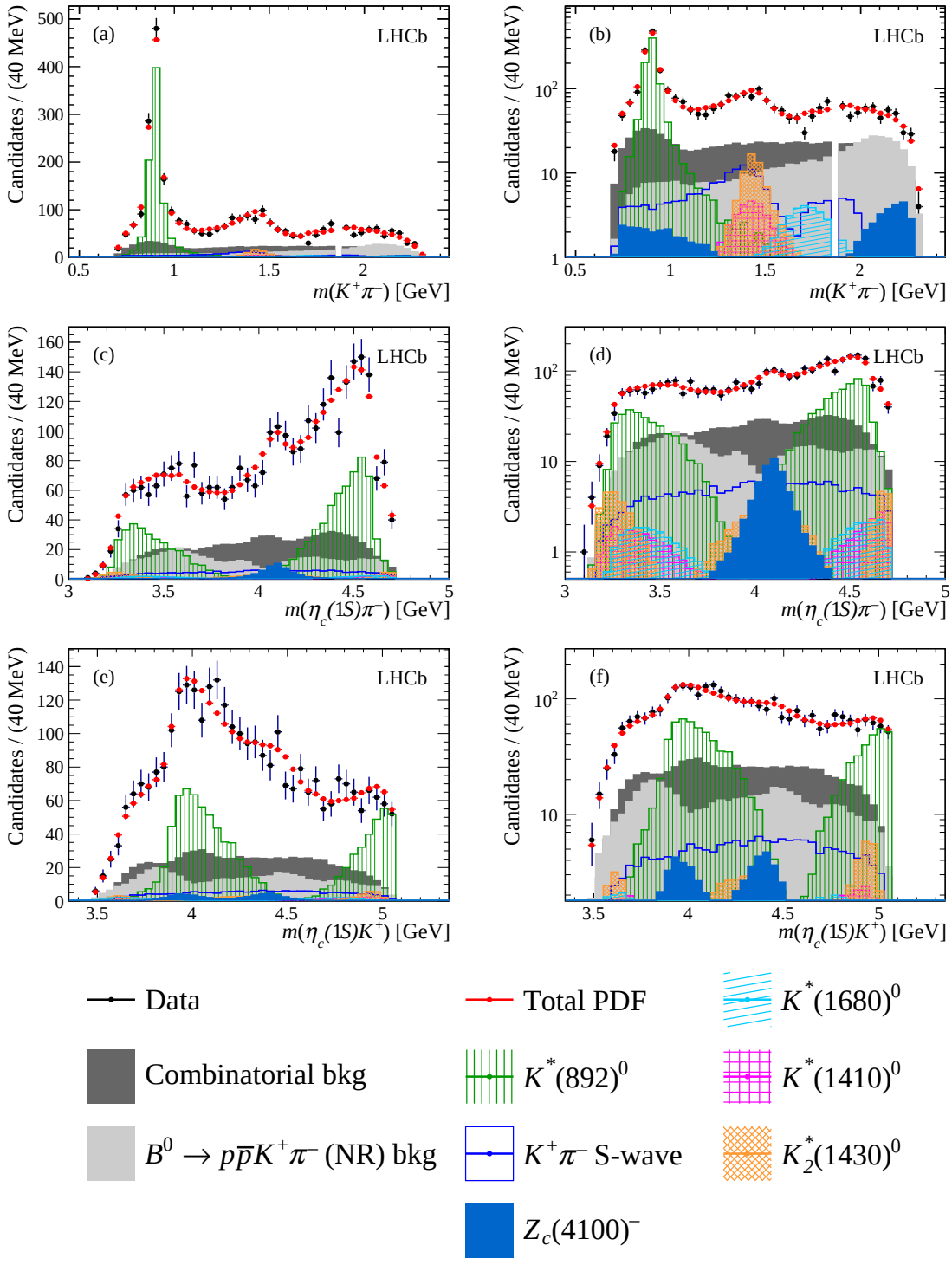

Figure 91: Projections of the data and amplitude fit using the baseline model plus a $J^P = 1^-$ exotic component onto (a) $m(K^+\pi^-)$, (c) $m(\eta_c\pi^-)$ and (e) $m(\eta_c K^+)$, with the same projections shown in (b), (d) and (f) with a logarithmic vertical-axis scale. The veto of $B^0 \to p\bar{p}\overline{D}^0$ decays is visible in plot (b). The $K^+\pi^-$ S-wave component comprises the LASS and $K_0^*(1950)^0$ meson contributions. The components are described in the legend at the bottom.

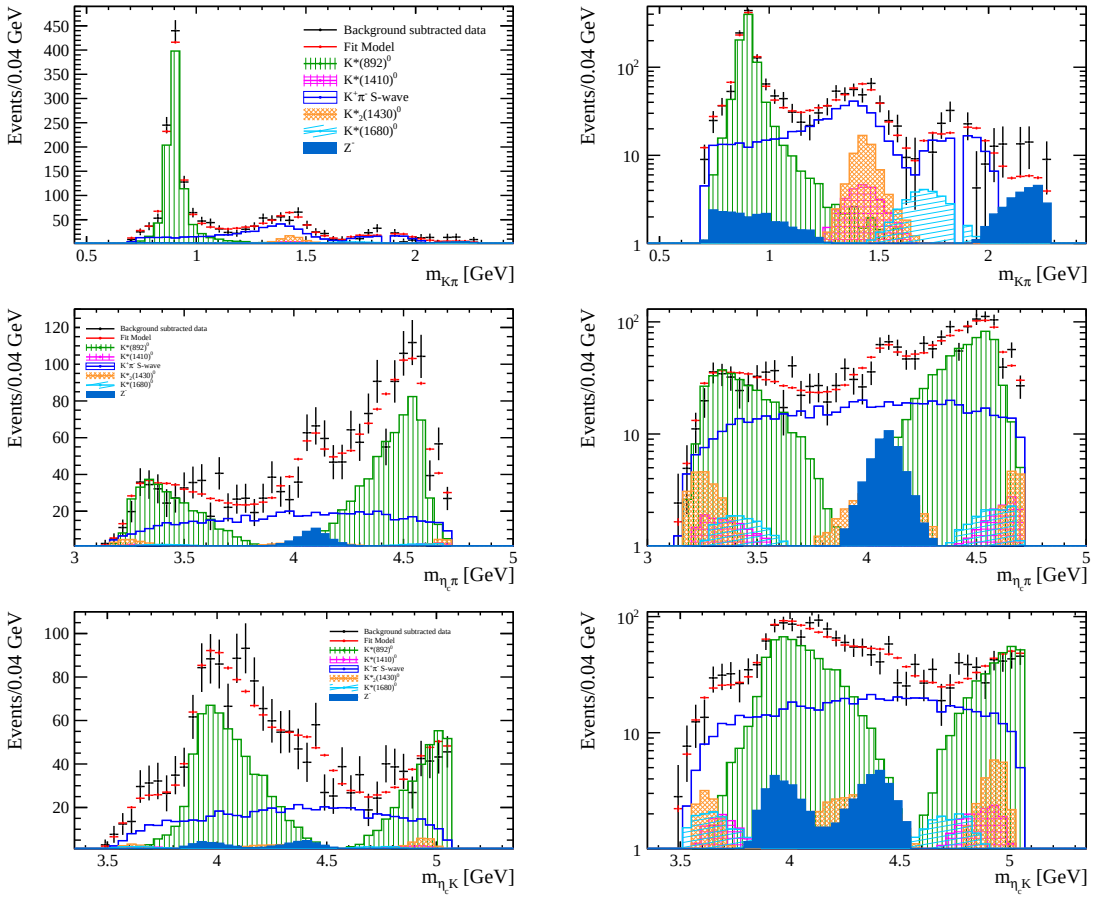

Figure 92: Projections of the background-subtracted data and amplitude fit using the baseline model plus a $J^P = 1^-$ exotic component onto (a) $m(K^+\pi^-)$, (c) $m(\eta_c\pi^-)$ and (e) $m(\eta_c K^+)$, with the same projections shown in (b), (d) and (f) with a logarithmic vertical-axis scale. The veto of $B^0 \to p\bar{p}\bar{D}^0$ decays is visible in plot (b). The $K^+\pi^-$ S-wave component comprises the LASS and $K_0^*(1950)^0$ meson contributions. The components are described in the legend at the bottom.

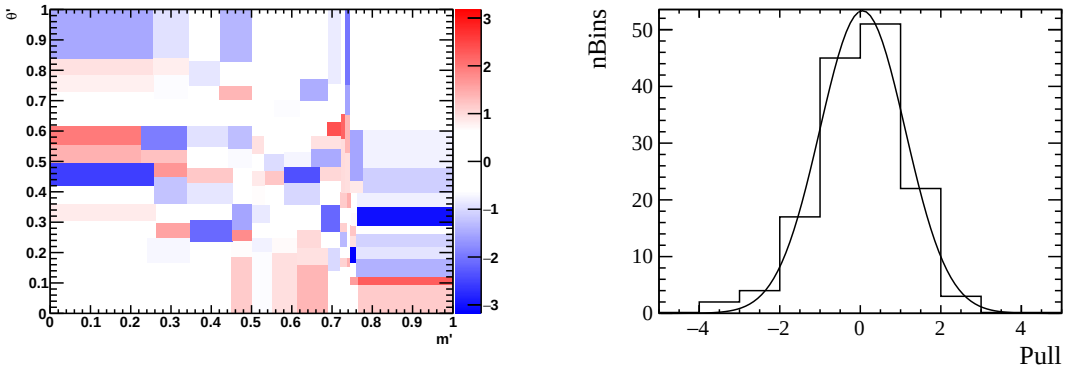

Figure 93: Left: 2D pull distribution for the Baseline Model plus a $J^P = 1^-$ component. Right: 1D pull distribution computed from the bin contents of the 2D pull distribution. This distribution is fitted with a Gaussian obtaining $\mu = 0.01 \pm 0.09$ and $\sigma = 1.06 \pm 0.07$.

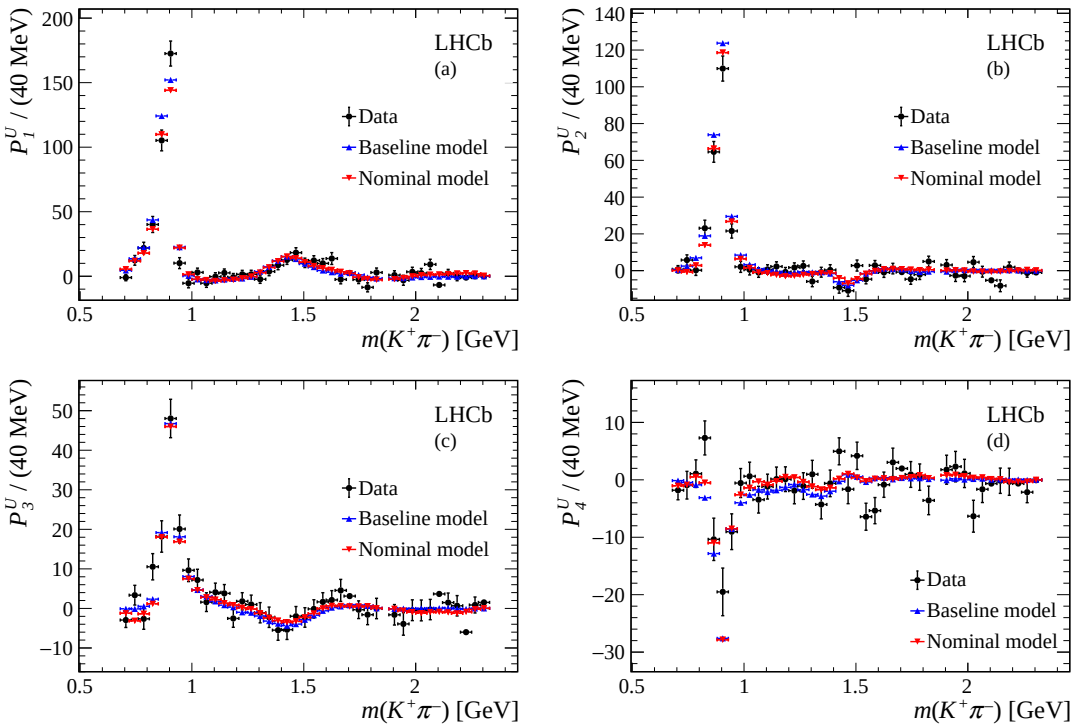

Figure 94: Comparison of the first four $K^+\pi^-$ Legendre moments determined from background-subtracted data (black points) and from the results of the amplitude fit using the baseline model (red triangles) and nominal model (blue triangles) as a function of $m(K^+\pi^-)$.

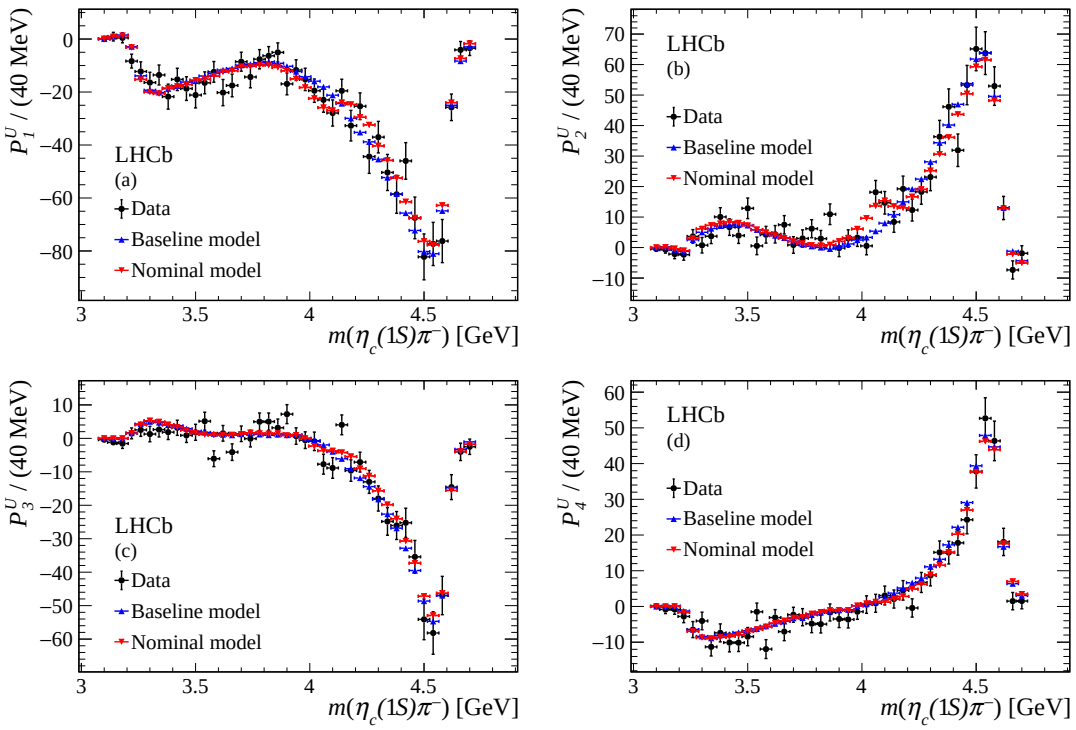

Figure 95: Comparison of the first four $\eta_c\pi^-$ Legendre moments determined from background-subtracted data (black points) and from the results of the amplitude fit using the baseline model (red triangles) and nominal model (blue triangles) as a function of $m(\eta_c\pi^-)$.

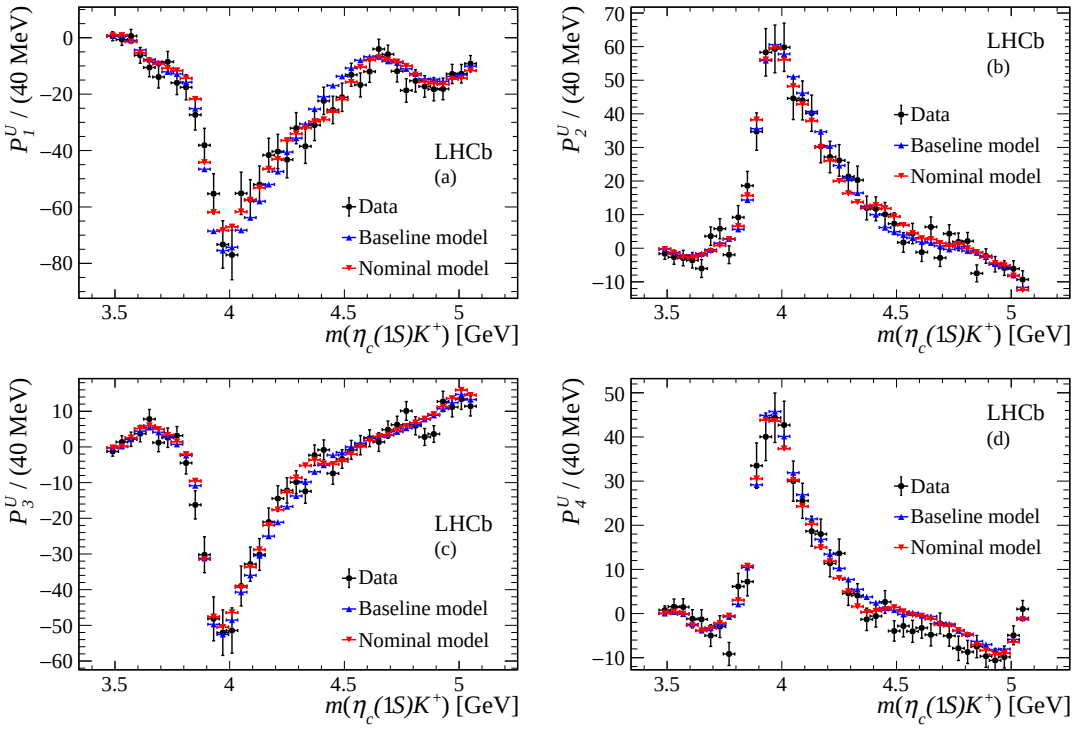

Figure 96: Comparison of the first four $\eta_c K^+$ Legendre moments determined from background-subtracted data (black points) and from the results of the amplitude fit using the baseline model (red triangles) and nominal model (blue triangles) as a function of $m(\eta_c K^+)$.

4.6.7 Significance determination

The discrimination between fits with and without the Z_c^- component is of fundamental importance in order to establish the sensitivity to a $Z_c^- \to \eta_c\pi^-$ state in the data. For this reason I generate pseudoexperiments according to the amplitude models described above, with free parameters fixed to the corresponding results in the fit to data. Each pseudoexperiment is fitted to the generated hypothesis, as well as to any alternative hypothesis (e.g. with and without the Z_c^-). The generation of pseudoexperiments is also need to validate and calibrate statistical methods used to determine the significance of the signal of interest.

The significance of a Z_c^- component in the pseudoexperiments is quantified by testing the hypothesis that the Z_c^- does not exist (null hypothesis, H_0) against the hypothesis that the Z_c^- does exist (alternative hypothesis, H_1). The probability to make a Type-I error, defined as the probability to reject a true null hypothesis, is called p-value: the lower the p-value the more significant the Z_c^- is, whatever statistical test is used. The choice of the statistical test is actually driven by the need to have a low probability to make a Type-II error, defined as the probability to accept a false null hypothesis.

The profile likelihood ratio test is usually the most powerful test to distinguish between H_0 and H_1, the power of the test being defined as one minus the probability of a Type-II error. The profile likelihood ratio is defined as

$$\lambda = -2\ln\frac{\mathcal{L}(H_0)}{\mathcal{L}(H_1)} = \Delta(-2\ln\mathcal{L}) \tag{48}$$

In order to calculate the p-value for the profile likelihood ratio, the PDF of $\Delta(-2\ln\mathcal{L})$ must be known under the null hypothesis. The Wilks' theorem states that for continuous hypothesis, for instance when H_0 is a special case of a more general H_1 (H_0 is nested in H_1), $\Delta(-2\ln\mathcal{L})$ asymptotically follows a χ^2 distribution with a number of degrees of freedom (ndof) equals to the number of constrained parameters with respect to H_1. When including the look-elsewhere effect, the effective number of degrees of freedom is given by twice the number of constrained parameters. This means that if the Wilks' theorem is applicable, the significance can be expressed in standard deviations using

$$n_\sigma(\Delta(-2\ln\mathcal{L}) = \sqrt{2}\ \text{TMath::ErfcInverse(TMath::Prob}(\Delta(-2\ln\mathcal{L}), \text{ndof})) \tag{49}$$

Wilks' theorem is strictly correct only asymptotically but it usually provides a good approximation for finite data samples.

In the search for exotic contributions in the $B^0 \to \eta_c K^+\pi^-$ decay channel, the null hypothesis H_0 is the Baseline Model, called K^* model in this section, and the alternative hypothesis H_1 is the $K^* + Z$ model. In order for H_0 to be nested in H_1, the pseudoexperiment are generated according to the K^* model and adding the Z_c^- component used in the $K^* + Z$ model (same mass, width and quantum numbers) but fixing its isobar amplitude and phase to zero. This is needed since if the phase is not constrained it becomes undefined when the magnitude is fixed to zero affecting the regularity of the likelihood around the point of constraint. As a consequence, according to Wilks' theorem, $\Delta(-2\ln\mathcal{L})$ should follow a $\chi^2/(\text{ndof})$ distribution, where ndof is the effective number of degrees of freedom corresponding to the additional four free parameters resulting from the addition of the Z_c^- component.

The effective number of degrees of freedom is determined generating 1000 pseudo-experiments according to the K^* model. These toys are fitted using both the K^* and $K^* + Z$ models, obtaining the NLL distribution for the corresponding hypothesis. The fit to the $\Delta(-2\ln\mathcal{L}) = 2(NLL_{K^*+Z} - NLL_{K^*})$ distribution with a χ^2/ndof distribution, leaving floating the number of degrees of freedom, gives the effective number of degrees of freedom to be used.

The discrimination between quantum numbers assignments is achieved generating pseudoexperiments following the null hypothesis and fitting them with both the null and alternative hypotheses. In this case the models corresponding to the null and alternative hypotheses differ for the quantum numbers assigned to the Z_c^-. The null hypothesis is given by the disfavoured quantum numbers assignment when fitting data, while the alternative hypothesis is given by the favoured quantum numbers assignment hypothesis for the Z_c^- state.

4.6.8 Significance of the $J^P = 0^+$ exotic component

I generate 1000 toys according to the Baseline Model, each pseudoexperiment having the same statistics as in the data sample. Each toy is fitted with the K^* model (adding to this model the Z_c^- with mass, width and quantum numbers obtained in the corresponding amplitude fit, and fixing its isobar coefficients to 0.0) and with the $K^* + Z_c^-$ model with free mass and width parameters and with $J^P = 0^+$ quantum numbers. The $\Delta(-2\ln\mathcal{L})$ distribution shown in Fig. 97 is obtained.

The fit with a χ^2 pdf with floating ndof gives ndof $= 7.45 \pm 0.14$, compatible with the statement of the Wilks' theorem taking into account the look-elsewhere effect. Using the NLL values obtained in the amplitude fit to data and the formula reported in 49, the significance of the $J^P = 0^+$ exotic component is 3.1σ. Using a more conservative estimate for ndof, corresponding to ndof $= 8$, the significance of the $J^P = 0^+$ Z_c^- component is 2.9σ.

4.6.9 Significance of the $J^P = 1^-$ exotic component

The same strategy described for the determination of the significance of the $J^P = 0^+$ exotic component is repeated for the $J^P = 1^-$ hypothesis. The $\Delta(-2\ln\mathcal{L})$ distribution shown in Fig. 98 is obtained.

The fit with a χ^2 pdf with floating ndof gives ndof $= 6.96 \pm 0.13$. Using the NLL values obtained in data and the formula reported in 49, the significance of the Z_c^- resonance with $J^P = 1^-$ quantum numbers assignment is 5.0σ for the $J^P = 1^-$ Z_c^-. Using a more conservative estimate of ndof $= 8$, the significance is 4.8σ.

4.6.10 Spin analysis

Toys generated according to $K^* + Z_c^-$ model, with the disfavoured J^P quantum numbers assignment for the Z_c^- state, are used to determine the rejection level of the disfavoured hypothesis with respect to the favoured J^P assignment. The toys are generated with the same statistics as in the data sample. The $\Delta(-2\ln\mathcal{L}) = 2(-\ln\mathcal{L}(J^P_{\text{disfavoured}}) - (-\ln\mathcal{L}(J^P_{\text{favoured}}))$ distribution shown in Fig. 99 is obtained fitting these toys with both the hypotheses. The $\Delta(-2\ln\mathcal{L})$ is fitted with a Gaussian distribution obtaining $\mu = -17.8 \pm 0.3$ and $\sigma = 8.29 \pm 0.21$. The $\Delta(-2\ln\mathcal{L})$ obtained from the amplitude fit results to data is

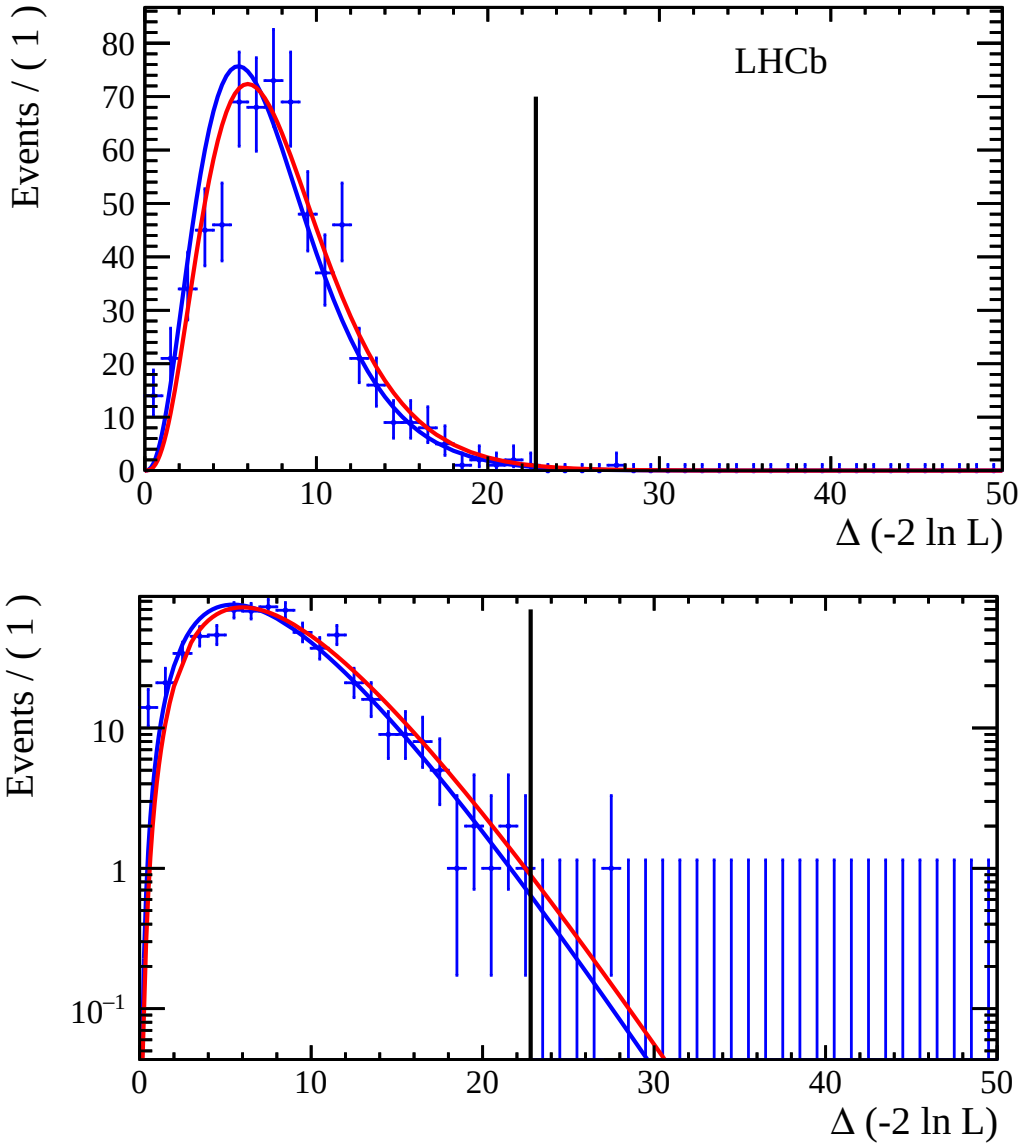

Figure 97: Distribution of $\Delta(-2\ln\mathcal{L}) = (-2\mathcal{L}(K^*)) - (-2\mathcal{L}(K^* + Z_c^-))$ for about 1000 toys generated according to the amplitude fit to data without the Z_c^- contribution, each fit without and with the $J^P = 0^+$ Z_c^- with floating mass and width. The fit with a χ^2 pdf with floating ndof gives ndof $= 7.45 \pm 0.14$ and it is superimposed (blue curve). The red curve shows the χ^2 pdf with ndof $= 8$. The vertical black line is the $\Delta(-2\ln\mathcal{L})$ obtained in the fit to data.

$\Delta(-2\ln\mathcal{L}) = 18.6$, obtaining a rejection of the disfavoured hypothesis with respect to the favoured one of 4.3σ.

4.7 Evaluation of systematic uncertainties and cross-checks

The systematic uncertainties are evaluated on the mass and width of the Z_c^- candidate, referred to as the $Z_c(4100)^-$ state, and on the fit fractions resulting from the amplitude fit giving the best NLL value, corresponding to the Default Model with the addition of a $J^P = 1^-$ state. The uncertainty on each quantity is taken as the difference between the

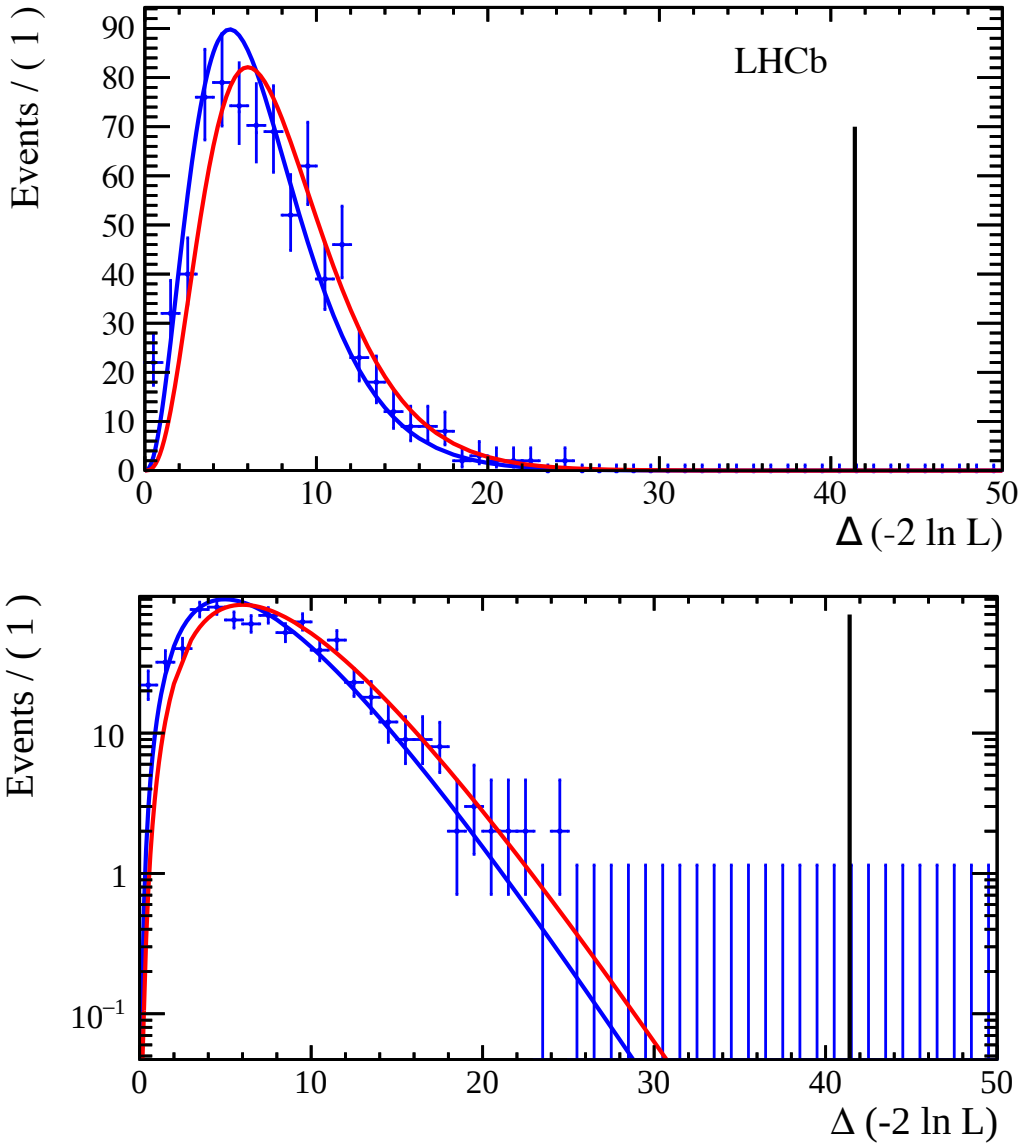

Figure 98: Distribution of $\Delta(-2\ln\mathcal{L}) = (-2\mathcal{L}(K^*)) - (-2\mathcal{L}(K^* + Z_c^-))$ for about 1000 toys generated according to the amplitude fit to data without the Z_c^- contribution, each fit without and with the $J^P = 1^-$ Z_c^- with floating mass and width. The fit with a χ^2 pdf with floating ndof gives ndof $= 6.96 \pm 0.13$ and it is superimposed (blue curve). The red curve shows the χ^2 pdf with ndof $= 8$. The vertical black line is the $\Delta(-2\ln\mathcal{L})$ obtained in the fit to data.

value returned by the modified amplitude fit and the nominal amplitude fit result. For the total systematic errors, I sum up positive and negative deviations in quadrature for each contribution.

The systematic uncertainties can be divided in two categories: the experimental and amplitude fit model uncertainties. I consider the following sources of systematic uncertainties:

- experimental uncertainties:
  - fixed signal and background yields;

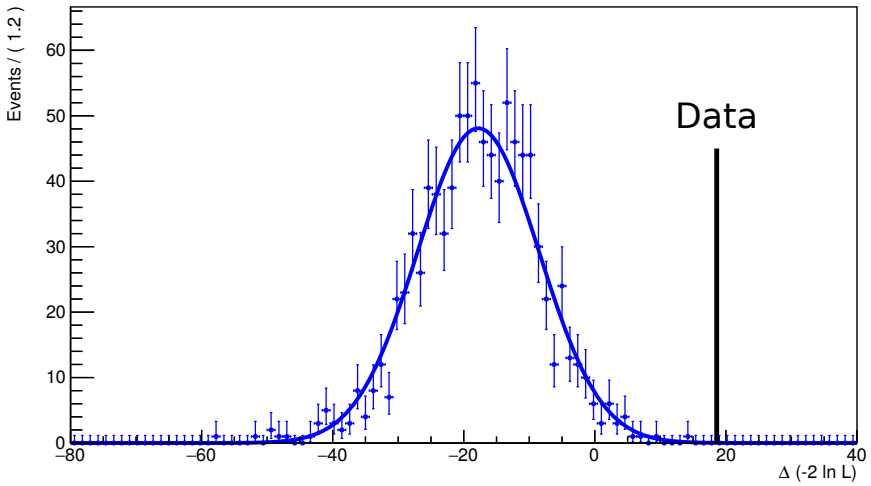

Figure 99: Distribution of $\Delta(-2\ln\mathcal{L}) = (-2\mathcal{L}(J^P = 0^+)) - (-2\mathcal{L}(J^P = 1^-))$ for about 1000 toys generated according to the amplitude fit to data with the Z_c^- set to the disfavoured $J^P = 0^+$ (blue datapoints) fitted with the disfavoured $J^P = 0^+$ and favoured $J^P = 1^-$ spin hypotheses. The fit with a gaussian is superimposed. The vertical black line is the $\Delta(-2\ln\mathcal{L})$ obtained in the fit to data.

  - amplitude fit bias;
  - background parameterisation;
  - efficiency parameterisation.

- amplitude fit model uncertainties:
  - $\eta_c(1S)$ mass value used to build the DP kinematics;
  - fixed resonance parameters;
  - marginal $K^+\pi^-$ components;
  - $K^+\pi^-$ S-wave parameterisation.

The procedure to determine the corresponding systematic uncertainty is described in more details in the following. Cross-checks, considering the inclusion of additional exotic components and other possible systematics effects as an eventual systematic bias arising from the 2D mass fit used to extract the signal and background yields, are carried out as described in section 4.7.4.
To probe the sensitivity of the significance of the $Z_c(4100)^-$ state to systematic effects, I use the fit variations producing the largest changes in the values of the mass, width or fit fraction of the exotic candidate. Fitting data with both the modified K^* and $K^* + Z_c^-$ models (considering $J^P = 1^-$ for the exotic candidate), I determine the $\Delta(-2\log\mathcal{L})$ value and I convert it in the corresponding significance value using Eq. 49 and considering the conservative ndof = 8.

I perform a similar strategy to evaluate the sensitivity of the rejection of the $J^P = 0^+$ hypothesis to systematics effects, but fitting data with both the modified $K^* + Z_c^-$ models differing for the quantum numbers assignment to the $Z_c(4100)^-$. The rejection of the $J^P = 0^+$ hypothesis is determined using the χ^2 method, hence evaluating the $\sqrt{\Delta(-2\log\mathcal{L})}$ value.

The effect of the systematic uncertainties on the significances is described in Sec. 4.7.3.

4.7.1 Experimental uncertainties

The signal and background yields used in the amplitude fit are fixed to the values obtained from the 2D mass fit. The statistical uncertainties on the yields are propagated into the amplitude fit by Gaussian constraining the yields within their statistical uncertainties.

A systematic uncertainty related to the fit bias is determined using the same procedure used to determine the statistical uncertainty on the fit fractions. The distribution for each parameter is fitted with a Gaussian in order to obtain its mean x_i^{fitted} and the error on the mean δ_i^{fitted}. The systematic uncertainty associated to the bias introduced by the amplitude fit procedure is determined as the square root of the mean squared error, given by

$$\sigma_i = \sqrt{(x_i^{\text{fitted}} - x_i^{\text{true}})^2 + (\delta_i^{\text{fitted}})^2}, \tag{50}$$

where x_i^{true} is the generated value.

The background maps describing the distribution of each background across the phase space are varied within uncertainties. For each bin of the combinatorial and nonresonant background maps, I randomly extract a number from the Gaussian distribution having the mean equal to the bin content and the standard deviation equal to the corresponding bin uncertainty. Repeating the procedure 100 times, new background maps are built, and for each set of maps I repeat the amplitude fit. For each measured quantity, a Gaussian is used to fit the distribution of the 100 values obtained, and its standard deviation is taken as the systematic uncertainty assigned to the background parameterisation.

In order to take into account the uncertainty due to the limited statistics of the simulated samples, the same strategy used for the systematic uncertainty associated to the background parameterisation is considered for the offline selection efficiency maps.

In order to probe the eventual correlated variations of efficiencies in neighbouring bins, I select 10 bins over the 10x10 offline selection efficiency map. I varied these bins within their uncertainties, and the neighbouring bins are varied by linear interpolation.

Regarding the PID efficiency I change the binning scheme chosen in PIDCalib, roughly halving the number of bins in momentum and pseudorapidity for both Run1 and Run2 and roughly doubling the number in nSPDHits for Run2 only.

Another systematic uncertainty is associated to the cut I applied to the DP borders because of concerns about the parameterisation of the efficiencies in those regions. The amplitude fit is repeated removing these cuts.

The summary of systematics uncertainties associated to the efficiency parameterisation is reported in Tabs. 35 and 36 for the $Z_c(4100)^-$ parameters and the fit fractions, respectively.

Parameter	Nominal value	MC statistics	Corr. Variations	PIDCalib binning	DP boundaries
m_Z	4096 ± 20	± 0.7	± 0.6	-0.06	-10
Γ_Z	152 ± 58	± 4	± 6	$+0.8$	$+17$

Table 35: Breakdown of systematic uncertainties on the mass and width of the $Z_c(4100)^-$ component associated to the efficiency parameterisation. Values are in MeV units. The corresponding value returned by the nominal amplitude fit is reported in the second column with its statistical uncertainty.

Component	Nominal value	MC statistics	Corr. Variations	PIDCalib binning	DP boundaries
$K^*(892)$	51.4 ± 1.9	± 0.27	± 0.4	-0.08	-2.5
$K^*(1410)$	2.1 ± 1.1	± 0.06	± 0.09	-0.024	$+0.30$
LASS nonres	10.3 ± 1.4	± 0.08	± 0.11	-0.04	-0.32
$K_0^*(1430)$	25.3 ± 3.5	± 0.21	± 0.28	-0.12	-0.8
$K_2^*(1430)$	4.1 ± 1.5	± 0.11	± 0.08	$+0.018$	-0.4
$K^*(1680)$	2.2 ± 2.0	± 0.06	± 0.07	$+0.013$	-0.4
$K_0^*(1950)$	3.8 ± 1.8	± 0.08	± 0.010	-0.024	$+0.10$
$Z_c(4100)^-$	3.3 ± 1.1	± 0.11	± 0.16	-0.023	$+0.7$
Interference terms					
$K^*(892) - K^*(1410)$	1.7 ± 1.9	± 0.14	± 0.17	-0.06	$+0.09$
$K^*(892) - K^*(1680)$	-2.1 ± 1.1	± 0.06	± 0.07	$+0.011$	$+0.07$
$K^*(892) - Z_c(4100)^-$	1.4 ± 1.0	± 0.10	± 0.10	$+0.07$	$+0.004$
$K^*(1410) - K^*(1680)$	-2.5 ± 1.6	± 0.07	± 0.11	-0.004	$+0.10$
$K^*(1410) - Z_c(4100)^-$	-0.4 ± 0.4	± 0.030	± 0.030	$+0.014$	-0.005
LASS nonres-$K_0^*(1430)$	-5.8 ± 1.3	± 0.08	± 0.10	$+0.04$	$+0.30$
LASS nonres-$K_0^*(1950)$	-3.2 ± 2.8	± 0.4	± 0.35	$+0.13$	$+1.5$
LASS nonres-$Z_c(4100)^-$	1.11 ± 0.23	± 0.025	± 0.035	$+0.012$	$+0.07$
$K_0^*(1430)$-$K_0^*(1950)$	4.7 ± 0.7	± 0.08	± 0.11	$+0.04$	$+0.20$
$K_0^*(1430)$-$Z_c(4100)^-$	2.8 ± 0.4	± 0.04	± 0.06	$+0.020$	$+0.28$
$K_2^*(1430)$-$Z_c(4100)^-$	0.0 ± 0.3	± 0.021	± 0.017	$+0.019$	$+0.7$
$K^*(1680)$-$Z_c(4100)^-$	0.7 ± 0.5	± 0.024	± 0.021	-0.015	-0.11
$K_0^*(1950)$-$Z_c(4100)^-$	0.6 ± 0.5	± 0.027	± 0.030	-0.005	$+0.12$

Table 36: Breakdown of systematic uncertainties on (interference) fit fractions associated to the efficiency parameterisation. Components labelled like A0-A1 stand for the interference fit fraction between amplitudes A0 and A1. Values are in % units. The corresponding value returned by the nominal amplitude fit is reported in the second column with its statistical uncertainty.

4.7.2 Uncertainties due to the amplitude fit model

The DP kinematics variables are computed starting from the B^0, K^+, π^- and $\eta_c(1S)$ mass values. These variables are then used to compute the amplitudes entering the amplitude fit. In the nominal amplitude fit I used the $\eta_c(1S)$ mass values returned by the 2D fit, reported in Tab. 19. In order to estimate the effect of the $\eta_c(1S)$ natural width I repeated the amplitude fit varying the $\eta_c(1S)$ mass value. Using the $\eta_c(1S)$ width resulting from the 2D fit, we repeated two times the joint amplitude fit: once using the $m + \Gamma/2$ value

Parameter	Nominal value	fixed yields	fit bias	background	efficiency	Total
m_Z	4096 ± 20	-2.4	$+3.2$	± 11.8	$^{+0.9}_{-10.0}$	$^{+12.3}_{-15.7}$
Γ_Z	152 ± 58	$+41.5$	$+7.5$	± 30.8	$^{+18.5}_{-7.2}$	$^{+55.4}_{-31.6}$

Table 37: Breakdown of experimental systematic uncertainties on the mass and width of the $Z_c(4100)^-$ component. Values are in MeV units. The corresponding value returned by the nominal amplitude fit is reported in the second column with its statistical uncertainty.

and once using the $m - \Gamma/2$ value. In case of same-sign variations, I take the largest variation as the systematic uncertainty related to the $\eta_c(1S)$ mass value.

The masses and widths of the K^* resonances (beside the LASS parameters) and the Blatt-Weisskopf barrier factor radii have been fixed in the nominal amplitude fit.

The uncertainties associated to the fixed masses and widths are determined varying simultaneously and randomly each parameter using the world average values and uncertainties reported by [15] and repeating the amplitude fit. The procedure is repeated 100 times.

The systematics due to the fixed Blatt-Weisskopf barrier factor radii for the K^* and the $Z_c(4100)^-$ resonances are determined changing the nominal value of $4\,\mathrm{GeV}^{-1}$ to $3\,\mathrm{GeV}^{-1}$ and $5\,\mathrm{GeV}^{-1}$.

The assigned systematics to the amplitude fit model fixed parameters are the combination in quadrature of all the contributions.

The $K_3^*(1780)$ and $K_4^*(2045)$ resonances are established states known to decay to the $K^+\pi^-$ final state, but they have not been included in the nominal model since their significance is small. We repeat the amplitude fit adding these two states.

The LASS pdf has been used to parameterise the $K^+\pi^-$ S-wave in the nominal fit, in addition to the $K_0^*(1950)$ at high $K^+\pi^-$ mass. In order to determine the systematic uncertainty associated to the choice of the LASS pdf, I repeat the DP fit replacing the LASS shape with a RBW for the $K^*(1430)$, adding the $K^*(800)$ amplitude parameterised with a RBW and adding a non-resonant S-wave $K^+\pi^-$ amplitude as a uniform amplitude within the DP.

4.7.3 Effect of systematic uncertainties on the significances

To probe the sensitivity of the significance of the $Z_c(4100)^-$ candidate to systematics effects, I investigate fit variations producing the largest changes in the values of its mass, width and fit fraction. I perform the amplitude fits with the modified K^* and K^*+Z_c^- models and recompute the significance using Eq. 49 with the conservative effective number of degrees of freedom ndof=8.

The largest variations in the $Z_c(4100)^-$ parameters come from:

- the fixed yields requirement;
- the background parameterisation;
- the veto to the outer regions of the DP;
- the value of the $\eta_c(1S)$ mass used to build the DP kinematics;

Component	Nominal value	fixed yields	fit bias	background	efficiency	Total
$K^*(892)$	51.4 ± 1.9	-3.5	± 1.0	± 1.1	$^{+0.5}_{-2.5}$	$^{+1.6}_{-4.6}$
$K^*(1410)$	2.1 ± 1.1	-0.22	± 0.4	± 0.7	$^{+0.31}_{-0.11}$	$^{+0.9}_{-0.8}$
LASS nonres	10.3 ± 1.4	-0.20	± 0.4	± 0.8	$^{+0.14}_{-0.35}$	$^{+0.9}_{-1.0}$
$K_0^*(1430)$	25.3 ± 3.5	-0.5	± 1.0	± 2.0	$^{+0.35}_{-0.9}$	$^{+2.3}_{-2.5}$
$K_2^*(1430)$	4.1 ± 1.5	-0.8	± 0.37	± 0.9	$^{+0.14}_{-0.4}$	$^{+1.0}_{-1.3}$
$K^*(1680)$	2.2 ± 2.0	-0.12	± 0.4	± 0.9	$^{+0.09}_{-0.4}$	$^{+1.0}_{-1.1}$
$K_0^*(1950)$	3.8 ± 1.8	$+0.08$	± 0.6	± 0.9	$^{+0.13}_{-0.08}$	± 1.1
$Z_c(4100)^-$	3.3 ± 1.1	$+0.31$	± 0.14	± 0.8	$^{+0.7}_{-0.20}$	$^{+1.1}_{-0.8}$
Interference terms						
$K^*(892) - K^*(1410)$	1.7 ± 1.9	-0.04	± 0.20	± 1.2	$^{+0.24}_{-0.23}$	± 1.2
$K^*(892) - K^*(1680)$	-2.1 ± 1.1	$+0.5$	± 0.08	± 0.8	$^{+0.12}_{-0.09}$	$^{+1.0}_{-0.8}$
$K^*(892) - Z_c(4100)^-$	1.4 ± 1.0	$+0.39$	± 0.21	± 0.6	$^{+0.16}_{-0.14}$	$^{+0.8}_{-0.7}$
$K^*(1410) - K^*(1680)$	-2.5 ± 1.6	$+0.5$	± 0.13	± 1.1	$^{+0.16}_{-0.13}$	$^{+1.2}_{-1.1}$
$K^*(1410) - Z_c(4100)^-$	-0.4 ± 0.4	$+0.06$	± 0.022	± 0.4	$^{+0.04}_{-0.04}$	± 0.4
LASS nonres-$K_0^*(1430)$	-5.8 ± 1.3	$+1.1$	± 0.4	± 1.7	$^{+0.33}_{-0.13}$	$^{+2.1}_{-1.8}$
LASS nonres-$K_0^*(1950)$	-3.2 ± 2.8	$+0.9$	± 0.28	± 1.0	$^{+1.6}_{-0.5}$	$^{+2.1}_{-1.2}$
LASS nonres-$Z_c(4100)^-$	1.11 ± 0.23	$+0.13$	± 0.035	± 0.30	$^{+0.08}_{-0.04}$	$^{+0.34}_{-0.30}$
$K_0^*(1430)$-$K_0^*(1950)$	4.7 ± 0.7	$+0.7$	± 0.08	± 0.9	$^{+0.25}_{-0.14}$	$^{+1.2}_{-0.9}$
$K_0^*(1430)$-$Z_c(4100)^-$	2.8 ± 0.4	$+0.23$	± 0.06	± 0.28	$^{+0.29}_{-0.07}$	$^{+0.5}_{-0.29}$
$K_2^*(1430)$-$Z_c(4100)^-$	0.0 ± 0.3	$+0.0034$	± 0.08	± 0.14	$^{+0.7}_{-0.027}$	$^{+0.7}_{-0.16}$
$K^*(1680)$-$Z_c(4100)^-$	0.7 ± 0.5	$+0.11$	± 0.024	± 0.31	$^{+0.032}_{-0.12}$	± 0.33
$K_0^*(1950)$-$Z_c(4100)^-$	0.6 ± 0.5	$+0.4$	± 0.14	± 0.4	$^{+0.13}_{-0.028}$	$^{+0.6}_{-0.4}$

Table 38: Breakdown of experimental systematic uncertainties on (interference) fit fractions. Components labelled like A0-A1 stand for the interference fit fraction between amplitudes A0 and A1. Values are in % units. The corresponding value returned by the nominal amplitude fit is reported in the second column with its statistical uncertainty.

- the $K^+\pi^-$ S-wave parameterisation.

In order to determine the effect of the background parameterisation, I repeat the amplitude fits using every new background map obtained as described in Section 4.6.4. The minimum ΔNLL is taken to report the corresponding significance level. Results are summarised in Tab. 43. In order to evaluate the effect of possible correlated or anti-correlated sources of systematic uncertainty, the fits are repeated using the pessimistic

Parameter	Nominal value	Fixed pars	$r_{\rm BW} = 3\,{\rm GeV}^{-1}$	$r_{\rm BW} = 5\,{\rm GeV}^{-1}$
m_Z	4096 ± 20	± 2.4	-1.8	$+1.7$
Γ_Z	152 ± 58	± 9.2	-5.0	$+4.7$

Table 39: Breakdown of systematic uncertainties associated to the fixed parameters in the amplitude fit model on the mass and width of the $Z_c(4100)^-$ component. Values are in MeV units. The corresponding value returned by the nominal amplitude fit is reported in the second column with its statistical uncertainty. The Fixed pars column corresponds to the amplitude fit performed varying simultaneously and randomly the masses and widths of the K^* contributions.

Parameter	Nominal value	Fixed pars	$r_{\rm BW} = 3\,{\rm GeV}^{-1}$	$r_{\rm BW} = 5\,{\rm GeV}^{-1}$
$K^*(892)$	51.4 ± 1.9	± 0.5	$+0.39$	-0.18
$K^*(1410)$	2.1 ± 1.1	± 0.6	-0.04	$+0.016$
LASS nonres	10.3 ± 1.4	± 0.5	-0.06	$+0.027$
$K_0^*(1430)$	25.3 ± 3.5	± 0.9	-0.014	$+0.07$
$K_2^*(1430)$	4.1 ± 1.5	± 0.32	-0.0008	-0.017
$K^*(1680)$	2.2 ± 2.0	± 1.0	-0.0024	$+0.017$
$K_0^*(1950)$	3.8 ± 1.8	± 0.9	$+0.14$	-0.12
$Z_c(4100)^-$	3.3 ± 1.1	± 0.31	-0.09	$+0.09$
Interference terms				
$K^*(892) - K^*(1410)$	1.7 ± 1.9	± 0.8	-0.017	$+0.025$
$K^*(892) - K^*(1680)$	-2.1 ± 1.1	± 0.9	-0.21	$+0.10$
$K^*(892) - Z_c(4100)^-$	1.4 ± 1.0	± 0.17	$+0.12$	-0.10
$K^*(1410) - K^*(1680)$	-2.5 ± 1.6	± 1.3	-0.07	$+0.04$
$K^*(1410) - Z_c(4100)^-$	-0.4 ± 0.4	± 0.18	$+0.06$	-0.05
LASS nonres-$K_0^*(1430)$	-5.8 ± 1.3	± 0.4	-0.03	$+0.009$
LASS nonres-$K_0^*(1950)$	-3.2 ± 2.8	± 0.8	-0.05	$+0.02$
LASS nonres-$Z_c(4100)^-$	1.11 ± 0.23	± 0.11	$+0.0011$	-0.0021
$K_0^*(1430)$-$K_0^*(1950)$	4.7 ± 0.7	± 0.4	-0.017	$+0.0014$
$K_0^*(1430)$-$Z_c(4100)^-$	2.8 ± 0.4	± 0.09	-0.0016	$+0.004$
$K_2^*(1430)$-$Z_c(4100)^-$	0.0 ± 0.3	± 0.06	$+0.039$	-0.034
$K^*(1680)$-$Z_c(4100)^-$	0.7 ± 0.5	± 0.30	-0.11	$+0.08$
$K_0^*(1950)$-$Z_c(4100)^-$	0.6 ± 0.5	± 0.33	-0.05	$+0.038$

Table 40: Breakdown of systematic uncertainties associated to the amplitude fit model on (interference) fit fractions. Components labelled like A0-A1 stand for the interference fit fraction between amplitudes A0 and A1. Values are in % units. The corresponding value returned by the nominal amplitude fit is reported in the second column with its statistical uncertainty. The Fixed pars column corresponds to the amplitude fit performed varying simultaneously and randomly the masses and widths of the K^* contributions.

background parameterisation together with the alternative $K^+\pi^-$ S-wave model, and with different $\eta_c(1S)$ mass values. The lower limit on the significance of the Z_c state is found to be 3.2σ.

The same studies are repeated to determine the rejection level of the $J^P = 0^+$ hypothesis, using $\sqrt{\Delta(-2\log\mathcal{L})}$. Results are summarised in Tab. 44.

Parameter	Nominal value	m_{η_c}	Fixed pars.	Marginal components	$K^+\pi^-$ S-wave	Total
m_Z	4096 ± 20	$^{+12.8}_{-12.1}$	$^{+2.9}_{-3.0}$	-5.5	-6.8	$^{+13.1}_{-15.2}$
Γ_Z	152 ± 58	$+20.0$	$^{+10.3}_{-10.5}$	-5.2	-8.2	$^{+22.5}_{-14.3}$

Table 41: Breakdown of systematic uncertainties associated to the amplitude fit model on the mass and width of the $Z_c(4100)^-$ component. Values are in MeV units. The corresponding value returned by the nominal amplitude fit is reported in the second column with its statistical uncertainty.

4.7.4 Additional cross-checks

I investigate the $J^P = 2^+$ assignment to the Z_c^- component, obtaining a $\Delta\text{NLL} = -3.5$ with respect to the Default Model. This assignment is not investigated further.

The possible presence of a second exotic amplitude decaying to the $\eta_c\pi^-$ spectrum is investigated adding a $J^P = 0^+$ amplitude of floating mass and width to the best fit model including the $J^P = 1^-$ $Z_c(4100)^- \to \eta_c(1S)\pi^-$. The amplitude fit is repeated 100 times in order to find the absolute minimum. The best ΔNLL is -4.8, indicating the second amplitude is not significant.

The possible presence of an exotic amplitude decaying to the $\eta_c K^+$ spectrum is investigated as well, using an analogue strategy. The best ΔNLL is -4.4. Also in this case the additional amplitude is not significant.

The possible effect of the $\eta_c(1S)$ natural width is studied splitting the full data sample in the $m_{p\bar{p}} < m_{\eta_c(1S)}$ and $m_{p\bar{p}} > m_{\eta_c(1S)}$ subsamples. The amplitude fit using the Default Model is repeated obtaining fit fractions consistent with the results of Tab. 25.

Additional studies are performed in order to check the Run2 protons ProbNN output, the possible presence of biases in the 2D fit model and the agreement between data and simulation.

In order to check the protons ProbNN variables, in addition to the nominal PID cut, I apply other cuts and calculated the corresponding PID efficiency corrected signal yields.

For each cut I carried out the 2D fit to determine N_{η_c}. We corrected the yield dividing by the PID efficiency value returned by the PIDCalib procedure. The results are reported in Tab. 45. The PID efficiency corrected value do not show any trending, indicating the reliability of the protons ProbNN variable.

I use the 2D mass fit to extract the sWeights to build the background models and to determine the signal and background yields. The yields should not show a large bias. In order to check the presence of potential biases on the parameters of the 2D mass fit model, we perform, for both Run1 and Run2 data, MC studies generating and fitting 1000 samples, using the pdf described in section 68. I introduce a Poisson fluctuation on the number of generated events (the expected value is the number of events resulting from the nominal 2D fit). I estimate the pull of the floating fit parameters given by

$$b_i = \frac{x_i^{\text{fitted}} - x_i^{\text{true}}}{\sigma_i^{\text{fitted}}}, \tag{51}$$

where x_i^{fitted} and σ_i^{fitted} correspond to the fitted value of a parameter and its fit uncertainty, while x_i^{true} is the generated value.

Component	Nominal value	m_{η_c}	Fixed pars.	Marginal components	$K^+\pi^-$ S-wave	Total
$K^*(892)$	51.4 ± 1.9	$^{+0.4}_{-0.8}$	$^{+0.6}_{-0.5}$	-0.14	-0.8	$^{+0.7}_{-1.2}$
$K^*(1410)$	2.1 ± 1.1	$^{+0.19}_{-0.16}$	± 0.6	-0.10	-0.5	$^{+0.6}_{-0.8}$
LASS nonres.	10.3 ± 1.4	-0.35	± 0.5	-0.14	-0.2	$^{+0.5}_{-0.7}$
$K_0^*(1430)$	25.3 ± 3.5	-0.7	± 0.9	-0.4	$+2.5$	$^{+2.7}_{-1.2}$
$K_2^*(1430)$	4.1 ± 1.5	$^{+0.019}_{-0.018}$	± 0.32	$+0.05$	-0.8	$^{+0.32}_{-0.9}$
$K^*(1680)$	2.2 ± 2.0	$^{+0.4}_{-0.28}$	± 1.0	-0.23	-0.8	$^{+1.1}_{-1.3}$
$K_0^*(1950)$	3.8 ± 1.8	-0.34	± 0.9	-0.31	-2.1	$^{+0.9}_{-2.3}$
$Z_c(4100)^-$	3.3 ± 1.1	$+0.28$	± 0.31	-0.07	-0.6	$^{+0.4}_{-0.7}$
Interference terms						
$K^*(892) - K^*(1410)$	1.7 ± 1.9	$^{+0.05}_{-0.24}$	± 0.8	$+0.20$	$+1.9$	$^{+2.1}_{-0.8}$
$K^*(892) - K^*(1680)$	-2.1 ± 1.1	$^{+0.4}_{-0.19}$	± 0.9	-0.11	-0.9	$^{+1.0}_{-1.3}$
$K^*(892) - Z_c(4100)^-$	1.4 ± 1.0	$^{+0.9}_{-0.6}$	$^{+0.21}_{-0.20}$	-0.008	-0.6	± 0.9
$K^*(1410) - K^*(1680)$	-2.5 ± 1.6	$^{+0.10}_{-0.05}$	± 1.3	$+0.16$	$+0.8$	$^{+1.5}_{-1.3}$
$K^*(1410) - Z_c(4100)^-$	-0.4 ± 0.4	± 0.25	± 0.19	$+0.07$	$+0.5$	$^{+0.6}_{-0.31}$
LASS nonres-$K_0^*(1430)$	-5.8 ± 1.3	$^{+0.4}_{-0.32}$	± 0.4	$+0.15$	-0.7	$^{+0.6}_{-0.9}$
LASS nonres-$K_0^*(1950)$	-3.2 ± 2.8	$^{+1.4}_{-0.25}$	± 0.8	$+0.4$	$+4.1$	$^{+4.4}_{-0.8}$
LASS nonres-$Z_c(4100)^-$	1.11 ± 0.23	$^{+0.11}_{-0.14}$	± 0.11	-0.04	$+0.29$	$^{+0.33}_{-0.18}$
$K_0^*(1430)$-$K_0^*(1950)$	4.7 ± 0.7	$^{+0.04}_{-0.09}$	± 0.4	-0.4	-1.0	$^{+0.4}_{-1.2}$
$K_0^*(1430)$-$Z_c(4100)^-$	2.8 ± 0.4	$^{+0.05}_{-0.07}$	± 0.09	-0.05	$+0.2$	$^{+0.22}_{-0.12}$
$K_2^*(1430)$-$Z_c(4100)^-$	0.0 ± 0.3	$^{+0.24}_{-0.19}$	± 0.07	-0.0007	$+0.15$	$^{+0.29}_{-0.20}$
$K^*(1680)$-$Z_c(4100)^-$	0.7 ± 0.5	$^{+0.16}_{-0.17}$	$^{+0.31}_{-0.32}$	-0.11	-0.7	$^{+0.35}_{-0.8}$
$K_0^*(1950)$-$Z_c(4100)^-$	0.6 ± 0.5	$^{+0.5}_{-0.4}$	± 0.33	$+0.06$	-0.8	$^{+0.6}_{-1.0}$

Table 42: Breakdown of systematic uncertainties associated to the amplitude fit model on (interference) fit fractions. Components labelled like A0-A1 stand for the interference fit fraction between amplitudes A0 and A1. Values are in % units. The corresponding value returned by the nominal amplitude fit is reported in the second column with its statistical uncertainty.

The results of the 2D fit model pull studies are listed in Tab. 46 for Run1 and in Tab. 47 for Run2. The pull distributions are shown in Fig. 100 for Run1 and in Fig. 101 for Run2. Pull results are consistent with no significant biases in the fit parameters and in particular in the yields.

L0 trigger variables may not be well described by the simulation. For this reason I perform TIS-TOS cross-checks on these numbers. The TIS efficiency is defined as the

Source	ΔNLL	Significance
Default	-20.7	4.8σ
Fixed Yields	-22.9	5.2σ
Background	-13.7	$\mathbf{3.4\sigma}$
DP borders	-22.3	5.1σ
$\eta_c(1S)$ mass	-18.3	4.3σ
$K^+\pi^-$ S-wave	-15.9	3.9σ

Table 43: Significance of the $Z_c(4100)^-$ candidate for the systematic variations producing the largest variations in the $Z_c(4100)^-$ parameters. The lowest significance is highlighted. In the first row are shown the values obtained in the nominal amplitude fit.

Source	ΔNLL	Significance
Default	9.3	4.3σ
Fixed Yields	11.9	4.9σ
Background	1.7	1.8σ
DP borders	12.2	4.9σ
$\eta_c(1S)$ mass	2.1	2.0σ
$K^+\pi^-$ S-wave	0.7	$\mathbf{1.2\sigma}$

Table 44: Rejection level of the $J^P = 0^+$ hypothesis with respect to the $J^P = 1^+$ hypothesis for the systematic variations producing the largest variations in the $Z_c(4100)^-$ parameters. The lowest rejection level is highlighted. In the first row are shown the values obtained in the nominal amplitude fit.

	ProbNNp>0.1	ProbNNp>0.15	ProbNNp>0.25 (nominal)	ProbNNp>0.35	ProbNNp>0.7
$\epsilon_{\rm PID}$	0.89	0.87	0.85	0.81	0.70
$N_{\eta_c}^{\rm corr}$	1261	1285	1278	1309	1308

Table 45: PID efficiency and $B^0 \to \eta_c K^+\pi^-$ number of events corrected for the corresponding PID efficiency value for the different cuts used to check the protons ProbNN response in Run2 data.

fraction of events that pass both L0 TIS and L0 TOS over the events that pass L0 TOS only:

$$\epsilon^{TIS} = \frac{\text{L0Physics\_TIS \&\& L0Hadron\_TOS}}{\text{L0Hadron\_TOS}} \tag{52}$$

while the TOS efficiency is defined as the fraction of events that pass both L0 TIS and L0 TOS over the events that pass L0 TIS only:

$$\epsilon^{TOS} = \frac{\text{L0Physics\_TIS \&\& L0Hadron\_TOS}}{\text{L0Physics\_TIS}} \tag{53}$$

L0Physics is the OR between the electron, photon, muon, dimuon and hadron lines. For

Parameter	true	μ	σ
$N_{B^0\to\eta_c K\pi}$	825	0.017 ± 0.034	1.087 ± 0.024
$N_{B^0\to p\bar{p}K\pi}$ (non resonant)	351	-0.053 ± 0.033	1.058 ± 0.024
$N_{\text{Comb. bkg}}$	763	0.022 ± 0.032	1.026 ± 0.023
m_{B^0}	5282.9	-0.04 ± 0.06	1.17 ± 0.09
σ_B	14.9	-0.12 ± 0.07	1.20 ± 0.10
$m(B)_{\text{bkg slope}}$	-0.00031	0.024 ± 0.032	1.012 ± 0.023
$m_{\eta_c(1S)}$	2985.2	0.006 ± 0.032	1.087 ± 0.024
$m(p\bar{p})_{\text{bkg slope}}$	0.001	0.045 ± 0.034	1.077 ± 0.024
$m(p\bar{p})_{B^0\to p\bar{p}K\pi \text{ slope}}$	-0.0063	0.045 ± 0.033	1.054 ± 0.024

Table 46: MC toy study results of the Run1 2D fit model to the joint $m(p\bar{p}K^+\pi^-) \times m_{p\bar{p}}$ distribution, obtained with 1000 pseudoexperiments. In the table are reported the parameter, its true value, i.e. the central value returned by the 2D fit, as well as the mean μ and the standard deviation σ of the gaussian distribution obtained from the fit to the pull distribution.

Parameter	true	μ	σ
$N_{B^0\to\eta_c K\pi}$	1086	-0.059 ± 0.032	1.011 ± 0.022
$N_{B^0\to p\bar{p}K\pi}$ (non resonant)	441	0.017 ± 0.034	1.079 ± 0.024
$N_{\text{Comb. bkg}}$	867	-0.0755 ± 0.032	1.012 ± 0.023
m_{B^0}	5279.0	-0.04 ± 0.04	1.21 ± 0.64
σ_B	15.3	-0.13 ± 0.17	1.20 ± 0.09
$m(B)_{\text{bkg slope}}$	-0.0017	-0.041 ± 0.032	1.00 ± 0.22
$m_{\eta_c(1S)}$	2984.0	-0.080 ± 0.031	0.993 ± 0.022
$m(p\bar{p})_{\text{bkg slope}}$	0.0023	0.128 ± 0.032	1.017 ± 0.023
$m(p\bar{p})_{B^0\to p\bar{p}K\pi \text{ slope}}$	-0.0054	0.0157 ± 0.032	1.017 ± 0.023

Table 47: MC toy study results of the Run2 2D fit model to the joint $m(p\bar{p}K^+\pi^-) \times m_{p\bar{p}}$ distribution, obtained with 1000 pseudoexperiments. In the table are reported the parameter, its true value, i.e. the central value returned by the 2D fit, as well as the mean μ and the standard deviation σ of the gaussian distribution obtained from the fit to the pull distribution

each L0 trigger selection, I perform a 2D fit to extract the sWeights corresponding to the $B^0 \to J/\psi K^+\pi^-$ component to build the sWeighted m' and θ' distributions. These distributions are compared to the m' and θ' distributions obtained applying the same cuts to the MC sample. The comparisons between MC and data are shown in Fig. 102 for Run1 and in Fig. 103 for Run2.

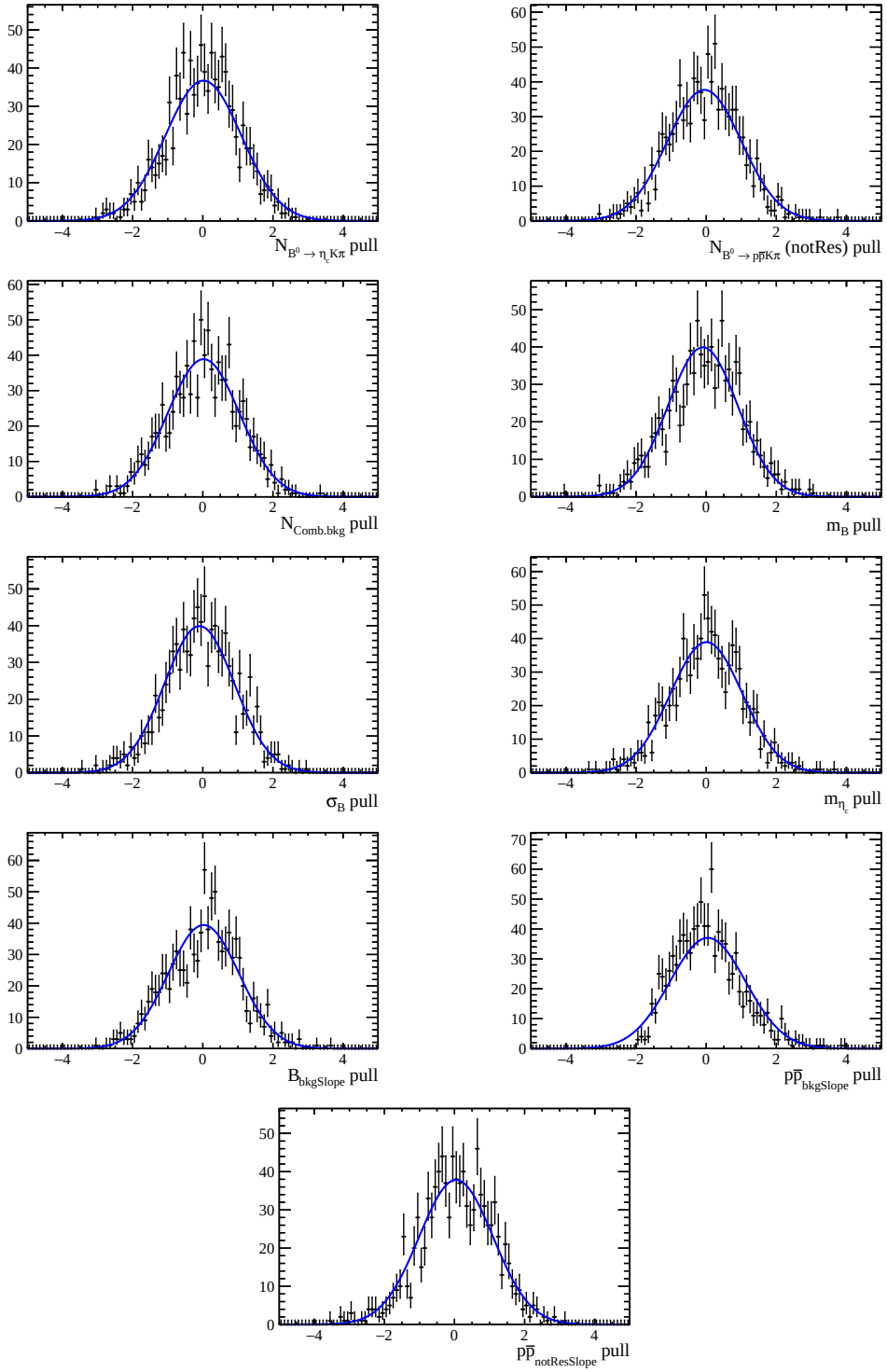

Figure 100: Pull distributions for Run1 2D fit free parameters.

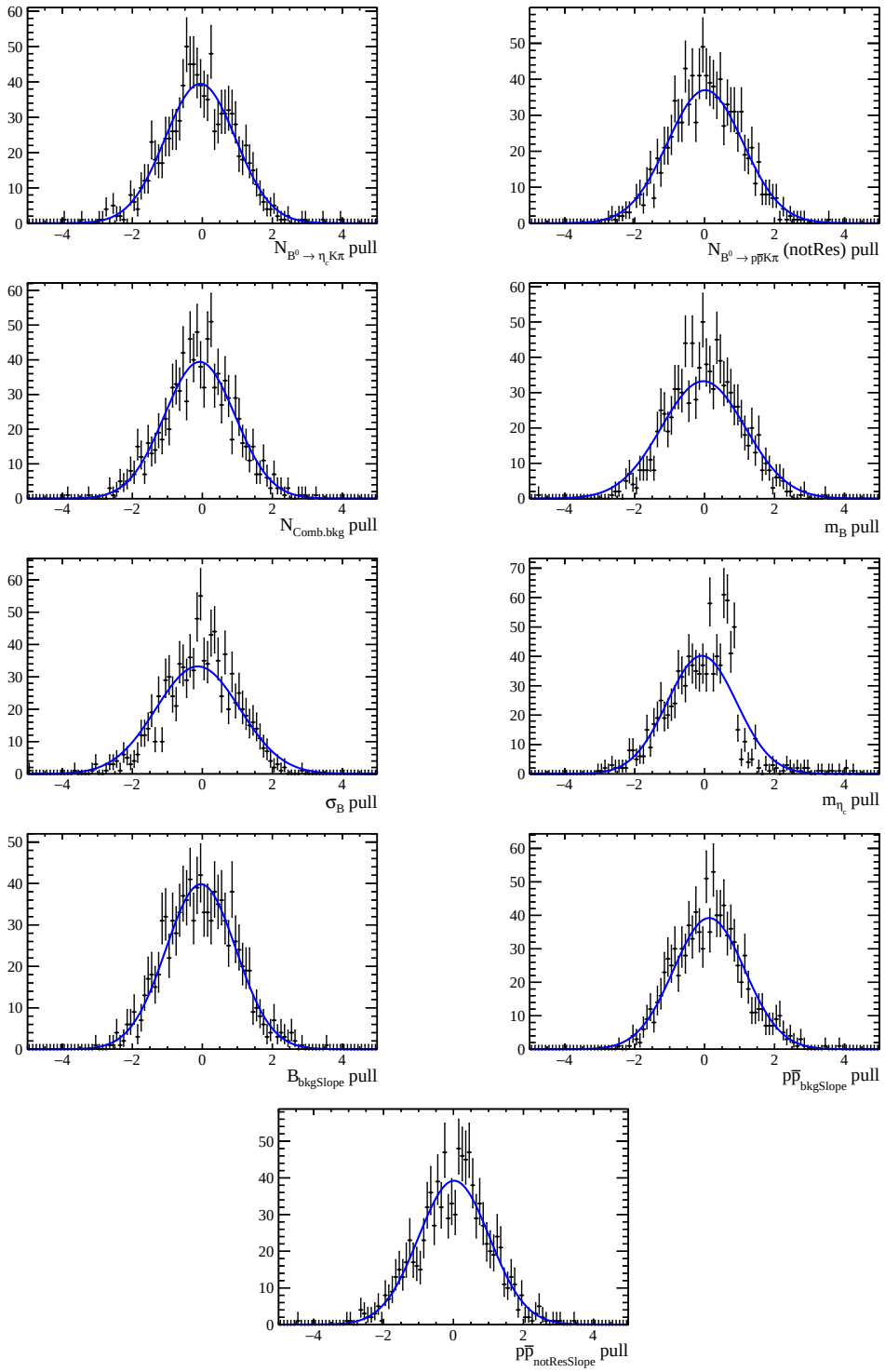

Figure 101: Pull distributions for Run2 2D fit free parameters.

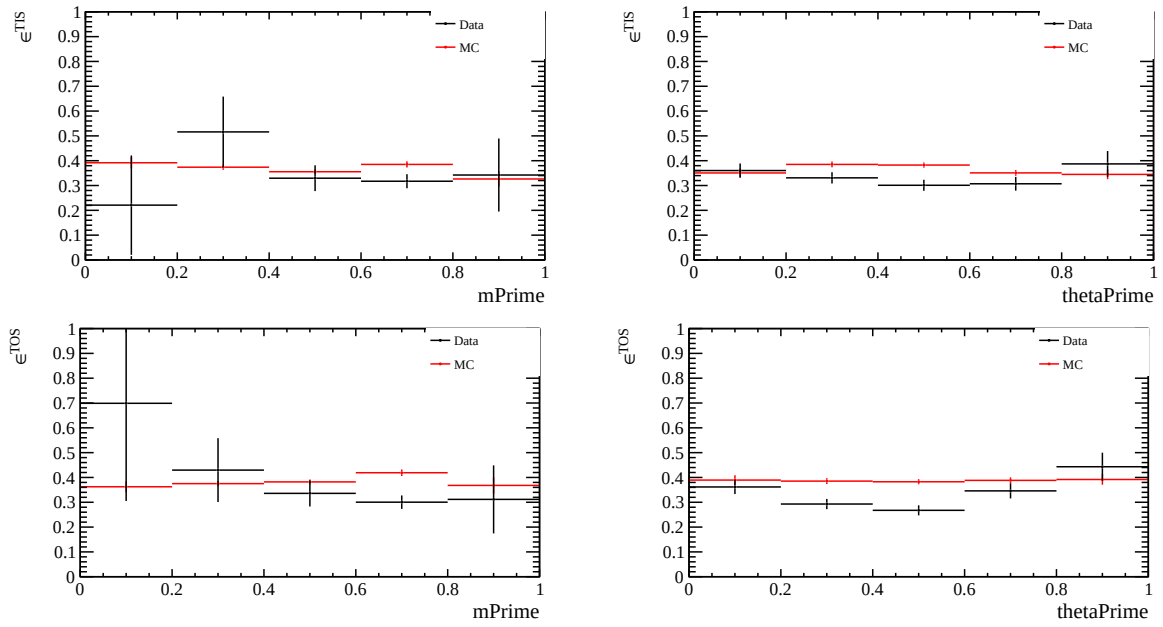

Figure 102: L0 TIS-TOS cross-checks on Run1. Red: MC, black: data. Top left: TIS efficiency as a function of m', Top right: TIS efficiency as a function of θ', Bottom left: TOS efficiency as a function of m', Bottom right: TOS efficiency as a function of θ'.

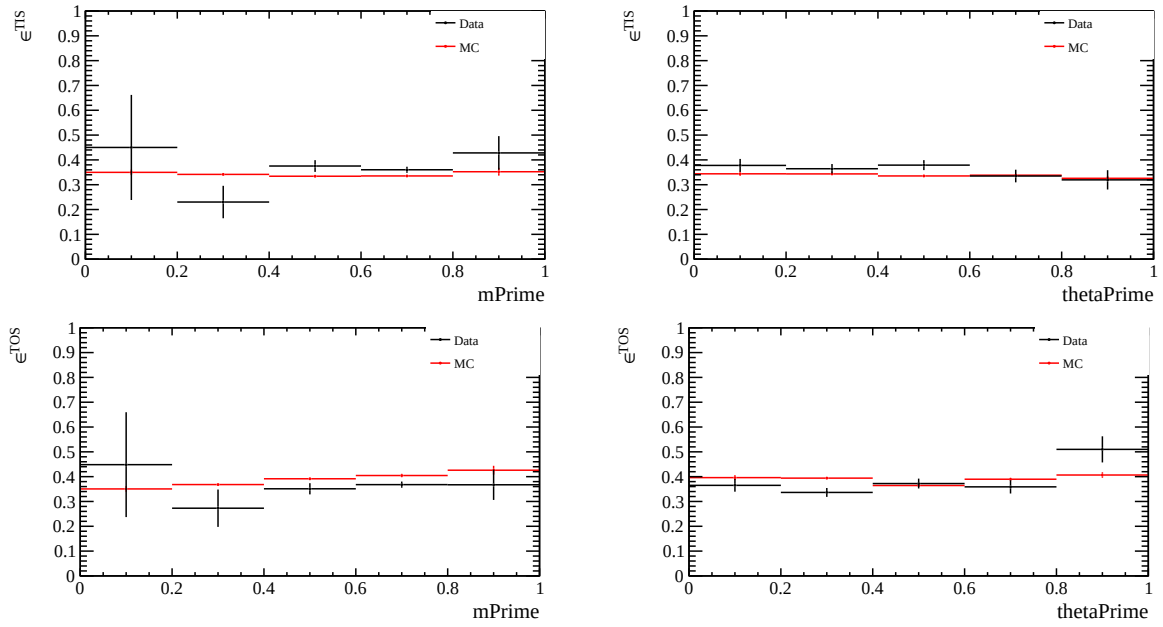

Figure 103: L0 TIS-TOS cross-checks on Run2. Red: MC, black: data. Top left: TIS efficiency as a function of m', Top right: TIS efficiency as a function of θ', Bottom left: TOS efficiency as a function of m', Bottom right: TOS efficiency as a function of θ'.

4.8 Results

In summary, the first measurement of the $B^0 \to \eta_c K^+\pi^-$ branching fraction is reported and gives

$$\mathcal{B}(B^0 \to \eta_c K^+\pi^-) = (5.73 \pm 0.24 \pm 0.13 \pm 0.66) \times 10^{-4},$$

where the first uncertainty is statistical, the second systematic, and the third is due to limited knowledge of external branching fractions. The first Dalitz plot analysis of the $B^0 \to \eta_c K^+\pi^-$ decay is performed. A good description of data is obtained when including a charged charmonium-like resonance decaying to the $\eta_c\pi^-$ final state with $m_{Z_c^-} = 4096 \pm 20\ ^{+18}_{-22}$ MeV and $\Gamma_{Z_c^-} = 152 \pm 58\ ^{+60}_{-35}$ MeV. The fit fractions are reported in Table 48. The fit fractions for resonant and nonresonant contributions are converted into quasi-two-body branching fractions by multiplying by the $B^0 \to \eta_c K^+\pi^-$ branching fraction. The corresponding results are shown in Table 49. The $B^0 \to \eta_c K^*(892)^0$ branching fraction is compatible with the world-average value [15], taking into account the $K^*(892)^0 \to K^+\pi^-$ branching fraction. The values of the interference fit fractions are given in Table 50.

The significance of the $Z_c(4100)^-$ candidate is more than three standard deviations when including systematic uncertainties. This is the first evidence for an exotic state decaying into two pseudoscalars. The favoured spin-parity assignments, $J^P = 0^+$ and $J^P = 1^-$, cannot be discriminated once systematic uncertainties are taken into account, which prohibits unambiguously assigning the $Z_c(4100)^-$ as one of the states foreseen by the models described in Sec. 4.1. Furthermore, the mass value of the $Z_c(4100)^-$ charmonium-like state is above the open-charm threshold, in contrast with the predictions of such models. More data will be required to conclusively determine the nature of the $Z_c(4100)^-$ candidate.

Table 48: Fit fractions and their uncertainties. The quoted uncertainties are statistical and systematic, respectively.

Amplitude	Fit fraction (%)
$B^0 \to \eta_c K^*(892)^0$	$51.4 \pm 1.9\ ^{+1.7}_{-4.8}$
$B^0 \to \eta_c K^*(1410)^0$	$2.1 \pm 1.1\ ^{+1.1}_{-1.1}$
$B^0 \to \eta_c K^+\pi^-$ (NR)	$10.3 \pm 1.4\ ^{+1.0}_{-1.2}$
$B^0 \to \eta_c K_0^*(1430)^0$	$25.3 \pm 3.5\ ^{+3.5}_{-2.8}$
$B^0 \to \eta_c K_2^*(1430)^0$	$4.1 \pm 1.5\ ^{+1.0}_{-1.6}$
$B^0 \to \eta_c K^*(1680)^0$	$2.2 \pm 2.0\ ^{+1.5}_{-1.7}$
$B^0 \to \eta_c K_0^*(1950)^0$	$3.8 \pm 1.8\ ^{+1.4}_{-2.5}$
$B^0 \to Z_c(4100)^- K^+$	$3.3 \pm 1.1\ ^{+1.2}_{-1.1}$

Table 49: Branching fraction results. The four quoted uncertainties are statistical, $B^0 \to \eta_c K^+\pi^-$ branching fraction systematic (not including the contribution from the uncertainty associated to the efficiency ratio, to avoid double counting the systematic uncertainty associated to the evaluation of the efficiencies), fit fraction systematic and external branching fractions uncertainties, respectively.

Decay mode	Branching fraction (10^{-5})
$B^0 \to \eta_c K^*(892)^0(\to K^+\pi^-)$	$29.5 \pm 1.6 \pm 0.6\ ^{+1.0}_{-2.8} \pm 3.4$
$B^0 \to \eta_c K^*(1410)^0(\to K^+\pi^-)$	$1.20 \pm 0.63 \pm 0.02 \pm 0.63 \pm 0.14$
$B^0 \to \eta_c K^+\pi^-$ (NR)	$5.90 \pm 0.84 \pm 0.11\ ^{+0.57}_{-0.69} \pm 0.68$
$B^0 \to \eta_c K_0^*(1430)^0(\to K^+\pi^-)$	$14.50 \pm 2.10 \pm 0.28\ ^{+2.01}_{-1.60} \pm 1.67$
$B^0 \to \eta_c K_2^*(1430)^0(\to K^+\pi^-)$	$2.35 \pm 0.87 \pm 0.05\ ^{+0.57}_{-0.92} \pm 0.27$
$B^0 \to \eta_c K^*(1680)^0(\to K^+\pi^-)$	$1.26 \pm 1.15 \pm 0.02\ ^{+0.86}_{-0.97} \pm 0.15$
$B^0 \to \eta_c K_0^*(1950)^0(\to K^+\pi^-)$	$2.18 \pm 1.04 \pm 0.04\ ^{+0.80}_{-1.43} \pm 0.25$
$B^0 \to Z_c(4100)^- K^+$	$1.89 \pm 0.64 \pm 0.04\ ^{+0.69}_{-0.63} \pm 0.22$

Table 50: Symmetric matrix of the fit fractions (%) from the amplitude fit using the nominal model. The quoted uncertainties are statistical and systematic, respectively. The diagonal elements correspond to the values reported in Table 48.

	$K^*(892)^0$	$K^*(1410)^0$	LASS NR	$K_0^*(1430)^0$	$K_2^*(1430)^0$	$K^*(1680)^0$	$K_0^*(1950)^0$	$Z_c(4100)^-$
$K^*(892)^0$	$51.4 \pm 1.9\ ^{+1.7}_{-4.8}$	$1.7 \pm 1.9\ ^{+2.4}_{-1.4}$	0	0	0	$-2.1 \pm 1.1\ ^{+1.4}_{-1.5}$	0	$1.4 \pm 1.0\ ^{+1.2}_{-1.1}$
$K^*(1410)^0$		$2.1 \pm 1.1\ ^{+1.1}_{-1.1}$	0	0	0	$-2.5 \pm 1.6\ ^{+1.9}_{-1.7}$	0	$-0.4 \pm 0.4\ ^{+0.7}_{-0.5}$
LASS NR			$10.3 \pm 1.4\ ^{+1.0}_{-1.2}$	$-5.8 \pm 1.3\ ^{+2.2}_{-2.0}$	0	0	$-3.2 \pm 2.8\ ^{+4.9}_{-1.4}$	$1.11 \pm 0.23\ ^{+0.54}_{-0.35}$
$K_0^*(1430)^0$				$25.3 \pm 3.5\ ^{+3.5}_{-2.8}$	0	0	$4.7 \pm 0.7\ ^{+1.3}_{-1.5}$	$2.8 \pm 0.4\ ^{+0.6}_{-0.4}$
$K_2^*(1430)^0$					$4.1 \pm 1.5\ ^{+1.0}_{-1.6}$	0	0	$0.00 \pm 0.31\ ^{+0.76}_{-0.26}$
$K^*(1680)^0$						$2.2 \pm 2.0\ ^{+1.5}_{-1.7}$	0	$0.7 \pm 0.5\ ^{+0.5}_{-0.9}$
$K_0^*(1950)^0$							$3.8 \pm 1.8\ ^{+1.4}_{-2.5}$	$0.6 \pm 0.5\ ^{+0.8}_{-1.1}$
$Z_c(4100)^-$								$3.3 \pm 1.1\ ^{+1.2}_{-1.1}$

5 The LHCb and RICH detectors upgrade

The LHCb experiment will undergo a major upgrade in 2019-2020, during the LHC Long Shutdown 2 (LS2), that will make it feasible to collect at least $50\,\text{fb}^{-1}$ of data in less than 10 years [157]. The analysis of this dataset will produce unprecedented precision on the main observables of b and c-quark flavour sectors. The physics motivations for the LHCb upgrade are described in Section 5.1.

The upgrade will enable the experiment to run at an instantaneous luminosity of $2 \times 10^{33}\,\text{cm}^{-2}\text{s}^{-1}$ and the LHCb detector will be readout at the full 40 MHz LHC bunch crossing rate. The online event selection will be performed by a flexible software trigger that will allow to significantly enhance detection efficiencies, especially for b- and c-hadrons decays to hadronic final states. Furthermore, the flexibility assured by the new trigger strategy, will allow to explore different kind of physics during different phases of data taking. The triggerless readout system and the software trigger system will be described in Section 5.2.

All the subdetectors of the LHCb experiment will be modified to comply with these new operating conditions, as summarised in section 5.3. In particular I will focus on the RICH detectors upgrade that comprises the replacement of the HPDs, having an embedded 1 MHz readout electronics, with multianode photomultipliers (MaPMTs) and a brand new external frontend (FE) electronics able to work at 40 MHz. The RICH detectors upgrade is described in Section 5.4.

5.1 Physics motivations for the LHCb upgrade

The analyses using the data collected by LHCb during Run 1 and 2 data are already providing excellent results demonstrating the potential of flavour physics at the LHC, including the first promising deviations from the SM. However, since the measurement of many flavour physics observables will still be limited by statistical uncertainties after Run 2, a five-fold increase in the instantaneous luminosity, from the current $4 \times 10^{32}\,\text{cm}^{-2}\text{s}^{-1}$ to $2 \times 10^{33}\,\text{cm}^{-2}\text{s}^{-1}$, is needed in order to achieve precisions of the order of the theoretical uncertainties in a reasonable amount of time. The bottleneck due to the L0-trigger must be removed to fully exploit the increase in the instantaneous luminosity. As shown in Fig. 104, the yield from the hardware trigger stage is already saturated for hadronic channels, making the increase in luminosity ineffective with the current trigger strategy. Indeed, while decay channels involving muons would be handled efficiently also at higher luminosities, the efficiency of purely hadronic modes, triggered by the deposit of several GeV of E_T by charged hadrons, muons, electrons or photons in the PS, SPD or M1 subsystems, saturates due to the need to tight the typical E_T threshold to respect the 1 MHz bottleneck.

An overview of the main flavour observables with their expected experimental uncertainties after the LHCb upgrade is shown in Fig. 105.

The production of beyond the SM virtual particles is investigated in loop processes of heavy flavour hadrons decays. In particular, the loop processes involving the exchange of the Higgs, $W^\pm$, Z^0 and γ bosons, are predicted with high precision within the SM. For this reason they are the ideal environment to search for NP. These processes are very rare, of the order of 1 over a billion b-decays in the case of Higgs penguins, and for most of them a very high statistics is therefore necessary to be sensitive to NP contributions that

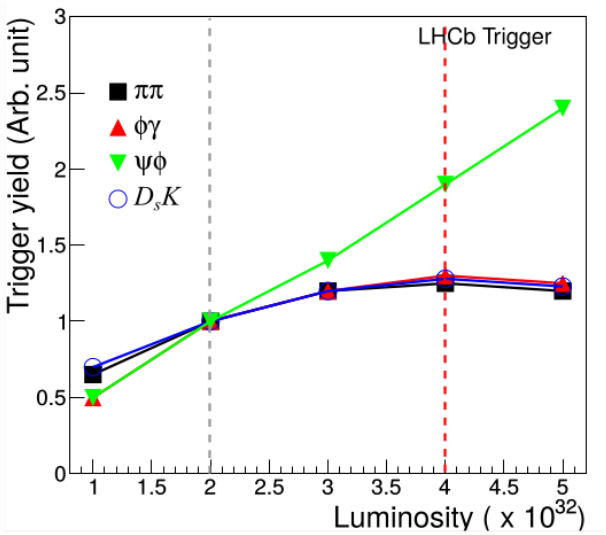

Figure 104: Trigger yield dependance on the instantaneous luminosity.

Type	Observable	Current precision	LHCb 2018	**Upgrade** ($50\ \text{fb}^{-1}$)	Theory uncertainty
B_s^0 mixing	$2\beta_s(B_s^0 \to J/\psi\phi)$	0.10 [139]	0.025	0.008	∼0.003
	$2\beta_s(B_s^0 \to J/\psi\, f_0(980))$	0.17 [219]	0.045	0.014	∼0.01
	a_{sl}^s	6.4×10^{-3} [44]	0.6×10^{-3}	0.2×10^{-3}	0.03×10^{-3}
Gluonic penguins	$2\beta_s^{\text{eff}}(B_s^0 \to \phi\phi)$	–	0.17	0.03	0.02
	$2\beta_s^{\text{eff}}(B_s^0 \to K^{*0}\overline{K}^{*0})$	–	0.13	0.02	< 0.02
	$2\beta^{\text{eff}}(B^0 \to \phi K_S^0)$	0.17 [44]	0.30	0.05	0.02
Right-handed currents	$2\beta_s^{\text{eff}}(B_s^0 \to \phi\gamma)$	–	0.09	0.02	<0.01
	$\tau^{\text{eff}}(B_s^0 \to \phi\gamma)/\tau_{B_s^0}$	–	5 %	1 %	0.2 %
Electroweak penguins	$S_3(B^0 \to K^{*0}\mu^+\mu^-; 1 < q^2 < 6\ \text{GeV}^2/c^4)$	0.08 [68]	0.025	0.008	0.02
	$s_0 A_{\text{FB}}(B^0 \to K^{*0}\mu^+\mu^-)$	25 % [68]	6 %	2 %	7 %
	$A_{\text{I}}(K\mu^+\mu^-; 1 < q^2 < 6\ \text{GeV}^2/c^4)$	0.25 [77]	0.08	0.025	∼0.02
	$\mathcal{B}(B^+ \to \pi^+\mu^+\mu^-)/\mathcal{B}(B^+ \to K^+\mu^+\mu^-)$	25 % [86]	8 %	2.5 %	∼10 %
Higgs penguins	$\mathcal{B}(B_s^0 \to \mu^+\mu^-)$	1.5×10^{-9} [13]	0.5×10^{-9}	0.15×10^{-9}	0.3×10^{-9}
	$\mathcal{B}(B^0 \to \mu^+\mu^-)/\mathcal{B}(B_s^0 \to \mu^+\mu^-)$	–	∼100 %	∼35 %	∼5 %
Unitarity triangle angles	$\gamma(B \to D^{(*)}K^{(*)})$	∼10–12° [252, 266]	4°	0.9°	negligible
	$\gamma(B_s^0 \to D_s K)$	–	11°	2.0°	negligible
	$\beta(B^0 \to J/\psi K_S^0)$	0.8° [44]	0.6°	0.2°	negligible
Charm *CP* violation	A_Γ	2.3×10^{-3} [44]	0.40×10^{-3}	0.07×10^{-3}	–
	ΔA_{CP}	2.1×10^{-3} [18]	0.65×10^{-3}	0.12×10^{-3}	–

Eur. Phys. J. C (2013) 73:2373

Figure 105: List of observables sensitive to NP effects. Current, before and after the upgrade statistical errors and corresponding theoretical uncertainty are shown.

could manifest themselves through an increase of branching ratios or through deviations from predicted angular distributions. Higgs penguins are mainly studied through the $B_{(s)}^0 \to \mu^+\mu^-$ decays [158]. The statistical error on the branching ratio $\mathcal{B}(B_s^0 \to \mu^+\mu^-)$ is expected to be lower than the theoretical one after the upgrade. The uncertainty on the

ratio $\mathcal{B}(B^0 \to \mu^+\mu^-)/\mathcal{B}(B_s^0 \to \mu^+\mu^-)$ will move from $\sim 100\%$ with the current detector data to $\sim 35\%$ with the upgraded LHCb data. Electroweak penguins are currently probed studying decays involving $b \to s\mu^+\mu^-$ transitions, like $B^0 \to K^*\mu^+\mu^-$. First tensions with the SM have been observed [159], to be investigated from both the theoretical and experimental point of view. With the upgrade a complete angular analysis will be achievable and the statistics will also allow to study processes such as $b \to se^+e^-$ and $b \to dl^+l^-$ ($l = \mu,\ e$). Electroweak penguins are very interesting because they can also probe the lepton universality through precision measurements of observables like $\mathcal{R}(K^*)$. Some deviations from the SM predictions have already been observed [64, 159–165]. The increase of statistics will be crucial to confirm them. Photonic penguins, corresponding to $b \to s\gamma$ transitions, are interesting because they are sensitive to models that predict new right-handed currents as a possible extension of the SM. The uncertainties in the related observables with the statistics that will be collected by the upgraded LHCb detector will be comparable to the theoretical errors.

The precise measurement of the CKM matrix elements and of the $B^0_{(s)}$ mixing parameters will allow to search for new sources of CP violation. The uncertainty on β_s will be comparable to the theoretical one after the upgrade. The uncertainty on γ and β CKM parameters and on the CP violation parameters in the charm sector will be lower of about one order of magnitude with respect to the current detector.

The huge production rate of heavy flavour hadrons, like quarkonium and B_c^+ states, will make it possible to acquire a better knowledge of the non-perturbative QCD domain and of the hadronisation processes. New opportunities will open for conventional spectroscopy, for example in the search for the Ξ_{bc} state. The search for new exotic hadrons will be feasible in many b hadrons decay channels.

The potential of the upgraded LHCb extends far beyond quark flavour physics. The unique acceptance, coupled with the flexible trigger strategy, will enable LHCb to make measurements and searches that are either complementary to, or of higher sensitivity than, those which are possible at ATLAS, CMS and other detectors. The search for long-lived exotic particles, the most precise measurement of the electroweak mixing angle $\sin^2\theta_{\rm W}$, the production rate and asymmetry of $W^\pm$ and Z bosons, top quark physics measurements and the search for $H \to b\bar{b}$ decays, are some of the possible physics goals that can be achieved by the upgraded LHCb experiment. Important studies are also possible in the leptonic sector, including the search for lepton flavour violating $\tau^\pm$ decays and for low mass Majorana neutrinos.

5.2 The LHCb Trigger and Online upgrade

One of the main objectives of the LHCb upgrade is the removal of the L0 trigger bottleneck by implementing a trigger-less readout system at 40 MHz, performing solely a software triggering, with an overall output of about 20 kHz of events written to disk [166]. The trigger scheme for the upgraded LHCb is shown in Fig. 106(b).

As shown in Figure 106(a) the current trigger input rate is 40 MHz. This is because for the current detector the readout is limited to 1 MHz so what matters is the overall bunch crossing rate which has to be reduced by the hardware trigger. For the upgraded detector, all the subdetectors will be readout at the full LHC bunch crossing rate, so what matters is the non-empty bunch crossing rate because this is what has to be reduced by the HLT. Therefore the upgrade diagram has the input rate at 30 MHz. The full software

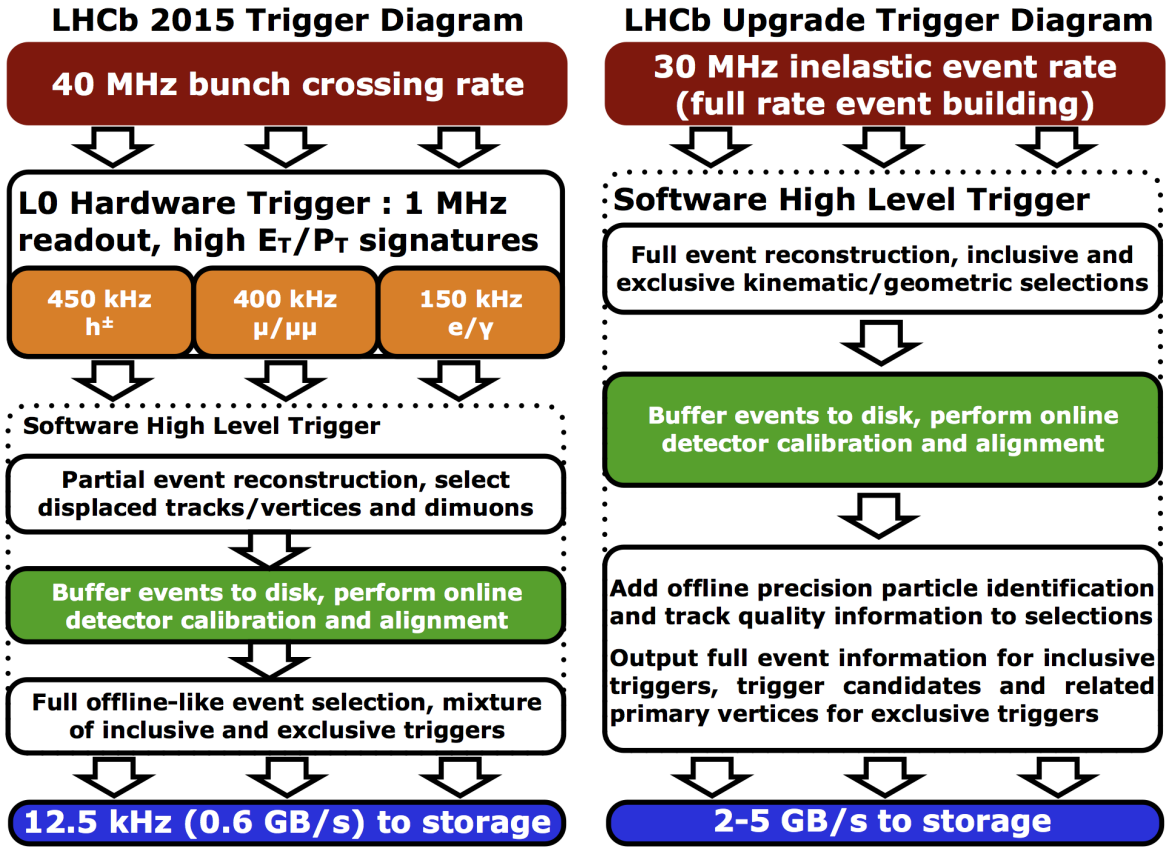

(a) (b)

Figure 106: (a): The Run2 trigger scheme illustrating the central place of the detector alignment and calibration. (b): The upgrade diagram illustrating the continuing use of real time alignment and calibration, as well as giving some details on how events will be split into full/turbo streams.

trigger will run on the LHCb Event Filter Farm (EFF). The event selections applied at the trigger level must be as similar as possible to those applied in offline analyses to maximise trigger efficiencies and to minimise systematic uncertainties.

By removing the L0 trigger, LHC events are recorded and transmitted from the FE electronics to the readout network at the full LHC bunch crossing rate of 40 MHz, resulting in a DAQ bandwidth up to ~ 4 TB/s (event frequency $\times$ expected event size: 40 MHz $\times$ 100 kB). A new readout architecture is required to cope with this dataflow.

The Timing and Fast Control system (TFC) [167] is responsible for keeping the synchronicity across the readout system, tagging each event with the bunch crossing identifier (BXID). Once all the event fragments corresponding to a particular BXID are received by the readout board, the so-called TELL40, it will compile a packet of events. It will be sent across the event-building network (DAQ) to a particular processing node using optical links. The TFC system is also responsible for the control of the FE electronics and for the distribution of the clock and of the synchronous information to the whole readout system (e.g. calibration commands, reset commands, periodic commands). The TFC will exploit the capabilities of the GigaBit Transceiver chipset (GBT) [168]. The logical architecture of the upgraded TFC system is shown in Figure 107.

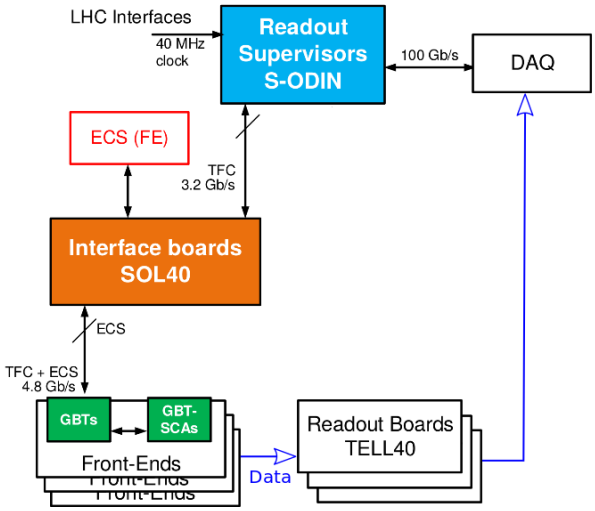

Figure 107: Logical architecture of the upgraded TFC system.

A pool of Readout Supervisors, named SODIN, centrally manages the readout of events by generating synchronous and asynchronous commands, by distributing the LHC clock and by managing the dispatching of events to the EFF. Each SODIN is associated with a subdetector partition, that within the TFC system logic is a cluster of TELL40 and interface boards, the so-called SOL40. The TELL40 boards receive fragments of events from the FE and send them to the DAQ network for the software processing. SOL40 boards are dedicated to distribute fast and slow control from SODIN to the FE, by relaying timing information and clock onto the optical link to the FE, and by appending ECS information onto the same data frame. The SOL40 boards are also dedicated to receive ECS data from the FE, like, for instance, monitored environmental conditions. Clock, fast and slow control are therefore transmitted on the same bidirectional optical link, thanks to the characteristics of the GBT protocol. Due to the huge amount of data which are transmitted from the FE to the TELL40, it has been chosen to separate the links between control and data.

At the FE, the synchronous fast control information are decoded and fanned out by the GBT chip associated to the control links, named Master GBT. The Master GBT is also used to generate the clock to be used at the FE electronics to record data and to drive data GBTs. The slow control configuration data is relayed to the GBT-SCA (standing for Slow Control Adapter) chip, via electrical links (e-links) from the Master GBT. The GBT-SCA chip is capable of distributing ECS configuration data to the FE chips by means of a complete set of buses and interfaces. Monitoring data is sent back via the same optical link by following the return path, from detector components, e.g. a temperature sensor, to GBT-SCA to the Master GBT to the corresponding SOL40.

The same generic hardware, namely the PCIe40 board, based on the PCI Express standard, will be used for the TELL40, SOL40 and SODIN boards, only the different firmware changing the flavour of the board. Each PCIe40 will be equipped with 48 bidirectional optical links.

5.3 The LHCb subdetectors upgrade

The layout of the upgraded LHCb detector is shown in Figure 108. Besides the changes in the subdetectors FE required by the new trigger strategy, the increased luminosity implies challenges as high occupancies, pile-up and radiation damages to be faced. This means that higher granularities and radiation tolerances with respect to the current LHCb detector are needed.

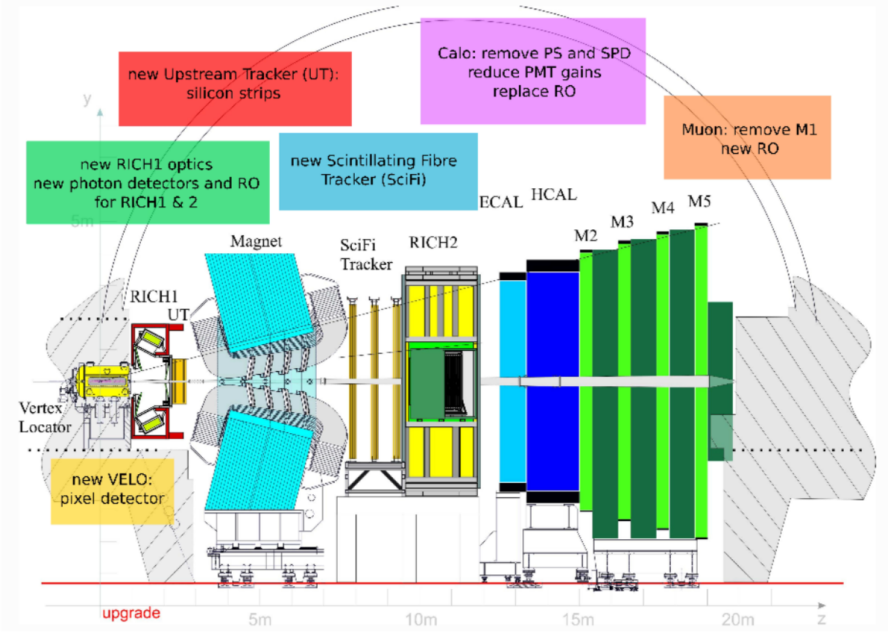

Figure 108: Layout of the upgraded LHCb detector.

The current VELO will be replaced by 26 tracking layers based on $55 \times 55\,\mu m^2$ hybrid pixel sensors that will ensure a better hit resolution and simpler track reconstruction. Figure 109 shows a sketch of the upgraded VELO [169]. It will be closer to the beam axis, from the current 8.4 mm up to 5.1 mm from it. The thickness of RF foil will be reduced and the material budget will move from the current 4.6 % to 1.7 % radiation lengths before the interaction with the first layer, improving the impact parameter resolution by a factor of $\sim 40\,\%$. The VELO tracking efficiency for low momentum tracks will increase and the decay time resolution will be better. In order to cope with the radiation damage, an innovative microchannel two-phase CO_2 cooling technology will be used to cool down the sensors at the temperature of -20 °C.

The Upstream Tracker (UT) [170] will be used for downstream reconstruction of long lived neutral particles decaying outside the VELO acceptance. It will be also essential to improve the trigger timing and the momentum resolution, reconstructing the low momentum tracks deflected outside of the tracking stations. The UT will be composed by four tracking layers based on silicon strip technology. UT is sketched in Figure 110.

The inner sensors will be closer to the beam pipe with respect to the current TT, in order to increase the geometrical acceptance. The segmentation and technology of the sensors is driven by the expected particle occupancy and radiation dose. In the outer region, the strips will be 99.7 mm long with 190 μm pitch, and based on the p^+-in-n technology. The strips in the central region will have same length but 95 μm pitch, and

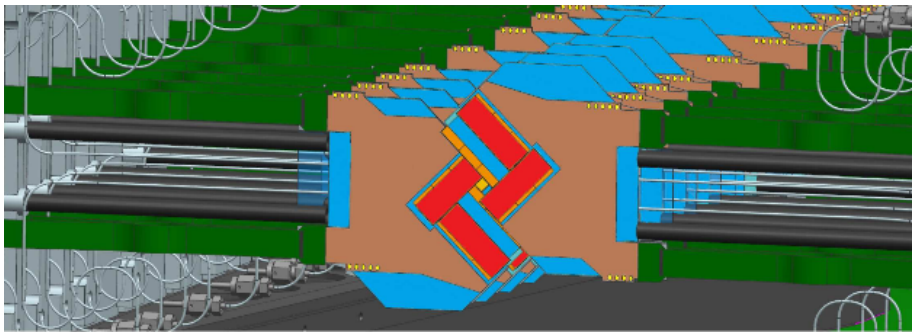

Figure 109: Sketch of the upgraded VELO detector.

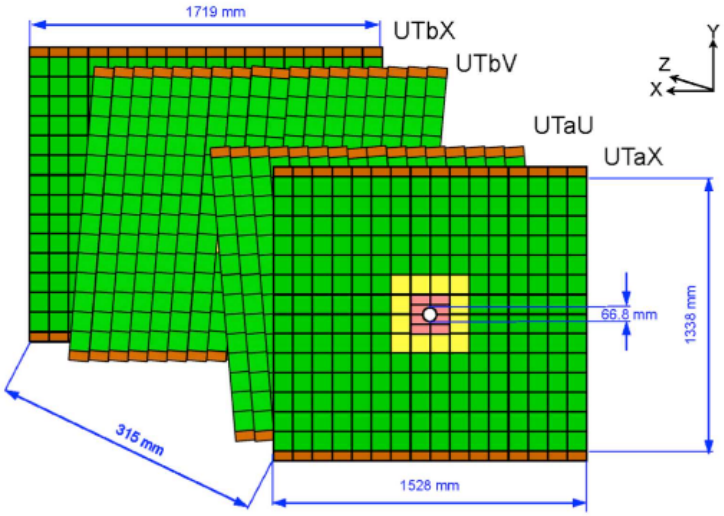

Figure 110: Sketch of the Upstream Tracker.

they will be based on n^+-in-p technology in order to better sustain the higher radiation dose. Finally, the strips closest to the beam will be 49 mm long, with 95 μm pitch and based on n^+-in-p technology. No gaps are present within each layer, increasing the active area. The material budget is lower with respect to the current TT. Since the FE is located in the active area close to the sensors, a better signal to noise ratio will be achieved.

The Scintillating Fibres (SciFi) detector [170] will be structured in 12 detector layers. Figure 111 shows a sketch of SciFi.

SciFi will be based on 2.5 m long plastic scintillating fibres with 250 μm diameter, arranged along the vertical direction. Fibres mats will transport signal outside the acceptance volume, each mat being composed by 6 layers of fibres, with a total layer thickness of 1.35 mm and transversal dimensions of about $6 \times 5\,m^2$. On the vertical direction the layers will be made of two series of fibres separated by mirrors. The fibres will be readout by Silicon Photo-Multipliers (SiPMs) placed at the top and at the bottom of the detector layers, reading arrays of 50 μm^2 sized pixels grouped in modules of 128 channels. SiPMs will be cooled at the temperature of -40 °C in order to decrease the radiation damage and the dark counts rate. SiPM readout will allow an homogeneous coverage with very high granularity resulting in a spatial efficiency better than 70 μm and a single hit efficiency $> 99\,\%$. The usage of UT hits in the track extrapolation from the

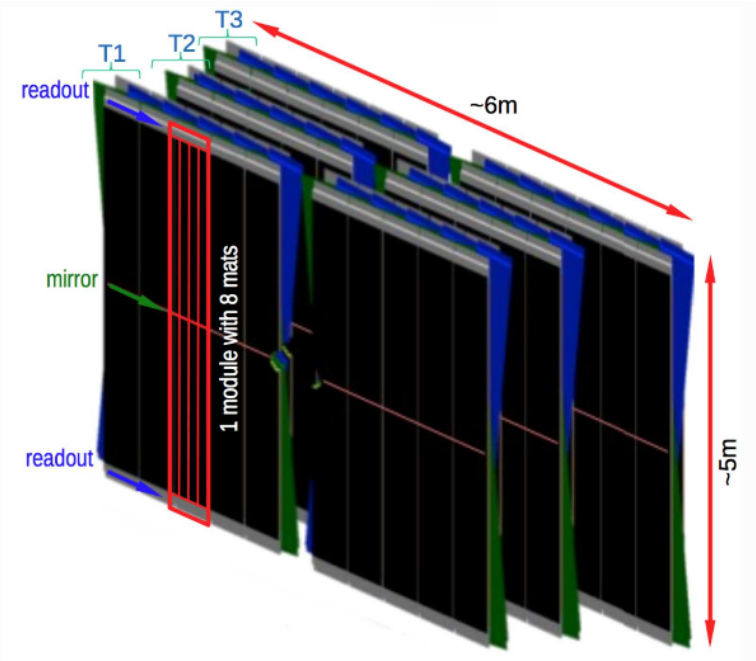

Figure 111: Sketch of SciFi.

VELO to the SciFi detectors will allow to reduce the number of fake tracks reconstructed by the tracking algorithms, by a factor 50-70 %. Consequently, the trigger timing will be largely improved. SciFi will improve the tracking efficiency, reducing in the meanwhile the amount of reconstructed fake tracks, with respect to the eventual usage of the current tracking stations in the upgrade.

The calorimeter and muon systems [171] will undergo minor upgrades with respect to the other subdetectors. PS, SPD and M1 will be removed since they are currently used in the L0 trigger. Regarding CALO, the PMT gains will be reduced and the FE electronics will be modified to cope with the new readout system. Regarding the muon system, the readout electronics will be replaced and a shielding in front of M2 around the beam pipe will be added to reduce the rate in the central region.

5.4 The RICH detectors upgrade

The external layout of both RICH detectors will remain unchanged in the upgrade [171]. Cherenkov radiators will remain the same: C_4F_{10} in RICH 1 and CF_4 in RICH 2. However, the higher luminosity of the upgrade leads to an higher detector occupancy. Currently, with a luminosity of $\mathcal{L} \sim 4 \times 10^{32}\,\mathrm{cm}^{-2}\mathrm{s}^{-1}$ the peak occupancy of the RICH detectors is up to 30% in limited regions of RICH 1. With a luminosity of $\mathcal{L} \sim 2 \times 10^{33}\,\mathrm{cm}^{-2}\mathrm{s}^{-1}$ and the current RICH 1 geometry, the simulated peak occupancy would exceed the 50%. An occupancy of 30% is an upper limit given by the experience with the current RICH detectors and by simulation studies. Indeed the pattern recognition efficiency and hence the PID performance will start to degrade at occupancy values above 30%. In order to reduce the expected peak occupancy below this critical value, the optical layout of RICH 1 will be modified in order to obtain a magnification in the photodetectors planes which is twice the current one. Indeed the occupancy scales inversely with the image surface. This

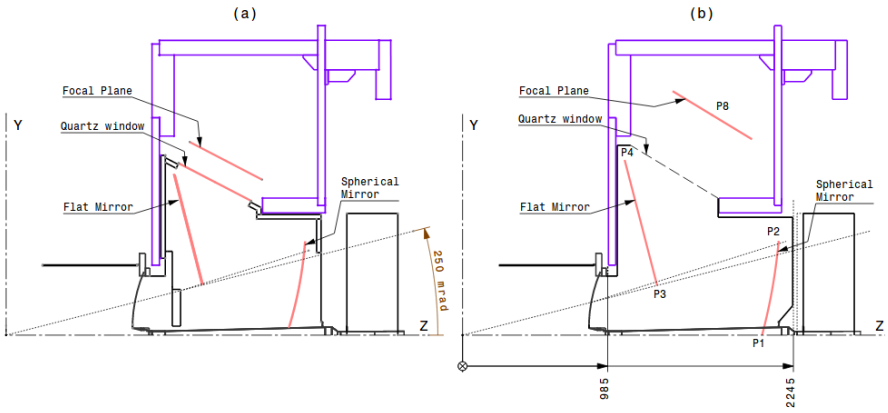

Figure 112: The optical geometries of the current (a) and the upgraded (b) RICH 1. Note that in the upgraded configuration the photodetector plane is moved further away from the beam-line to cope with the increased focal length of the spherical mirrors.

will be achieved increasing the radius of curvature of the spherical mirrors from 2710 mm to 3650 mm, leading to an increased focal length, and rearranging positions, tilt angles and sizes of flat mirrors and photodetectors arrays positions, as shown in Figure 112.

Another major consequence of the increased luminosity, and hence of the required 40 MHz readout, is the replacement of the current photodetectors, the HPDs, having an embedded 1 MHz readout electronics, with Multi-anode Photo-Multiplier Tubes (MaPMTs) and a completely new external FE electronics.

A modular arrangement has been adopted for mounting the photodetectors plane. The mechanics housing the photodetectors arrays has been re-designed for both RICH 1 and RICH 2. The new components and the modular structures will be described in Section 5.4.1, together with the expected performance.

The photodetection system, from the MaPMTs to the digital board interfacing the FE with the LHCb readout system, has been fully characterised in the lab and during testbeams. Tests performed in the lab at CERN, the SysLab, and on the beam will be described in Section 5.6, where I will focus on my contributions to the RICH upgrade project, explained in more detail in the next chapters.

5.4.1 The RICH upgrade photodetection system

The RICH upgrade detectors are conceived as totally modular systems. The main advantage of such a modularity is the flexibility to apply different requirements and settings to different areas of the detectors, for instance depending on the occupancy. Moreover it allows an easier maintenance of the detectors given the independence of the various devices described below. The bricks of the upgraded RICH detectors are the **Elementary Cells** (ECs), housing the MaPMTs and the FE electronics. The EC components are:

- **MaPMTs**: the main reasons behind the choice of MaPMTs as photosensors are the low noise, i.e. the capability to detect single photon signals in the near UV region where the Cherenkov radiation intensity is larger, the fast time response, the pixel granularity, assuring the position sensitivity, and the large active area,

Figure 113: Picture of H-type (left) and R-type (right) MaPMTs. The focusing mesh, providing the separation between different pixels, can be seen.

properties entering the Cherenkov angle resolution and hence the pattern recognition requirements, i.e. the PID performance. Hamamatsu R13742, also referred as R-type MaPMT in the following, are 8×8 pixels 1-inch MaPMTs with pixel size of $\sim 3 \times 3\,\mathrm{mm}^2$, that will be used in the whole RICH 1 and in the central part of the RICH 2 focal plane. Hamamatsu R13743, also referred as H-type MaPMT in the following, are 8×8 pixels 2-inches MaPMTs with pixel size of $\sim 6 \times 6\,\mathrm{mm}^2$, that will be used in the upper and lower parts of RICH 2 focal plane, where the occupancy is lower and hence a coarse pixel granularity does not induce a degradation of the PID performance. R-type and H-type MaPMTs are shown in Figure 113.

The R13742 and R13743 entrance windows are made of UV-glass, having a good light transmittivity in the UV wavelengths and a low ageing due to radiation damage. The R13742 and R13743 have ultra- or super-bialkali photocathodes, improving the quantum efficiency in the near UV region.

A photoelectron is accelerated by an electric field and focused to strike the first electrode (dynode), where electron multiplication takes place by secondary emission. This secondary emission is repeated at each of the subsequent dynodes, resulting in a charge collected by the corresponding anode of the order of $1\,\mathrm{Me}^-$. The R13742 MaPMTs have 12-stage channel dynodes, while the R13743 MaPMTs have 10-stage channel dynodes. Each pixel has its dynode chain, that means that each pixel has in general a different gain.

The collection efficiency at the first dynode affects the total photodetection efficiency. Indeed, if the photoelectron misses the first dynode, the photon hit on the MaPMT is not counted, while if some of the secondary emission electrons miss the next amplification stages, the result is a reduction of the gain. Both the collection efficiency and the gain are functions of several variables, like the angle of the incident photon with respect to the photocatode and the high voltage (HV) applied across the photocatode and the anode. For MaPMTs the typical applied HV is of 1 kV, with negative HV applied to the photocatode and with anode grounding, in order to eliminate the potential difference between the anodes and the FE. The HV will be tuned depending on the conditions at which the MaPMTs will operate and depending on their gains. In the central region of RICH 1, the high occupancy will lead to an high anode current, speeding up the ageing of the MaPMT and resulting

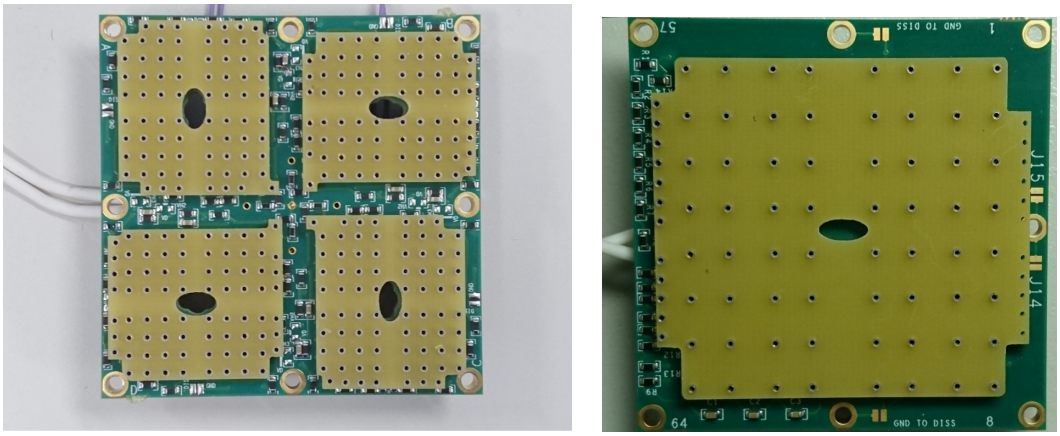

(a) (b)

Figure 114: (a): front view of the Baseboard-R. (b): front view of Baseboard-H. Both pictures show the sockets housing the corresponding MaPMT types anode pins.

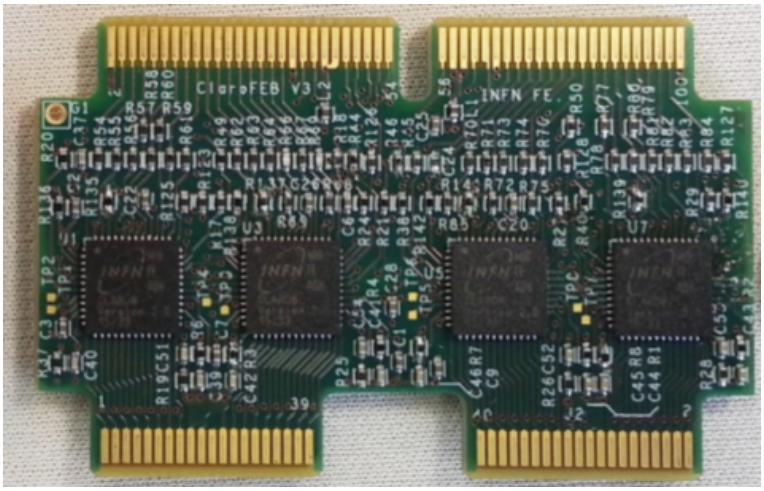

Figure 115: View of one side of a FEB, hosting four CLARO ASICs. The other four chips are hosted on the other side.

in a gain non-linearity affecting the photodetection efficiency. To mitigate these effects, the last dynode will be supplied by a dedicated HV channel.

- **Baseboards**: PCBs providing the mechanical support, the voltage divider biasing the MaPMTs and the low thermal impedance path driving the heat dissipated by the voltage divider towards the aluminium case surrounding and packing the EC components. Baseboard-R, housing four R-type MaPMTs, has four 3 MΩ voltage dividers in parallel, while Baseboard-H, housing one single H-type MaPMT, has a single voltage divider. The Baseboard is also responsible to route the MaPMTs anode signals towards the FE. Both types of Baseboard are shown in Figure 114.

- **FEBs**: each FE Board, shown in Figure 115, comprises 8 CLARO ASICs, responsible for the digitisation of the MaPMT output signals, radiation tolerant 8-channel chips designed in 0.35 μm CMOS technology and developed for the RICH upgrade.

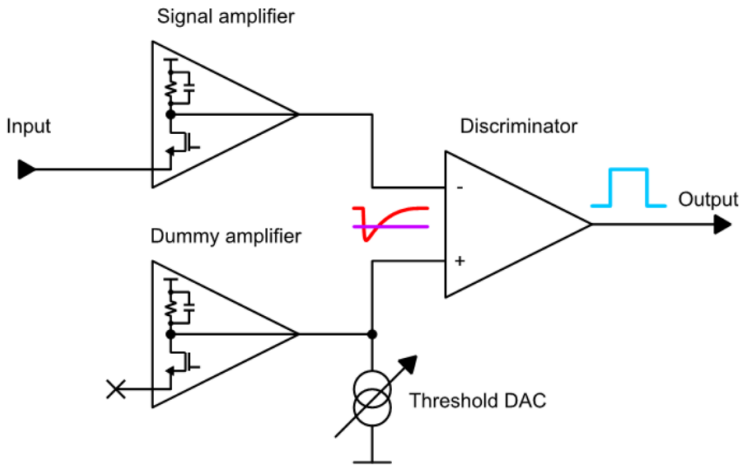

Figure 116: Block diagram showing the functioning of a CLARO channel. The input is the analog signal coming from an MaPMT anode. The dummy amplifier allows to give each channel a differential structure. The binary output is 1 if the charge at the MaPMT anode is larger than the threshold set for this CLARO channel.

Each CLARO channel consists of a charge-sensitive preamplifier coupled to a fast discriminator output stage. The CLARO is able to recover the baseline level after each pulse in less than 25 ns, making possible the 40 MHz readout rate. The power consumption is of the order of 1 mW per channel, with no need for a dedicated FE cooling system. Each CLARO channel can be configured to apply different gain values of the the signal preamplifier and 64 threshold values. CLARO settings will be tuned to obtain the best signal to noise ratio. Indeed, at the CLARO output a digital pulse is provided if the integrated charge collected at the MaPMT anode is larger than the desired threshold, allowing for the separation between spurious counts, e.g. dark counts, and a count due to a photon hitting the corresponding pixel at the MaPMT surface.

- **Backboards**: PCBs responsible to route the digital signals from the FEBs to the digital boards, described later on. Backboard-R will read four FEBs, while Backboard-H will read two FEBs. Backboards also provide the electro-mechanical interface between the FEBs, the readout digital boards and the mechanics housing the RICH columns. Both types of Backboards are shown in Figure 117.

Therefore, in the whole RICH 1 and in the central region of RICH 2, the EC-R, composed by four R-type MaPMTs, one Baseboard-R, four FEBs, one Backboard-R, the structural aluminium case and the magnetic shield (if needed) will be used. In the low occupancy regions of RICH 2, the EC-H, composed by one single H-type MaPMT, one Baseboard-H, two FEBs, one Backboard-H and the structural aluminium case, will be used. CAD models for the EC-R and the EC-H are shown in Figure 118. An exploded view of EC-R components is shown in Figure 119(a). A photograph of the R-type and H-type ECs is reported in Figure 119(b).

The last hardware component building the upgraded RICH detectors is the Photo-Detector Module Digital Board (**PDMDB**), providing the interface between the RICH FE and the upgraded LHCb common readout architecture. There are two flavours of

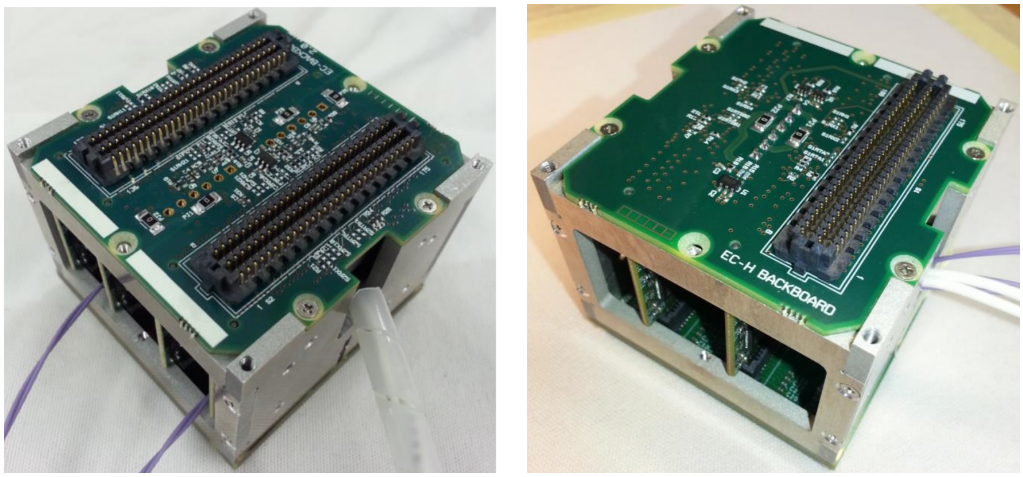

(a) (b)

Figure 117: (a): View of the Backboard-R and EC-R assembly from the back side. (b): View of the Backboard-H and EC-H assembly from the back side.

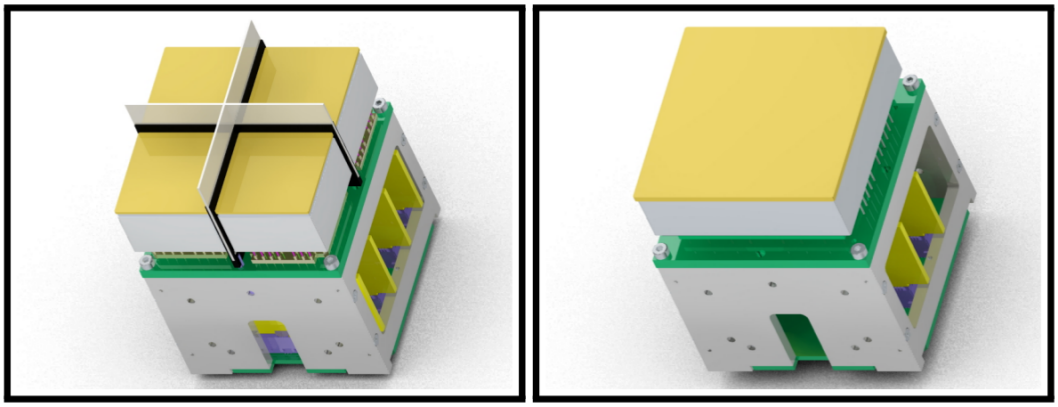

Figure 118: CAD models of the EC-R (left) and EC-H (right). A cross-shaped magnetic shield is foreseen for ECs-R in RICH 1, due to the not negligible residual magnetic field.

PDMDBs: the PDMDB-R, in the EC-R regions, and the PDMDB-H, in the EC-H regions. Pairs of face-to-face PDMDB-R or one single PDMDB-H, together with four ECs-R or ECs-H in a row, build the higher level of modularity of the RICH detectors, the Photo-Detector Module (**PDM**). A PDM is a logical concept, in the sense that no mechanical structure is foreseen for it in the final detector. However, it is the first level of modularity able to completely interact with the new LHCb readout. Moreover, different PDMs are powered by different HV channels. This means that the 16 MaPMTs (or 4 in the ECs-H case) within a PDM must have similar average gains in order to make possible the fine tuning of the HV to optimise the signal to noise ratio. In order to cope with the differences in the pixel gains within each MaPMT, the CLARO threshold bit will be used.

The connection between the PDMBs and the new LHCb readout architecture, introduced in Section 5.2, is implemented using optical links. Each PDMDB will require up to $6 \times 4.8\,\text{Gbit/s}$ links to transmit data to the corresponding TELL40 board. In addition, one receiver (RX) and one transmitter (TX) $4.8\,\text{Gbit/s}$ links will be used to

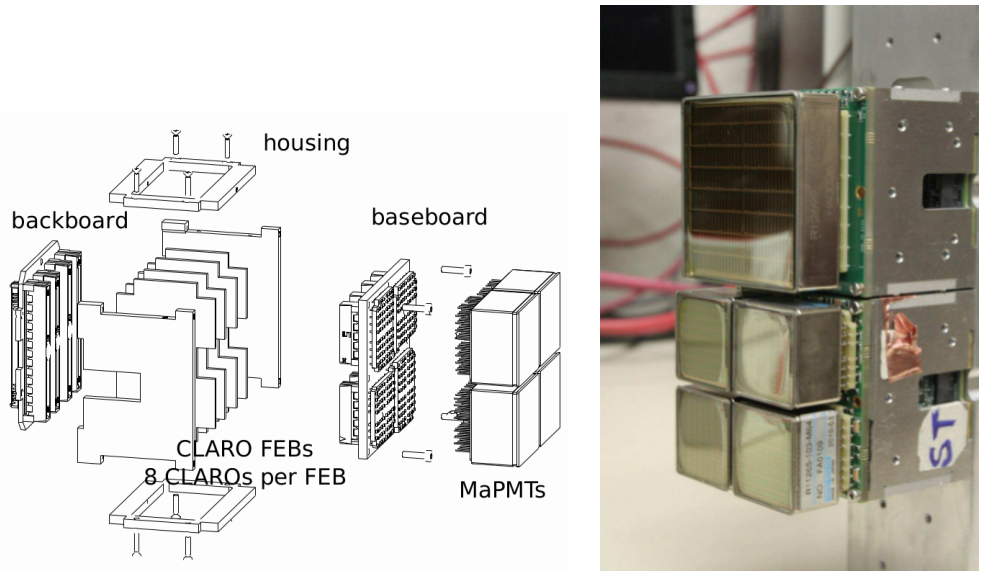

(a) (b)

Figure 119: (a): Exploded view of EC-R components. (b): EC-H (top) and EC-R (bottom) mounted on a custom mechanical structure used for tests in the SysLab and during testbeams.

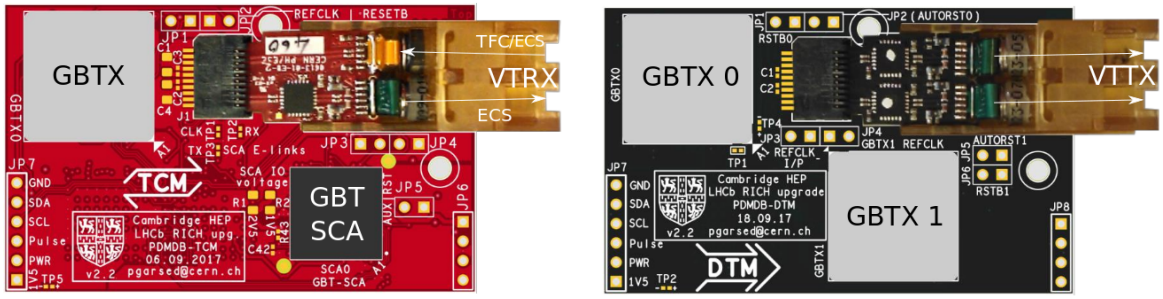

(a) (b)

Figure 120: (a): Timing and Control Module. (b): Data Transmission Module.

receive and transmit TFC and ECS data from and to the corresponding SOL40 board. These links are implemented using the radiation-hard versatile link components developed at CERN [172]. Data packets will be transmitted using three identical VTTX dual optical transmitter modules, each driven by a single GBTX chip for each transmitter. TFC and ECS data will be received and transmitted using a single VTRX optical transceiver module, in tandem with a GBTX chip operating in transceiver mode and a GBT-SCA to provide slow controls interface to the digital board. Two types of plug-in modules are foreseen: the Data Transmission Module (**DTM**), implementing the GBT chipset and the versatile link components for a dual optical data transmitter, and the Timing and Control Module (**TCM**), implementing the GBT chipset and versatile link component for an optical transceiver. Plug-in modules are shown in Figure 120.

PDMDBs-R will contain three DTMs and one TCM, while PDMDB-H will contain two DTMs and one TCM. The GBTX on the TCM is the Master GBT receiving the 40 MHz

LHC reference clock from the corresponding SOL40 board. The Master GBT fans out the clock to the GBTX-0 chip on the DTMs, while GBTX-1 is synchronised using a reference clock from GBTX-0. These clocks are used to latch the digital output signal from the CLAROs and routed by backboards to the PDMDBs. Several interfaces are available within the TCM module. In particular it provides an SPI interface to the FE used as the communication protocol for the configuration of the CLAROs. The distribution of the Low Voltage (LV) among the different active components of the PDMDBs will be provided by DC-DC converters designed and produced at CERN.

6 PDMs in a row will build a RICH column, an independent subsystem having its own mechanical infrastructure, an aluminium T-bar realising also the thermal exchange and heat transfer among the various active components of the column. This is achieved by means of a coolant circulation inside two 10 mm diameter holes running along the T-bar, where a Novec coolant fluid flows in opposite directions. Beside the circulating coolant to maintain the temperature of the MaPMTs and readout electronics within safety limits, each column will require several services: optical fibres to transmit/receive data from the PDMDBs, the LV power supplies for the PDMDBs and the HV power supplies for the operations of the MaPMTs. The columns mechanical infrastructure has been designed in order to provide optimal access when maintenance will be needed, i.e. each column can be extracted independently from the others. RICH 1 columns will be made by 22 ECs-R while RICH 2 columns will be made by 24 ECs, 8 ECs-R and 16 ECs-H. A sketch of a RICH 2 column is shown in Figure 121(a). A 2D array made of columns is called Photo-Detector Assembly (PDA). As in the current RICH detectors, both RICH 1 and RICH 2 will be composed by two PDAs. Each PDA will be composed by 11 columns in RICH 1 and by 12 columns in RICH 2. A CAD representation of a RICH 2 PDA is shown in Figure 121(b).

5.5 Performance of the upgraded RICH detectors

Simulation studies have been performed within the LHCb software framework to evaluate the performance of the upgraded RICH detectors [173]. The generated signal events are $B_s^0 \to \phi(\to K^+K^-)\phi(\to K^+K^-)$. The PID performance is defined in terms of the efficiency of identifying a true kaon as a kaon and the misidentification probability of a true pion to be identified as a kaon or heavier particle. These quantities are plotted in Figure 122.

5.6 Tests of the photodetection system in the SysLab and on beam

All the prototypes of the RICH upgrade photodetection system have been operated in various testbeam sessions carried out since 2014 [174] at the SPS North Area at CERN, in order to progressively test the components as long as they were developed and produced, using them to build the first ECs and PDMs.

Starting from 2017, a system demonstrator laboratory, the SysLab, has been setup at CERN to perform systematic studies on the opto-electronic chain integrating the tests done during testbeams.

I actively contributed to the commissioning of the SysLab and to the tests and developments carried out therein. As an example, tests with an high rate source were

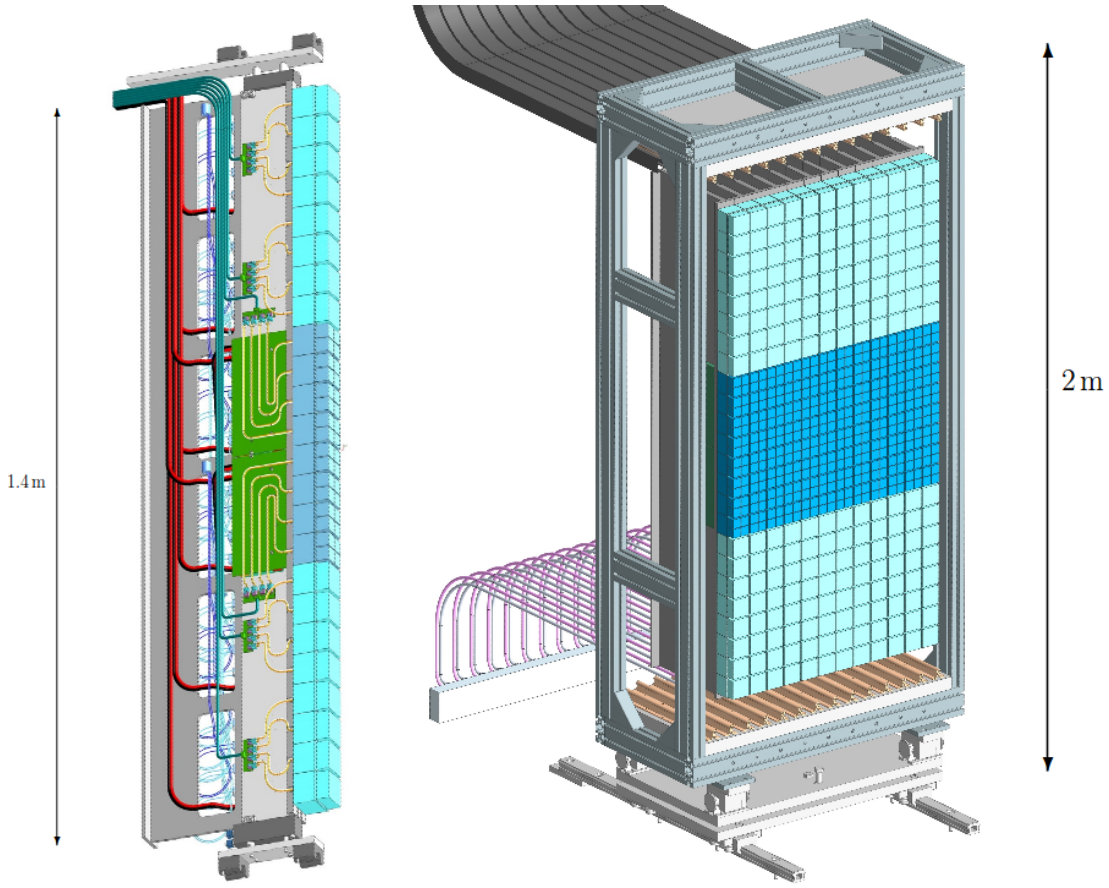

Figure 121: (a): View of a RICH 2 column including the routing of the HV and LV cables and fibres. (b): A CAD representation of a RICH 2 PDA.

needed to get a response on the MaPMTs powering scheme to adopt in the high occupancy regions. I carried out these measurements confirming the need to power the last dynode in RICH 1.

Several activities have been performed and are still ongoing in the SysLab, with the goal to develop all the functionality that will be required for the characterisation of the RICH columns and hence for the commissioning of the final upgraded RICH detectors. Within these activities there is the development and management of the RICH upgrade database, that I implemented as described in Chapter 6. It will be used to build ECs, PDMs and columns grouping MaPMTs with similar characteristics and it will contain more information as possible to make easier the maintenance and repair of the detector during operations.

A crucial development activity is the integration between the RICH FE and the upgraded LHCb readout prototypes. I contributed to this task especially on the control side, comprising the configuration of the FE and the Run Control (including the implementation of the automated procedures to perform detector calibrations), the monitoring, control and archiving of the power supplies and the monitoring and archiving of environmental conditions like temperatures. I developed the control software during my PhD, since the first testbeam in which I was involved. The prototype of this RICH upgrade ECS is

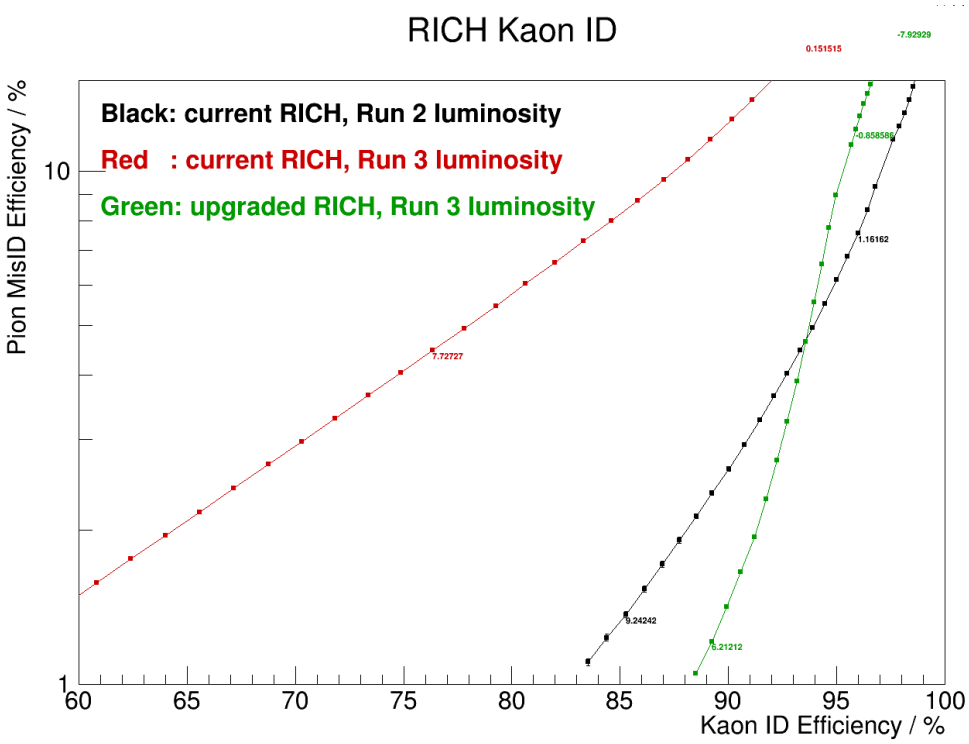

Figure 122: Comparison of the PID performances from the RICH in the current configurations (black curve), with the current detectors and upgraded luminosity (red curve) and with the upgraded configurations (green curve).

described in Chapter 7. The improvements on both the RICH FE and Online readout sides obtained in the SysLab, lead to a testbeam with a full PDM composed by the latest and final versions of most of the hardware components, reading out data with the MiniDAQ2, a server containing the integration of SODIN, SOL40 and TELL40 in a single PCIe40. The RICH upgrade has been the first LHCb upgrade project that used the MiniDAQ in a testbeam. A schematic view of the setup used in the last testbeam in October 2017 is shown in Figure 123.

A picture of the setup characterised in the SysLab and used during the last testbeam is shown in Figure 124. It includes a PDM composed by 3 ECs-R, 1 EC-H and 2 PDMDBs. The TFC, ECS and data packing functionality worked as expected during the testbeam, validating not only the RICH FE and the PDMDBs but also the Online framework developed as the prototype for the final readout architecture.

Thanks to the advances achieved in the integration of the RICH upgrade prototypes and the upgraded LHCb architecture, the module shown in Figure 124 has been recently installed in the current RICH 2. The PDM will be readout at 40 MHz, receiving the LHC clock thanks to the connection of the MiniDAQ to the LHCb ODIN system. The PDM will be therefore operated for the whole 2018 data taking year, providing an exceptional way to test the RICH upgrade components in the LHC environment. I contributed to the installation in RICH 2 and I developed the control software, also comprising the sending of automatic messages to make easier the operations of the module.

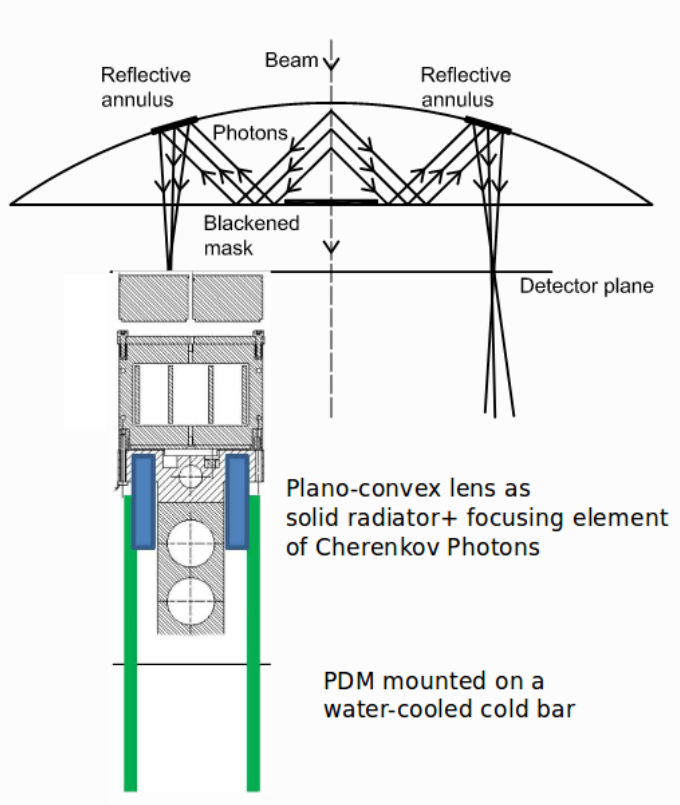

Figure 123: Schematic view of the testbeam setup used in the last testbeam.

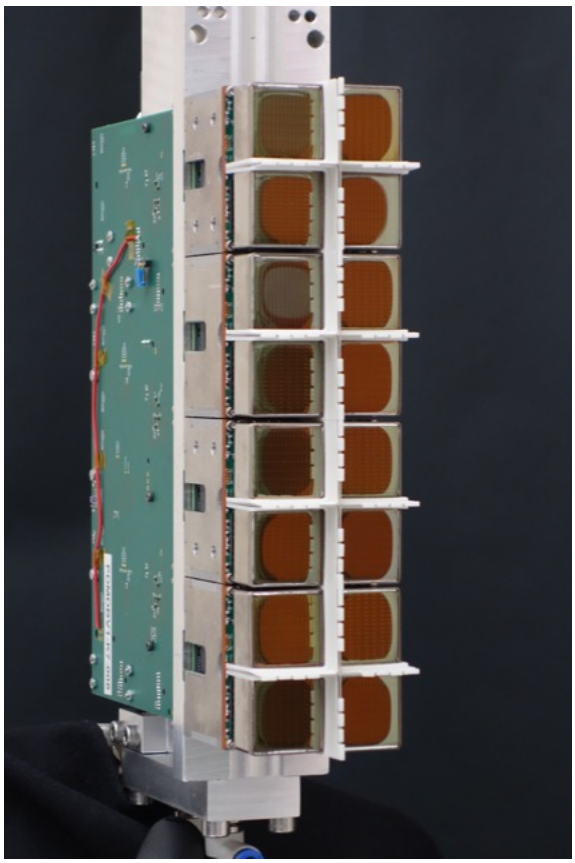

Figure 124: Picture of the PDM assembled at CERN for testing of pre-production components, composed by four ECs-R and two PDMDBs-R. From the front the the back, the 16 MaPMTs, the magnetic shields with their insulator (in white), the mechanical structures enveloping each EC-R and a PDMDB-R can be seen. Moreover, the prototype of the coolant bar also acting as a support structure is shown. The system is used during tests in the SysLab, during testbeams and is now installed in RICH 2.

6 Development of the RICH upgrade Inventory, Bookkeeping and Connectivity Database

As described in Chapter 5, the upgraded RICH detectors are conceived as modular assemblies, based on fully autonomous functional units, the ECs. A total of 1056 ECs will be installed in the upgraded RICH detectors; considering the necessity for spares, a total of 1225 ECs is targeted for production (775 ECs-R and 450 ECs-H). These numbers translate into a large number of hardware units:

- 3100 R-type MaPMTs;
- 450 H-type MaPMTs;
- 775 R-type Baseboards;
- 450 H-type Baseboards;
- 4000 FEBs, each one hosting 8 CLARO chips, for a total of 32000 CLARO chips;
- 775 R-type Backboards;
- 450 H-type Backboards;
- 310 PDMDBs.

All these units are tested by dedicated facilities in different institutes. Moreover, measurements of the interesting properties for each device, *e.g.* the average and pixel-by-pixel gains at different HV for each MaPMT, are performed. The flow of the EC components from production to the final RICH detectors assembling at CERN is shown in Fig. 125.

The large number of components, their connectivity into the modules that will build large surface detectors such as RICH 1 and RICH 2 and their qualification and test performed in scattered locations outside CERN, motivated the development of a central database as a traceability and bookkeeping system. The measurements provided by the quality assurance facilities need to be stored in this central database also to have a complete and self-consistent set of information during the assembling of ECs, PDMs and columns, that is based on criteria depending on MaPMTs and FE parameters aiming to optimise the PID performance of the upgrade RICH detectors.

6.1 Main requirements for the IBCDB project

Keeping into account the motivations introduced above, the main requirements for the database are the following:

- full detector inventory and bookkeeping with hardware information (settings and calibration data) and location of each device, accounting for the hierarchical structure of all the different levels of modularity;

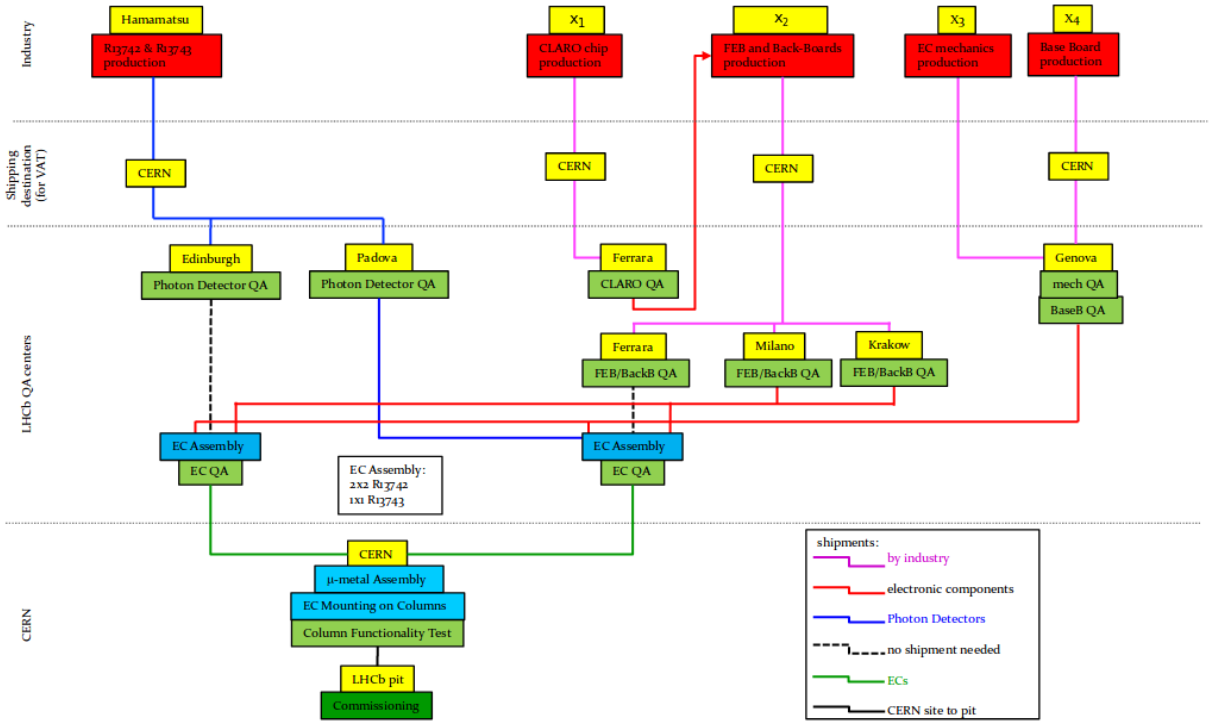

Figure 125: Flow of EC device units from factory to CERN. In addition, PDMDBs will be produced and tested in Cambridge and then shipped to CERN.

- capability to save records with interval of validity date/time and transaction date/time, *e.g.* to allow changes in time of the assembly content and to allow the insertion of improved settings and/or calibration data, without loosing track of the historical records;
- capability to group together devices depending on variables of interest, *e.g.* gains and dark counts of MaPMTs, parameters of the CLARO ASICs, etc;
- capability to take a snapshot of all detector data, retrieving all and only the data valid during a certain period of time (device data and locations);
- capability to easily and quickly retrieve data of devices installed in a specific location in the detector;
- a user-friendly interface and easy access;
- multi-user access, with access control and logging of date/time and user for any transaction;
- users cannot delete records, they can only insert a new record with appropriate time interval of validity range, in order to keep track of the full history;
- capability to load channel-by-channel running configurations, in particular during the commissioning phase;

- easy integration with the LHCb Experiment Control System (ECS) [175] and with the standard LHCb Conditions (CondDB) [176] and Configuration (ConfDB) [177] databases.

Given the impossibility to find a tool matching all these requirements, the database, referred to as the Inventory, Bookkeeping and Connectivity Database (IBCDB) in the following, is developed from scratch.

6.2 Implementation of the IBCDB project

Given the impossibility to find a tool satisfying all the requirements listed in the previous section, I developed the IBCDB from scratch using the WinCC-OA SCADA tool exploiting the functionality already available within the JCOP framework [126]. The main motivation for this choice is due to the fact that, following the strategy adopted for the current LHCb ECS (described in section 3.4), the upgraded LHCb ECS will be developed within the JCOP framework.

WinCC-OA, being a control software, is *device oriented*. Variables can be grouped, allocated in memory and used collectively [127]. The group description is the *Datapoint Type* (DPT). An instance in memory of a DPT is a *Datapoint* (DP). The individual variables are called *Datapoint elements* (DPEs). For each DPE, apart from the corresponding value, further information can be kept: the corresponding hardware address, a range of values outside which one should define an alarm, whether the values has to be stored in an archive, etc. All this meta information are held in *configs*. A practical example of a DP is the declaration of a HV channel. The HV channel DP has different variables (DPEs) used to monitor and control the hardware, e.g. the voltage setting. The voltage setting DPE will have the Address config, used by WinCC-OA to communicate with the hardware (for example the OPC address for the channel). Since a lot of channels having the same structure are required, the structure of the channels is defined once as a DPT, and each channel is then declared as an instance of this DPT. Therefore WinCC-OA has capabilities for device description, through DPs and DPEs, and for archiving, through an archive config appended to the corresponding datapoint element. These WinCC-OA features fit well with the necessity to describe the upgraded RICH detectors modularity and with the requirement to keep track of the history of each devices. Details on the IBCDB DPT structure are described in subsection 6.3, while the description of the archiving strategy is described in subsection 6.4.

A WinCC-OA project comprises different layers. Basic elements are the *User Interface Layer*, which assures the IBCDB to be user-friendly and allows simplified actions through simple WinCC-OA panels, the *Processing Layer*, which handles the execution of background scripts, and the *Communication and Memory Layer*, which handles the communication between DPs and the processes started by other layers. WinCC-OA can also be used to build a *distributed system*: a cluster of projects where each system can display and process data from other systems. The development of the IBCDB as a distributed system within the WinCC-OA and JCOP frameworks will allow an easy integration with the ECS of the upgraded LHCb [166], with low network load (only requested data is transferred).

The ConfDB is the ORACLE [178] database used by the ECS and containing all the parameters required to configure the electronics equipment of the subdetectors during

data taking. Therefore all the information like hardware addresses, geographical location and operational parameters, as well as the connectivity between devices, are extracted from the ConfDB and loaded into WinCC using panels provided by the JCOP framework. Configurations are stored as named *Recipes*, applied automatically according to the currently set activity in the Run Control. The integration of the IBCDB with the LHCb ConfDB [177] will be straightforward and the IBCDB can be used as a source of information for the ConfDB.

The LHCb CondDB [176] contains the detector description and the conditions needed for reconstruction and analysis, e.g. "single-version" data (like the numbers read by a temperature probe) and "multi-version" data (like the numbers coming from alignment tasks). As such it is used in the High Level Trigger, reconstruction, analysis and simulation. The LHCb ECS writes to ORACLE via a DB Writer Process. The IBCDB capability to save data with interval of validity date/time and transaction date/time matches with the versioned data required by the CondDB.

Moreover, WinCC-OA is a multi-platform software, running on both Windows and Linux, allowing for operations of the projects that are mostly independent from the machine OS. The IBCDB project is running on a CentOS 7 machine, the same OS used by the majority of virtual machines where the current LHCb ECS is running.

6.3 The IBCDB Datapoint Types

The IBCDB project is structured in two domains:

- the **Hardware domain**, used to insert and retrieve hardware related information (e.g. MaPMTs calibration data), to establish the connectivity between the hardware units and the RICH assemblies (e.g. which MaPMTs, Baseboard, FEBs and Backboards are used to build an EC), and to retrieve the hierarchy of the different devices;

- the **Logical domain**, used to move devices between different locations (e.g. quality assurance labs) to keep track of the different device locations during quality assurance programmes. Furthermore, the logical domain will allow to retrieve data of devices installed in a specific location of the detector.

Given the RICH upgrade modularity, a DPT has been created for each hardware unit and device assembly type: **MAPMT**, **BaseBoard**, **FEB**, **BackBoard**, **EC**, **PDMDB**, **PDM**, **Array**, **PDA**. These DPTs belong to the Hardware domain.
In addition, the **ALIAS** DPT has been created to handle the movement of devices between different physical locations. The ALIAS DPT refers to the Logical domain.

The DPTs have been created with a structure as flexible and homogeneous as possible. Instances of these DPTs, i.e. DPs, correspond to devices or locations. The former are uniquely identified by their *serial number* datapoint element, the latter by their *alias* datapoint element.

Some efforts have been made to separate the IBCDB scripts, libraries and also user interfaces, as much as possible, from the RICH upgrade specific parts. In this way the IBCDB project, once defined specific datapoint types, could also be used by other subdetectors.

6.3.1 Hardware domain datapoint elements

An example of Hardware domain datapoint type instance is shown in Figure 126. The datapoints have the following datapoint elements:

- *serialNumber*: unique string identifier of a device throughout the database. Each hardware unit has the corresponding QR-code to be used as serial number;
- *status*: integer identifying the status of the device. Currently the possible values are:
  - status = -1 ⇒ DP is empty, can be used to insert a new device in the database;
  - status = 1 ⇒ device is NOT_READY to be used for the data taking, e.g. device exists but has not been tested yet;
  - status = 0 ⇒ device is READY to be used for data taking;
  - status = 100 ⇒ device is BROKEN, to be repaired;
  - status = 255 ⇒ device has been REJECTED by the corresponding quality assurance programme;
  - status = x ⇒ any other state can be defined depending on the user requirements.
- *id* (structure): it contains all the delivery information from the industry to the quality assurance facility;
- *location* (structure): it contains the position of the device during time, accessed through the *valid* subnode. The location node is the link between the Hardware domain and the Logical domain;
- *alias*: the current location of the device;
- *logfile* and *userDefined* nodes: structures where device type specific information can be inserted;
- *parents*: it contains the serial number of the higher level of modularity (e.g. in a MaPMT datapoint it is the serial number of the EC where the MaPMT is inserted);
- *children* node: it contains the serial numbers of the lower level of modularity, device type specific (e.g. in an EC datapoint it contains the serial numbers of the EC components);
- *datasheet*: it contains the production datasheet of the device, device type specific (not all the devices have datasheet);
- *calibration* node: it contains the calibration data of the device;
- *settings*: dynamic array containing the parameters corresponding to a device working point, device type specific.

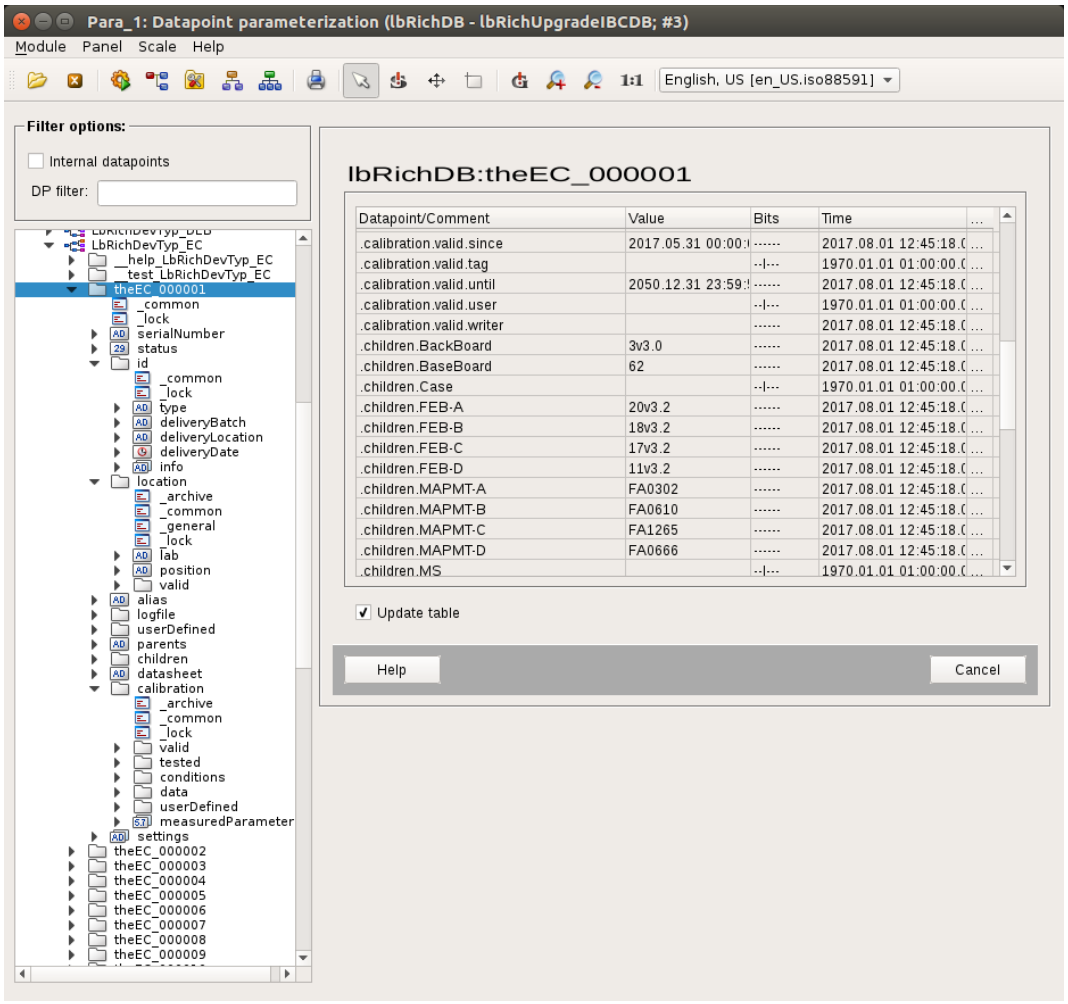

Figure 126: Example of IBCDB hardware DPT structure. The hardware DPT structure is shown through the "theEC_000001" instance

6.3.2 Logical domain datapoint elements

An example of Logical domain datapoint type instance is shown in Figure 127. The datapoints have the following datapoint elements:

- *alias*: unique string identifier of a lab or a location in the detector, e.g. RICH1/RICH1-U/Column0/EC3/MaPMT-A;
- *containsDeviceType*: hardware DPT inserted in this location;
- *containsDevice*: serial number of the device inserted in this location in the time range specified by the *valid* node;
- *valid* node: it contains the since and until date/time of a device inserted in this location;
- *fwAlias, fwNode, correspondsToFwNode, aliasSequenceNumber*: used to exploit the Logical View provided by the JCOP framework.

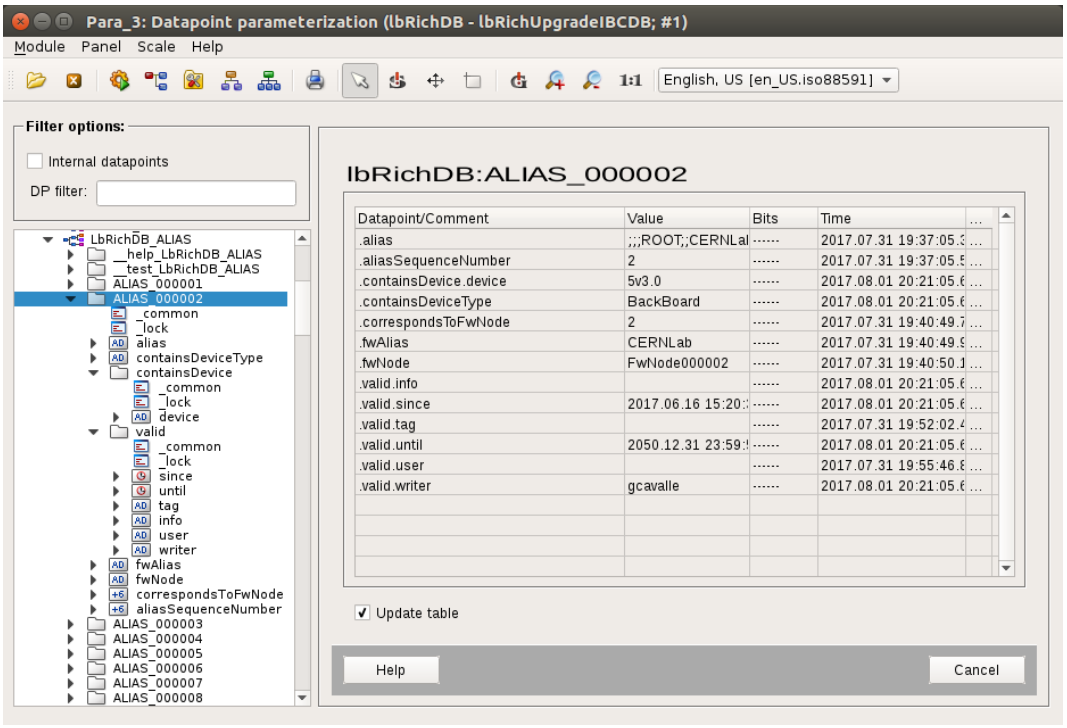

Figure 127: Example of IBCDB logical DPT structure. The hardware DPT structure is shown trough the "theALIAS_000002" instance

6.4 IBCDB archives organisation

The capability to save records with interval of validity date/time and transaction date/time, involves the archiving of data after value changes. The *History DB* provided by WinCC-OA suits this concept. Several archives are possible, each archive being managed by a separate archiving process and consisting of a series of chronologically ordered archive files. The advantages of the History DB are a space-saving storage structure, an efficient write logic using direct access, a fast chronological reading of values for each DPE, simple archiving management through configurable archive record sizes and no multiple access problems.

Each archive is configured for a maximum number of DPE and values, the space on disk being allocated when the archive is created. While the maximum number of DPE cannot be exceeded, reaching of the maximum number of values leads to an automatic file switch. After switching to a new file, the old file can be compressed to reduce the associated space on disk. For example, an archive file with a maximum of 40000 DPE and 1000 values has an online size of 1.8 GB that becomes 197 kB after the compression, with negligible effects on the speed of queries.

To optimise the retrieval of data, i.e. to speed up the queries, at least one archive for IBCDB datapoint type has been created, each one with a maximum of 40000 DPEs and 1000 entries. The association of DPEs to an archive is done appending an archive config to the corresponding DPE. In order to be able to keep track of the history of each device, the archive config has been added to:

- the *calibration* node, to allow multiple calibration measurements for each device;
- the *children* and *parents* nodes, to allow for changes in time of the composition of

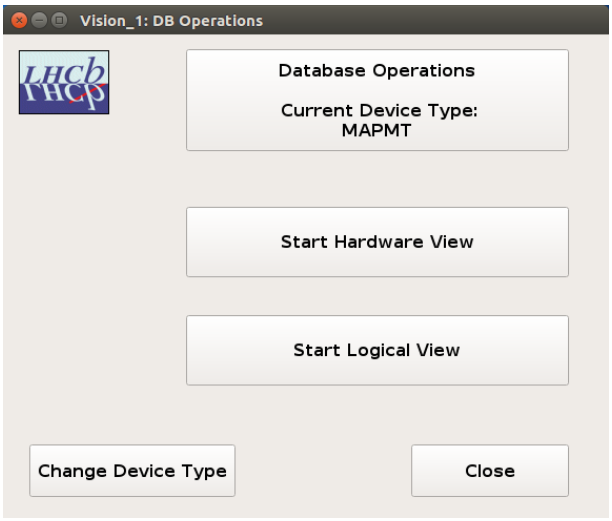

Figure 128: Starting panel of the IBCDB. Default device type can be changed clicking on the button at the bottom left side of the panel. The operations related to the hardware and logical domains of the IBCDB can be started clicking on the corresponding button on the panel.

each sub-assembly;

- the *location* node, to follow the movements of devices in different labs;
- the *settings* node, to cope with different working points during time.

With this archive configuration and DPT structures, 700 DP can be added to each archive. This means that a total of 23 archives will be sufficient to cope with all the RICH upgrade requirements, corresponding to about 50 GB of required space on disk. However, in order to have a more performant and centralised archiving architecture with the scale-up of the number of devices inserted in the IBCDB, the migration to the CERN ORACLE database is foreseen.

6.5 Functionality and operations of the IBCDB

Since the IBCDB is running on a CentOS 7 machine at CERN, a multi-user access to the IBCDB operations is guaranteed to each user connected to the CERN network, *e.g.* to an lxplus node.

The operation of the IBCDB takes place through WinCC-OA panels, user-friendly interfaces. As shown in Figure 128, the operational view reflects the super-structure of the IBCDB consisting in an Hardware domain and in a Logical domain. When the DB is started, a pop-up panel appears asking for the default device type to be used, speeding up the query of data of interest for the user. In the following, the description of the IBCDB functionality will be mainly restricted to the ones available for the MaPMT device type, since MaPMTs are the first devices that have been tested and characterised. Analogue features have also been developed for the other device types.

6.6 Hardware View

The Hardware View allows to access the overview of the devices inserted in the IBCDB, to insert and retrieve calibration and test data and to export data dumping values to a file. Moreover, being the IBCDB project interfaced with ROOT, it is also possible to produce plots relative to variables selected by the user, making it possible to perform analyses on data collected by the quality assurance facilities. The connectivity between hardware components in order to build the higher levels of modularity, *e.g.* an EC, is available as well within the hardware domain of the IBCDB.

The summary UI for the MaPMT device type is shown in Fig. 129, as a list of serial numbers and corresponding states. Devices can be searched by serial number patterns, delivery batch numbers and status values using the filters at the top of the UI. This feature gives an overall view of the devices inserted in the database. For instance, as shown in Fig. 129, the search of devices being READY returns the list of the hardware units that can be used for the data taking, *i.e.* having calibration data and respecting the quality assurance requirements. Moreover the statistics of READY, NOT_READY and BROKEN devices is given in text fields at the bottom right of the UI.

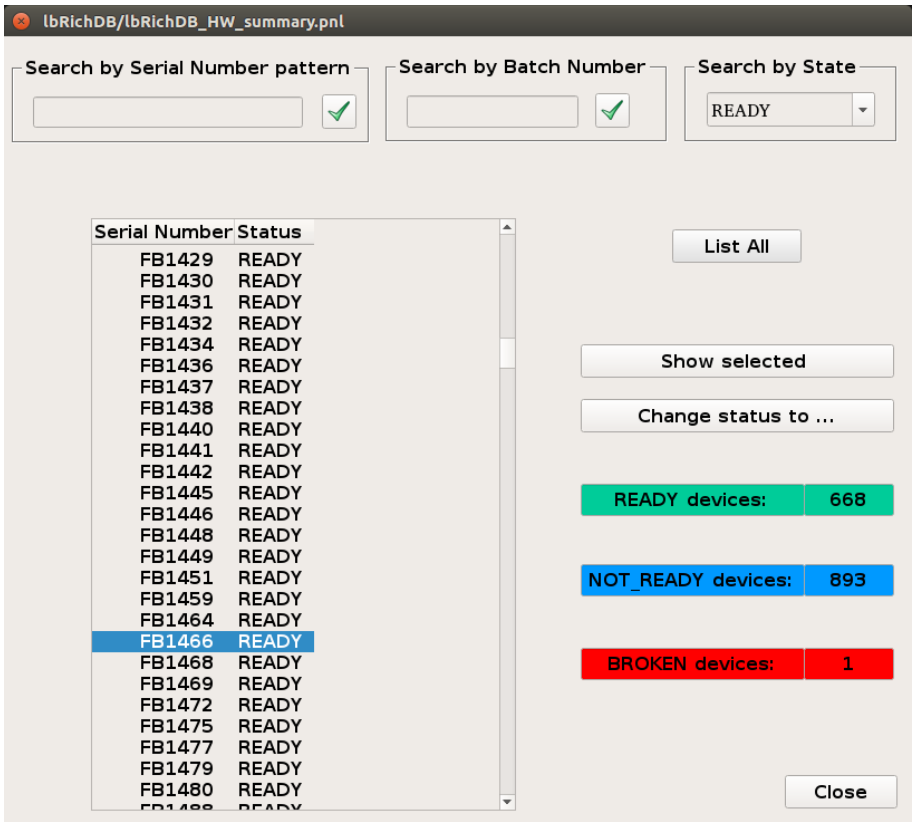

Figure 129: Summary of MaPMTs currently inserted in the IBCDB.

Selecting a serial number between the listed ones, it is possible to query the corresponding data or to change the status of the device. The available type of data changes depending on the device type under consideration. When selecting an assembly such as an EC or a PDM, the available data that can be queried are the components building the assembly. When selecting an hardware unit, such as an MaPMT or a BaseBoard, the

available data are the calibration values measured by the quality assurance facilities. The data are accessed by clicking on the *Show selected* button, that opens the UI shown in Fig. 130, specific for the MaPMT device type.

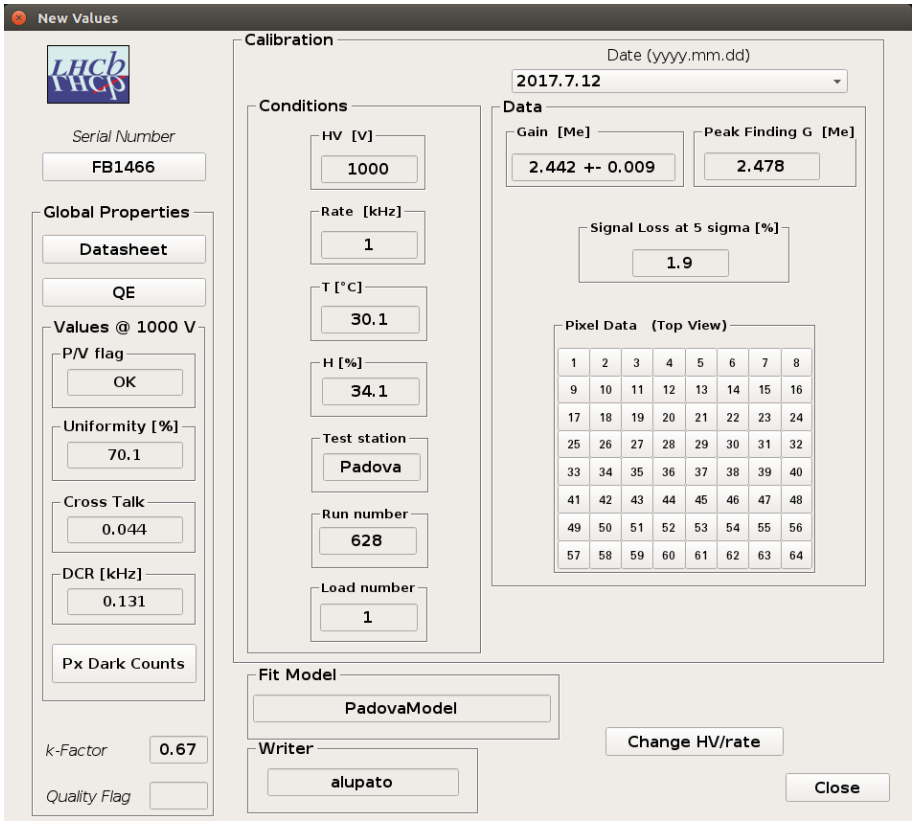

Figure 130: Calibration data inserted in the IBCDB at HV=1000 V for the MaPMT of serial number FB1466.

By clicking on the *Datasheet* button, the datasheet provided by Hamamatsu for this MaPMT can be accessed, shown in Fig. 131, as well as the Quantum Efficiency and pixel dark counts data.

Since the values provided by Hamamatsu are measured at V = 1000 V, some values like the peak-to-valley (P/V) flag and the average pixel-by-pixel uniformity, cross-talk and dark counts rate (DCR) are reported in the left side of the UI. Also dark counts for each pixel are accessible by clicking the *Px Dark Counts* button. The k-factor value is given in the text field at the bottom-left side of the UI. The other data shown in the UI correspond to the valued measured at the High-Voltage (HV) value and illumination rate value shown in the corresponding text fields. If multiple measurements are available with these HV and rate conditions, the date can be changed through the combobox at the top-right side of the UI. By clicking the *Change HV/rate* button it is possible to access the data corresponding to different HV or illumination values. For each date, HV and rate values, the conditions of the measurements, such as the temperature (T) and humidity (H), are reported. The average gain measured through the fit to the pulse-height spectra of each pixel and by using a peak finding method, are reported. The signal-loss field correspond to the percentage of the signal that is lost, in average, when a cut at 5σ is applied to the spectrum, being σ the width of the pedestal.

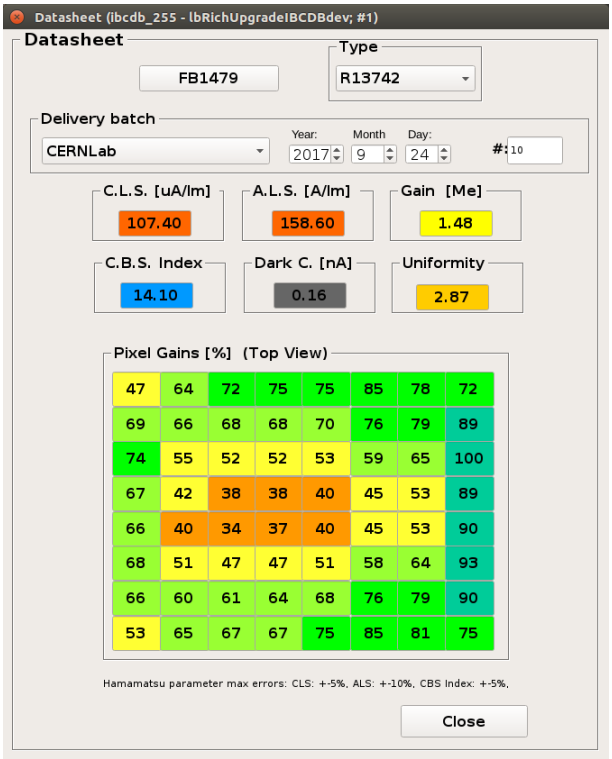

Figure 131: Datasheet for MaPMT of serial number FB1479.

Pixel data, shown in Fig. 132, can be accessed by clicking on the corresponding pixel number in the pixel map shown in Fig. 130. The stored values per pixel are the gain measured through the fit to the pulse-height spectrum and by using a peak finding method, root mean square (Rms) of the single-photon peak, μ-parameter that is related to the average number of photons, peak-to-valley ratio, signal loss defined above, cross-talk and a parameter related to the missing probability at the first dynode.

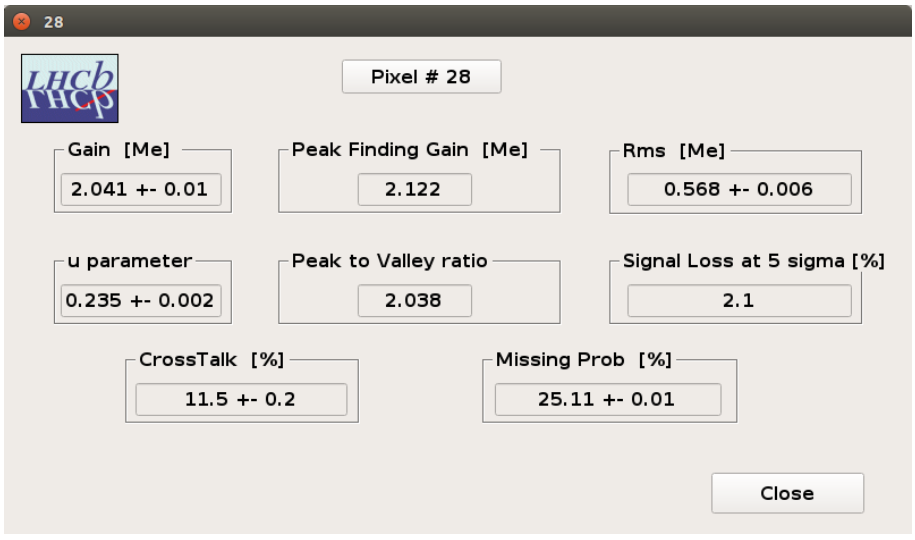

Figure 132: Calibration data inserted in the IBCDB at HV=1000 V for pixel 28 of the MaPMT of serial number FB1466.

The contents and the structure of this UI is MaPMT specific; depending on the quantities measured for the other device types, this UI changes shape and functionality, as shown for instance in Fig. 133 for the BaseBoard device type. In the left side of the figure it is present the UI reporting the overview for the BaseBoard, including information such as the connection of the jumpers for the supply of the last (Dy12) and last-but-one (Dy11) dynodes, magnetic shield (MS) connection and the presence of a filtering capacitor (C0). The overall result of the test on this device is reported under the Global status text field. By clicking on a button corresponding to one of the sockets, it is possible to access the values corresponding to the measurements of the anode continuity and of the voltage divider values.

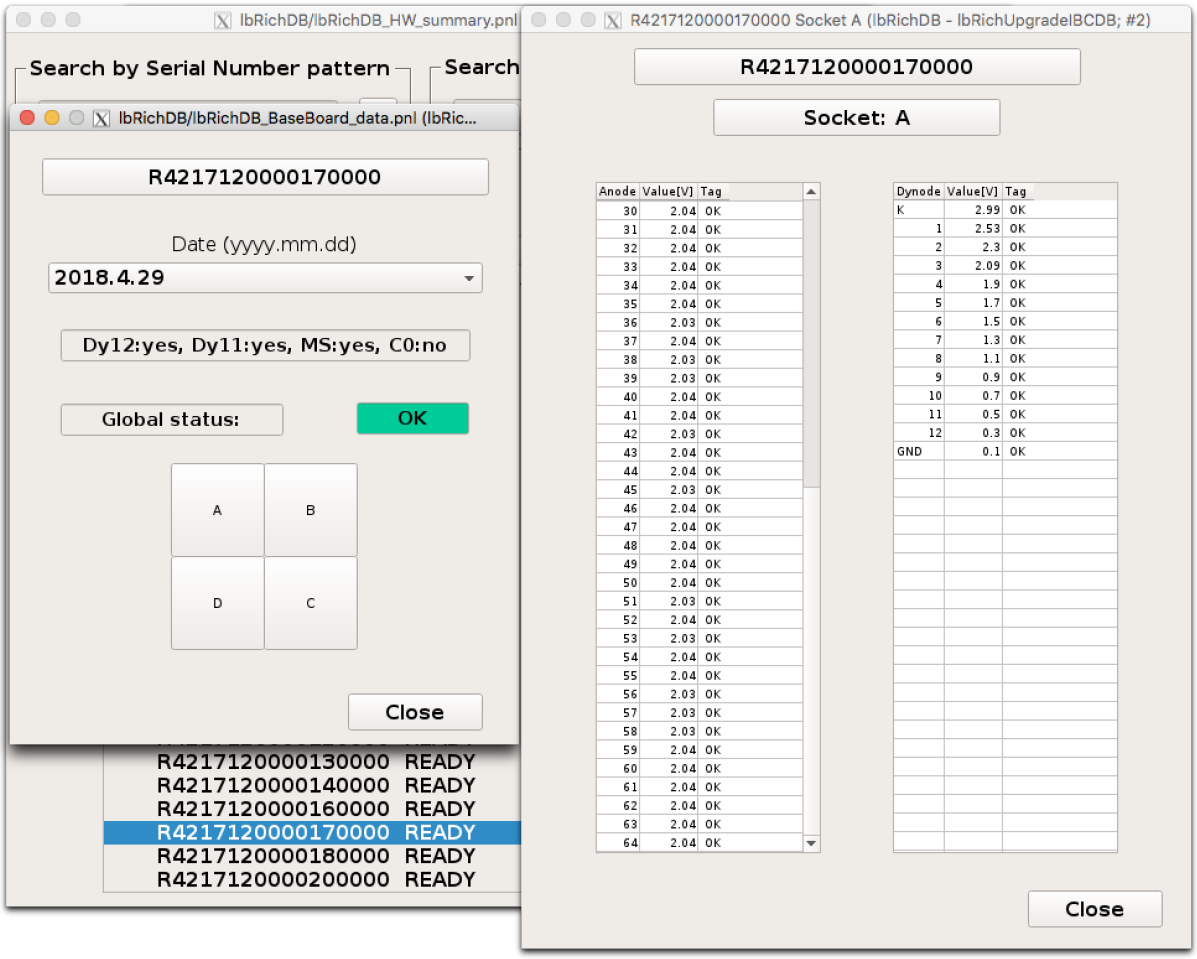

Figure 133: Calibration data for the baseboard of serial number R4217120000170000.

Given the large number of hardware components, multiple devices can be imported in the IBCDB at the same time through a script able to read files produced as output by the test facilities or by the factories (*e.g.* the datasheet provided by Hamamatsu for the MaPMTs). Similarly, calibration and test data can be imported for a freely large number of devices starting from text files. Multiple insertions for the same device are allowed according to the requirement to save other sets of calibration and test data for the same hardware unit. The procedure to create devices and import their data is completely transparent to the user. Once selected the file to be imported, it is sufficient to click a

button to insert data.

The IBCDB can also be used as a bookkeeping system through the UI shown in Fig. 134. The users, depending on the device type, can select a variable of interest, dump the values to a file and perform analyses on these data. The export data user interface first ask to select the variable of interest. The IBCDB also allows to plot distributions, values over time and values over values of the variables of interest, thanks to its interface with ROOT.

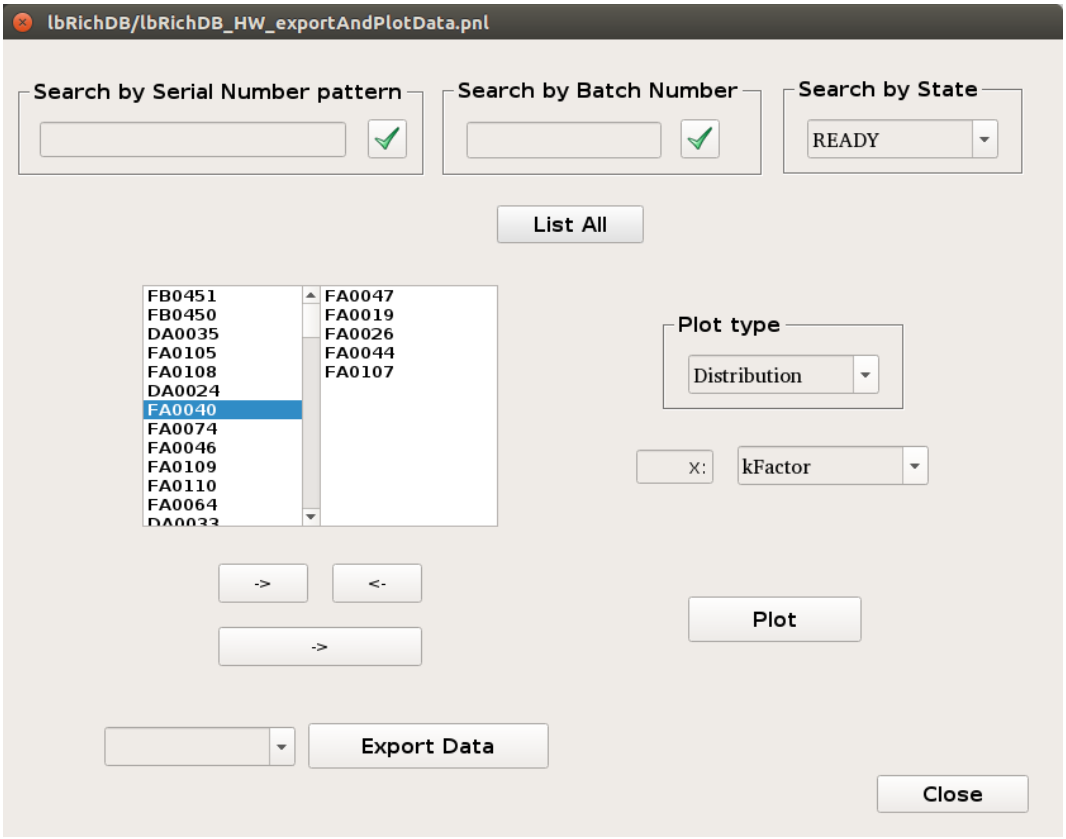

Figure 134: Export data user interface. The user can select devices from the left side list; data are dumped on the user's home folder clicking on the export data button.

One of the main IBCDB functionality is the capability to group devices in order to build higher levels of modularity. For example, MaPMTs of similar gains will be grouped together to build ECs and PDMs. Furthermore, each assembly working point, e.g. CLARO configuration parameters, will be saved in the IBCDB. Interval of validity ranges are implemented to allow the components and the configuration parameters to change during time. The UI shown in Fig. 135, specific for the EC device type, allows to select between READY devices to build an EC. The Start Validity field allows to tag the version of the EC, *i.e.* its components since that date. The info text field allows to insert generic information about the EC, *e.g.* if the magnetic shield is installed. A similar UI with the same functionality allows to select READY ECs and PDMDBs to build a PDM.

An example of visualisation of RICH assemblies is given in Fig. 136. From the summary of the hardware view it is possible to show the components of a PDM. At the top of the UI it is present the start validity date for which the ECs and PDMDBs shown in the UI are valid. Changing this tag, it is possible to access the components in previous versions

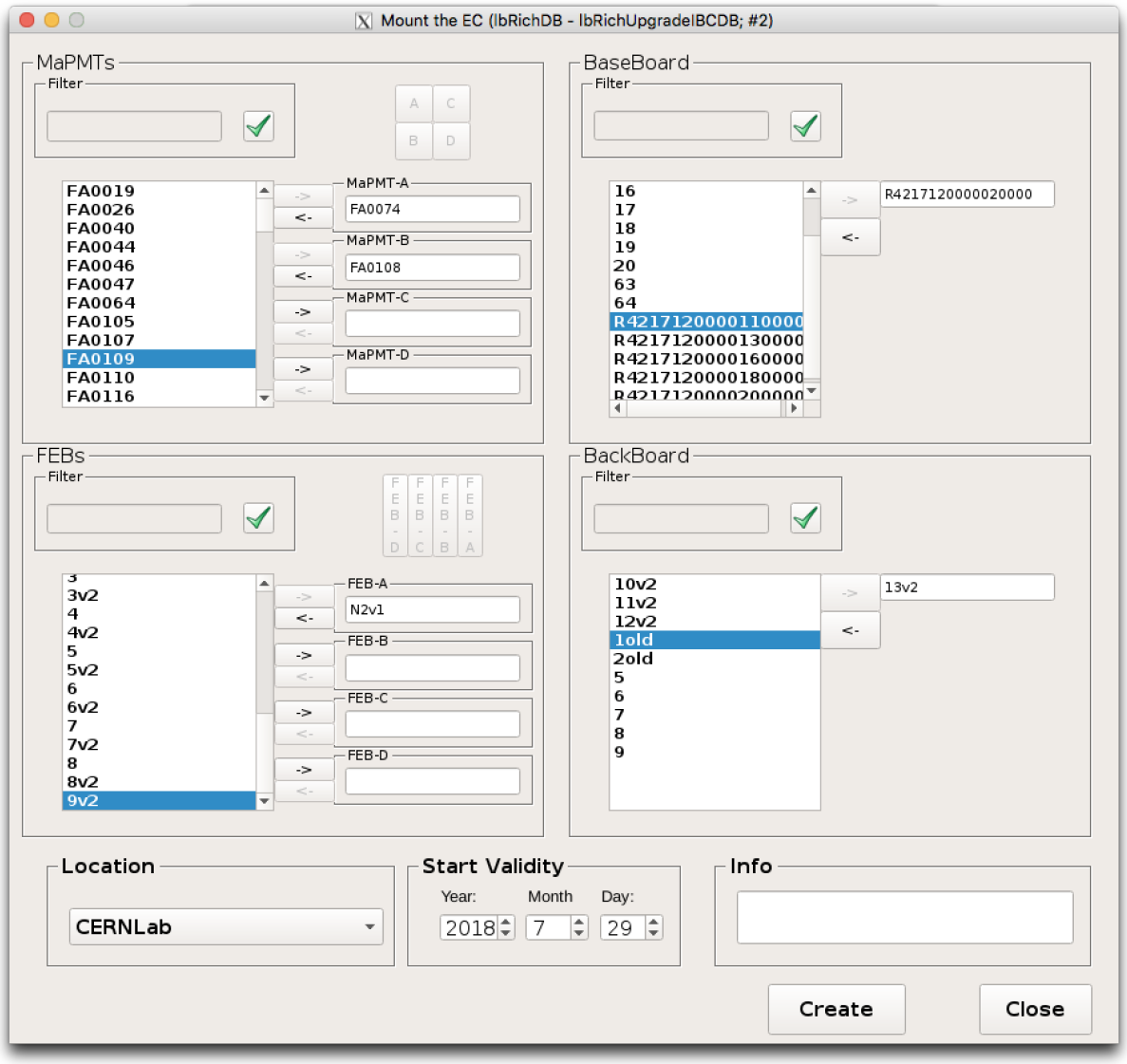

Figure 135: User interface allowing to build ECs selecting between READY MaPMTs, Baseboards, FEBs and Backboards.

of the PDM. It is possible to access the data of one of the components by clicking on one of the them. On the right part of Fig. 136 it is shown the composition of one of the ECs building the PDM. The start validity tag is present for each EC as well and the serial numbers of the used hardware units are reported in the other buttons. By clicking on these buttons it is possible to access the calibration data of the corresponding device, like the ones shown in Fig. 130 and 133.

6.7 Logical View

The Logical View panel is shown in Figure 137. The buttons allow to start different types of actions related to the locations of the devices during their lifetime, described in the following subsections.

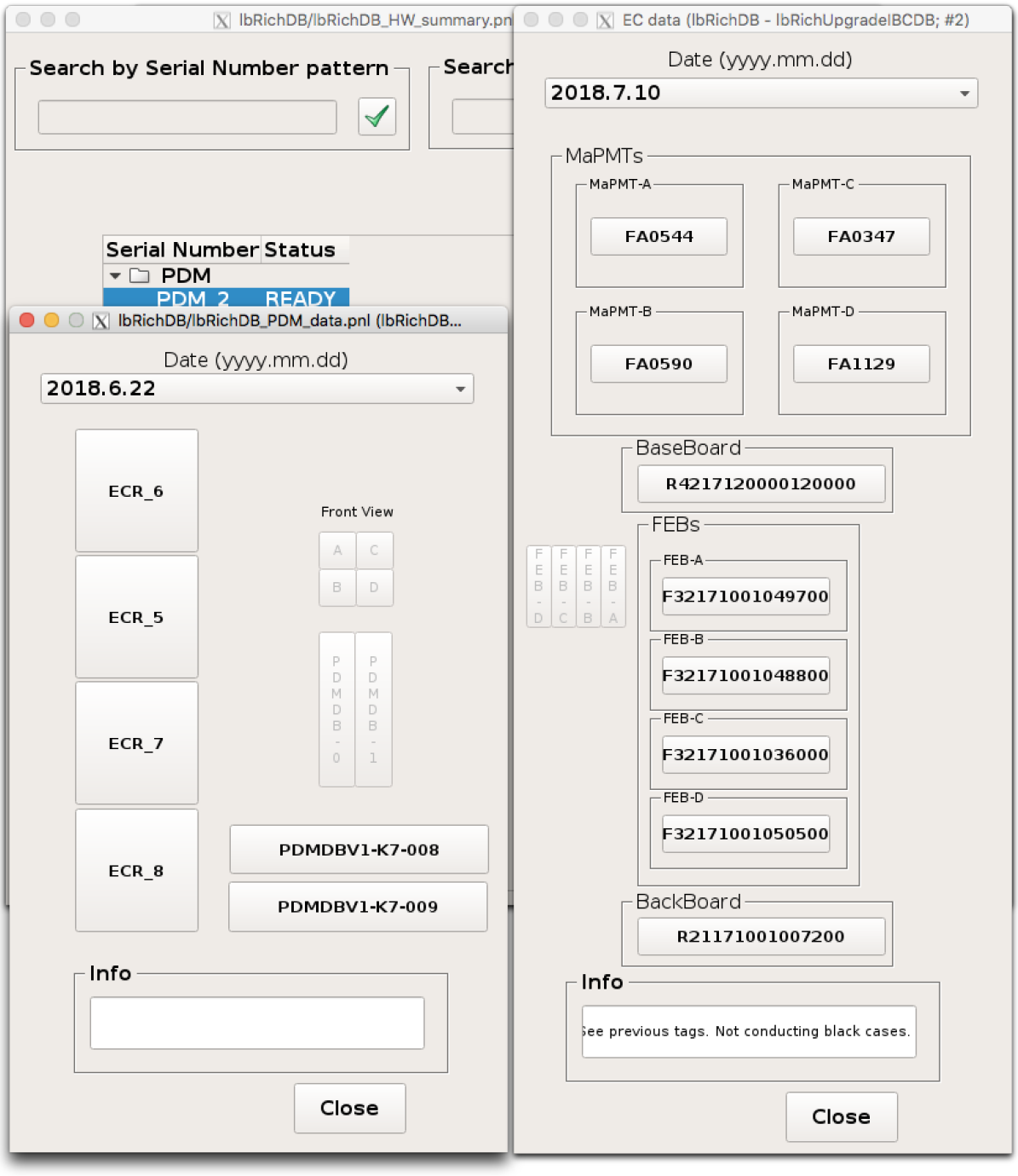

Figure 136: Visualisation of the ECs and the PDMDBs mounted on the PDM_2

.

6.7.1 Search by device type

This button allows to retrieve the history of the positions of a device unit or assembly, as shown in Figure 138. For each location, the since and until date and the writer are retrieved.

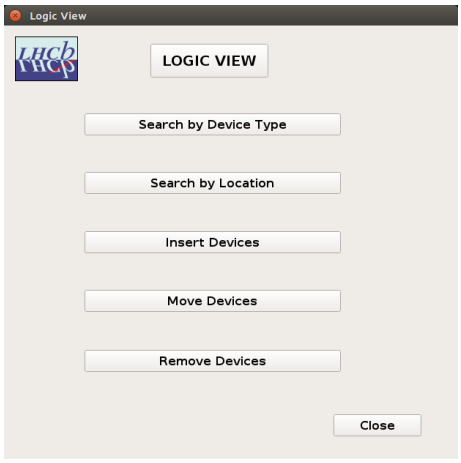

Figure 137: Starting panel of the IBCDB logical view.

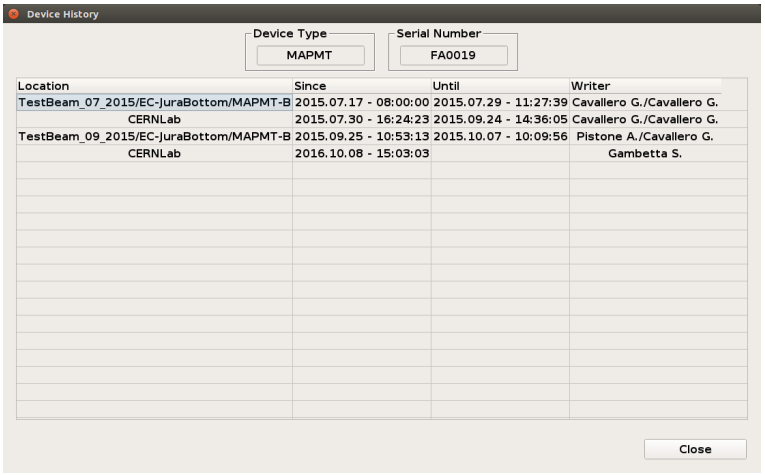

Figure 138: History of the locations taken by the FA0019 MaPMT.

6.7.2 Search by location

This button allows to find all the devices inserted in a location, as shown in Figure 139. For each device inserted in the selected location, the since and until date and the writer are retrieved. Indeed, as shown in Figure 125, devices will be tested in many different labs and it is important to keep track of the historical locations of each device.

An important feature for the upgraded RICH operations will be the capability to retrieve data inserted in a specific part of the detector. This will be achieved using a tree structure, like the one shown in Figure 140.

6.7.3 Insert, Move, Remove devices

These buttons allows to change device locations. During testing and quality assurance activities, a lot of devices move between one lab and the other. For this reason, massive insertion, move and removal of devices have been implemented, through a user interfaces like the one shown in Figure 141.

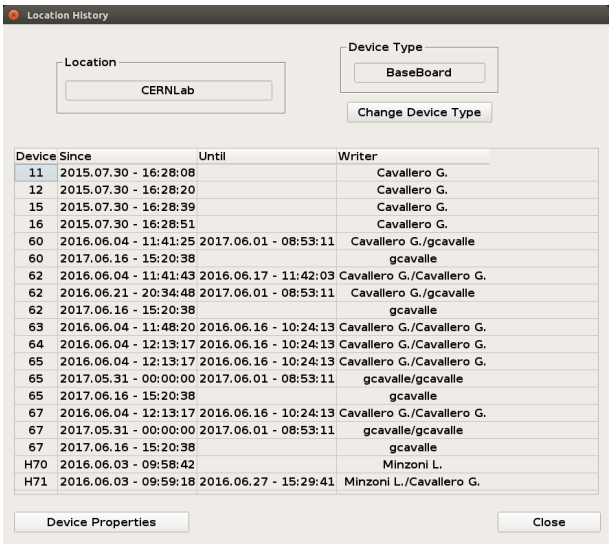

Device	Since	Until	Writer
11	2015.07.30 - 16:28:08		Cavallero G.
12	2015.07.30 - 16:28:20		Cavallero G.
15	2015.07.30 - 16:28:39		Cavallero G.
16	2015.07.30 - 16:28:51		Cavallero G.
60	2016.06.04 - 11:41:25	2017.06.01 - 08:53:11	Cavallero G./gcavalle
60	2017.06.16 - 15:20:38		gcavalle
62	2016.06.04 - 11:41:43	2016.06.17 - 11:42:03	Cavallero G./Cavallero G.
62	2016.06.21 - 20:34:48	2017.06.01 - 08:53:11	Cavallero G./gcavalle
62	2017.06.16 - 15:20:38		gcavalle
63	2016.06.04 - 11:48:20	2016.06.16 - 10:24:13	Cavallero G./Cavallero G.
64	2016.06.04 - 12:13:17	2016.06.16 - 10:24:13	Cavallero G./Cavallero G.
65	2016.06.04 - 12:13:17	2016.06.16 - 10:24:13	Cavallero G./Cavallero G.
65	2017.05.31 - 00:00:00	2017.06.01 - 08:53:11	gcavalle/gcavalle
65	2017.06.16 - 15:20:38		gcavalle
67	2016.06.04 - 12:13:17	2016.06.16 - 10:24:13	Cavallero G./Cavallero G.
67	2017.05.31 - 00:00:00	2017.06.01 - 08:53:11	gcavalle/gcavalle
67	2017.06.16 - 15:20:38		gcavalle
H70	2016.06.03 - 09:58:42		Minzoni L.
H71	2016.06.03 - 09:59:18	2016.06.27 - 15:29:41	Minzoni L./Cavallero G.

Figure 139: History of the CERNLab location concerning the baseboard device type.

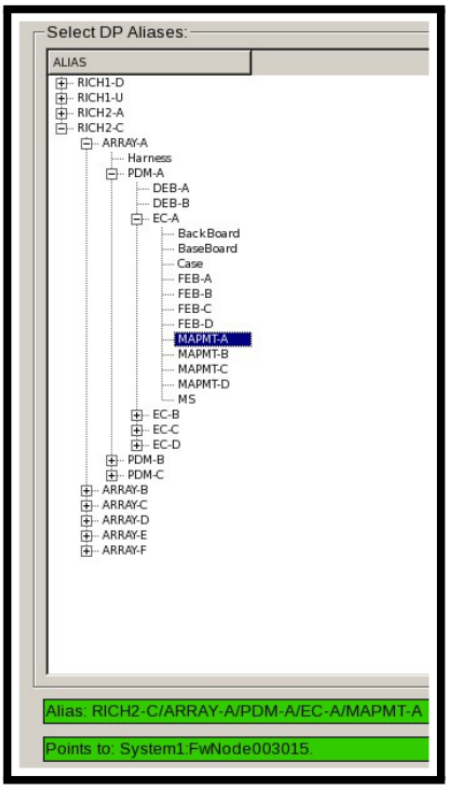

Figure 140: Tree used to find device information that will be installed in the future RICH detectors.

6.8 Conclusions and future perspectives

The IBCDB project is running and currently used by the RICH upgrade collaboration to store test and calibration data of devices in production. As such, the IBCDB functionality evolve and change to meet quality assurance facilities requests.

The IBCDB contains the basic functionality required to group photodetectors depend-

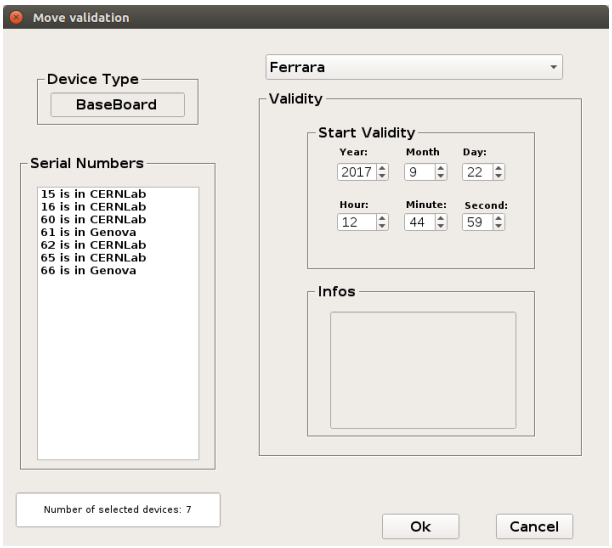

Figure 141: Example of a panel that can be used to move devices from one location to the other. In this case, Baseboard that are currently in CERNLab or Genova lab will be moved to the Ferrara lab. The Start Validity field is required to save date/time ranges.

ing on their average gain as a function of the HV. As such it can be used to build the higher level of modularity foreseen by the RICH upgrade detectors, e.g. EC. A more sophisticated grouping system, including calibration data of CLARO chips and measured properties of the MaPMTs is under development, taking into account feedbacks from quality assurance facilities.

Using the packager tool provided by the JCOP framework, the IBCDB framework component has been developed. A panel has been developed to install the user interfaces, scripts, libraries and datapoints required by the project to work. Furthermore, the panel allows the automatic creation and configuration of the archives [5].

The IBCDB project, beside some RICH specific user interfaces, could be re-used by any subdetector, provided that the required new datapoint types are defined. A more generic user interface allowing to install the IBCDB framework component with new user-defined datapoint types, is under development.

Further development to integrate the IBCDB with the upgraded RICH ECS, whose development is described in Chapter 7, are ongoing. Indeed, the configuration bits of the frontend will be stored (applied) in (from) the IBCDB during the testing and commissioning phases. Also the connectivity between the devices under test, like the correspondence between optical fibres and MaPMT pixels, will be stored in the IBCDB.

[5] The IBCDB component is available on gitlab at https://gitlab.cern.ch/gcavalle/lbRichUpgradeIBCDB.

7 Development of the RICH upgrade Experiment Control System

As introduced in subsection 3.4, the ECS is the framework within LHCb in charge of the configuration, control, monitoring, archiving, operation and running of the LHCb experiment [175]. The ECS is a uniform and homogeneous control system developed within the JCOP framework [126].

The JCOP framework, providing common tools and guidelines for the development of the LHC control systems, is based on the WinCC-OA Supervisory Control And Data Acquisition (SCADA) tool and on the Finite State Machine (FSM) concept through the State Management Interface (SMI++) tool [179] used for the system automation. Standard common usage configurable systems are also available, e.g. to control power supplies, to monitor temperatures etc. The use of common hardware components and a common software control system amongst all the LHC experiments allows the standardisation of solutions for common tasks. Each subdetector has its own ECS interfaced with the central LHCb ECS. Therefore each subdetector ECS has to follow the LHCb-JCOP conventions and guidelines. The ECS for the LHCb upgrade will take advantage, as much as possible, from the current system, introduced in sub-section 3.4.

In order to have an idea of the complexity and level of automation required by the control system of one subdetector, the switching off and on of the current RICH detectors during standard data taking can be taken as example. When LHC wants to inject new beams, the RICH detectors must be switched off, since particle showers can damage the HPDs. The LV chains have two levels, LV_HI and LV_LO, the former powering a regulator. For this reason, during the switch off procedure, LV_LO must be switched off first, followed by LV_HI and the Silicon Bias channels. At this point the RICH detectors are off and LHC can inject the beams. When the injection is finished, the RICH detectors can be switched on again. HV is ramped up and when all the HV channels are on, five minutes are waited to let the HV currents stabilise. LV_HI channels are then switched on, followed by the LV_LO and Silicon Bias channels. At this point the Front-End (FE) can be configured and the RICHes are ready for the data taking. This procedure is fully automated within the current RICH ECS. Only two commands from the shift leader are needed: the Go_To_INJECTION action, switching off all the LHCb sub-systems, and the Go_To_RAMP action, switching them back on.

I developed the prototype of the RICH upgrade ECS starting from the need to have a slow control, monitoring and archiving system during the first testbeam for the RICH upgrade. This has been the starting point for the evolution towards a more complex and automated control system, including the integration in an unique FSM of the high voltage (HV) and low voltage (LV) power supplies control, the temperature, humidity and pressure monitoring, the configuration of the RICH FE and the prototype of the LHCb upgraded DAQ control system. The development of the prototype of the RICH upgrade ECS will be described in this chapter, after an introduction to the standard LHCb solutions for the building of an homogeneous and scalable control system.

7.1 Hardware control within the JCOP framework

In order to follow the LHCb-JCOP guidelines, standard equipments should be used as much as possible and common hardware interfaces, such as Ethernet and CANbuses,

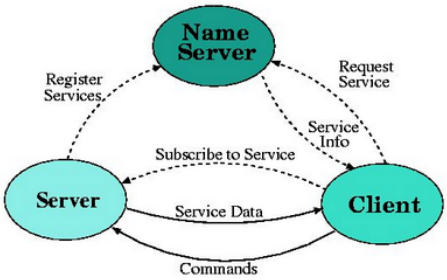

Figure 142: DIM system architecture. The DIM Name Server handles the list of services that can be obtained from a DIM Server, univocally identified by their names. The services are registered by the DIM Server to the DIM Name Server. The DIM Client can now send a request for the service to the DIM Name Server that will in turn send the service information to the DIM Client required by the latter to subscribe to the service. Once the subscription is done, service data can be received by the DIM Client from the DIM Server, and the DIM Client can send commands to the DIM Server.

should be chosen. The software interface should be an Open Platform Communications (OPC) server developed by the hardware manufacturer. WinCC-OA provides an OPC client.

If the equipment manufacturer does not provide an OPC server, the devices can be interfaced using a Distributed Information Management (DIM) [180] client-server architecture. DIM is a publisher/subscriber system for cross-platform information exchange. DIM servers publish data structures as services to clients. The services have names by which clients can subscribe them. When a server updates services all subscribed clients get the update. The list of services can be obtained from the DIM name server. Together with the service data the clients get a format string and a quality longword. The DIM server and clients interactions are shown in Figure 142.

A naming convention for the services provides a hierarchical name space. DIM is extensively used within the LHCb control system. For example, the DIM protocol is currently used for the configuration and monitoring of all DAQ and Trigger electronics, the control of all non-standard equipments, the configuration and monitoring of trigger/monitoring processes, the transportation of data for data quality checks, the interface to the Conditions database, to publish data for the web, etc.

The JCOP framework provides dedicated components setting up automatically the OPC group and items when declaring JCOP supported devices in WinCC-OA, making straightforward the communication with the hardware. Also DIM is fully supported by the JCOP framework. Furthermore, a set of libraries and user interfaces are available making easier the control of hardware.

Figure 143 shows a possible architecture of a control system exploiting the different functionality available within the JCOP framework. A user defined application is on top of the control system and can be developed using the Device Editor and Navigator (DEN) and the FSM framework tools. The DEN is the main user interface to the framework and it has two modes of operations: the editor mode allows to declare devices in the control system, comprising the easy configuration of many channels with alerts, settings etc., and the navigator mode allows to operate devices for expert use. The FSM tool allows to implement an high level view of the control system and to operate the system in a

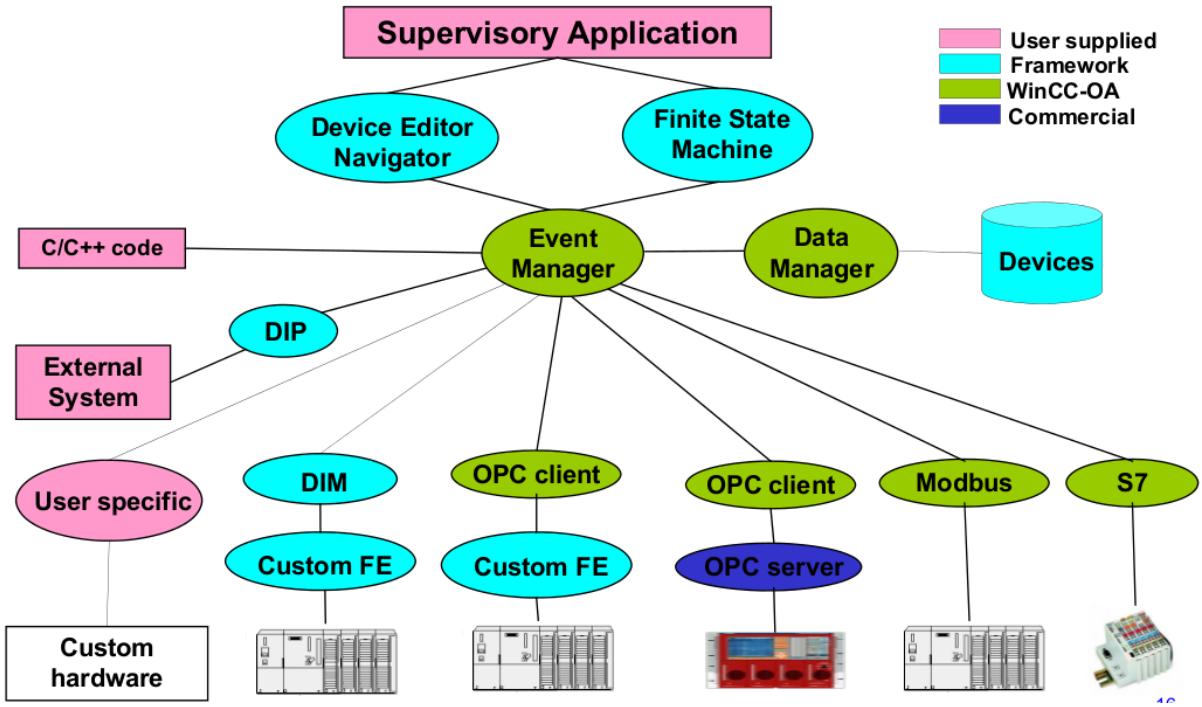

Figure 143: A schematic view of a control system within the JCOP framework.

user friendly way. Both the DEN and the FSM tools are handled by the Event Manager, responsible to handle data coming from the devices through a Data Manager and to manage the communication with the hardware through the available software interfaces or through user defined layers. Other important components are the Trending tool, allowing to plot values over time, and the Configuration DB tool, allowing to save the settings for some devices.

7.2 Architecture of the LHCb control systems

The structure of LHCb subdetectors, subsystems and hardware components is represented in a hierarchical, tree-like structure within the JCOP framework. This guarantees independence between sub-detectors and sub-systems during calibration or test phases while allowing an integrated control during physics data taking, when all the sub-detectors must run together. The hierarchical controls allow the definition and operation of hierarchies of objects behaving as FSMs, allowing the sequencing and automation of operations. Each component in the tree provides **Information** and can receive **Commands**, i.e. a **State** is flowing up in the tree and a **Command** is flowing down in the tree. There are two kinds of nodes in the tree:

- **Device Units** (DU), the tree leaves, i.e. they have no children, implementing the interface with the lower level components (hardware or software). DU receive commands and act on the device and receive device data translating it into a state. DU do not implement logic behaviour;

- **Control Units** (CU) and **Logical Units** (LU), the logical decision units able to send commands to their children, i.e. a group of DU or CU/LU, depending on their

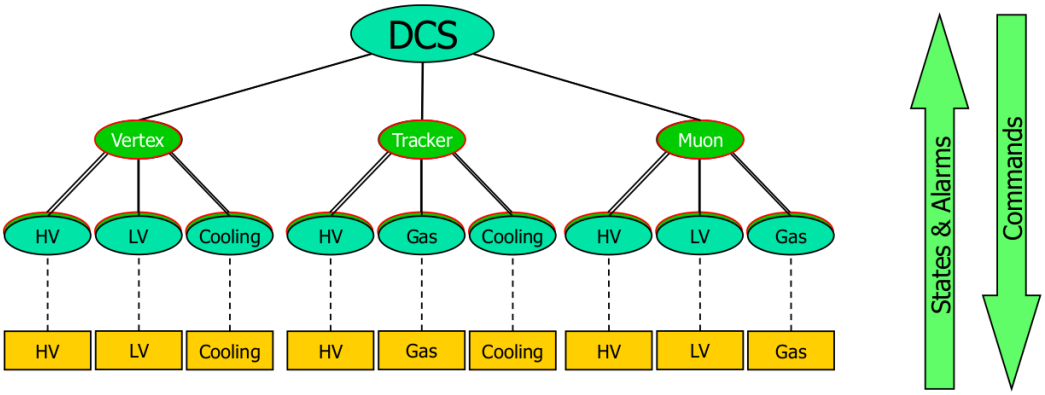

Figure 144: Example of a generic control system tree. In this example, the Detector Control System (DCS) is the top node, a CU summarising the state of the three LU corresponding to the Vertex, Tracker and Muon sub-detectors. The leaf nodes, in yellow, are the DU directly interfaced with the hardware.

states. The logic behaviour is defined in terms of FSMs and the state transitions can be triggered by a command reception, e.g. from an operator or from the CU/LU parent, or by the state changes of the CU/LU children. The evaluation of logical conditions are caused by state transitions. Depending on the state some commands can be sent to the CU children, propagating actions down the tree, allowing for automatic actions and to recover from error situations. A CU differs from a LU for the capability to operate the former independently from the other sub-systems.

A generic example of a hierarchical schema, showing a practical application of the concepts introduced above, is shown in Figure 144.

As introduced previously, the FSM C++ toolkit incorporated in the JCOP framework is called SMI++. Basic concepts of SMI++ are the decomposition of complex systems in objects instantiated from classes, the behaviour modelling for objects through a FSM implementation, the automation and error recovery following user defined rules. The behavioural model is defined in classes; classes instances can be abstract objects (e.g. Vertex sub-detector referring to Figure 144), corresponding to a CU or a LU, or physical objects (e.g. a Vertex HV channel), corresponding to a DU. The interface between physical objects and real devices is provided by proxies, driving the hardware using C, C++ or WinCC-OA control scripts. A collection of one or more abstract objects is called a **domain** in SMI and corresponds to a CU. Domains have a dedicated user friendly language, State Management Language (SML), implementing the abstract object description as FSMs, having the **state** as the main attribute.

The FSM objects are grouped into SMI domain processes. The individual processes communicate via the DIM protocol and thus can be distributed within a LAN. In order to be able to operate different detector parts independently, individual SMI domains can be separated from the control hierarchy. The partitioning capabilities of the FSM toolkit allow operating parts of the hierarchy in distinct modes. DU instances can be included in the tree (**enabled**) or detached from the tree (**disabled**) such that they do not propagate their state nor receive commands, for example in case of a faulty hardware component. A CU can be **included** in the control hierarchy, i.e. it receives commands from and send its

state to its parent, or **excluded** from the control tree, i.e. it does not receive commands and its state is not taken into account by its parent. In the latter scenario, the CU could be either faulty or ready to work in stand-alone for calibration or test purposes.

7.3 Implementation of the RICH upgrade ECS prototype

In the following, I will summarise the work I have done to develop a control system easily scalable to the multiplicity required by the upgraded RICH detectors and following the LHCb-JCOP conventions to allow the integration with the global LHCb ECS. Different prototypes of the control system has been used during RICH upgrade testbeams and during tests in the lab at CERN, where R&D activities are on-going, e.g. LHCb upgrade DAQ integration test with the RICH FE, for which the hardware control trough WinCC-OA is essential.

The RICH ECS is the top domain summarising the state of the HV, DCS and DAQ domains. In the evolution of the project I followed a bottom-top approach, starting from the definition of the DU and arriving to the logical abstraction of the different domains in the RICH ECS partition.

7.4 The RICH HV partition

The HV partition must be able to change its state depending on the LHC state. For example, during injection when some particle showers are expected, the HV must be off to prevent the losses to damage the RICH detectors.
A commercial equipment supported by the JCOP framework has been chosen to control and monitor the HV power supplies during testbeams and during the tests in the lab at CERN. The equipment uses Ethernet as the hardware interface and an OPC Data Access (OPC DA) server as the software interface.

The DU class implementing the interface of the HV control system with the hardware is such that its state is calculated depending on the **status** bit received by the considered HV channel. Available states are OFF, RAMPING_READY, READY, RAMPING_OFF, EMERGENCY_OFF (e.g. interlock is active) and ERROR. The commands act on the **settings** bits. Available commands are Go_READY, Go_OFF, Recover and Clear_Emergency. The Recover and Clear_Emergency actions switch on the channel setting its voltage to zero and switch off again the channel, procedure needed by the equipment to clear the alarm in a safe way accordingly to the LHCb-JCOP conventions. Having integrated the JCOP Configuration DB tool within the HV partition, the HV configurations, i.e. nominal voltage settings, current limits, ramp speeds etc., has been stored in a **recipe**. The recipe is automatically applied when the Go_READY command is sent, restoring the configurations before the Recover or the Clear_Emergency actions.

The instances of the DU class represent the concrete HV channels used in the control system. Devices can be added to the control system using the DEN WinCC panel, allowing the adaptations needed by the system, e.g. the need to switch from EC-R only to an hybrid system composed by EC-R.

All of the HV DU are grouped together in the RICH_HV domain, a CU implementing the logic behaviour of the HV channels as an whole. From the RICH HV domain, or partition, the operator can send commands to all of the HV channels included in the control system. The available actions depend, as in the case of the DU, from the current

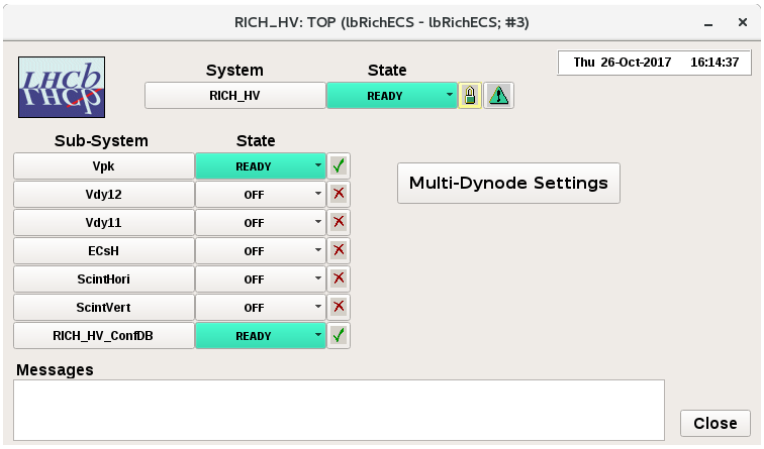

Figure 145: Operations panel of the RICH HV domain. Only the Vpk channel is enabled.

state. The state of the HV channels is summarised in the RICH_HV partition, e.g. if any of the children DU is in state ERROR, the RICH_HV domain moves to ERROR. The operations panel of the HV domain is shown in Figure 145.

Actions can be sent from both the top and children nodes, the latter representing the physical HV channels, e.g. the channel Vpk used to power the MaPMT photocathodes. In Figure 145 this is the only enabled channel. During testbeams, ScintHori and ScintVert channels have been used to power the scintillator systems. EcsH channel has been used to power the ECs of type H. When testing the operations of the MaPMTs powering the last and/or last-but-one dynodes, also the DU instances Vdy12 and Vdy11 were enabled. During these tests, the panel shown in Figure 146 has been used, accessible clicking the **Multi-Dynode Settings** button. The panel allows to control and perform tests using these alternative powering schemes, allowing for an automated switching on and switching off sequence, switching on first the photocathode channel and then the dynode channels and viceversa, through the **Go_READY** and **Go_OFF** buttons, to automatically fine tune the voltage settings for the dynodes, etc.

For example, an automated procedure to adjust the Vdy12 setting has been implemented. In principle, Vdy12 must be set to $\frac{1}{10} \cdot$ vPK, but differences due to the tolerances of the voltage dividers and to the not ideal power supply, result in a current drawn by the channel also in the dark, meaning that this Vdy12 setting is not optimal for MaPMT operations. In order for the dy12 channel to not draw current in the dark, different automated procedures have been implemented only requiring the sending of the Go_READY command. The simplest procedure, assuming that no light is present, is as follows:

- the Go_READY action switches on the photocathode only;
- after the photocathode channel is ON, Vdy12 is set to the value monitored by the dy12 channel
- the Go_READY command completes its action switching on the dy12 channel.

Each channel can be operated independently from the others using the operations panel shown in Figure 147, already provided by the JCOP framework.

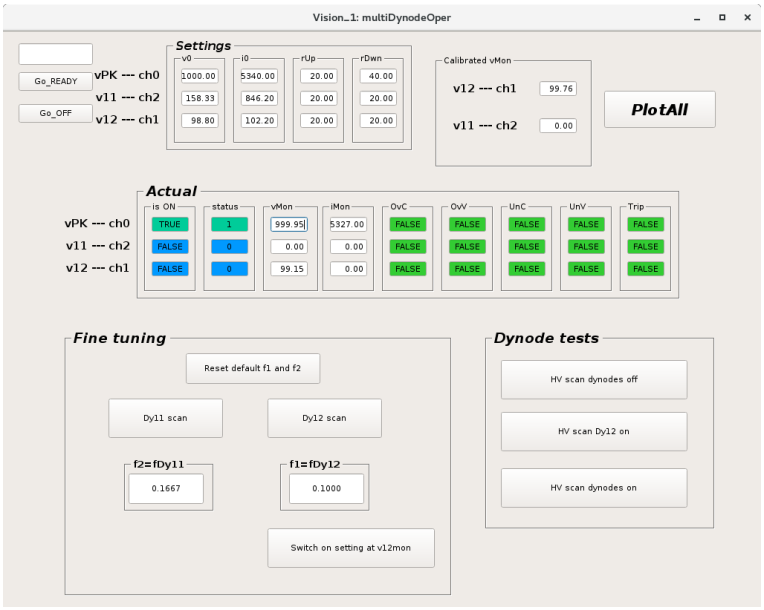

Figure 146: User interface used to perform tests powering the last and/or the last-but-one MaPMT dynodes.

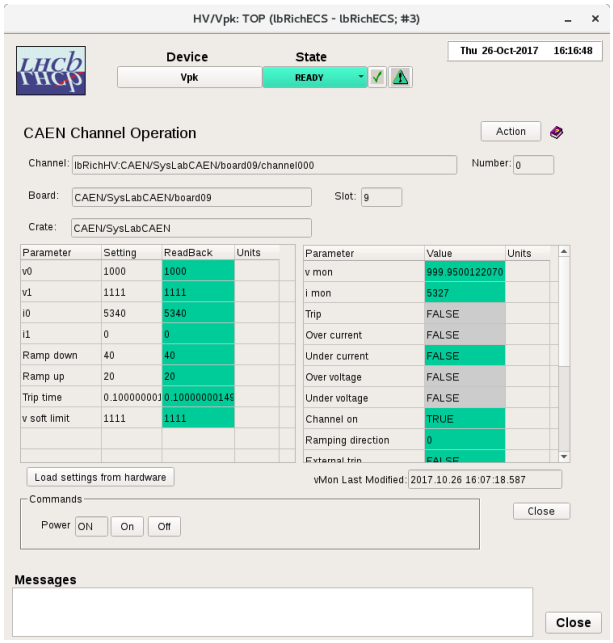

Figure 147: User interface used to change the settings for the Vpk channel and to readback the values from the hardware.

7.5 The RICH DCS partition

The DCS partition is the control domain responsible for all the slow control equipment, i.e. control and monitoring of the LV, temperature, humidity, pressure etc., with the exception of the HV, as stated in sub-section 7.4.

Currently the RICH upgrade DCS partition includes the LV control and monitoring and the temperature monitoring.

7.5.1 LV control and monitoring

The same commercial equipment used for the HV system has been used to control and monitor the LV power supplies used to power the PDMDBs. Therefore, from the point of view of the hardware control, the same hardware and software interfaces have been used and the calculation of the DU states is similar to the one used for the HV. However, since different LHCb-JCOP conventions must be followed in order to integrate the RICH DCS partition with the LHCb DCS partition, the available states and actions are slightly different with respect to the HV partition: the available states do not include the RAMPING_READY and RAMPING_OFF ones, replaced by the NOT_READY state, and the Go_READY and Go_OFF actions are replaced by the Switch_ON and Switch_OFF commands. Different DU states and available actions translate into a different implementation of the RICH_DCS_LV domain. (schema e spiegazione). The LV operations panels are analogue to the HV ones.

7.5.2 Temperature monitoring

The Embedded Local Monitor Board (ELMB) [181], developed by CERN, NIKHEF and the PNPI, is characterised by the large number of input/output channels and by the radiation hardness. The ELMB is based on the industry standard CANbus as the hardware interface and a CANopen OPC DA server has been implemented as the high-level communication protocol. The ELMB can be used to read analog inputs (such as temperature, pressure and humidity sensors, voltages, etc.) and for digital I/O. I inherited the work done in previous testbeams to read-out Pt100 and Pt1000 temperature sensors via ELMB and I integrated it in the FSM framework.

Being temperature sensors input only devices, the DU class implementing the interface with the hardware does not have available actions. WinCC-OA allows to define ranges of values outside of which alarms can be raised and DU states can be defined. Following the LHCb-JCOP guidelines, the available states for the temperature sensors DU are OK, NOT_OK and ERROR. Depending on the position of the sensor within the setup, different limits must be chosen, according to the nominal operations values and safety instructions. For example, MaPMTs can operate at a maximum temperature of 40 °C: the OK state is defined for values less than 30 °C, the transition to the NOT_OK state happens when the temperature is between 30 °C and 40 °C while the ERROR state is reached if the temperature is above 40 °C.

The RICH_DCS_TEMP domain groups all the temperature DU instances and summarises the state of all the temperatures sensors in the READY (if all the children are in state OK), NOT_READY (if any children is in state NOT_OK) and ERROR (if any children is in state ERROR), giving highest priority to the ERROR state. The operations panel of the RICH_DCS_TEMP CU is shown in Figure 148(a). The individual monitoring of a sensor can be accessed double-clicking on the corresponding sub-system name, opening the user interface shown in Figure 148(b).

The ELMB itself is part of the equipment and must be included in the control system. ELMB is powered by two 10 V channels and checks on the communication between hardware and software must be performed. For this reason, another domain handling the ELMB device has been added to the control system, including the management of the ELMB CANbus and its LV channels. The reason why these LV channels are not included

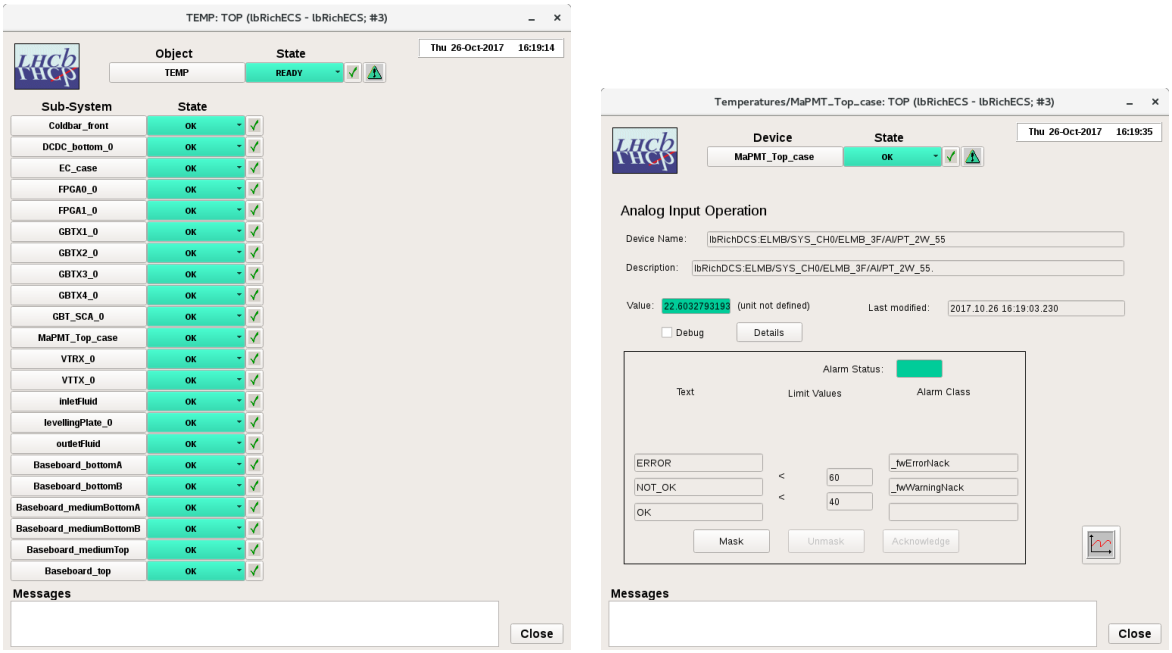

(a) (b)

Figure 148: (a): Operations panel summarising the state the temperature sensors; (b): User interface used to monitor each temperature sensor. The user interface is provided by the JCOP framework. The panel shows the alarm limits and the trending plot of the temperature value over time is accessible clicking on the button to the right.

in the LV partition is the need to perform automatic actions in case of any temperature sensor going to state ERROR, as explained later in section 7.7.

7.5.3 The RICH DCS domain

The LV, ELMB and TEMP control and monitoring domains have been grouped in the RICH DCS domain summarising their conditions in a single overall state. The RICH_DCS operations panel is shown in Figure 149. Clicking on one of the sub-system name the corresponding operations panel is opened.

The Configuration DB tool has also been used within the DCS partition. The recipe contains the LV and ELMB settings used during data taking and loaded when the Switch_ON command is sent.

7.6 The RICH DAQ partition

The DAQ partition comprises the control of the LHCb readout boards and of the sub-detector back-end (BE) and FE boards. Readout boards are common for all the sub-detectors and physically they are of one board type, named PCIe40, logically separated into the TELL40, SODIN and SOL40 components, having different functionality in the upgraded LHCb readout. On the other hand, the BE and FE electronics are sub-detector specific. An introduction to the upgraded LHCb readout and to the upgraded RICH detectors BE, i.e. the PDMDB, and FE electronics is reported in chapter 5.

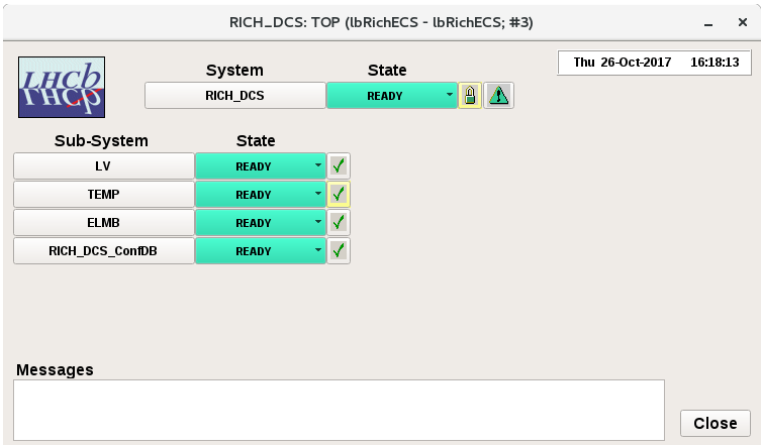

Figure 149: The RICH DCS partition.

Low-level libraries and command line tools to access different registers of the PCIe40, a DIM server to implement higher level commands to configure and monitor the readout board and a WinCC-OA component providing the access to all electronics component through an high-level description are provided centrally by the LHCb Online group. The WinCC-OA MiniDAQ component also provides an FSM aggregating all of the MiniDAQ devices into a control tree, shown in Figure 150. From the top of the FSM tree it is possible to send the LOAD command, allowing to load all the software processes necessary for the correct data taking, the CONFIGURE command, to setup all the devices with the required configuration for the data taking, the START_RUN command, bringing all the devices into the level where data taking is undergoing, and the START_TRIGGER command that will activate the TFC triggers. This sequence of commands is able to bring up the system from the state OFFLINE to the state RUNNING. If at any point an error occurs, the relevant device goes to state ERROR which will be propagated up the tree and devices can be recovered sending the RECOVER command. Similarly, there is a sequence of commands to bring the state down from RUNNING to NOT_READY.

Each node has its own operation panels allowing to setup the communication with the GBT Server, the subscription of the devices registers from the GBT Server and the restart of the WinCC-OA ctrl managers (from the MiniDAQ top node), to change the trigger configuration (from the SODIN node), etc.

As described in chapter 5, the control and monitoring of the sub-detectors electronics will be achieved with the usage of the GBT and SCA chips. Other WinCC-OA components have been developed by the Online group providing the basic communication with the BE and FE via the GBT Server and to model hardware into WinCC-OA datapoint structures.

I contributed to the development of the RICH upgrade DAQ control system integrating it with the MiniDAQ FSM. The MiniDAQ partition operations panel is shown in Figure 151(a). The DAQ, MEP and TFC are the CU used to handle the TELL40 configuration, the writing of data and the trigger configuration.

The MiniDAQ operations panel has been customised in order to meet the functionality needed to test the RICH FE. The fields **Fibres to align**, **BXID Offset** and **TELL40 correction** are used to write on the registers of the PCIe40 through a user friendly interface. The user can enable or disable the readout of each data link, modify the bunch cross ID offset in order to adjust the latency between data sent out by the PDMDBs and

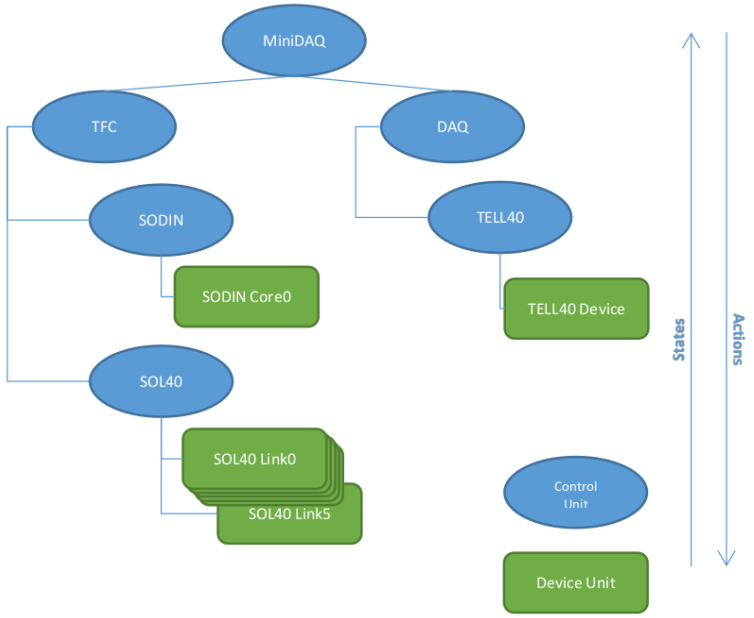

Figure 150: MiniDAQ FSM tree.

data read by the TELL40, and to enable a feature implemented by the RICH upgrade group in order to provide the timing alignment within each PDMDB FPGA. The panel

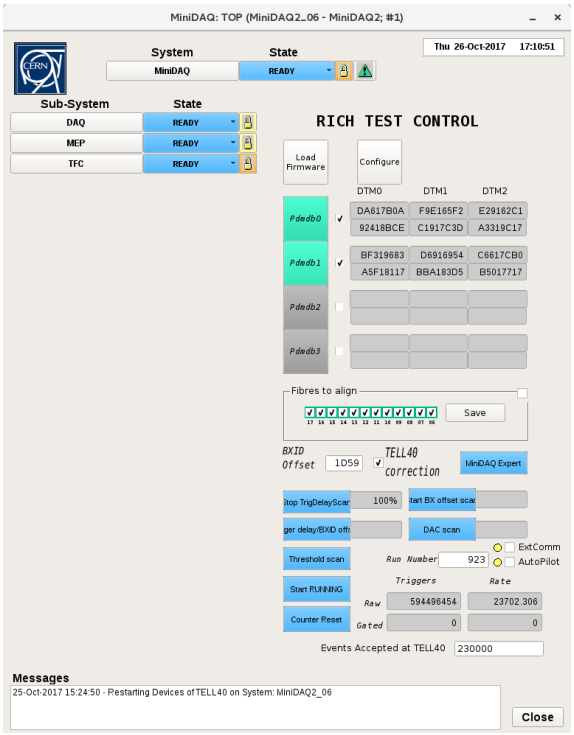

(a)

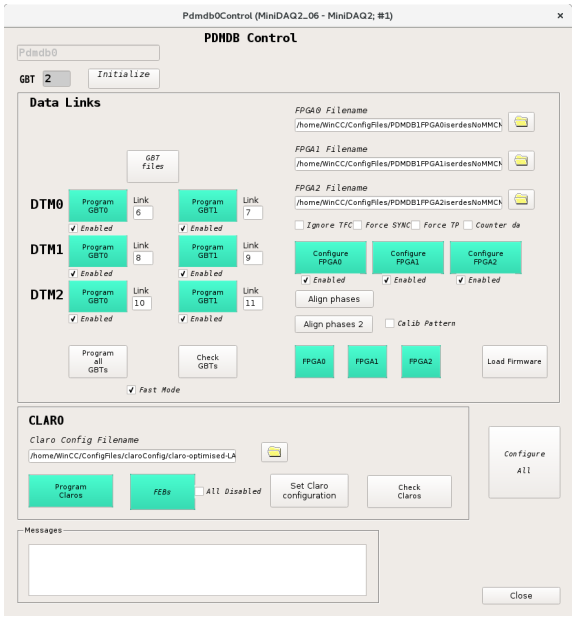

(b)

Figure 151: (a): RICH customised MiniDAQ operations panel; (b): PDMDB configuration panel.

allows to access the PDMDB configuration panel shown in Figure 151(b). The GBT text field at the top corresponds to the SOL40 link used to interface the PDMDB and the TELL40 and it is the identifier of the board within the PCIe40. The **Initialize** button at the top send the initialisation of all the interfaces between the PCIe40 and the PDMDB and between the PDMDB and the corresponding FEBs through the SOL40 link. The initialisation comprises the setting of the registers for the master GBT link, the initialisation of FEB and GBT reset lines setting the corresponding GPIO registers, the activation of I^2C and SPI channels for the programming of the CLAROs and the activation of the JTAG channel used to load the firmware into the PDMDB. Each of the **Program GBT** button allows to write into the GBTx registers the bits required to start up correctly. Each **FPGA** button allows to load the firmware in the corresponding FPGA through the JTAG channel. The **Set Claro Configuration** button opens a panel allowing the user to set the threshold code, offset bit, etc., of the CLARO channels and to program them through the SPI protocol converting the settings into a 128 bit register for each CLARO behind the scene.

I contributed to the development of all the features described above. In particular I implemented the procedure to configure the CLAROs through the user interface and I automatised all the steps required to configure the PDMDBs. The code has been organised in a WinCC-OA ctrl library, splitting each part in a different function, in order to perform all the steps using the **Configure All** button in Figure 151(b) without loosing the capability to send again the single commands from specific buttons for error recovery. Furthermore, the structure of the code allows to configure multiple PDMDBs in sequence, through the **Configure** button in Figure 151(a), making straightforward the scalability to an high multiplicity system. This kind of automation has been the first step towards the implementation of the PDMDB DU class. Indeed I defined and selected the **state** bit of the PDMDB as the element to be used to define state transitions of each PDMDB instance. The CONFIGURE action is available to bring up the system from the NOT_READY state to the READY state, doing the same job of the Configure All button in Figure 151(b) but within the FSM framework. In case of errors, e.g. a failure programming a CLARO, the PDMDB will go to state ERROR, from where is possible to send the RECOVER command, allowing a partial recovery of the PDMDB, i.e. program again the misconfigured CLARO in this case. The same actions and states have been defined in the PDMDB CU grouping all the PDMDBs used for the data taking. The PDMDB and MiniDAQ CU have been aggregated in the RICH DAQ top node.

I also implemented automated runs with steps that will be used to calibrate the RICH upgrade detectors and to perform timing studies. **DAC scans** are runs used to calibrate each CLARO channel, converting the threshold code (from 0 to 63) and the threshold step width in ke^-. They are also used to find each CLARO channel offset in ke^-. In order to perform a DAC scan, a threshold must be set for each channel first. Afterwards, a fixed amount of charge from the 8 bits DAC having output range from 0 to 1 V, hosted by the PDMDB, is injected at the input of all the enabled CLARO channels. The amount of injected charge is controlled and sent to the discriminator input of each CLARO channel by the GBT-SCA of the PDMDB. Since the CLARO input test capacitance is 640 fF, the maximum charge that can be injected is $4\,Me^-$ in steps of $15\,ke^-$/bit. The user interface used to perform DAC scans is shown in Figure 152. The top left side of the panel allows to define the CLARO channel settings common for all the enabled FEBs and CLAROs within each FEB. The **Program Claros** button converts the codes to a 128 bit registers

and sends the configuration to each CLARO. The bottom part of the panel allows to define the run parameters, i.e. the DAC start and end value and the number of events to be acquired per step. The **Start** button begins the procedure injecting the charge corresponding to the value written in the **Current Step** text field and then sending commands to the MiniDAQ FSM in order to acquire data using an internal calibration trigger. The procedure is fully automated and an automatic recovery procedure has been implemented in case of errors.

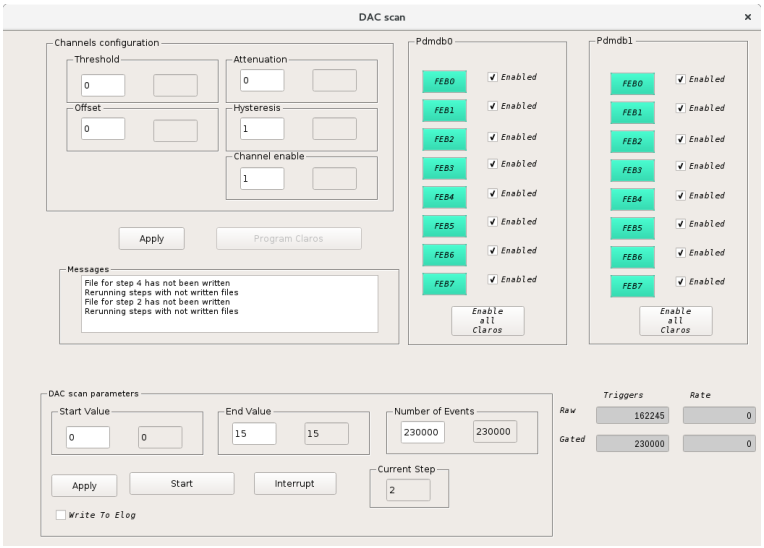

Figure 152: User interface used to perform DAC scans. The messages box shows message in case of errors during the run. The Write to Elog checkbox allows to send the DAC scans information to the LHCb RICH upgrade logbook for the bookkeeping of the runs.

Threshold scans are runs used to obtain the integrated pulse-height spectrum of each MaPMT channel. They are very important for the upgraded RICH detectors since they allow to determine the threshold having the optimal signal/noise ratio and the best photodetection efficiency for each MaPMT channel. During threshold scans, CLARO channels are programmed with different threshold values and a fixed number of events is acquired at each threshold step. Using the user interface shown in Figure 153, first the 128 bit register corresponding to the user defined values is built and written to the CLAROs through SPI, then a run is started sending commands to the MiniDAQ FSM and a user defined number of events is acquired using an external trigger source, like a laser during tests in the lab or a beam during testbeams. After that the run is stopped, the threshold value is decremented and the procedure is repeated until the end value is reached.

Finally the **latency scans**, or trigger delay scans, are runs where the external trigger offset is changed and a run with a fixed number of events is taken for each step in order to find the maximum number of events, i.e. to find the right latency of the system. They can be started from the MiniDAQ operations panel shown in Figure 151(a).

7.7 The RICH ECS domain

The RICH HV, RICH DCS and RICH DAQ domains have been integrated in the RICH ECS FSM. The RICH ECS domain allows to summarise the state of the HV, DCS and

Figure 153: User interface used to perform threshold scans. The messages box shows message in case of errors during the run. The Write to Elog checkbox allows to send the DAC scans information to the LHCb RICH upgrade logbook for the inventory.

DAQ sub-systems in a single overall state and to operate the RICH upgrade prototypes with a control system as close as possible to the final one. The RICH ECS operations panel is shown in Figure 154.

7.8 Run Control user interface

Several functionality are available within this user interface. Information on the ongoing run are available within the panel. Threshold, DAC and trigger delay scans, described in Section 7.6 are directly accessible from here. The **Select and Plot** button allows to show the trending plots of the monitored variables like temperatures, voltages and currents. The panel shown in Figure 155 allows to select up to 8 variables and to show the corresponding trending plot like the one shown in Figure 156. The **Power Supplies Overview** button is used to open the summary of the numeric values of the voltages and currents of the power supplies shown in Figure 157. These monitoring tools have been extensively used during testbeams and tests in the lab. Finally the **Start IBCDB** button allows to start the operations of the RICH upgrade database, described in Chapter 6, allowing to check the properties of the hardware installed in the setup.

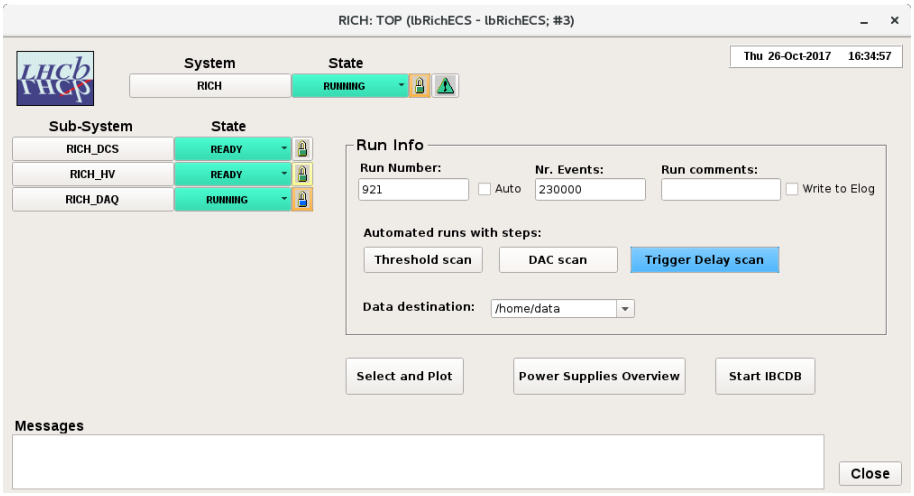

Figure 154: RICH ECS operations panel. The RICH state summarises the RICH DCS, RICH HV and RICH DAQ states. Actions can be sent from the top node allowing the switching on/off of the HV and of the LV sub-systems, the configuration of the DAQ sub-system and the run control.

7.9 RICH ECS states and commands

The RICH ECS states and available commands have been developed in order to cope with the different functionality required by each sub-system. Each sub-system can be accessed from the top panel, as shown in Figure 158, allowing the independent operations of each sub-system.

An example of operations allowed by the control system is like the following. Starting from a situation where everything is OFF, a Go_READY command can be sent from the RICH node allowing to switch on the LV and the HV. When the LV and the HV are on, a CONFIGURE command can be sent from the top in order to configure the RICH DAQ, i.e. the MiniDAQ and PDMDB devices, as described in Section 7.6. When all the sub-system are in state READY, the RICH system goes to state READY. At this point the START_RUN command followed by the START_TRIGGER command can be sent from the top to go in the RUNNING state and take data. These actions can also be sent from the corresponding individual partitions if needed. In case of errors occurring within any of the sub-systems, the RICH node moves to state ERROR. Within this state the only available action is the Recover one. This action is automatically propagated to the sub-system in state ERROR. For example, one possible situation is the failure in the programming of one CLARO. Thanks to the features described in Section 7.6, the Recover action will only act on the faulty CLARO, speeding up the restoration of the system to the READY state. This situation is illustrated in Figure 159.

The integration of the different sub-systems in a single FSM facilitates the operations of the setup. Furthermore, it allows the implementation of automatic actions. For example, as stated in Section 7.5, the temperature sensors DU can go to state ERROR if the measured values are above the safety threshold. An automatic action has been implemented to cope with this scenario. If any temperature sensor goes to state ERROR, the RICH DCS TEMP LU goes to state ERROR. This is recognised by the RICH DCS CU, that is the parent of RICH DCS TEMP, as an emergency, since high temperatures can damage the

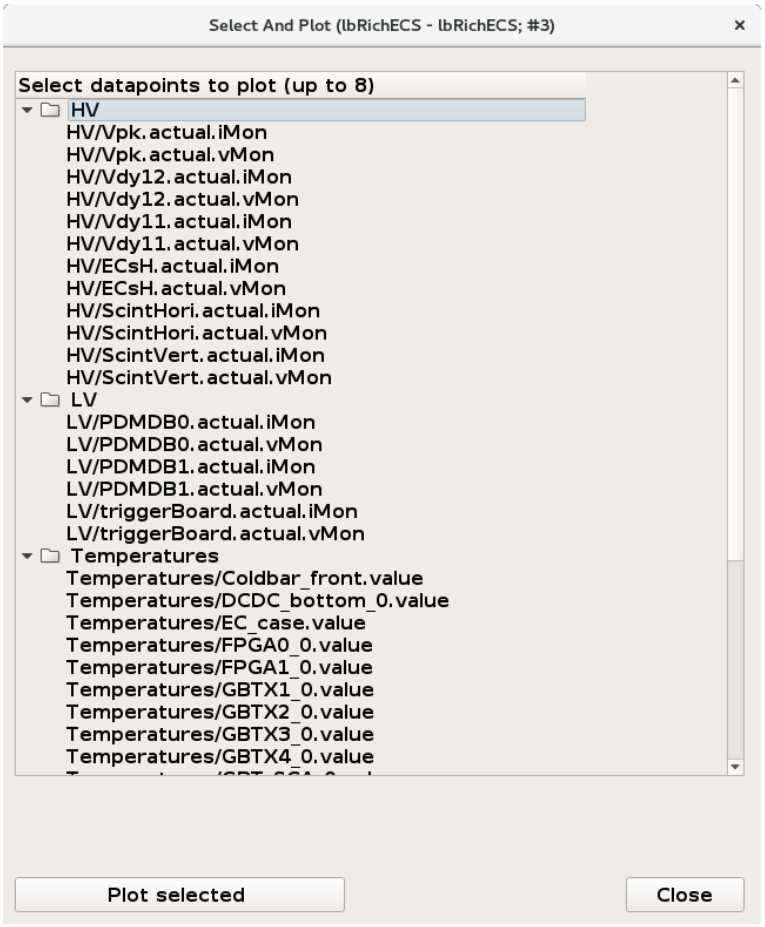

Figure 155: Panel allowing to select the variables to plot. They are divided into the HV, LV and Temperatures sections.

photodetectors. Indeed the RICH DCS partition moves to state EMERGENCY. This state is propagated to the RICH ECS node that triggers the switching off of the HV and of the LV channels powering the PDMDBs, being the power supplies the sources of heat in the system. An illustration of this scenario is shown in Figure 160. Once all the measured temperatures are within the safety limits, or the DU in state ERROR has been disabled in case of a faulty sensor, the RICH DCS TEMP partition moves from the state ERROR. A Clear_Emergency action can be sent from the RICH top node, switching on the HV and the LV setting the voltage to zero and then switching off again. Sending the Go_READY action, the nominal configurations are loaded from the Configuration DB and the system can be run again.

7.10 Conclusions and future perspectives

The prototype for the RICH upgrade ECS has been developed for the control of the setup used during testbeams and tests in the lab at CERN. The control system has been built following the LHCb-JCOP conventions in order to be easily scalable towards the final modularity of the RICH upgrade detectors and to make possible the integration with the LHCb upgrade ECS.

The DCS partition will be integrated with other domains implementing the abstraction

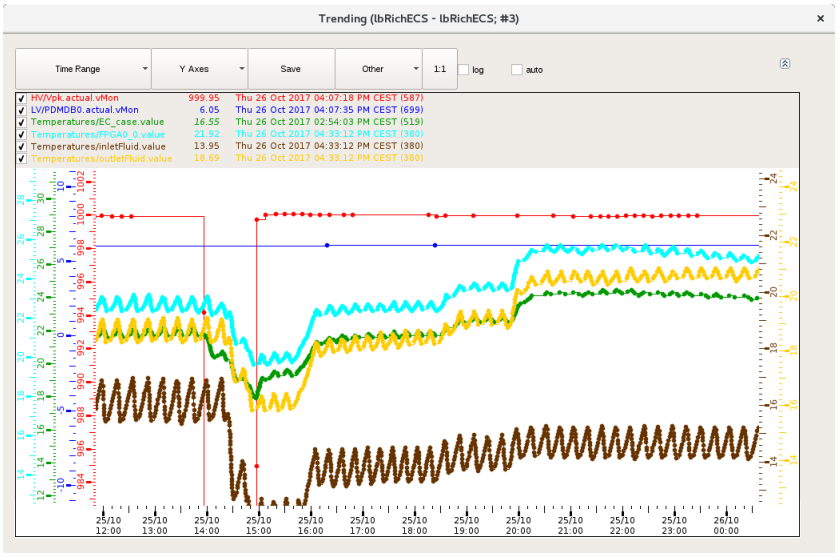

Figure 156: Trending plot shown after clicking on the Plot selected button of Figure 155. This tool has been extensively used during testbeams and tests in the lab to monitor LV and HV currents and during thermal tests.

Figure 157: Overview of the values monitored by the power supplies. From this panel is also possible to control each channel and to show its current and voltage trending. Also the crate status can be monitored using the corresponding button.

of at least humidity and pressure measurements using the interface provided by the ELMB. These parameters, as well as the temperatures, must be monitored at several different positions in and around the RICH detectors.

The RICH ECS could also be integrated with a RICH specific Detector Safety System (DSS), integrating the LHCb DSS. The latter one will have the responsibility of safeguarding experimental equipment taking coarse automatic actions, e.g. switching off the power to rows of racks, in case of serious problems, not only to the RICH ones. As such the DSS

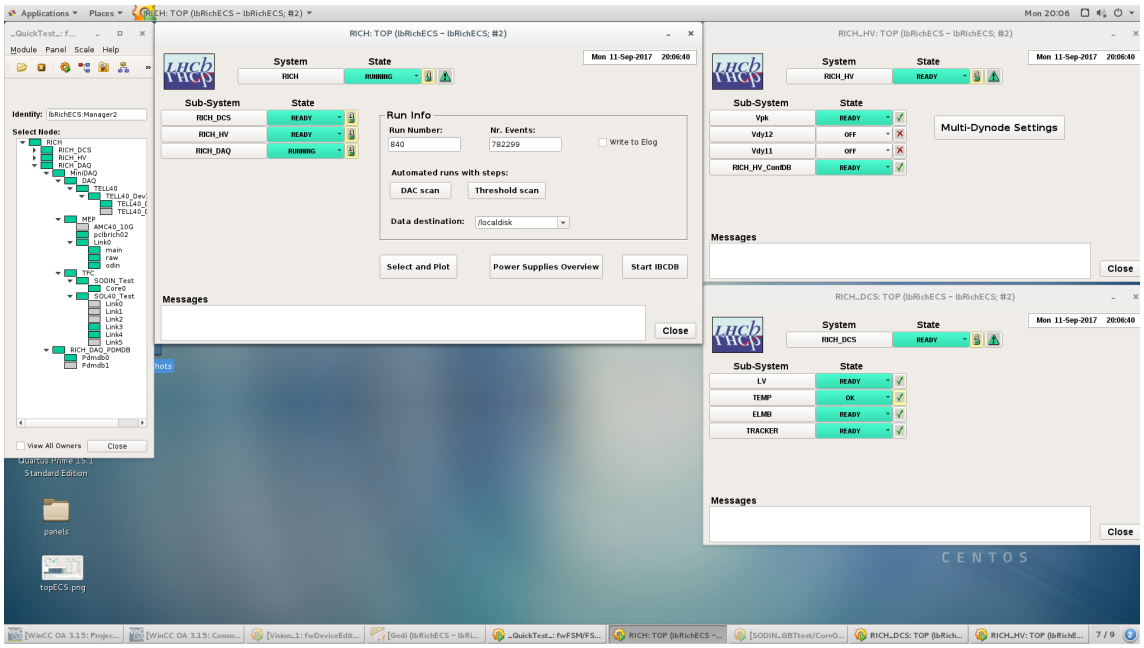

Figure 158: Screenshot showing the control system user interfaces during normal operations.

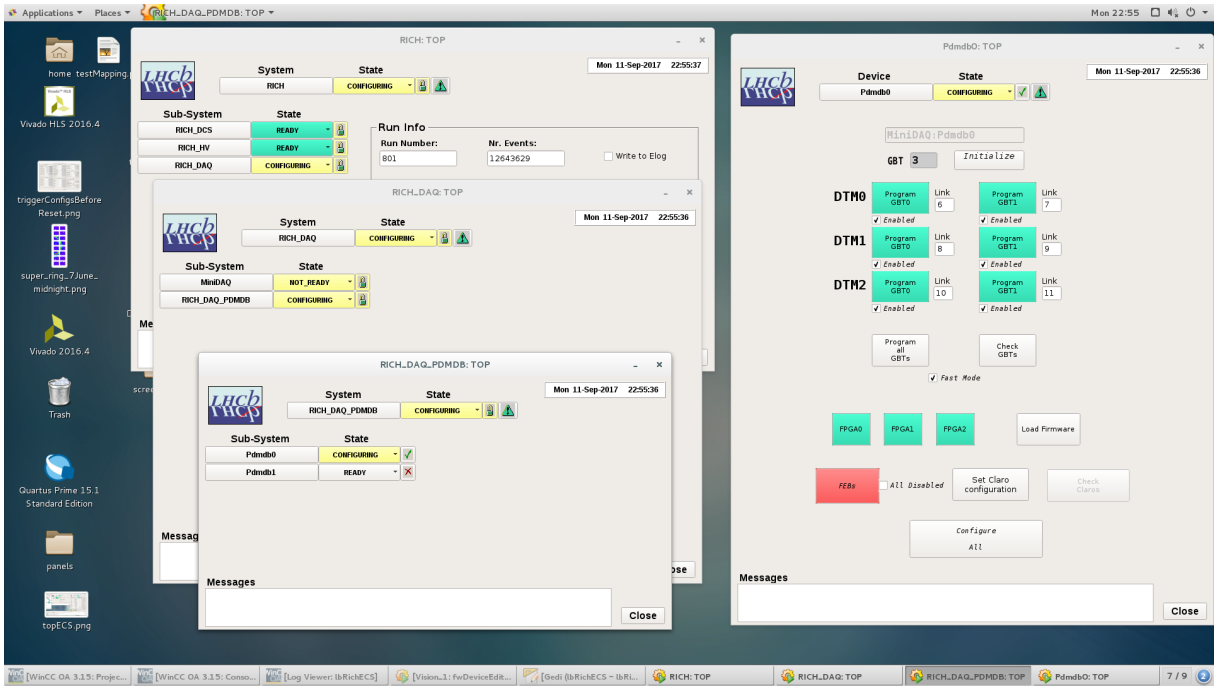

Figure 159: Picture showing the scenario of reconfiguring of the RICH FE after sending the Recover command. In this case one of the CLAROs of one PDMDB (the other one was disabled) failed to be programmed correctly, as indicated by the red coloured FEBs button in the PDMDB panel (clicking on the button it is possible to investigate which CLARO of which FEB failed). The CONFIGURING state is propagated from the Pdmdb0 DU to the RICH top node. The MiniDAQ partition was in state NOT_READY since it has just been recovered.

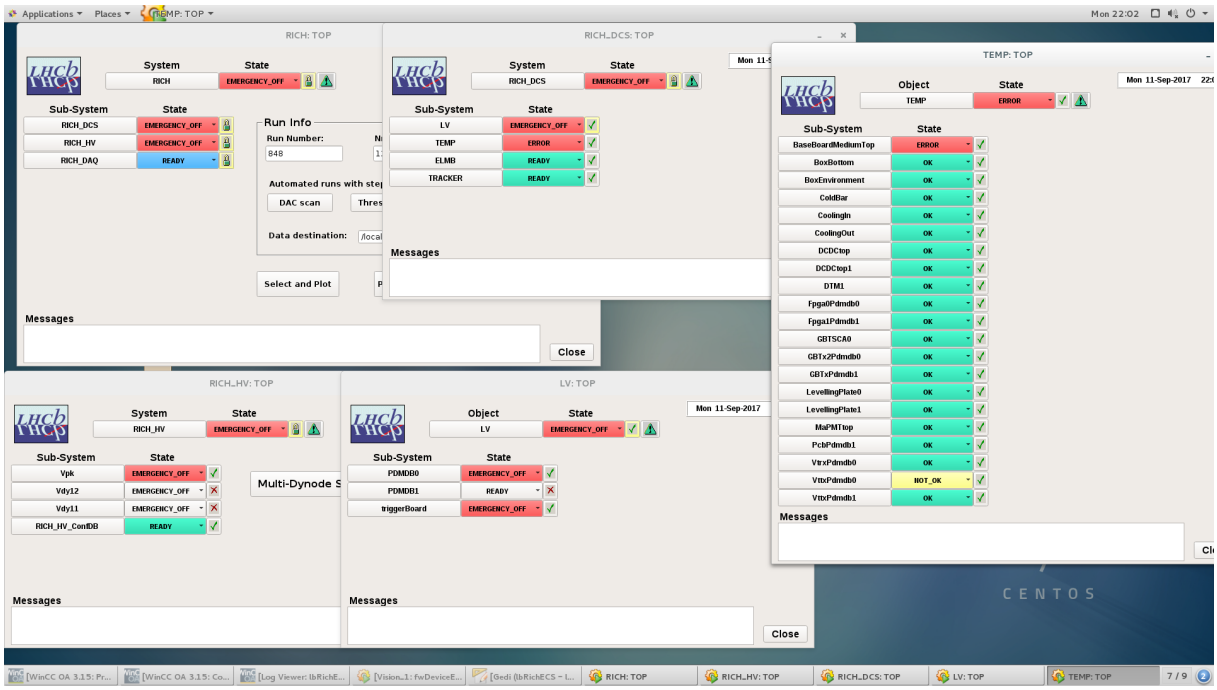

Figure 160: Emergency off scenario. The temperature measured by a Pt1000 integrated in a baseboard was above the limit and the BaseBoardMediumTop DU went to state ERROR, and hence the TEMP partition went to state ERROR. The propagation of the states towards the RICH ECS top node triggered the Do_Emergency_Off automatic action sent to the HV and LV partitions.

has its own sensors and it receives sensor inputs from subdetectors. The DSS complements the DCS and the CERN Safety System. However, an independent RICH DSS could be implemented to have a further level of safety.

The control system, in particular the DAQ partition, is continuously evolving in parallel with the developments of new features by the LHCb online group, regarding the multiplicity of PCIe40 required by the RICH upgrade detectors, and with new requirements resulting from the RICH FE tests towards the final configuration aiming to the optimal operations of the detectors.

8 Conclusions

The LHCb experiment physics programme was by design focused on the study of CP violating processes and rare decays. Thanks to the excellent performance of the LHC and of the LHCb detector, the physics output of the LHCb experiment extends well beyond this core programme. Indeed, the high performance of the LHCb tracking and PID systems, together with the copious production of b-hadrons at the LHC, allows to use LHCb as a general purpose detector in the forward region, as demonstrated by several LHCb publications showing world leading results in the heavy flavour sectors: from precision measurements of the CKM matrix parameters to the observation of the $B^0 \to p\bar{p}$ decay, the rarest decay mode of a B^0 meson ever observed so far; from SM measurements in the forward region to LFU tests and searches for exotica particles; from high precision measurements of b-hadron lifetimes to quarkonium production measurements; from proton-ion physics to conventional and exotic hadrons spectroscopy. These results have established LHCb as the next generation flavour physics experiment.

The capability to perform full amplitude analyses with unprecedented statistics makes LHCb extremely competitive on the searches for exotic hadrons, having led to important discoveries of charmonium-like mesons and to the first observation of a pentaquark candidate. These observations provide new insights in the understanding of how quarks and gluons bind together to build hadrons, description currently provided by the long-distance non-perturbative QCD, relying on phenomenological models and on lattice QCD calculations. Moreover, a more precise understanding of hadron structures will provide important inputs to other heavy flavour sectors, including CP violation and LFU measurements, reducing the theoretical uncertainties on hadronic form factors.

In this thesis, I discussed the amplitude analysis of the $B^0 \to \eta_c K^+\pi^-$ decay channel, of which I am the main contributor and corresponding author for the relative publication [182]. The article has been accepted by the European Physics Journal C.

It is the first time that a search for exotic hadrons has been carried out in this decay mode. The low branching ratio of the $B^0 \to \eta_c(\to p\bar{p})K^+\pi^-$ decay channel, the relatively small overall reconstruction efficiency and the large level of backgrounds, make challenging the $B^0 \to \eta_c K^+\pi^-$ signal extraction. However, thanks to the performance of the LHCb detector, about 2000 events of $B^0 \to \eta_c K^+\pi^-$ candidates has been obtained by using $4.7\,\text{fb}^{-1}$ of pp-collision data collected at $\sqrt{s} = 7\,\text{TeV}$, $\sqrt{s} = 8\,\text{TeV}$ and $\sqrt{s} = 13\,\text{TeV}$. The selection procedure allowed to obtain a good purity to perform the $B^0 \to \eta_c K^+\pi^-$ decay channel amplitude analysis. I analysed the resonant structures in the $B^0 \to \eta_c K^+\pi^-$ decay channel by performing an amplitude fit to the Dalitz Plot variables. The $K^+\pi^-$ system up to $\sim 2.3\,\text{GeV}$ has been studied for the first time in this decay channel, providing new insights of the $K^+\pi^-$ dynamics.

The first measurement of the $B^0 \to \eta_c K^+\pi^-$ branching fraction has been performed, and it gives

$$\mathcal{B}(B^0 \to \eta_c K^+\pi^-) = (5.73 \pm 0.24 \pm 0.13 \pm 0.66) \times 10^{-4},$$

where the first uncertainty is statistical, the second systematic, and the third is due to limited knowledge of external branching fractions.

The data are significantly better described by including a charged charmonium-like resonance decaying to the $\eta_c\pi^-$ system, with $m_{Z_c^-} = 4096 \pm 20\,^{+18}_{-22}\,\text{MeV}$, $\Gamma_{Z_c^-} = 152 \pm 58\,^{+60}_{-35}\,\text{MeV}$. The significance of the so-called $Z_c(4100)^-$ exotic candidate

is more than three standard deviations when including systematic uncertainties. This is the first evidence for an exotic state decaying into two pseudoscalars. The favoured spin-parity assignments, $J^P = 0^+$ and $J^P = 1^-$, cannot be discriminated once systematic uncertainties are taken into account. More data will be required to be conclusive on the nature of the $Z_c(4100)^-$ meson.

The importance of the result has been acknowledged with an outreach article on the public web page of the LHCb collaboration, and on the CERN Courier [183]. Moreover, the results have been presented for the first time in a CERN seminar dedicated to newest LHCb results on exotic hadrons spectroscopy.

While the current LHCb experiment is taking high quality data, the searches for new physics contributions in rare decays and in the measurement of CP violating processes, motivated the decision to upgrade the LHCb detector to efficiently exploit the five-fold increase in the instantaneous luminosity foreseen starting from Run 3. This upgrade, starting in 2019 during LS2, will be a unique opportunity for heavy flavour studies, allowing to increase the available statistics in many b-hadron decays, thanks to the implementation of an innovative flexible software trigger strategy that will allow to significantly enhance the trigger efficiency on fully hadronic final states. For instance, decay modes like $B^0 \to \eta_c(\to p\bar{p})K^+\pi^-$ will considerably profit from the new trigger strategy.

During my PhD I also contributed to the RICH upgrade project. The RICH detectors are crucial for the LHCb physics programme, providing charged hadrons particle identification. The photodetectors and the frontend electronics will be replaced in the upgraded RICH detectors, in order to readout RICH1 and RICH2 at the full 40 MHz LHC bunch crossing rate. The goal is to keep the current excellent PID performance with the higher instantaneous luminosity of the upgrade.

I contributed to the validation and characterisation of the RICH upgrade opto-electronics chain prototypes, in the lab and during testbeams. In particular I had the opportunity to be involved in the integration of the RICH upgrade frontend electronics with the upgraded LHCb readout architecture.

I developed from scratch the inventory, bookkeeping and connectivity database for the RICH upgrade devices. The database is the central repository containing the history and the properties of all the components that will be installed in the upgraded RICH detectors. It will also be used during column assembly in order to group photodetectors having similar properties taking into account the different occupancies foreseen in the upgraded RICH photodetector planes. The flexibility of the database is such that its functionality can be extended depending on the eventual new requirements that can be faced during the construction of the RICH upgrade detectors. Moreover, beside the RICH detectors specific parts, the database could also be adopted from other subdetectors with minimal changes. The database has been developed using the WinCC-OA SCADA tool and the JCOP framework. One of the main motivations for this choice is the easy integration with the LHCb ECS.

During my PhD I also developed the prototype for the RICH upgrade ECS, including the HV, DCS and DAQ partitions. The functionality of the ECS have been tested during testbeams, and it is also used in the lab at CERN, where DAQ integration activities are ongoing. The DAQ partition, allowing for the configuration of the RICH frontend and being responsible for the control of the data-flow from the RICH frontend to the LHCb readout prototypes, is evolving. Indeed, the re-design of the LHCb readout architecture will require a new organisation of the LHCb ECS partitioning, on which I am contributing.

Also some integrations to the DCS partition are ongoing, including the humidity and pressure monitoring systems. The design of the RICH upgrade ECS prototype allows to easily scale the system to the final multiplicity, and to integrate the control and monitoring of new hardware in a straightforward way.

9 Glossary of Terms

- BW: Breit-Wigner
- CondDB: Conditions Database
- ConfDB: Configuration Database
- CU: Control Unit
- DCS: Detector Control System
- DEN: Device Editor and Navigator
- DIM: Distributed Information Management
- DP: Dalitz Plot (analysis) or Data-Point (WinCC-OA)
- DPT: Data-Point Type
- DU: Device Unit
- EC: Elementary Cell
- ECS: Experiment Control System
- ELMB: Embedded Local Monitor Board
- FOM: Figure of Merit
- FSM: Finite State Machine
- GBT: GigaBit Transceiver
- HPD: Hybrid Photon Detector
- IBCDB: Inventory, Bookkeeping and Connectivity Data-Base
- IP: Impact Parameter
- ISR: Initial State Radiation
- JCOP: Joint Control Project
- LHC: Large Hadron Collider
- LU: Logical Unit
- MaPMT: Multi-anode Photo-Multiplier Tube
- MVA: Multivariate Analysis
- NLL: Negative Log-Likelihood
- NP: New Physics

- OPC: Open Platform Communications
- PDF: Probability Density Function
- PDM: Photo-Detector Module
- PDMDB: Photo-Detector Module Digital Board
- PV: Primary Vertex
- QCD: Quantum Chromodynamics
- RBW: Relativistic Breit-Wigner
- RICH: Ring Imaging Cherenkov
- RF: Radio-Frequency
- ROC: Receiver Operating Characteristic
- SCA: Slow Control Adapter chip
- SDP: Square Dalitz Plot
- SM: Standard Model
- SMI: State Management Interface
- SML: State Management Language
- SV: Secondary Vertex
- TFC: Timing and Fast Control
- TIS: Triggered Independently of Signal
- TOS: Triggered On Signal

References

[1] M. Gell-Mann, *A Schematic Model of Baryons and Mesons*, Phys. Lett. **8** (1964) 214.

[2] G. Zweig, *An SU_3 model for strong interaction symmetry and its breaking; Version 1*, Tech. Rep. CERN-TH-401, CERN, Geneva, Jan, 1964.

[3] Belle collaboration, S.-K. Choi *et al.*, *Observation of a narrow charmoniumlike state in exclusive $B^{\pm} \to K^{\pm}\pi^{+}\pi^{-}J/\psi$ decays*, Phys. Rev. Lett. **91** (2003) 262001, arXiv:hep-ex/0309032.

[4] H.-X. Chen, W. Chen, X. Liu, and S.-L. Zhu, *The hidden-charm pentaquark and tetraquark states*, Phys. Rept. **639** (2016) 1, arXiv:1601.02092.

[5] R. F. Lebed, R. E. Mitchell, and E. S. Swanson, *Heavy-quark QCD exotica*, Prog. Part. Nucl. Phys. **93** (2017) 143, arXiv:1610.04528.

[6] A. Esposito, A. Pilloni, and A. D. Polosa, *Multiquark resonances*, Phys. Rept. **668** (2016) 1, arXiv:1611.07920.

[7] F.-K. Guo *et al.*, *Hadronic molecules*, Rev. Mod. Phys. **90** (2018) 015004, arXiv:1705.00141.

[8] A. Ali, J. S. Lange, and S. Stone, *Exotics: Heavy pentaquarks and tetraquarks*, Prog. Part. Nucl. Phys. **97** (2017) 123, arXiv:1706.00610.

[9] S. L. Olsen, T. Skwarnicki, and D. Zieminska, *Nonstandard heavy mesons and baryons: Experimental evidence*, Rev. Mod. Phys. **90** (2018) 015003, arXiv:1708.04012.

[10] LHCb collaboration, R. Aaij *et al.*, *Observation of the resonant character of the $Z(4430)^{-}$ state*, Phys. Rev. Lett. **112** (2014) 222002, arXiv:1404.1903.

[11] LHCb collaboration, R. Aaij *et al.*, *Model-independent confirmation of the $Z(4430)^{-}$ state*, Phys. Rev. **D92** (2015) 112009, arXiv:1510.01951.

[12] LHCb collaboration, R. Aaij *et al.*, *Observation of $J/\psi p$ resonances consistent with pentaquark states in $\Lambda_b^0 \to J/\psi p K^{-}$ decays*, Phys. Rev. Lett. **115** (2015) 072001, arXiv:1507.03414.

[13] LHCb collaboration, R. Aaij *et al.*, *Observation of exotic $J/\psi\phi$ structures from amplitude analysis of $B^{+} \to J/\psi\phi K^{+}$ decays*, Phys. Rev. Lett. **118** (2016) 022003, arXiv:1606.07895.

[14] LHCb collaboration, R. Aaij *et al.*, *Amplitude analysis of $B^{+} \to J/\psi\phi K^{+}$ decays*, Phys. Rev. **D95** (2016) 012002, arXiv:1606.07898.

[15] Particle Data Group, M. Tanabashi *et al.*, *Review of particle physics*, Phys. Rev. **D98** (2018) 030001.

[16] V. E. Barnes *et al.*, *Observation of a Hyperon with Strangeness -3*, Phys. Rev. Lett. **12** (1964) 204.

[17] H. D. Politzer, *Reliable Perturbative Results for Strong Interactions?*, Phys. Rev. Lett. **30** (1973) 1346, [,274(1973)].

[18] D. J. Gross and F. Wilczek, *Ultraviolet Behavior of Nonabelian Gauge Theories*, Phys. Rev. Lett. **30** (1973) 1343, [,271(1973)].

[19] A. Deur, S. J. Brodsky, and G. F. de Teramond, *The QCD running coupling*, Prog. Part. Nucl. Phys. **90** (2016) 1, arXiv:1604.08082.

[20] A. Chodos *et al.*, *New extended model of hadrons*, Phys. Rev. **D9** (1974) 3471.

[21] T. A. DeGrand, R. L. Jaffe, K. Johnson, and J. E. Kiskis, *Masses and other parameters of the light hadrons*, Phys. Rev. **D12** (1975) 2060.

[22] N. Isgur and J. E. Paton, *Flux-tube model for hadrons in QCD*, Phys. Rev. **D31** (1985) 2910.

[23] M. A. Shifman, A. I. Vainshtein, and V. I. Zakharov, *QCD and resonance physics. Theoretical foundations*, Nucl. Phys. **B147** (1979) 385.

[24] W. E. Caswell and G. P. Lepage, *Effective lagrangians for bound state Problems in QED, QCD, and other field theories*, Phys. Lett. **167B** (1986) 437.

[25] G. T. Bodwin, E. Braaten, and G. P. Lepage, *Rigorous QCD analysis of inclusive annihilation and production of heavy quarkonium*, Phys. Rev. **D51** (1995) 1125, arXiv:hep-ph/9407339, [Erratum: Phys. Rev.D55,5853(1997)].

[26] N. Brambilla *et al.*, *QCD and strongly coupled gauge theories: challenges and perspectives*, Eur. Phys. J. **C74** (2014) 2981, arXiv:1404.3723.

[27] S. Okubo, *Phi meson and unitary symmetry model*, Phys. Lett. **5** (1963) 165.

[28] J. Iizuka, *Systematics and phenomenology of meson family*, Prog. Theor. Phys. Suppl. **37** (1966) 21.

[29] E. Eichten *et al.*, *Charmonium: The model*, Phys. Rev. **D17** (1978) 3090, [Erratum: Phys. Rev.D21,313(1980)].

[30] E. Eichten *et al.*, *Charmonium: Comparison with experiment*, Phys. Rev. **D21** (1980) 203.

[31] A. Pineda and J. Soto, *Effective field theory for ultrasoft momenta in NRQCD and NRQED*, Nucl. Phys. Proc. Suppl. **64** (1998) 428, arXiv:hep-ph/9707481, [,428(1997)].

[32] N. Brambilla, A. Pineda, J. Soto, and A. Vairo, *Potential NRQCD: An Effective theory for heavy quarkonium*, Nucl. Phys. **B566** (2000) 275, arXiv:hep-ph/9907240.

[33] S. Godfrey and N. Isgur, *Mesons in a relativized quark model with chromodynamics*, Phys. Rev. **D32** (1985) 189.

[34] BaBar collaboration, B. Aubert *et al.*, *The BaBar detector*, Nucl. Instrum. Meth. **A479** (2002) 1, arXiv:hep-ex/0105044.

[35] Belle collaboration, A. Abashian *et al.*, *The Belle Detector*, Nucl. Instrum. Meth. **A479** (2002) 117.

[36] H. Stock, *The CLEO-c research program*, AIP Conf. Proc. **717** (2004) 515, arXiv:hep-ex/0310021, [,515(2003)].

[37] BESIII collaboration, M. Ablikim *et al.*, *Design and Construction of the BESIII Detector*, Nucl. Instrum. Meth. **A614** (2010) 345, arXiv:0911.4960.

[38] CDF collaboration, F. Abe *et al.*, *The CDF Detector: An Overview*, Nucl. Instrum. Meth. **A271** (1988) 387.

[39] D0 collaboration, V. M. Abazov *et al.*, *The Upgraded D0 detector*, Nucl. Instrum. Meth. **A565** (2006) 463, arXiv:physics/0507191.

[40] ATLAS collaboration, G. Aad *et al.*, *The ATLAS Experiment at the CERN Large Hadron Collider*, JINST **3** (2008) S08003.

[41] CMS collaboration, S. Chatrchyan *et al.*, *The CMS Experiment at the CERN LHC*, JINST **3** (2008) S08004.

[42] LHCb collaboration, A. A. Alves Jr. *et al.*, *The LHCb detector at the LHC*, JINST **3** (2008) S08005.

[43] M. Beneke, G. Buchalla, M. Neubert, and C. T. Sachrajda, *QCD factorization for $B \to \pi\pi$ decays: Strong phases and CP violation in the heavy quark limit*, Phys. Rev. Lett. **83** (1999) 1914, arXiv:hep-ph/9905312.

[44] Belle collaboration, K. Abe *et al.*, *Observation of a new charmonium state in double charmonium production in e^+e^- annihilation at $\sqrt{s} \approx 10.6$ GeV*, Phys. Rev. Lett. **98** (2007) 082001, arXiv:hep-ex/0507019.

[45] P. Nason *et al.*, *Bottom production*, in *1999 CERN Workshop on standard model physics (and more) at the LHC, CERN, Geneva, Switzerland, 25-26 May: Proceedings*, pp. 231–304, 1999, arXiv:hep-ph/0003142.

[46] V. N. Gribov and L. N. Lipatov, *Deep inelastic e p scattering in perturbation theory*, Sov. J. Nucl. Phys. **15** (1972) 438, [Yad. Fiz.15,781(1972)].

[47] G. Altarelli and G. Parisi, *Asymptotic freedom in parton language*, Nucl. Phys. **B126** (1977) 298.

[48] S. Godfrey and S. L. Olsen, *The Exotic XYZ Charmonium-like Mesons*, Ann. Rev. Nucl. Part. Sci. **58** (2008) 51, arXiv:0801.3867.

[49] ATLAS collaboration, M. Aaboud *et al.*, *Measurements of $\psi(2S)$ and $X(3872) \to J/\psi\pi^+\pi^-$ production in pp collisions at $\sqrt{s} = 8$ TeV with the ATLAS detector*, JHEP **01** (2017) 117, arXiv:1610.09303.

[50] BaBar collaboration, B. Aubert *et al.*, *Study of the $B \to J/\psi K^- \pi^+ \pi^-$ decay and measurement of the $B \to X(3872) K^-$ branching fraction*, Phys. Rev. **D71** (2005) 071103, arXiv:hep-ex/0406022.

[51] BESIII collaboration, M. Ablikim *et al.*, *Observation of $e^+e^- \to \gamma X(3872)$ at BESIII*, Phys. Rev. Lett. **112** (2014) 092001, arXiv:1310.4101.

[52] CDF collaboration, D. Acosta *et al.*, *Observation of the narrow state $X(3872) \to J/\psi \pi^+ \pi^-$ in $\bar{p}p$ collisions at $\sqrt{s} = 1.96$ TeV*, Phys. Rev. Lett. **93** (2004) 072001, arXiv:hep-ex/0312021.

[53] CMS collaboration, S. Chatrchyan *et al.*, *Measurement of the $X(3872)$ production cross section via decays to $J/psi\pi^+\pi^-$ in pp collisions at $\sqrt{s} = 7$ TeV*, JHEP **04** (2013) 154, arXiv:1302.3968.

[54] D0 collaboration, V. M. Abazov *et al.*, *Observation and properties of the $X(3872)$ decaying to $J/\psi \pi^+ \pi^-$ in $p\bar{p}$ collisions at $\sqrt{s} = 1.96$ TeV*, Phys. Rev. Lett. **93** (2004) 162002, arXiv:hep-ex/0405004.

[55] LHCb collaboration, R. Aaij *et al.*, *Observation of $X(3872)$ production in pp collisions at $\sqrt{s} = 7$ TeV*, Eur. Phys. J. **C72** (2012) 1972, arXiv:1112.5310.

[56] Belle collaboration, S.-K. Choi *et al.*, *Bounds on the width, mass difference and other properties of $X(3872) \to \pi^+ \pi^- J/\psi$ decays*, Phys. Rev. **D84** (2011) 052004, arXiv:1107.0163.

[57] LHCb collaboration, R. Aaij *et al.*, *Determination of the $X(3872)$ meson quantum numbers*, Phys. Rev. Lett. **110** (2013) 222001, arXiv:1302.6269.

[58] LHCb collaboration, R. Aaij *et al.*, *Quantum numbers of the $X(3872)$ state and orbital angular momentum in its $\rho^0 J/\psi$ decays*, Phys. Rev. **D92** (2015) 011102(R), arXiv:1504.06339.

[59] E. J. Eichten, K. Lane, and C. Quigg, *New states above charm threshold*, Phys. Rev. **D73** (2006) 014014, arXiv:hep-ph/0511179, [Erratum: Phys. Rev.D73,079903(2006)].

[60] BaBar collaboration, P. del Amo Sanchez *et al.*, *Evidence for the decay $X(3872) \to J/\psi\omega$*, Phys. Rev. **D82** (2010) 011101, arXiv:1005.5190.

[61] Belle collaboration, K. Abe *et al.*, *Observation of a near-threshold $\omega J/\psi$ mass enhancement in exclusive $B \to K\omega J/\psi$ decays*, Phys. Rev. Lett. **94** (2005) 182002, arXiv:hep-ex/0408126.

[62] BaBar collaboration, B. Aubert *et al.*, *Observation of Y(3940) $\to J/\psi\omega$ in $B \to J/\psi\omega K$ at BABAR*, Phys. Rev. Lett. **101** (2008) 082001, arXiv:0711.2047.

[63] Belle collaboration, S. Uehara *et al.*, *Observation of a charmonium-like enhancement in the $\gamma\gamma \to \omega J/\psi$ process*, Phys. Rev. Lett. **104** (2010) 092001, arXiv:0912.4451.

[64] BaBar collaboration, J. P. Lees *et al.*, *Study of $X(3915) \to J/\psi\omega$ in two-photon collisions*, Phys. Rev. **D86** (2012) 072002, arXiv:1207.2651.

[65] CDF collaboration, T. Aaltonen *et al.*, *Evidence for a Narrow Near-Threshold Structure in the $J/\psi\phi$ Mass Spectrum in $B^+ \to J/\psi\phi K^+$ Decays*, Phys. Rev. Lett. **102** (2009) 242002, arXiv:0903.2229.

[66] LHCb collaboration, R. Aaij *et al.*, *Search for the $X(4140)$ state in $B^+ \to J/\psi\phi K^+$ decays*, Phys. Rev. **D85** (2012) 091103(R), arXiv:1202.5087.

[67] BaBar collaboration, J. P. Lees *et al.*, *Study of $B^{\pm,0} \to J/\psi K^+K^-K^{\pm,0}$ and search for $B^0 \to J/\psi\phi$ at BABAR*, Phys. Rev. **D91** (2015) 012003, arXiv:1407.7244.

[68] BESIII collaboration, M. Ablikim *et al.*, *Search for the $Y(4140)$ via $e^+e^- \to \gamma\phi J/\psi$ at $\sqrt{s}$=4.23 , 4.26 and 4.36 GeV*, Phys. Rev. **D91** (2015) 032002, arXiv:1412.1867.

[69] CMS collaboration, S. Chatrchyan *et al.*, *Observation of a peaking structure in the $J/\psi\phi$ mass spectrum from $B^\pm \to J/\psi\phi K^\pm$ decays*, Phys. Lett. **B734** (2014) 261, arXiv:1309.6920.

[70] D0 collaboration, V. M. Abazov *et al.*, *Search for the $X(4140)$ state in $B^+ \to J/\psi\phi K^+$ decays with the D0 Detector*, Phys. Rev. **D89** (2014) 012004, arXiv:1309.6580.

[71] D0 collaboration, V. M. Abazov *et al.*, *Inclusive Production of the X(4140) State in $p\overline{p}$ Collisions at D0*, Phys. Rev. Lett. **115** (2015) 232001, arXiv:1508.07846.

[72] Belle collaboration, C. P. Shen *et al.*, *Evidence for a new resonance and search for the Y(4140) in the $\gamma\gamma \to \phi J/\psi$ process*, Phys. Rev. Lett. **104** (2010) 112004, arXiv:0912.2383.

[73] Belle collaboration, P. Pakhlov *et al.*, *Production of New Charmoniumlike States in $e^+e^- \to J/\psi D^{(*)}\overline{D}^{(*)}$ at $\sqrt{s} \approx 10.6$ GeV*, Phys. Rev. Lett. **100** (2008) 202001, arXiv:0708.3812.

[74] Belle collaboration, K. Chilikin *et al.*, *Observation of an alternative $\chi_{c0}(2P)$ candidate in $e^+e^- \to J/\psi D\bar{D}$*, Phys. Rev. **D95** (2017) 112003, arXiv:1704.01872.

[75] BaBar collaboration, B. Aubert *et al.*, *The $e^+e^- \to \pi^+\pi^-\pi^+\pi^-$, $K^+K^-\pi^+\pi^-$, and $K^+K^-K^+K^-$ cross sections at center-of-mass energies 0.5-GeV - 4.5-GeV measured with initial-state radiation*, Phys. Rev. **D71** (2005) 052001, arXiv:hep-ex/0502025.

[76] CLEO collaboration, T. E. Coan *et al.*, *Charmonium decays of $Y(4260)$, $\psi(4160)$ and $\psi(4040)$*, Phys. Rev. Lett. **96** (2006) 162003, arXiv:hep-ex/0602034.

[77] Belle collaboration, C. Z. Yuan *et al.*, *Measurement of $e^+e^- \to \pi^+\pi^- J/\psi$ cross-section via initial state radiation at Belle*, Phys. Rev. Lett. **99** (2007) 182004, arXiv:0707.2541.

[78] Belle collaboration, Z. Q. Liu *et al.*, *Study of $e^+e^- \to \pi^+\pi^- J/\psi$ and Observation of a Charged Charmoniumlike State at Belle*, Phys. Rev. Lett. **110** (2013) 252002, arXiv:1304.0121.

[79] BaBar collaboration, B. Aubert *et al.*, *Evidence of a broad structure at an invariant mass of 4.32 GeV/c^2 in the reaction $e^+e^- \to \pi^+\pi^-\psi(2S)$ measured at BaBar*, Phys. Rev. Lett. **98** (2007) 212001, arXiv:hep-ex/0610057.

[80] Belle collaboration, X. L. Wang *et al.*, *Observation of Two Resonant Structures in $e^+e^- \to \pi^+\pi^-\psi(2S)$ via Initial State Radiation at Belle*, Phys. Rev. Lett. **99** (2007) 142002, arXiv:0707.3699.

[81] BaBar collaboration, J. P. Lees *et al.*, *Study of the reaction $e^+e^- \to \psi(2S)\pi^-\pi^-$ via initial-state radiation at BaBar*, Phys. Rev. **D89** (2014) 111103, arXiv:1211.6271.

[82] Belle collaboration, G. Pakhlova *et al.*, *Observation of a near-threshold enhancement in the $e^+e^- \to \Lambda_c^+\Lambda_c^-$ cross section using initial-state radiation*, Phys. Rev. Lett. **101** (2008) 172001, arXiv:0807.4458.

[83] BESIII collaboration, M. Ablikim *et al.*, *Measurement of the $e^+e^- \to \eta J/\psi$ cross section and search for $e^+e^- \to \pi^0 J/\psi$ at center-of-mass energies between 3.810 and 4.600 GeV*, Phys. Rev. **D91** (2015) 112005, arXiv:1503.06644.

[84] BESIII collaboration, M. Ablikim *et al.*, *Study of $e^+e^- \to \omega\chi_{cJ}$ at center-of-mass energies from 4.21 to 4.42 GeV*, Phys. Rev. Lett. **114** (2015) 092003, arXiv:1410.6538.

[85] BESIII collaboration, M. Ablikim *et al.*, *Precise measurement of the $e^+e^- \to \pi^+\pi^- J/\psi$ cross section at center-of-mass energies from 3.77 to 4.60 GeV*, Phys. Rev. Lett. **118** (2017) 092001, arXiv:1611.01317.

[86] W.-S. Hou, *Searching for the bottom counterparts of $X(3872)$ and $Y(4260)$ via $\pi^+\pi^-\Upsilon$*, Phys. Rev. **D74** (2006) 017504, arXiv:hep-ph/0606016.

[87] Belle collaboration, D. Santel *et al.*, *Measurements of the $\Upsilon(10860)$ and $\Upsilon(11020)$ resonances via $\sigma(e^+e^- \to \Upsilon(nS)\pi^+\pi^-)$*, Phys. Rev. **D93** (2016) 011101, arXiv:1501.01137.

[88] Belle collaboration, K. F. Chen *et al.*, *Observation of anomalous $\Upsilon(1S)\pi^+\pi^-$ and $\Upsilon(2S)\pi^+\pi^-$ production near the $\Upsilon(5S)$ resonance*, Phys. Rev. Lett. **100** (2008) 112001, arXiv:0710.2577.

[89] Belle collaboration, S. K. Choi *et al.*, *Observation of a resonance-like structure in the $\pi^\pm\psi'$ mass distribution in exclusive $B \to K\pi^\pm\psi'$ decays*, Phys. Rev. Lett. **100** (2008) 142001, arXiv:0708.1790.

[90] BaBar collaboration, B. Aubert *et al.*, *Search for the $Z(4430)^-$ at BABAR*, Phys. Rev. **D79** (2009) 112001, arXiv:0811.0564.

[91] Belle collaboration, R. Mizuk *et al.*, *Dalitz analysis of $B \to K\pi^+\psi'$ decays and the $Z(4430)^+$*, Phys. Rev. **D80** (2009) 031104, arXiv:0905.2869.

[92] Belle collaboration, K. Chilikin *et al.*, *Experimental constraints on the spin and parity of the $Z(4430)^+$*, Phys. Rev. **D88** (2013) 074026, arXiv:1306.4894.

[93] P. Pakhlov and T. Uglov, *Charged charmonium-like $Z^+(4430)$ from rescattering in conventional B decays*, Phys. Lett. **B748** (2015) 183, arXiv:1408.5295.

[94] Belle collaboration, K. Chilikin *et al.*, *Observation of a new charged charmoniumlike state in $\bar{B}^0 \to J/\psi K^- \pi^+$ decays*, Phys. Rev. **D90** (2014) 112009, arXiv:1408.6457.

[95] Belle collaboration, R. Mizuk *et al.*, *Observation of two resonance-like structures in the $\pi^+ \chi_{c1}$ mass distribution in exclusive $\bar{B}^0 \to K^- \pi^+ \chi_{c1}$ decays*, Phys. Rev. **D78** (2008) 072004, arXiv:0806.4098.

[96] BaBar collaboration, J. P. Lees *et al.*, *Search for the $Z_1(4050)^+$ and $Z_2(4250)^+$ states in $\bar{B}^0 \to \chi_{c1} K^- \pi^+$ and $B^+ \to \chi_{c1} K^0_S \pi^+$*, Phys. Rev. **D85** (2012) 052003, arXiv:1111.5919.

[97] Belle collaboration, A. Bondar *et al.*, *Observation of two charged bottomonium-like resonances in $\Upsilon(5S)$ decays*, Phys. Rev. Lett. **108** (2012) 122001, arXiv:1110.2251.

[98] Belle collaboration, P. Krokovny *et al.*, *First observation of the $Z_b^0(10610)$ in a Dalitz analysis of $\Upsilon(10860) \to \Upsilon(nS)\pi^0\pi^0$*, Phys. Rev. **D88** (2013) 052016, arXiv:1308.2646.

[99] BESIII collaboration, M. Ablikim *et al.*, *Observation of a charged charmoniumlike structure in $e^+e^- \to \pi^+\pi^- J/\psi$ at $\sqrt{s}$=4.26 GeV*, Phys. Rev. Lett. **110** (2013) 252001, arXiv:1303.5949.

[100] T. Xiao, S. Dobbs, A. Tomaradze, and K. K. Seth, *Observation of the Charged Hadron $Z_c^{\pm}(3900)$ and Evidence for the Neutral $Z_c^0(3900)$ in $e^+e^- \to \pi\pi J/\psi$ at $\sqrt{s} = 4170$ MeV*, Phys. Lett. **B727** (2013) 366, arXiv:1304.3036.

[101] BESIII collaboration, M. Ablikim *et al.*, *Observation of a charged $(D\bar{D}^*)^{\pm}$ mass peak in $e^+e^- \to \pi D\bar{D}^*$ at $\sqrt{s} = 4.26$ GeV*, Phys. Rev. Lett. **112** (2014) 022001, arXiv:1310.1163.

[102] BESIII collaboration, M. Ablikim *et al.*, *Observation of $Z_c(3900)^0$ in $e^+e^- \to \pi^0\pi^0 J/\psi$*, Phys. Rev. Lett. **115** (2015) 112003, arXiv:1506.06018.

[103] BESIII collaboration, M. Ablikim *et al.*, *Observation of a Neutral Structure near the $D\bar{D}^*$ Mass Threshold in $e^+e^- \to (D\bar{D}^*)^0\pi^0$ at $\sqrt{s} = 4.226$ and 4.257 GeV*, Phys. Rev. Lett. **115** (2015) 222002, arXiv:1509.05620.

[104] BESIII collaboration, M. Ablikim *et al.*, *Observation of a Charged Charmoniumlike Structure $Z_c(4020)$ and Search for the $Z_c(3900)$ in $e^+e^- \to \pi^+\pi^- h_c$*, Phys. Rev. Lett. **111** (2013) 242001, arXiv:1309.1896.

[105] BESIII collaboration, M. Ablikim *et al.*, *Observation of $e^+e^- \to \pi^0\pi^0 h_c$ and a Neutral Charmoniumlike Structure $Z_c(4020)^0$*, Phys. Rev. Lett. **113** (2014) 212002, arXiv:1409.6577.

[106] BESIII collaboration, M. Ablikim *et al.*, *Observation of a charged charmoniumlike structure in $e^+e^- \to (D^*\bar{D}^*)^{\pm}\pi^{\mp}$ at $\sqrt{s} = 4.26$ GeV*, Phys. Rev. Lett. **112** (2014) 132001, arXiv:1308.2760.

[107] R. L. Jaffe, *Multiquark hadrons. I. Phenomenology of $Q^2\bar{Q}^2$ mesons*, Phys. Rev. **D15** (1977) 267.

[108] S. Dubynskiy and M. B. Voloshin, *Hadro-charmonium*, Phys. Lett. **B666** (2008) 344, arXiv:0803.2224.

[109] S. Dubynskiy, A. Gorsky, and M. B. Voloshin, *Holographic hadro-quarkonium*, Phys. Lett. **B671** (2009) 82, arXiv:0804.2244.

[110] E. Braaten and M. Lu, *Line shapes of the X(3872)*, Phys. Rev. **D76** (2007) 094028, arXiv:0709.2697.

[111] ATLAS collaboration, G. Aad *et al.*, *Observation of a new particle in the search for the Standard Model Higgs boson with the ATLAS detector at the LHC*, Phys. Lett. **B716** (2012) 1, arXiv:1207.7214.

[112] CMS collaboration, S. Chatrchyan *et al.*, *Observation of a new boson at a mass of 125 GeV with the CMS experiment at the LHC*, Phys. Lett. **B716** (2012) 30, arXiv:1207.7235.

[113] L. Evans and P. Bryant, *LHC Machine*, JINST **3** (2008) S08001.

[114] Pierre Auger collaboration, P. Abreu *et al.*, *Measurement of the proton-air cross-section at $\sqrt{s} = 57$ TeV with the Pierre Auger Observatory*, Phys. Rev. Lett. **109** (2012) 062002, arXiv:1208.1520.

[115] T. Sjöstrand, S. Mrenna, and P. Skands, *A brief introduction to PYTHIA 8.1*, Comput. Phys. Commun. **178** (2008) 852, arXiv:0710.3820.

[116] R. Aaij *et al.*, *Performance of the LHCb Vertex Locator*, JINST **9** (2014) P09007, arXiv:1405.7808.

[117] LHCb collaboration, P. R. Barbosa-Marinho *et al.*, *LHCb inner tracker: Technical Design Report*, Technical Design Report LHCb, CERN, Geneva, 2002. revised version number 1 submitted on 2002-11-13 14:14:34.

[118] LHCb collaboration, P. R. Barbosa-Marinho *et al.*, *LHCb outer tracker: Technical Design Report*, Technical Design Report LHCb, CERN, Geneva, 2001.

[119] LHCb collaboration, R. Aaij *et al.*, *LHCb detector performance*, Int. J. Mod. Phys. **A30** (2015) 1530022, arXiv:1412.6352.

[120] M. Adinolfi *et al.*, *Performance of the LHCb RICH detector at the LHC*, Eur. Phys. J. **C73** (2013) 2431, arXiv:1211.6759.

[121] P. A. Cherenkov, *Visible luminescence of pure liquids under the influence of γ-radiation*, Dokl. Akad. Nauk SSSR **2** (1934) 451, [Usp. Fiz. Nauk93,no.2,385(1967)].

[122] I. M. Frank and I. E. Tamm, *Coherent visible radiation of fast electrons passing through matter*, Compt. Rend. Acad. Sci. URSS **14** (1937) 109, [Usp. Fiz. Nauk93,no.2,388(1967)].

[123] R. Aaij *et al.*, *Performance of the LHCb calorimeters*, LHCb-DP-2013-004, in preparation.

[124] A. A. Alves Jr. *et al.*, *Performance of the LHCb muon system*, JINST **8** (2013) P02022, arXiv:1211.1346.

[125] A. Puig, *The LHCb trigger in 2011 and 2012*, LHCb-PUB-2014-046, do not cite this note in a paper. Its purpoe is to document the trigger for data preservation.

[126] D. R. Myers, *The LHC experiments' joint controls project, JCOP*, in *Proceedings, 7h International Conference on Accelerator and Large Experimental Physics Control Systems (ICALEPCS 1999): Trieste, Italy, October 4-8, 1999*, vol. C991004, pp. 633–635, 1999.

[127] *WinCC-OA*, https://w3.siemens.com/mcms/human-machine-interface/en/visualization-software/scada/pages/default.aspx.

[128] The LHCb Collaboration, *The Moore Project*, http://lhcbdoc.web.cern.ch/lhcbdoc/moore/.

[129] The LHCb Collaboration, *The Brunel Project*, http://lhcbdoc.web.cern.ch/lhcbdoc/brunel/.

[130] The LHCb Collaboration, *The DaVinci Project*, http://lhcbdoc.web.cern.ch/lhcbdoc/davinci/.

[131] The LHCb Collaboration, *The Gauss Project*, http://lhcbdoc.web.cern.ch/lhcbdoc/gauss/.

[132] The LHCb Collaboration, *The Boole Project*, http://lhcbdoc.web.cern.ch/lhcbdoc/boole/.

[133] The LHCb Collaboration, *The Gaudi Project*, http://gaudi.web.cern.ch/gaudi/.

[134] Belle collaboration, Z. Q. Liu *et al.*, *Study of $e^+e^- \to \pi^+\pi^- J/\psi$ and observation of a charged charmoniumlike state at Belle*, Phys. Rev. Lett. **110** (2013) 252002, Erratum ibid. **111** (2013) 019901, arXiv:1304.0121.

[135] T. Xiao, S. Dobbs, A. Tomaradze, and K. K. Seth, *Observation of the charged hadron $Z_c^{\pm}(3900)$ and evidence for the neutral $Z_c^0(3900)$ in $e^+e^- \to \pi^+\pi^- J/\psi$ at $\sqrt{s} = 4170\,\text{MeV}$*, Phys. Lett. **B727** (2013) 366, arXiv:1304.3036.

[136] M. B. Voloshin, *$Z_c(3900)$—what is inside?*, Phys. Rev. **D87** (2013) 091501, arXiv:1304.0380.

[137] E. Braaten, *How the $Z_c(3900)$ reveals the spectra of charmonium hybrids and tetraquarks*, Phys. Rev. Lett. **111** (2013) 162003, arXiv:1305.6905.

[138] Hadron Spectrum collaboration, L. Liu *et al.*, *Excited and exotic charmonium spectroscopy from lattice QCD*, JHEP **07** (2012) 126, arXiv:1204.5425.

[139] Hadron Spectrum collaboration, G. K. C. Cheung *et al.*, *Excited and exotic charmonium, D_s and D meson spectra for two light quark masses from lattice QCD*, JHEP **12** (2016) 089, arXiv:1610.01073.

[140] L. Maiani, F. Piccinini, A. D. Polosa, and V. Riquer, *Diquark-antidiquarks with hidden or open charm and the nature of X(3872)*, Phys. Rev. **D71** (2005) 014028, arXiv:hep-ph/0412098.

[141] Z. Yang, Q. Wang, and U.-G. Meißner, *Isospin analysis of $B \to D^* \bar{D} K$ and the absence of the $Z_c(3900)$ in B decays*, Phys. Lett. **B775** (2017) 50, arXiv:1706.00960.

[142] COMPASS, A. Guskov, *Search for exclusive photoproduction of $Z_c(3900)$ at COMPASS*, PoS **EPS-HEP2015** (2015) 440, arXiv:1511.02832.

[143] HAL QCD, Y. Ikeda *et al.*, *Fate of the Tetraquark Candidate $Z_c(3900)$ from Lattice QCD*, Phys. Rev. Lett. **117** (2016) 242001, arXiv:1602.03465.

[144] S. Prelovsek, C. B. Lang, L. Leskovec, and D. Mohler, *Study of the Z_c^+ channel using lattice QCD*, Phys. Rev. **D91** (2015) 014504, arXiv:1405.7623.

[145] JPAC, A. Pilloni *et al.*, *Amplitude analysis and the nature of the $Z_c(3900)$*, Phys. Lett. **B772** (2017) 200, arXiv:1612.06490.

[146] J. Back *et al.*, LAURA^{++}*: A Dalitz plot fitter*, Comput. Phys. Commun. **231** (2018) 198, arXiv:1711.09854.

[147] R. H. Dalitz, *On the analysis of τ-meson data and the nature of the τ-meson*, Phil. Mag. **44** (1953) 1068.

[148] B. Meadows, *Low mass S-wave $K\pi$ and $\pi\pi$ systems*, eConf **C070805** (2007) 27, arXiv:0712.1605.

[149] D. Aston *et al.*, *A study of $K^-\pi^+$ scattering in the reaction $K^-p \to K^-\pi^+n$ at 11 GeV/c*, Nucl. Phys. **B296** (1988) 493.

[150] E. Ben-Haim, R. Brun, B. Echenard, and T. E. Latham, *JFIT: A framework to obtain combined experimental results through joint fits*, arXiv:1409.5080.

[151] W. D. Hulsbergen, *Decay chain fitting with a Kalman filter*, Nucl. Instrum. Meth. **A552** (2005) 566, arXiv:physics/0503191.

[152] L. Breiman, J. H. Friedman, R. A. Olshen, and C. J. Stone, *Classification and regression trees*, Wadsworth international group, Belmont, California, USA, 1984.

[153] Y. Freund and R. E. Schapire, *A decision-theoretic generalization of on-line learning and an application to boosting*, J. Comput. Syst. Sci. **55** (1997) 119.

[154] W. Verkerke, D. Kirkby, *The RooFit toolkit for data modeling*, arXiv:physics/0306116.

[155] M. Pivk and F. R. Le Diberder, *sPlot: A statistical tool to unfold data distributions*, Nucl. Instrum. Meth. **A555** (2005) 356, arXiv:physics/0402083.

[156] R. Aaij *et al.*, *Selection and processing of calibration samples to measure the particle identification performance of the LHCb experiment in Run 2*, arXiv:1803.00824.

[157] LHCb collaboration, *Framework TDR for the LHCb Upgrade: Technical Design Report*, CERN-LHCC-2012-007.

[158] LHCb collaboration, R. Aaij *et al.*, *Measurement of the $B^0_s \to \mu^+\mu^-$ branching fraction and effective lifetime and search for $B^0 \to \mu^+\mu^-$ decays*, Phys. Rev. Lett. **118** (2017) 191801, arXiv:1703.05747.

[159] LHCb collaboration, R. Aaij *et al.*, *Test of lepton universality with $B^0 \to K^{*0}\ell^+\ell^-$ decays*, JHEP **08** (2017) 055, arXiv:1705.05802.

[160] BaBar collaboration, J. P. Lees *et al.*, *Measurement of an Excess of $\bar{B} \to D^{(*)}\tau^-\bar{\nu}_\tau$ Decays and Implications for Charged Higgs Bosons*, Phys. Rev. **D88** (2013) 072012, arXiv:1303.0571.

[161] Belle collaboration, M. Huschle *et al.*, *Measurement of the branching ratio of $\bar{B} \to D^{(*)}\tau^-\bar{\nu}_\tau$ relative to $\bar{B} \to D^{(*)}\ell^-\bar{\nu}_\ell$ decays with hadronic tagging at Belle*, Phys. Rev. **D92** (2015) 072014, arXiv:1507.03233.

[162] Belle collaboration, Y. Sato *et al.*, *Measurement of the branching ratio of $\bar{B}^0 \to D^{*+}\tau^-\bar{\nu}_\tau$ relative to $\bar{B}^0 \to D^{*+}\ell^-\bar{\nu}_\ell$ decays with a semileptonic tagging method*, Phys. Rev. **D94** (2016) 072007, arXiv:1607.07923.

[163] LHCb collaboration, R. Aaij *et al.*, *Measurement of the ratio of branching fractions $\mathcal{B}(\overline{B}^0 \to D^{*+}\tau^-\overline{\nu}_\tau)/\mathcal{B}(\overline{B}^0 \to D^{*+}\mu^-\overline{\nu}_\mu)$*, Phys. Rev. Lett. **115** (2015) 111803, Publisher's Note ibid. **115** (2015) 159901, arXiv:1506.08614.

[164] LHCb collaboration, R. Aaij *et al.*, *Measurement of the ratio of the $\mathcal{B}(B^0 \to D^{*-}\tau^+\nu_\tau)$ and $\mathcal{B}(B^0 \to D^{*-}\mu^+\nu_\mu)$ branching fractions using three-prong τ-lepton decays*, Phys. Rev. Lett. **120** (2018) 171802, arXiv:1708.08856.

[165] LHCb collaboration, R. Aaij *et al.*, *Measurement of the ratio of branching fractions $\mathcal{B}(B_c^+ \to J/\psi\tau^+\nu_\tau)/\mathcal{B}(B_c^+ \to J/\psi\mu^+\nu_\mu)$*, Phys. Rev. Lett. **120** (2018) 121801, arXiv:1711.05623.

[166] LHCb collaboration, *LHCb Trigger and Online Technical Design Report*, CERN-LHCC-2014-016.

[167] F. Alessio and R. Jacobsson, *System-level Specifications of the Timing and Fast Control system for the LHCb Upgrade*, .

[168] P. Moreira *et al.*, *The GBT-SerDes ASIC prototype*, JINST **5** (2010) C11022.

[169] LHCb collaboration, *LHCb VELO Upgrade Technical Design Report*, CERN-LHCC-2013-021.

[170] LHCb collaboration, *LHCb Tracker Upgrade Technical Design Report*, CERN-LHCC-2014-001.

[171] LHCb collaboration, *LHCb PID Upgrade Technical Design Report*, CERN-LHCC-2013-022.

[172] C. Soos *et al.*, *The Versatile transceiver: Towards production readiness*, JINST **8** (2013) C03004.

[173] LHCb RICH, S. Easo, *Overview of LHCb-RICH upgrade*, Nucl. Instrum. Meth. **A876** (2017) 160.

[174] M. K. Baszczyk *et al.*, *Test of the photon detection system for the LHCb RICH Upgrade in a charged particle beam*, JINST **12** (2017) P01012, arXiv:1610.02879.

[175] C. Gaspar *et al.*, *Configuring and automating an LHC experiment for faster and better physics output*, in *Proceedings, 16th International Conference on Accelerator and Large Experimental Physics Control Systems (ICALEPCS 2017): Barcelona, Spain, October 8-13, 2017*, p. THDPL01, 2018. doi: 10.18429/JACoW-ICALEPCS2017-THDPL01.

[176] M. Clemencic, *LHCb distributed conditions database*, J. Phys. Conf. Ser. **119** (2008) 072010.

[177] L. Abadie *et al.*, *The LHCb configuration database*, in *Proceedings, 10th International Conference on Accelerator and Large Experimental Physics Control systems (ICALEPCS 2005): Geneva, Switzerland, October 10-14, 2005*, pp. MO4A.2–7O, 2005.

[178] https://www.oracle.com/customers/viewpoints/cern.html.

[179] B. Franek and C. Gaspar, *SMI++ object oriented framework for designing and implementing distributed control systems*, IEEE Trans. Nucl. Sci. **45** (1998) 1946.

[180] C. Gaspar, M. Dönszelmann, and P. Charpentier, *DIM, a portable, light weight package for information publishing, data transfer and inter-process communication*, Comput. Phys. Commun. **140** (2001) 102.

[181] https://edms.cern.ch/ui/file/684947/LAST_RELEASED/ElmbUserGuide.pdf.

[182] LHCb, R. Aaij *et al.*, *Evidence for an $\eta_c(1S)\pi^-$ resonance in $B^0 \to \eta_c(1S)K^+\pi^-$ decays*, Submitted to: Eur. Phys. J. (2018) arXiv:1809.07416.

[183] *LHCb discovers two new baryons*, https://cerncourier.com/lhcb-discovers-two-new-baryons/.